DIGITAL ACCESS TO SCHOLARSHIP AT HARVARD
DASH.HARVARD.EDU

HARVARD LIBRARY
Office for Scholarly Communication

A genetic dissection of the interactions between the CbtA toxin of Escherichia coli and the bacterial cytoskeleton

Citation

Heller, Danielle M. 2016. A genetic dissection of the interactions between the CbtA toxin of Escherichia coli and the bacterial cytoskeleton. Doctoral dissertation, Harvard University, Graduate School of Arts & Sciences.

Permanent link
http://nrs.harvard.edu/urn-3:HUL.InstRepos:33840744

Terms of Use
This article was downloaded from Harvard University's DASH repository, and is made available under the terms and conditions applicable to Other Posted Material, as set forth at http://nrs.harvard.edu/urn-3:HUL.InstRepos:dash.current.terms-of-use#LAA

Share Your Story
The Harvard community has made this article openly available.
Please share how this access benefits you. Submit a story .

Accessibility

A genetic dissection of the interactions between the CbtA toxin of *Escherichia coli* and the bacterial cytoskeleton

A dissertation presented

by

Danielle Marie Heller

to

The Division of Medical Sciences

in partial fulfillment of the requirements

for the degree of

Doctor of Philosophy

in the subject of

Genetics and Genomics

Harvard University

Cambridge, Massachusetts

August 2016

© 2016 Danielle Marie Heller

All rights reserved.

Dissertation Advisor: Professor Ann Hochschild Danielle Marie Heller

A genetic dissection of the interactions between the CbtA toxin of *Escherichia coli* and the bacterial cytoskeleton

Abstract

Prokaryotic chromosomal toxin-antitoxin (TA) systems, consisting of a stable toxin and a labile, cotranscribed antitoxin, have been shown to target a number of essential processes in bacteria. The *Escherichia coli* genome encodes multiple chromosomal TA systems, including a family of three homologous systems, *cbtA/cbeA*, *ykfI/yafW*, and *ypjF/yfjZ*, that targets the bacterial cytoskeleton. Upon overproduction of the CbtA, YkfI, or YpjF toxins, *E. coli* cells adopt a lemon-like morphology, reminiscent of that seen upon simultaneous inhibition of cell division and cell elongation pathways. Consistent with this observed morphology, previously published work has shown that the CbtA toxin interacts with both the tubulin-homolog FtsZ, the master regulator of cell division, and the actin-homolog MreB, an essential cell elongation factor. Despite these findings, it has not been demonstrated that the interactions of CbtA with MreB and FtsZ are directly responsible for its observed cellular toxicity, nor have any mechanistic details been revealed. The goal of this research was to elucidate the molecular basis for CbtA toxicity by genetically characterizing the interactions between CbtA and its cytoskeletal targets.

By means of a transcription-based bacterial two-hybrid system, we can detect interactions between CbtA and both FtsZ and MreB. In Chapter 2 of this dissertation, I describe the isolation and characterization of two CbtA mutants, each of which interacts with only a single cytoskeletal target. CbtA-F65S is unable to bind FtsZ, but maintains interaction with MreB, whereas CbtA-R15C exhibits the reverse interaction profile. Morphological observation of cells overproducing each of these variants establishes that the observed effects of CbtA on cell division and cell elongation are genetically separable. I show further that in combination, the substitutions F65S and R15C alleviate the toxicity of CbtA, consistent with the premise that CbtA toxicity depends on its interactions with both FtsZ and MreB.

In Chapters 3 and 4, I describe our efforts to map the CbtA-binding determinants on FtsZ and MreB, respectively. Through bacterial two-hybrid studies and the development of a *Bacillus subtilis*

heterologous system, we have identified the H6/H7 loop of FtsZ as the CbtA-binding site and provided additional evidence that the CbtA-FtsZ interaction contributes directly to the observed cellular toxicity. Two-hybrid studies indicate that YkfI and YpjF also interact with the H6/H7 loop of FtsZ, and we believe that this represents a new FtsZ inhibitory interaction. Based on FtsZ structural studies, the H6/H7 loop is thought to be important for FtsZ protofilament formation, and thus we propose that CbtA binding to this surface loop blocks FtsZ polymerization. Furthermore, residues in this loop have been implicated in FtsZ bundling, suggesting that CbtA may also inhibit the formation of stabilizing lateral interactions. We employed similar genetic methods to characterize the interaction between MreB and CbtA. Two-hybrid and morphology data presented in Chapter 4 of this dissertation suggest that CbtA interacts with the flat MreB surface that mediates formation of the functionally active MreB double filament. In total, the genetic analysis presented in this dissertation establishes that CbtA toxicity depends on independent interactions of CbtA with the tubulin homolog FtsZ and the actin homolog MreB, as well as providing molecular insight into the basis of this dual inhibitory action.

Table of Contents

Title page i
Copyright page ii
Abstract iii
Table of contents v
List of figures vii
List of tables viii
Acknowledgements ix

Chapter 1: Introduction 1
  Chapter 1.1: Overview 1
  Chapter 1.2: Prokaryotic toxin-antitoxin systems exhibit diversity in regulation and targets 2
  Chapter 1.3: TA systems in plasmid maintenance and bacterial stress response 6
  Chapter 1.4: Rod-shape determination and the bacterial cytoskeleton 9
  Chapter 1.5: CbtA (YeeV), YpjF, and YkfI are a family of toxins that inhibit *E. coli* growth 11
  Chapter 1.6: CbtA (YeeV) causes a striking lemon-shape phenotype 13
  Chapter 1.7: Conflicting reports on the mechanism of the CbeA (YeeU) antitoxin 14
  Chapter 1.8: A testable model of CbtA toxicity 15

Chapter 2: The CbtA toxin mediates a simultaneous block of cell division and cell elongation via independent interactions with both FtsZ and MreB 25
  Chapter 2.1: The CbtA toxin of *E. coli* alters cell shape and interacts with the bacterial cytoskeleton 25
  Chapter 2.2: Results 28
    CbtA interacts with FtsZ and MreB and produces lemon-shaped cells 28
    Identification of a CbtA variant that interacts only with MreB 32
    Identification of a CbtA variant that interacts only with FtsZ 38
    The CbtA-R15C/F65S variant exhibits reduced toxicity 42
    CbtA-R15C disrupts Z rings 45
  Chapter 2.3: Discussion 45
  Chapter 2.4: Materials and Methods 48
  Chapter 2.5: References 60

Chapter 3: CbtA interacts directly with the H6/H7 loop of *E. coli* FtsZ 64
  Chapter 3.1: Introduction to the regulated assembly of FtsZ filaments 64
    The FtsZ subunit 65
    FtsZ polymerization and *in vitro* assembly 67
    In vivo observation of the Z ring 69
    Modulation of FtsZ assembly by positive and negative regulators 70
    FtsA and ZipA anchor *E. coli* FtsZ in the inner membrane 70
    Z ring stabilization 70
    Division site selection 72
    Inhibition of FtsZ assembly in response to the environment 73
    Motivation for the current study 75
  Chapter 3.2: Results 76
    E. coli FtsZ interacts with CbtA, ZipA, and itself in a transcription-based bacterial two-hybrid system 76
    CbtA maintains interaction with an FtsZ variant lacking the C-terminal tail domain 78
    Substitutions in the H6/H7 loop of FtsZ disrupt the FtsZ-CbtA interaction 78
    CbtA interacts directly with the H6/H7 loop of FtsZ 82
    CbtA homologs, YpjF and YkfI, also interact with the H6/H7 loop of FtsZ 84
  Chapter 3.3: Discussion 88
    CbtA interacts directly with the H6/H7 loop of *E. coli* FtsZ 88
    Genetic insight into the mechanism of CbtA-mediated cell division inhibition 89
    The H6/H7 loop represents a new inhibitory surface on FtsZ 90

Chapter 3.4: Materials and Methods **91**
Chapter 3.5: References **98**

Chapter 4: Genetic evidence suggests CbtA may interact with the MreB double filament interface 107
Chapter 4.1: The enigmatic MreB filament and its role in cell elongation **107**
The original model: the bacterial actin MreB forms helical filaments 108
The updated model: disconnected complexes and a unique double filament architecture 111
Membrane-bound MreB patches display circumferential rotation 111
MreB forms an antiparallel double protofilament 113
Motivation for the current study 116
Chapter 4.2: Results **116**
Substitutions in MreB that decrease CbtA interaction map to the double filament interface 116
MreB residue E262 is necessary for CbtA and YpjF inhibition of cell elongation 124
Chapter 4.3: Discussion **130**
The flat surface of the MreB subunit represents a putative CbtA-binding site 130
Genetic insight into the CbtA mechanism of cell elongation inhibition 134
Chapter 4.4: Materials and Methods **136**

Chapter 5: Mechanistic insights and contextual unknowns 155
Chapter 5.1: Summary of our findings and mechanistic considerations **155**
Chapter 5.2: CbtA in context **157**
Chapter 5.3: References **159**

Appendix 1: Supplemental results and methods for Chapter 3 161
Appendix 1.1: Supplemental results **161**
Description of additional α-FtsZ mutants identified in genetic screen for decreased FtsZ-CbtA interaction 161
ftsZ-L169P, *ftsZ-D180N*, and *ftsZ-S177P* complement growth of an *ftsZ* complementation strain. 161
Microscopic observation of *B. subtilis* strains 164
Appendix 1.2: Supplemental Methods **170**
Appendix 1.3: References **180**

List of Figures

Chapter 1:

Figure 1.1: There are six classes of TA systems 4
Figure 1.2: CbtA (YeeV), YpjF, and YkfI are a family of toxin proteins 12

Chapter 2:

Figure 2.1: Overproduction of CbtA causes lemon-like morphology 29
Figure 2.2: Detection of CbtA interaction with FtsZ and MreB in a transcription-based bacterial two-hybrid system 30
Figure 2.3: YpjF and YkfI cause lemon-like morphology 33
Figure 2.4: Toxin variants containing the F65S substitution interact only with MreB 36
Figure 2.5: CbtA-R15C inhibits cell division 40
Figure 2.6: CbtA-R15C/F65S has reduced toxicity and does not affect ZapA-GFP localization 43

Chapter 3:

Figure 3.1: The FtsZ subunit and protofilament 66
Figure 3.2: FtsZΔ66 interaction with ZipA-CTD, FtsZ, and CbtA 77
Figure 3.3: Residues in the H6/H7 loop are necessary for CbtA-FtsZ interaction 80
Figure 3.4: CbtA-V48E and FtsZ-D180K interact in an allele-specific manner 83
Figure 3.5: CbtA interacts with chimeric BsFtsZ containing the *E. coli* H6/H7 loop 85
Figure 3.6: YkfI and YpjF interact with chimeric BsFtsZ containing the *E. coli* H6/H7 loop 87

Chapter 4:

Figure 4.1: The bacterial actin MreB forms antiparallel filament pairs 110
Figure 4.2: MreB interacts with the N-terminal domain of RodZ in a transcription-based bacterial two-hybrid system 117
Figure 4.3: Substitutions in the MreB double filament interface alter CbtA interaction 119
Figure 4.4: Substitutions that alter CbtA binding cluster to the inter-protofilament interface of MreB 122
Figure 4.5: Assessment of the ability of MreB interface mutants to support rod-shaped growth 126
Figure 4.6: MreB residue E262 is necessary for CbtA-F65S toxicity and cell elongation inhibition 128
Figure 4.7: Residues at the MreB inter-protofilament interface are necessary for the YpjF-MreB interaction 131

Appendix I:

Figure A1.1: Mutation of FtsZ residues G19 and G22 decreases interaction with CbtA 162
Figure A1.2: Complementation phenotypes of H6/H7 loop mutant alleles 165
Figure A1.3: CbtA is not toxic in strains with wild-type *ftsZ* 166
Figure A1.4: CbtA overproduction leads to increased lysis in chimera strain 168

List of Tables

Chapter 2:

Table 2.1: Strains used in this study 54
Table 2.2: Plasmids used in this study 55
Table 2.3: Important oligonucleotides used in this study 58

Chapter 4:

Table 4.1: Summary of two-hybrid interactions of α-MreB mutants 121
Table 4.1: Strains used in this study 141
Table 4.2: Plasmids used in this study 142
Table 4.3: Important oligonucleotides used in this study 145

Appendix I:

Table A1.1: Strains used in this study 172
Table A1.2: Plasmids used in this study 173
Table A1.3: Important oligonucleotides used in this study 177

Acknowledgements:

I unwittingly scheduled my dissertation defense on the six-year anniversary of the day I started graduate school. This timing seems like a serendipitous alignment of calendars, yet at the same time feels somewhat incongruous. It is hard to believe that such a rich, challenging, and at times emotionally turbulent experience can fit so neatly into such an even interval. Looking back across those six years, I can see that there are so many people to thank for enhancing my experience and helping to transform me from the unsure 22-year old college graduate into the person and scientist I am today.

First and foremost, I must express my tremendous gratitude to my thesis advisor Ann Hochschild, a person who truly deserves the title of mentor. She is the rare intersection of a brilliant scientific mind, a great communicator, and a caring supporter. Thank you Ann, for the stellar scientific education, the constant words of encouragement, and for the unmatched guidance you have provided over the years. I must also thank Ann for fostering such a positive work environment filled with incredible scientists. Thank you to all the members of the Hochschild lab, both past and present, for providing helpful scientific discussions, a healthy dose of sarcasm, and engaging lunch conversations over the years. Special thanks to Viknesh Sivanathan (Vicky) for the constant laughter, the practical jokes, and most importantly for the scientific and personal counseling (always delivered with a sharp wit and a sincere heart).

I must also thank the members of my DAC (Tom Bernhardt, Simon Dove, and Rich Losick) for their scientific advice over the years, the Program in Genetics and Genomics and Fred Winston for exposing me to all things genetics and providing a wonderful community in which to talk about science, and the BBS office for their incomparable help (always provided with an infectious smile and laugh). Thank you to the MBIB department for being a fun and supportive community, the Journal of Emerging Investigators for giving me a rewarding outlet over the years, and Padraig Deighan and the faculty of Emmanuel College for the teaching opportunities that have helped to shape my future career goals.

Thank you to the friends I have made over the past 6 years, both in my class and in the outside world, for always reminding me that a failed experiment is just a bump in the road. Special thanks to Alex Meeske for the zany humor and for being a scientific sounding board; thank you to Stephanie Clark for being an all around amazing friend.

Thank you to my wonderful parents for your unswerving support and love and for always believing in me when I did not believe in myself. It has been so hard being so far away from you these past six years, but I hope you know that I could not have made it without you. Thank you to Michael John for absolutely everything. You have been such an incredible well of encouragement and support, and words cannot begin to describe my immense feelings of love and gratitude.

I dedicate this dissertation to two people who will unfortunately never get the chance to read it. To my Uncle Maurice, an avid scientist, and mischievous jokester- I wish we could take a long walk along the river discussing the ins and outs of this work. And to my Grandpa Kent, a man who instilled in me the value of knowledge, education, and a good nap. This is for you, Grandpa.

Chapter 1: Introduction

Attributions: I wrote this chapter in its entirety with helpful editorial assistance from my advisor, Ann Hochschild.

Chapter 1.1: Overview

The CbtA protein of *E. coli* is the toxin component of the chromosomally encoded CbtA-CbeA toxin-antitoxin (TA) system. As this designation implies, overexpression of the *cbtA* gene inhibits growth, which can be overcome by co-expression of the upstream antidote gene *cbeA* (1-3). Among the many TA modules characterized to date, the CbtA toxin is unique both in the cellular factors it targets and in the manner in which its cognate antitoxin is thought to neutralize its toxicity. CbtA is a potent modulator of cell shape; overproduction of this toxin causes cells to lose their characteristic rod-shape, becoming inflated lemons incapable of proper growth or propagation (2). The aim of this dissertation is to provide a genetic understanding of the mechanism by which CbtA mediates toxicity and disrupts cell shape. In *E. coli,* as in most other bacteria, morphology is defined by the peptidoglycan sacculus (4), which is built by the coordinated efforts of two major protein complexes, the cell elongation complex and the cell division complex (reviewed in (5,6)). As work described here will illustrate, the CbtA toxin has the remarkable ability to bind and inhibit an essential component in each of these shape-defining complexes.

In this introductory chapter, three main topics are discussed. First, I provide a brief overview of TA systems, a diverse group of bacterial growth inhibitors and their neutralizing partners that are increasingly thought to play a role in the bacterial stress response. Though the work presented in this dissertation focuses on the interactions between the CbtA toxin and its targets, it is important to consider the full picture of TA biology as it may be relevant to the regulation and physiological function of CbtA toxicity. Second, I discuss two essential pathways, cell division and cell elongation, and their role in cell morphogenesis; I introduce the essential bacterial cytoskeletal elements, FtsZ and MreB, that mediate these processes and which are targeted by the CbtA toxin. Finally, I describe what was known about the CbtA inhibitor prior to initiation of this work, establishing the driving questions that motivated our investigation.

Chapter 1.2: Prokaryotic toxin-antitoxin systems exhibit diversity in regulation and targets

Prokaryotic TA systems are genetic modules that consist of a small, stable toxin protein co-expressed with a less stable antitoxin (reviewed in (2,7-10)). The toxin protein causes growth arrest or cell death in the cell in which it is produced, and the antitoxin neutralizes this toxicity. Since their initial discovery in the 1980s, TA operons have been found on extra-chromosomal plasmids (4,11,12) and within phage (13) and prokaryotic genomes (14), showing them to be ubiquitous within prokaryotes. The characterization of many of these TA systems has revealed that this group of genetic elements is marked far more by diversity than uniformity. Currently, TA systems are classified as one of six different types (Type I-VI) based on the mechanism employed by the antitoxin to neutralize its cognate toxin effector (summarized in Figure 1.1 and reviewed in (9)). Types I-III are the best-characterized classes, while Types IV-VI have been described more recently with fewer identified members. Across all classes, toxin genes encode protein effectors, whereas cognate antitoxins are either non-coding RNAs (Type I and III) or small proteins.

In a Type I system, the antitoxin is a small RNA that binds to the toxin mRNA, preventing its translation through one of several identified mechanisms (15). The first Type I TA system identified was the *hok/sok* pair, homologs of which are found on the R1 plasmid (11) and the *E. coli* chromosome (16). The Hok toxin, like the majority of known Type I toxins is a small, hydrophobic peptide that inserts into the inner membrane, disrupting membrane function and causing cell death (17). The Sok sRNA antitoxin prevents translation of the *hok* mRNA by base pairing to the leader sequence of the *hok* mRNA and blocking the Shine-Dalgarno sequence of the leader-peptide required for efficient translation of Hok (15,18).

In a Type II TA system, the antitoxin and toxin are co-transcribed from the same promoter (located upstream of the antitoxin gene) and translated; the antitoxin protein directly binds the toxin protein, forming a neutralized complex (10). Type II antitoxins typically are composed of two domains, a toxin-binding domain that is intrinsically disordered in the absence of toxin, and an N-terminal DNA-binding domain (9,10,19,20). Antitoxins bind within their respective TA operon promoter region via this N-terminal domain, functioning as transcription autoregulators; in most cases the toxin acts as a co-repressor, not by directly accessing the DNA but by enhancing antitoxin binding to the promoter

(10,21,22). Type II toxins are relatively stable, whereas their cognate antitoxins are actively degraded by cellular proteases Lon (23-25) or ClpP (25-27). The majority of characterized Type II toxins are mRNases that inhibit translation in either a ribosome-dependent or ribosome-independent manner (9). One of the best-studied Type II TA systems is the *relBE* system, which is found both on plasmids and bacterial chromosomes (28); this module encodes the RelE toxin, a ribosome-dependent mRNA interferase that binds the 16S ribosomal subunit to mediate codon-specific cleavage of mRNAs positioned in the A site, thus inhibiting protein synthesis (29,30). The RelB antitoxin has only weak affinity for the *relBE* promoter sequence but binds very tightly to DNA when toxin and antitoxin levels are comparable; under these conditions, two $RelB_2$-RelE complexes can access the *relBE* promoter and strongly repress transcription. When RelE levels are increased, $RelB_2$-$RelE_2$ complexes are formed; however, the promoter cannot accommodate two $RelB_2$-$RelE_2$ complexes and repression is relieved (9,20,31). This conditional cooperativity of DNA-binding is exhibited by many Type II TA systems, including *phd/doc* (21), *parDE* (32), and *vapBC* (33), and may have important implications for reversing toxin-mediated growth arrest (9,34,35).

The representative Type III TA system, *toxIN*, was discovered on a cryptic plasmid in the bacterium *Pectobacterium atrosepticum* subsp. *atroseptica* (36); this system encodes the protein toxin, ToxN, and an upstream sRNA antitoxin, ToxI. ToxN is an enzyme with ribonuclease activity that cleaves several mRNAs, including its own transcript; this processing releases active ToxI RNA pseudoknots, which bind within the active site of ToxN (37). Three ToxI pseudoknots binds to three ToxN monomers, forming a neutralized trimeric complex (15,37).

In TA Types IV, V, VI, many of the schemes discussed above are rearranaged into alternative neutralization strategies. In the only known Type IV system, *cbeA/cbtA* (formerly named *yeeUV*), both toxin and antitoxin elements are proteins, but unlike the protein partners found in Type II modules, the TA components of this system do not physically interact (1,2,38). Instead, the CbeA antitoxin is thought to counteract CbtA toxicity by stabilizing its targets (38). This system will be described in more detail later in this chapter. The only identified Type V system, *ghoST* of *E. coli*, illustrates another variation of mRNA cleavage by TA elements; in this case, the GhoS antitoxin is an endoRNase that specifically cleaves the *ghoT* mRNA (39). Furthermore, the GhoT toxin is a highly hydrophobic transmembrane protein that, like

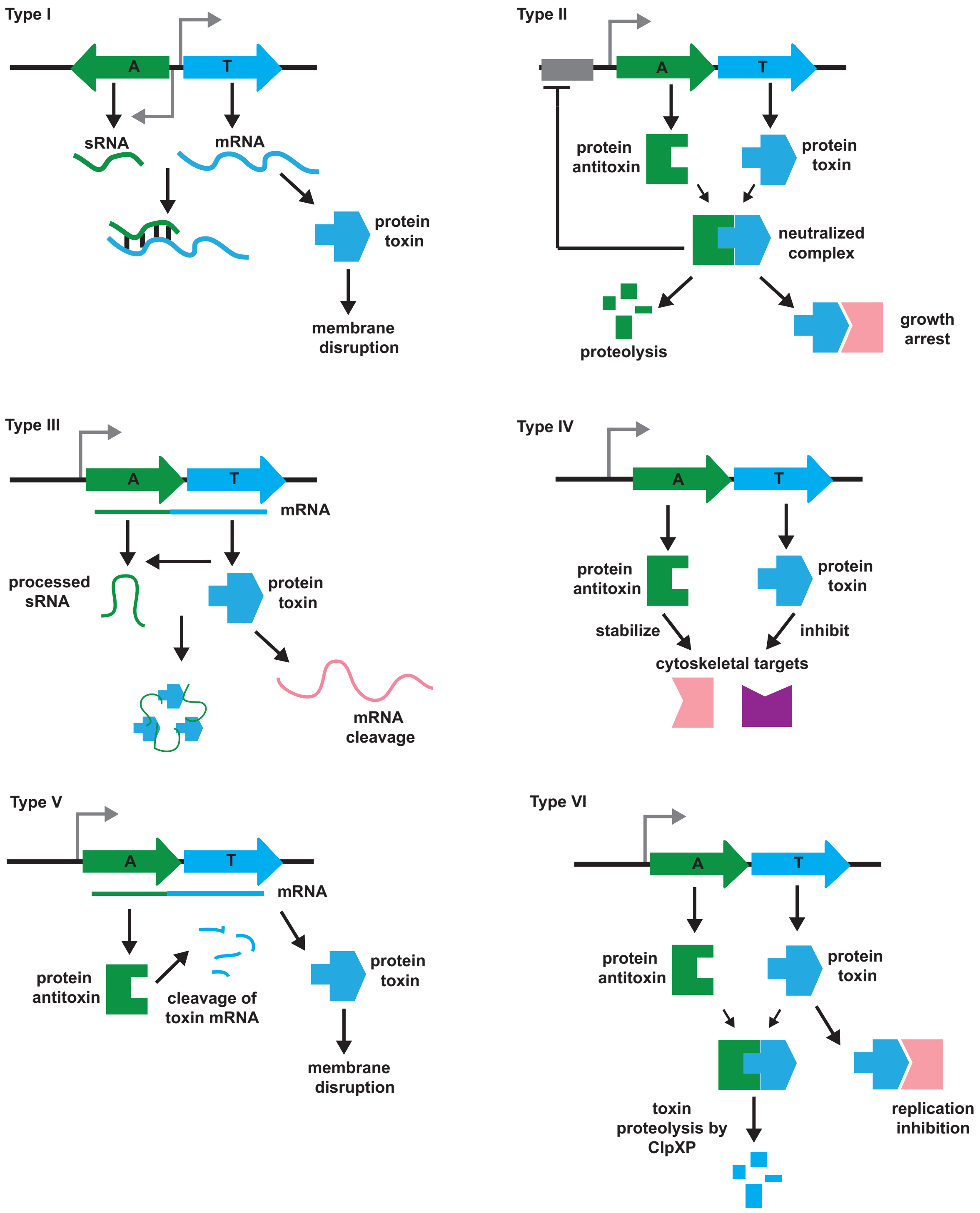
Type I
A
T
sRNA
mRNA
protein
toxin
membrane
disruption
Type II
A
T
protein
antitoxin
protein
toxin
neutralized
complex
proteolysis
growth
arrest
Type III
A
T
mRNA
processed
sRNA
protein
toxin
mRNA
cleavage
Type IV
A
T
protein
antitoxin
protein
toxin
stabilize
inhibit
cytoskeletal targets
Type V
A
T
mRNA
protein
antitoxin
cleavage of
toxin mRNA
protein
toxin
membrane
disruption
Type VI
A
T
protein
antitoxin
protein
toxin
toxin
proteolysis by
ClpXP
replication
inhibition

Figure 1.1: There are six classes of TA systems. A schematic of the operon arrangement, general growth inhibition strategy employed by the toxin, and the mechanism of antitoxin neutralization are shown

Figure 1.1 (Continued)

for TA Types I-VI. In each case, the antitoxin component is shown in green, and the toxin is shown in blue. The cellular targets are shown in pink for Types II, III, and VI. The two cytoskeletal targets inhibited by the Type IV toxin are shown in pink and purple.

Type I toxins, kills cells by damaging the inner membrane (39). Finally, in the Type VI *socAB* system of *Caulobacter crescentus,* the differential stabilities of the toxin and antitoxin components are reversed. The SocB toxin protein is constitutively degraded by the ClpXP protease; the SocA antitoxin protein binds both its cognate toxin and the N-terminal domain of ClpX, acting as an adaptor to promote SocB proteolysis (40). The labile SocB toxin also exhibits a novel mechanism of growth inhibition, targeting the DnaN sliding clamp and blocking DNA replication elongation (40).

Chapter 1.3: TA systems in plasmid maintenance and bacterial stress response

TA systems were first discovered in the context of plasmid-based “addiction” modules that promote stable plasmid maintenance within a growing population of cells (11,12,41). Both the Type II *ccdA/ccdB* module of the mini-F plasmid (12) and the Type I *hok/sok* system of the *E. coli* R1 plasmid (11) were found to promote plasmid maintenance through a mechanism termed post-segregational killing, which relies on the differential stabilities of the toxin and antitoxin molecules. A cell harboring the TA-encoding plasmid will continually replenish levels of the labile antitoxin, allowing for continued neutralization of the more stable cellular toxin. However, if during cell division, the TA-encoding plasmid is not properly partitioned, *de novo* synthesis of the antitoxin ceases in the plasmid-free daughter cell, levels of pre-existing antitoxin are rapidly depleted, and the toxin is liberated, ultimately causing cell death (23). This selective killing of plasmid-free cells renders the population addicted to the antitoxin and the gene encoding it, ensuring continued propagation of the plasmid.

Since their initial discovery on plasmids, mining of genomic sequences has revealed that TA systems are extremely well-represented on the chromosomes of prokaryotes (14,42). The genomes of most free-living bacteria and archaea contain at least one chromosomal TA locus, with some organisms harboring dozens (14); the human pathogen *Mycobacterium tuberculosis* contains a remarkable 88 putative TA loci, 30 of which were functionally validated by overexpression in *Mycobacterium smegmatis* (43). Most of these chromosomal systems seem to have been obtained through horizontal gene transfer and are found on mobile genetic elements such as prophages or insertion sequences (14,41).

Whereas the role of plasmid-encoded TA systems as stabilization elements is clear, the function of their chromosomally encoded counterparts is less obvious. A wide range of physiological roles have been ascribed to TA loci (44). Some researchers have suggested that chromosomal TA systems primarily function as selfish genetic elements that assure their preservation within a population but provide no benefit to the host cell (41), while others propose that these addiction modules may help maintain less stable chromosomal regions, preventing gene loss (45). It has been observed in many cases that chromosomal Type II TA systems are activated in response to environmental stress signals (7,10). Stressful conditions such as amino acid starvation or exposure to antibiotics lead to the depletion of antitoxin levels within the cell through activation of stress-responsive cellular proteases, allowing toxins access to their cellular targets (27,46-48). There has been some debate as to the ultimate effects of Type II toxin activation (10). Engelberg-Kulka and colleagues are proponents of the programmed cell death model, in which nutritional stress activates the lethal MazF toxin (a ribosome-independent mRNase) in a subset of cells; these cells commit altruistic suicide to provide resources to the rest of the clonal community (27). However, others have called this model into question (49), asserting instead that Type II toxins induce a bacteriostatic effect that can be overcome by renewed production of the relevant antitoxin (9).

The ability of chromosomal toxin-antitoxin systems to rapidly halt growth in response to environmental stress suggests that these systems may be functioning as prokaryotic stress response loci. One such role that has received extensive support in recent years is the involvement of toxin-dependent growth arrest in the formation of multi-drug tolerant persister cells (9,50). Cells in a persister state (which in a wild-type planktonic *E. coli* culture occur at a frequency of approximately 1 in a million) are dormant, allowing them to survive a range of environmental perturbations (9); importantly, once the environmental perturbation has been removed, persister cells can exit this dormant state, reinitiating division. The first gene found to be directly involved in this persistence phenotype was the *hipA* gene of *E. coli* (51); this gene is part of the *hipAB* Type II TA locus and encodes a serine-protein kinase that inactivates glutamyl-tRNA synthetase (GltX) by phosphorylation (52,53). The *hipA7* allele, first isolated in 1983, significantly increases the frequency of persister cells (100 to 1,000-fold) (51). Recent studies have shed light on the mechanism by which this high persister mutant provides heritable drug tolerance. Structural work shows that substitutions in the HipA dimerization interface or within the HipA-HipB interface destabilize neutralized higher-order TA promoter-bound assemblies, exposing the HipA active site (54). HipA-mediated inactivation of GltX induces the stringent response, which activates a complex cascade of downstream events (55,56). Production of the signaling molecule ppGpp is stimulated, which in turn causes accumulation of inorganic polyphosphate, activating Lon-dependent proteolysis of several Type II antitoxins; degradation of these antitoxins ultimately results in toxin-mediated growth arrest by Type II mRNases (52,53,55,56).

Several lines of evidence point to the direct involvement of these Type II mRNase toxins (e.g. RelE, MazF, YoeB) in persistence. Ectopic expression of several toxins has been seen to increase persister frequency, while deletion of ten Type II mRNases in *E. coli* caused a ~100-fold reduction in the number of antibiotic-tolerant persister cells (57). Furthermore, microarray studies have shown that many Type II toxin genes are upregulated in isolated *E. coli* persister cells (58,59). Mathematical modeling studies have suggested that the conditional cooperativity displayed by chromosomal Type II TA systems may allow for two stable situations within a bacterial population; in the majority of cells, promoter-bound TA complexes keep cellular toxin levels low, but in a small subset of cells, local starvation may lead to degradation of antitoxin and spikes in toxin levels (9,34,35). It has been predicted (but remains to be tested), that eventually, in the resulting subset of dormant cells, transcriptional controls will be restored, allowing for resuscitation of growth (9).

Type I TA systems have also been implicated in the formation of persister populations (9,15). Recently, Verstraeten et al. reported that ectopic expression of Obg, a broadly conserved, multifunctional GTPase, led to increased persistence by inducing expression of the *hokB* Type I toxin (60). HokB production led to membrane depolarization and an arrest of cellular respiration; it remains to be seen what molecular mechanisms reverse this Type I toxin-mediated dormancy (60).

Thus, TA systems are potent effectors of growth inhibition. Whatever their exact evolutionary origins may be, work in recent years has made it evident that in several cases, chromosomal TA systems have been co-opted by bacteria to help ensure the survival of a population in the face of environmental stress. As this discussion has highlighted, the list of strategies employed by toxins to disrupt growth and by antitoxins to rescue growth, is being continually updated. One TA target that has been recently described is the bacterial cytoskeleton (2,3); the essential functions of the bacterial cytoskeleton are considered in the next section.

Chapter 1.4: Rod-shape determination and the bacterial cytoskeleton

Bacterial species display a wide-range of cell morphologies, from rods, to cocci, to spirals (6). In the vast majority of these species, shape is dictated by the cell wall, a complex, continuous meshwork that surrounds the cytoplasmic membrane, providing mechanical support; indeed, isolated cell wall sacculi largely retain their shape even in the absence of cytoplasmic material (4,61). In Gram negative bacteria such as *E. coli*, strands of peptidoglycan (a polymer composed of alternating subunits of the aminosugars N-acetylglucosamine (GlcNAc) and N-acetylmuramic acid (MurNAc)) are linked together by short peptides (the composition of which varies amongst bacterial species) into a thin cell wall layer sandwiched between the inner and outer membranes (61). In Gram positive bacteria such as *Bacillus subtilis*, the cell wall is a thick, multi-layered structure (61)3.

The cell wall is assembled in three major stages. First, a team of cytoplasmic enzymes synthesizes the soluble, nucleotide precursors (UDP-GlcNAc and UDP-MurNAc-pentapeptide) (reviewed in (62)). At the inner leaflet of the cytoplasmic membrane, these precursors are then linked to the transport lipid (undecaprenyl phosphate), forming the lipid II intermediate (63), which is transported across the inner membrane by the MurJ flippase (64,65). Finally, in the periplasm, lipid II is polymerized into peptidoglycan strands by glycosyltransferase enzymes; these strands are incorporated into the existing sacculus by transpeptidase enzymes (5). The periplasmic synthetic reactions are carried out by the penicillin-binding proteins (PBPs), which are a family of monofunctional transpeptidases (in *E. coli*, PBP2 and PBP3/FtsI), monofunctional glycosyltransferases (MtgA), and bifunctional transpeptidase/glycosyltransferases (PBP1A, PBP1B, PBP1C) (5,61). In addition to these synthases, the shaping of the peptidoglycan layer involves a diverse group of peptidoglycan hydrolase enzymes, which are often highly redundant within a bacterial species; these hydrolases are involved in expanding the sacculus during cell growth, cleaving the septal wall during cytokinesis to allow for the separation of daughter cells, and they participate in the efficient recycling of peptidoglycan (5,66-68).

In rod-shaped organisms such as *E. coli,* the cell wall meshwork is built by two distinct modes of peptidoglycan insertion (reviewed in (5,6)). New cell wall material is incorporated into the lateral sidewall by a group of enzymes known as the cell elongation complex; the coordinated insertion of peptidoglycan by this complex causes a newly divided cell to double in length. This elongated cell is then divided into two daughter cells by the division complex (or divisome), which builds a new septal wall at mid-cell. Each of these modes is directed by a dedicated bacterial cytoskeletal element. In eukaryotes, the cytoskeleton is an intricate network of filament systems (actin, tubulins, and intermediate filaments) that dictates both cell shape and internal organization. The bacterial cytoskeleton contains homologous dynamic filament systems that are involved in similar processes as their eukaryotic counterparts (e.g. cell division and cell shape determination); however, whereas the eukaryotic cytoskeleton is a largely coherent structure that provides mechanical support and global coordination, the bacterial cytoskeleton is composed of filament systems that act by locally influencing cell wall insertion (reviewed in (69-71)). The dynamics and regulation of assembly also differ between eukaryotic and prokaryotic systems (69).

Several cytoskeletal elements have been discovered in bacterial species since the 1990s (72,73), but the two most broadly conserved elements are FtsZ and MreB, which govern cell division and cell elongation, respectively. FtsZ is a tubulin homolog with GTPase activity that forms a dynamic ring structure at mid-cell (74). This Z ring is composed of polymerized FtsZ filaments tethered to the inner membrane; in *E. coli* ZipA and the actin-homolog FtsA serve as membrane tethers (75). The exact positioning and timing of Z ring formation is regulated by a complex set of modulatory proteins that act by inhibiting or promoting FtsZ assembly (reviewed in (76,77)). Once properly assembled at mid-cell, this Z ring serves as a scaffold for a large set of essential and non-essential protein components which come together to form the mature division complex (reviewed in (78)). After all necessary components have been recruited to mid-cell, the division-specific peptidoglycan transpeptidase PBP3/FtsI in conjunction with at least one other synthase, synthesizes septal wall; additional divisome-associated proteins hydrolyze the septal peptidoglycan layer and invaginate the inner and outer membranes, allowing for complete separation of the two daughter cells (reviewed in (68,76,79)). The molecular details of regulated FtsZ assembly are discussed in Chapter 3 of this dissertation.

Cell elongation is mediated by the actin-homolog and ATPase, MreB (80,81). This essential cell-shape determinant, which is found only in rod-shaped bacteria (82), forms dynamic filament patches that move circumferentially along the long axis of the cell (83,84). MreB forms antiparallel double filaments (85) that are peripherally associated with the inner leaflet of the cytoplasmic membrane both by internal membrane-binding sequences (86) and via interaction with conserved transmembrane proteins RodZ, MreC, and MreD (87-91). RodZ has been shown to couple cytoplasmic MreB filaments to the periplasmic cell wall machinery (PBP2 and RodA), and peptidoglycan synthesis is thought to be the motor driving the dynamic motion of MreB (83,84,91,92). Although there are still many open questions about exactly how MreB functions in cell elongation, it is clear that it plays an essential role in directing lateral cell wall insertion and determining rod morphogenesis. Interestingly, recent evidence suggests that MreB directly interacts with FtsZ and may also influence septal wall synthesis (93). In Chapter 4, I discuss our evolving understanding of MreB polymerization and its role in cell elongation.

Thus, these two cytoskeletal elements (in conjunction with large protein complexes) dictate cell geometry by directing the coordinated construction of the shape-defining cell wall. The essential role of these cytoskeletal elements in morphogenesis is underscored by the striking cell morphologies that result from disruption of their functions. Inhibition of FtsZ (with, for example, production of the SOS inhibitor SulA (94,95)) or perturbation of other divisome components in *E. coli,* leads to the formation of long, filamentous cells. Disruption of MreB by either depletion or A22 treatment (an MreB-specific antibiotic that binds within the ATP binding pocket (85,96,97)) results in a loss of rod-shape (98,99). A similar morphology is seen with inhibition of cell wall synthesis via treatment with beta-lactam antibiotics or depletion of essential enzymes (96,97). Upon disruption of cell elongation in *E. coli*, cells stop growing laterally and increase in diameter, forming spheres. In fast growth conditions (LB at 37 ºC), the cells continue to enlarge, eventually lysing; however, in conditions that mediate slower growth or with increased levels of FtsZ, these spherical cells can continue to divide (99). Targeted inhibition of FtsZ and MreB has been an important strategy in the investigation of their cellular functions. In the next section of this chapter, I describe the discovery and initial characterization of the CbtA toxin, the first identified inhibitor that is capable of simultaneously interfering with both of these cytoskeletal proteins.

Chapter 1.5: CbtA (YeeV), YpjF, and YkfI are a family of toxins that inhibit *E. coli* growth

TA modules found throughout bacterial genomes have largely been identified via homology-based sequence mining, looking for orthologs of known TA components (14,42,100). However, in 2003, in an attempt to identify additional chromosomal toxin-antitoxin systems in the *E. coli* K-12 genome, Brown and Shaw used a bioinformatics mining approach that did not rely on sequence homology to

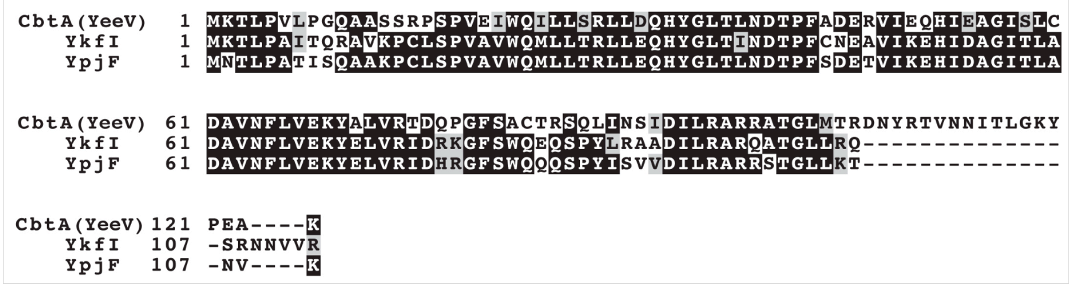

```
CbtA(YeeV)  1  MKTLPVLPGQAASSRPSPVEIWQILLSRLLDQHYGLTLNDTPFADERVIEQHIEAGISLC
    YkfI    1  MKTLPAITQRAVKPCLSPVAVWQMLLTRLLEQHYGLTINDTPFCNEAVIKEHIDAGITLA
    YpjF    1  MNTLPATISQAAKPCLSPVAVWQMLLTRLLEQHYGLTLNDTPFSDETVIKEHIDAGITLA

CbtA(YeeV) 61  DAVNFLVEKYALVRTDQPGFSACTRSQLINSIDILRARRATGLMTRDNYRTVNNITLGKY
    YkfI   61  DAVNFLVEKYELVRIDRKGFSWQEQSPYLRAADILRARQATGLLRQ--------------
    YpjF   61  DAVNFLVEKYELVRIDHRGFSWQQQSPYISVVDILRARRSTGLLKT--------------

CbtA(YeeV)121  PEA----K
    YkfI  107  -SRNNVVR
    YpjF  107  -NV----K
```

Figure 1.2: CbtA (YeeV), YpjF, and YkfI are a family of toxin proteins. Shown is a multiple sequence alignment of CbtA, YpjF, and YkfI amino acid sequences from *E. coli* K12 (Ecocyc). YpjF and YkfI are 79% identical; CbtA is 57% identical to YkfI and 63% identical to YpjF. The alignment was made using TCoffee, and the figure was prepared in Boxshade.

known TA systems, but instead identified small, co-transcribed gene pairs (1). Sorting through all annotated ORFs in the genome, they first identified genes encoding small proteins (65-135 amino acids in length), then further refined their dataset by selecting only those genes found in an operon downstream of a second candidate (separated by ≤ 150 bp). This method yielded 18 candidate pairs, including the genes *yeeU/yeeV*[a], *yafW/ykfI*, and *yfjZ/ypjF.* These three gene pairs are found on separate cryptic prophage elements in the *E. coli* (and other closely related species) genome.

Subsequent overexpression analysis demonstrated that expression of *yeeV*, *ykfI*, and *ypjF* from a multi-copy plasmid in *E. coli* caused a marked decrease in growth and viability after 2-3 hrs of induction, which, in the case of *yeeV* and *ykfI*, could be rescued by co-expression in *cis* of the gene immediately upstream (*yeeU* and *yafW*, respectively) (1). The proteins encoded by these three gene pairs exhibit high amino acid identity; the YafW/YkfI and YfjZ/YpjF pairs are ~80% identical, while the YeeU/YeeV pair is ~60% identical to the other two (Figure 1.2). The homology of these gene pairs was underscored by the observation that YafW and YeeU were able to partially neutralize the toxicity mediated by overproduction of their non-cognate partner (1). Based on the overexpression phenotypes as well as the sequence identity between the gene pairs, Brown and Shaw concluded that these gene pairs represent a family of homologous chromosomal toxin-antitoxin systems. Although, at the time, the cellular targets of the three toxin proteins were unknown, Brown and Shaw predicted that, due to the initial lag time and dose-dependency of growth inhibition, the toxins likely titrated some essential growth factor.

---

[a] Based on findings summarized in this chapter, the *yeeV* gene was renamed to *cbtA* (2), and the *yeeU* gene was renamed to *cbeA* (38). To be consistent with previously published nomenclature, I will use the *yeeU*/*yeeV* designation in this section while describing the work leading up to the shift to the *cbeA*/*cbtA* nomenclature.

Chapter 1.6: CbtA (YeeV) causes a striking lemon-shape phenotype

In 2011, Tan et al. observed that overproduction of the YeeV toxin in *E. coli* results in a striking phenotype (2). Over the course of several hours, cells induced for *yeeV* expression lost their characteristic rod-shape and formed swollen lemons with distinct poles; with prolonged induction, these lemons eventually lysed. This lemon-like morphology is reminiscent of the change in cell morphology induced by simultaneous block of cell elongation and cell division pathways in *E. coli* (2,101).

Prior to the work by Tan et al., Varma et al. observed that combined inhibition of FtsZ (by overexpression of the *sulA* SOS inhibitor) and MreB (with 5 μg/mL A22 treatment) resulted in the formation of bloated, lemon-shaped cells (101). Partial inhibition of MreB (using only 2 μg/mL A22) caused a milder phenotype, with cells forming elongated filaments with increased cell width. Simultaneous inhibition of FtsZ and PBP2 yielded a similar lemon phenotype, indicating that while a cell elongation block is necessary for lemon formation, it is not a specific consequence of MreB inhibition. Varma et al. saw that upon FtsZ and MreB inhibition, peptidoglycan incorporation continued but in an undirected, patchy manner, leading to an increase in cell diameter. Importantly, they observed that these swollen lemons are distinct from the spheres and sphere-like cells produced upon MreB-inhibition alone as they maintain distinct polar-regions, in some cases displaying pronounced tubular extensions. Varma et al. observed that tubular extensions were more common in a strain deleted for the low-molecular weight penicillin-binding proteins, PBP5 and PBP7. However, all morphologies described were also seen (albeit at lower frequency) in the wild-type MG1655 strain. Varma et al. postulated that the lack of uniform cell expansion near cell poles in these FtsZ$^-$/MreB$^-$ cells is a specific result of FtsZ inhibition. Indeed, when they observed incorporation of new peptidoglycan in cells filamented either by direct inhibition of FtsZ (i.e. with *sulA* overexpression) or by inhibition of downstream septal wall synthesis (i.e. through inhibition of PBP3/FtsI with the antibiotic aztreonam), a pronounced decrease in newly incorporated material in the sidewall adjacent to the poles was observed only with direction inhibition of FtsZ (101). It is important to note that this FtsZ-dependent decrease was seen only in a strain lacking PBP5; in the wild-type strain, there was no difference in peptidoglycan incorporation near the poles. Thus, the precise molecular details of lemon-shape formation are not yet fully understood; however, the work by Varma et al. clearly establishes that simultaneous inhibition of MreB and FtsZ in *E. coli* produces this distinctive phenotype.

Consistent with the lemon-morphology induced by *yeeV* overexpression, Tan et al. made several observations suggesting that the YeeV toxin interacts with both FtsZ and MreB (2). First, incubation of purified His_6-YeeV with a *ΔyeeUV E. coli* lysate[b] resulted in pull-down of FtsZ and MreB. Interaction of YeeV with both FtsZ and MreB was confirmed by use of a yeast two-hybrid system. Furthermore, purified His_6-YeeV was found to inhibit the in vitro assembly of both FtsZ and MreB, but only affected nucleotide hydrolysis by the GTPase FtsZ. Based on these findings, the authors proposed that YeeV mediates its toxicity via interaction with the bacterial cytoskeleton, earning it the new name CbtA (Cytoskeletal binding toxin A). This work presented the first report of a toxin/antitoxin system targeting the bacterial cytoskeleton, as well as the first description of a toxin with two distinct targets. I will use this CbtA designation throughout the remainder of this dissertation.

Chapter 1.7: Conflicting reports on the mechanism of the CbeA (YeeU) antitoxin

In their 2003 study, Brown and Shaw reported that they were unable to detect *in vivo* interaction between the CbtA toxin protein and its cognate antitoxin by coimmunoprecipitation, suggesting that the YeeU family of antitoxins does not inhibit toxin function via the standard Type II mechanism (1). YeeU-dependent neutralization of CbtA-toxicity was found to occur only when the two genes were encoded in *cis*, separated by a non-conserved 68-bp UTR located upstream of the *cbtA* gene (1). Interestingly, Western analysis indicated that co-expression of the *cbtA* and *ykfI* toxin genes with their cognate *yeeU* and *yafW* antitoxin genes resulted in a significant reduction in toxin protein levels (1). Subsequent structural analysis of the YeeU protein revealed that it contains a nucleic-acid binding domain homologous to that of the mRNA-cleaving RelE/YoeB Type II toxins (103); this combined with the observations by Brown and Shaw, supported a model where YeeU acts a post-transcriptional modulator of CbtA production, perhaps through interaction with some regulatory element within the 68-bp UTR.

---

[b] The *yeeUV* (*cbeA/cbtA*) genes are non-essential in *E. coli*, and single or combined deletion of these genes causes no obvious growth or morphology phenotype under normal lab conditions (2,102).

In 2012, Masuda et al. similarly reported that they could not detect physical interaction between CbtA and YeeU (38). However, unlike the earlier report by Brown and Shaw, this group saw that co-expression of *cbtA* and *yeeU* in trans was sufficient for growth rescue; the 68-bp UTR was not necessary for YeeU antitoxin activity (38). They further demonstrated that YeeU is able to rescue the growth and cell morphology defects caused by the cytoskeletal inhibitors SulA and A22 and can interact with FtsZ and MreB (as shown by pull-down assays using cell lysates and co-sedimentation experiments using purified proteins) (38). *In vitro* analyses indicated that YeeU promoted the nucleotide-dependent polymerization of both FtsZ and MreB, leading Masuda et al. to propose an alternative model in which YeeU counteracts CbtA toxicity by stabilizing the assembly of its cytoskeletal targets (38). As YeeU was also able to neutralize the effects of other cytoskeletal perturbations, these authors suggested that YeeU, which they renamed Cytoskeletal bundling element A (CbeA), is a global cytoskeletal stabilizer (38). I will use this CbeA designation throughout the remainder of this dissertation. The two models of CbeA function are not necessarily mutually exclusive. It is possible that CbeA, like Type II antitoxins, may also have a secondary role as a transcriptional or post-transcriptional regulator of *cbtA* expression; additional work will be needed to test this.

Chapter 1.8: A testable model of CbtA toxicity

Based on the work done in the three studies described above (1,2,38), the CbtA-CbeA module is considered the founding member of the Type IV TA class. CbtA production inhibits growth and induces a striking, lemon-like morphology, presumably through interaction with FtsZ and MreB. CbeA neutralizes this toxicity, likely through positive regulation of cytoskeletal assembly. However, what (up until this report) has been missing from our understanding of CbtA toxicity, is a detailed characterization of these reported CbtA-FtsZ and CbtA-MreB interactions and an assessment of their contributions to the CbtA-mediated inhibition of rod-shaped growth. The goal of the work presented here was to genetically dissect these interactions in an effort to answer three main questions. First, is CbtA interacting independently with both MreB and FtsZ? Second, if this toxin is indeed interacting with both factors, are these interactions functionally relevant to the observed CbtA toxicity and cell shape effects? Finally, what are the interacting surfaces? How is CbtA binding mediating toxicity? Our genetic analysis presented in Chapters 2, 3, and 4 of this dissertation provides important molecular insight into these questions.

Chapter 1.9: References

1. Brown JM, Shaw KJ. A novel family of Escherichia coli toxin-antitoxin gene pairs. J Bacteriol. 2003 Nov;185(22):6600–8.

2. Tan Q, Awano N, Inouye M. YeeV is an Escherichia coli toxin that inhibits cell division by targeting the cytoskeleton proteins, FtsZ and MreB. Mol Microbiol. 2011 Jan;79(1):109–18.

3. Masuda H, Tan Q, Awano N, Wu K-P, Inouye M. YeeU enhances the bundling of cytoskeletal polymers of MreB and FtsZ, antagonizing the CbtA (YeeV) toxicity in Escherichia coli. Mol Microbiol. 2012 May 17;84(5):979–89.

4. Höltje JV. Growth of the stress-bearing and shape-maintaining murein sacculus of Escherichia coli. Microbiology and Molecular Biology Reviews. 1998 Mar;62(1):181–203.

5. Typas A, Banzhaf M, Gross CA, Vollmer W. From the regulation of peptidoglycansynthesis to bacterial growth andmorphology. Nat Rev Micro. Nature Publishing Group; 2011 Dec 28;10(2):123–36.

6. Margolin W. Sculpting the Bacterial Cell. Curr Biol. Elsevier Ltd; 2009 Sep 15;19(17):R812–22.

7. Yamaguchi Y, Inouye M. Regulation of growth and death in Escherichia coli by toxin–antitoxin systems. Nat Rev Micro. 2011 Sep 19;9(11):779–90.

8. Yamaguchi Y, Park J-H, Inouye M. Toxin-Antitoxin Systems in Bacteria and Archaea. Annu Rev Genet. 2011 Dec 15;45(1):61–79.

9. Page R, Peti W. Toxin-antitoxin systems in bacterial growth arrest and persistence. Nature Chemical Biology. 2016 Mar 18;12(4):208–14.

10. Gerdes K, Christensen SK, Løbner-Olesen A. Prokaryotic toxin–antitoxin stress response loci. Nat Rev Micro. 2005 May;3(5):371–82.

11. Gerdes K, Rasmussen PB, Molin S. Unique type of plasmid maintenance function: postsegregational killing of plasmid-free cells. Proc Natl Acad Sci USA. 1986 May;83(10):3116–20.

12. Ogura T, Hiraga S. Mini-F plasmid genes that couple host cell division to plasmid proliferation.

Proc Natl Acad Sci USA. 1983 Aug;80(15):4784–8.

13. Lehnherr H, Maguin E, Jafri S, Yarmolinsky MB. Plasmid addiction genes of bacteriophage P1: doc, which causes cell death on curing of prophage, and phd, which prevents host death when prophage is retained. Journal of Molecular Biology. 1993 Oct 5;233(3):414–28.

14. Pandey DP. Toxin-antitoxin loci are highly abundant in free-living but lost from host-associated prokaryotes. Nucleic Acids Research. 2005 Feb 18;33(3):966–76.

15. Brantl S, Jahn N. sRNAs in bacterial type I and type III toxin-antitoxin systems. FEMS Microbiology Reviews. 2015 May 25;39(3):413–27.

16. Pedersen K, Gerdes K. Multiple hok genes on the chromosome of Escherichia coli. Mol Microbiol. 1999 Jun;32(5):1090–102.

17. Gerdes K, Bech FW, Jørgensen ST, Løbner-Olesen A, Rasmussen PB, Atlung T, et al. Mechanism of postsegregational killing by the hok gene product of the parB system of plasmid R1 and its homology with the relF gene product of the E. coli relB operon. EMBO J. 1986 Aug;5(8):2023–9.

18. Thisted T, Sørensen NS, Wagner EG, Gerdes K. Mechanism of post-segregational killing: Sok antisense RNA interacts with Hok mRNA via its 5“-end single-stranded leader and competes with the 3-”end of Hok mRNA for binding to the mok translational initiation region. EMBO J. 1994 Apr 15;13(8):1960–8.

19. De Jonge N, Garcia-Pino A, Buts L, Haesaerts S, Charlier D, Zangger K, et al. Rejuvenation of CcdB-Poisoned Gyraseby an Intrinsically Disordered Protein Domain. Molecular Cell. Elsevier Ltd; 2009 Jul 31;35(2):154–63.

20. Bøggild A, Sofos N, Andersen KR, Feddersen A, Easter AD, Passmore LA, et al. Short Article. Structure/Folding and Design. Elsevier Ltd; 2012 Oct 10;20(10):1641–8.

21. Magnuson R, Yarmolinsky MB. Corepression of the P1 addiction operon by Phd and Doc. J Bacteriol. 1998 Dec;180(23):6342–51.

22. Afif H, Allali N, Couturier M, Van Melderen L. The ratio between CcdA and CcdB modulates the transcriptional repression of the ccd poison-antidote system. Mol Microbiol. 2001 Jul;41(1):73–82.

23. Van Melderen L, Bernard P, Couturier M. Lon-dependent proteolysis of CcdA is the key control for activation of CcdB in plasmid-free segregant bacteria. Mol Microbiol. 1994 Mar;11(6):1151–7.

24. Christensen SK, Maenhaut-Michel G, Mine N, Gottesman S, Gerdes K, Van Melderen L.

Overproduction of the Lon protease triggers inhibition of translation in Escherichia coli: involvement of the yefM-yoeB toxin-antitoxin system. Mol Microbiol. 2004 Feb 4;51(6):1705–17.

25. Gerdes K. Toxin-antitoxin modules may regulate synthesis of macromolecules during nutritional stress. J Bacteriol. 2000 Feb;182(3):561–72.

26. Lehnherr H, Yarmolinsky MB. Addiction protein Phd of plasmid prophage P1 is a substrate of the ClpXP serine protease of Escherichia coli. Proc Natl Acad Sci USA. 1995 Apr 11;92(8):3274–7.

27. Aizenman E, Engelberg-Kulka H, Glaser G. An Escherichia coli chromosomal "addiction module" regulated by guanosine [corrected] 3“,5-”bispyrophosphate: a model for programmed bacterial cell death. Proc Natl Acad Sci USA. 1996 Jun 11;93(12):6059–63.

28. Gotfredsen M, Gerdes K. The Escherichia coli relBE genes belong to a new toxin-antitoxin gene family. Mol Microbiol. 1998 Aug;29(4):1065–76.

29. Pedersen K, Zavialov AV, Pavlov MY, Elf J, Gerdes K, Ehrenberg M. The bacterial toxin RelE displays codon-specific cleavage of mRNAs in the ribosomal A site. Cell. 2003 Jan 10;112(1):131–40.

30. Neubauer C, Gao Y-G, Andersen KR, Dunham CM, Kelley AC, Hentschel J, et al. The Structural Basis for mRNA Recognition and Cleavage by the Ribosome-Dependent Endonuclease RelE. Cell. Elsevier Ltd; 2009 Dec 11;139(6):1084–95.

31. Overgaard M, Borch J, Jørgensen MG, Gerdes K. Messenger RNA interferase RelE controls relBEtranscription by conditional cooperativity. Mol Microbiol. 2008 Aug;69(4):841–57.

32. Johnson EP, Strom AR, Helinski DR. Plasmid RK2 toxin protein ParE: purification and interaction with the ParD antitoxin protein. J Bacteriol. 1996 Mar;178(5):1420–9.

33. Winther KS, Gerdes K. Regulation of Enteric vapBC Transcription: Induction by VapC Toxin Dimer-Breaking. Nucleic Acids Research. 2012 May 21;40(10):4347–57.

34. Gelens L, Hill L, Vandervelde A, Danckaert J, Loris R. A General Model for Toxin-Antitoxin Module Dynamics Can Explain Persister Cell Formation in E. coli. Covert MW, editor. PLoS Comput Biol. 2013 Aug 29;9(8):e1003190.

35. Cataudella I, Sneppen K, Gerdes K, Mitarai N. Conditional Cooperativity of Toxin - Antitoxin Regulation Can Mediate Bistability between Growth and Dormancy. Saucerman JJ, editor. PLoS Comput Biol. 2013 Aug 29;9(8):e1003174.

36. Fineran PC, Blower TR, Foulds IJ, Humphreys DP, Lilley KS, Salmond GPC. The phage abortive infection system, ToxIN, functions as a protein-RNA toxin-antitoxin pair. Proc Natl Acad Sci USA.

2009 Jan 20;106(3):894–9.

37. Blower TR, Pei XY, Short FL, Fineran PC, Humphreys DP, Ben F Luisi, et al. A processed noncoding RNA regulates an altruistic bacterial antiviral system. Nat Struct Mol Biol. Nature Publishing Group; 2011 Jan 16;18(2):185–90.

38. Masuda H, Tan Q, Awano N, Wu K-P, Inouye M. YeeU enhances the bundling of cytoskeletal polymers of MreB and FtsZ, antagonizing the CbtA (YeeV) toxicity in Escherichia coli. Mol Microbiol. 2012 Jun;84(5):979–89.

39. Wang X, Lord DM, Cheng H-Y, Osbourne DO, Hong SH, Sanchez-Torres V, et al. A new type V toxin-antitoxin system where mRNA for toxin GhoT is cleaved by antitoxin GhoS. Nature Chemical Biology. Nature Publishing Group; 2012 Sep 2;8(10):855–61.

40. Aakre CD, Phung TN, Huang D, Laub MT. A Bacterial Toxin Inhibits DNA Replication Elongation through a Direct Interaction with the &beta; Sliding Clamp. Molecular Cell. Elsevier Inc; 2013 Dec 12;52(5):617–28.

41. Van Melderen L, De Bast MS. Bacterial toxin–antitoxin systems: more than selfish entities? PLoS Genet. 2009.

42. Guglielmini J, Szpirer CY, Milinkovitch MC. Automated Discovery and Phylogenetic Analysis of New Toxin-Antitoxin Systems. BMC Microbiol. 2008;8(1):104.

43. Ramage HR, Connolly LE, Cox JS. Comprehensive Functional Analysis of Mycobacterium tuberculosis Toxin-Antitoxin Systems: Implications for Pathogenesis, Stress Responses, and Evolution. Rosenberg SM, editor. PLoS Genet. 2009 Dec 11;5(12):e1000767.

44. Magnuson RD. Hypothetical Functions of Toxin-Antitoxin Systems. J Bacteriol. 2007 Aug 20;189(17):6089–92.

45. Szekeres S, Dauti M, Wilde C, Mazel D, Rowe-Magnus DA. Chromosomal toxin-antitoxin loci can diminish large-scale genome reductions in the absence of selection. Mol Microbiol. 2007 Jan 22;63(6):1588–605.

46. Christensen SK, Mikkelsen M, Pedersen K, Gerdes K. RelE, a global inhibitor of translation, is activated during nutritional stress. Proc Natl Acad Sci USA. 2001 Dec 4;98(25):14328–33.

47. Sat B, Hazan R, Fisher T, Khaner H, Glaser G, Engelberg-Kulka H. Programmed Cell Death in Escherichia coli: Some Antibiotics Can Trigger mazEF Lethality. J Bacteriol. 2001 Mar 15;183(6):2041–5.

48. Hazan R, Sat B, Engelberg-Kulka H. Escherichia coli mazEF-Mediated Cell Death Is Triggered

by Various Stressful Conditions. J Bacteriol. 2004 May 18;186(11):3663–9.

49. Pedersen K, Christensen SK, Gerdes K. Rapid induction and reversal of a bacteriostatic condition by controlled expression of toxins and antitoxins. Mol Microbiol. 2002 Jul;45(2):501–10.

50. Gerdes K, Maisonneuve E. Bacterial Persistence and Toxin-Antitoxin Loci. Annu Rev Microbiol. 2012 Oct 13;66(1):103–23.

51. Moyed HS, Bertrand KP. hipA, a newly recognized gene of Escherichia coli K-12 that affects frequency of persistence after inhibition of murein synthesis. J Bacteriol. 1983 Aug;155(2):768–75.

52. Germain E, Castro-Roa D, Zenkin N, Gerdes K. Molecular Mechanism of Bacterial Persistence by HipA. Molecular Cell. 2013 Oct;52(2):248–54.

53. Kaspy I, Rotem E, Weiss N, Ronin I, Balaban NQ, Glaser G. HipA-mediated antibiotic persistence via phosphorylation of the glutamyl-tRNA-synthetase. Nat Comms. Nature Publishing Group; 2014 Nov 23;4:1–7.

54. Schumacher MA, Balani P, Min J, Chinnam NB, Hansen S, Vulić M, et al. HipBA–promoter structures reveal the basis of heritable multidrug tolerance. Nature. 2015 Jul 29;524(7563):59–64.

55. Maisonneuve E, Castro-Camargo M, Gerdes K. (p)ppGpp Controls Bacterial Persistence by Stochastic Induction of Toxin-Antitoxin Activity. Cell. 2013 Aug;154(5):1140–50.

56. Germain E, Roghanian M, Gerdes K, Maisonneuve E. Stochastic induction of persister cells by HipA through (p)ppGpp-mediated activation of mRNA endonucleases. Proc Natl Acad Sci USA. 2015 Apr 21;112(16):5171–6.

57. Jørgensen MG, Gerdes K. Bacterial persistence by RNA endonucleases. 2011.

58. Keren I, Shah D, Spoering A, Kaldalu N, Lewis K. Specialized Persister Cells and the Mechanism of Multidrug Tolerance in Escherichia coli. J Bacteriol. 2004 Dec 2;186(24):8172–80.

59. Shah D, Zhang Z, Khodursky A, Kaldalu N, Kurg K, Lewis K. BMC Microbiol. 2006;6(1):53.

60. Verstraeten N, Knapen WJ, Kint CI, Liebens V, Van den Bergh B, Dewachter L, et al. Obg and Membrane Depolarization Are Part of a Microbial Bet-Hedging Strategy that Leads to Antibiotic Tolerance. Molecular Cell. Elsevier Inc; 2015 Jul 2;59(1):9–21.

61. Vollmer W, Blanot D, de Pedro MA. Peptidoglycan structure and architecture. FEMS Microbiology Reviews. 2008 Mar 1;32(2):149–67.

62. Barreteau H, Kovač A, Boniface A, Sova M, Gobec S, Blanot D. Cytoplasmic steps of peptidoglycan biosynthesis. FEMS Microbiology Reviews. 2008 Mar 1;32(2):168–207.

63. Bouhss A, Trunkfield AE, Bugg TDH, Mengin-Lecreulx D. The biosynthesis of peptidoglycan lipid-linked intermediates. FEMS Microbiology Reviews. 2008 Mar 1;32(2):208–33.

64. Sham LT, Butler EK, Lebar MD, Kahne D, Bernhardt TG, Ruiz N. MurJ is the flippase of lipid-linked precursors for peptidoglycan biogenesis. Science. 2014 Jul 10;345(6193):220–2.

65. Meeske AJ, Sham L-T, Kimsey H, Koo B-M, Gross CA, Bernhardt TG, et al. MurJ and a novel lipid II flippase are required for cell wall biogenesis in Bacillus subtilis. Proc Natl Acad Sci USA. 2015 May 19;112(20):6437–42.

66. Park JT, Uehara T. How Bacteria Consume Their Own Exoskeletons (Turnover and Recycling of Cell Wall Peptidoglycan). Microbiology and Molecular Biology Reviews. 2008 Jun 5;72(2):211–27.

67. Vollmer W, Joris B, Charlier P, Foster S. Bacterial peptidoglycan (murein) hydrolases. FEMS Microbiology Reviews. 2008 Mar 1;32(2):259–86.

68. Uehara T, Bernhardt TG. More than just lysins: peptidoglycan hydrolases tailor the cell wall. Current Opinion in Microbiology. Elsevier Ltd; 2011 Dec 1;14(6):698–703.

69. Cabeen MT, Jacobs-Wagner C. The Bacterial Cytoskeleton. Annu Rev Genet. 2010 Dec;44(1):365–92.

70. Cho H. The Role of Cytoskeletal Elements in Shaping Bacterial Cells. Journal of Microbiology and Biotechnology. 2015 Mar 28;25(3):307–16.

71. Eun Y-J, Kapoor M, Hussain S, Garner EC. Bacterial Filament Systems: Toward Understanding Their Emergent Behavior and Cellular Functions. Journal of Biological Chemistry. 2015 Jul 9;290(28):17181–9.

72. Bi E, Lutkenhaus J. FtsZ ring structure associated with division in Escherichia coli. Nature. 1991.

73. Bork P, Sander C, Valencia A. An ATPase domain common to prokaryotic cell cycle proteins, sugar kinases, actin, and hsp70 heat shock proteins. Proc Natl Acad Sci USA. 1992 Aug 15;89(16):7290–4.

74. Erickson HP, Anderson DE, Osawa M. FtsZ in Bacterial Cytokinesis: Cytoskeleton and Force Generator All in One. Microbiology and Molecular Biology Reviews. 2010 Nov 30;74(4):504–28.

75. Pichoff S, Lutkenhaus J. Unique and overlapping roles for ZipA and FtsA in septal ring assembly in Escherichia coli. EMBO J. 2002 Feb 15;21(4):685–93.

76. Lutkenhaus J, Pichoff S, Du S. Bacterial cytokinesis: From Z ring to divisome. Robinson DN, Bement WM, Balasubramanian MK, Sanger JW, editors. Cytoskeleton. 2012 Aug 30;69(10):778–90.

77. Huang KH, Durand-Heredia J, Janakiraman A. FtsZ Ring Stability: of Bundles, Tubules, Crosslinks, and Curves. J Bacteriol. 2013 Apr 9;195(9):1859–68.

78. Goehring NW, Beckwith J. Diverse paths to midcell: assembly of the bacterial cell division machinery. Curr Biol. 2005 Jul 12;15(13):R514–26.

79. de Boer PA. Advances in understanding E. coli cell fission. Current Opinion in Microbiology. 2010 Dec;13(6):730–7.

80. Jones L, Carballido-Lopez R, Errington J. Control of cell shape in bacteria: helical, actin-like filaments in Bacillus subtilis. Cell. 2001.

81. Typas A, Banzhaf M, Gross CA, Vollmer W. From the regulation of peptidoglycansynthesis to bacterial growth andmorphology. Nat Rev Micro. Nature Publishing Group; 2011 Dec 28;10(2):123–36.

82. Daniel RA, Errington J. Control of cell morphogenesis in bacteria: two distinct ways to make a rod-shaped cell. Cell. 2003 Jun 13;113(6):767–76.

83. Garner EC, Bernard R, Wang W, Zhuang X, Rudner DZ, Mitchison T. Coupled, Circumferential Motions of the Cell Wall Synthesis Machinery and MreB Filaments in B. subtilis. Science. 2011 Jul 7;333(6039):222–5.

84. van Teeffelen S, Wang S, Furchtgott L, Huang KC, Wingreen NS, Shaevitz JW, et al. The bacterial actin MreB rotates, and rotation depends on cell-wall assembly. Proc Natl Acad Sci USA. 2011 Sep 20;108(38):15822–7.

85. van den Ent F, Izoré T, Bharat TA, Johnson CM, Lowe J. Bacterial actin MreB forms antiparallel double filaments. eLife. 2014;3:e02634.

86. Salje J, van den Ent F, de Boer P, Lowe J. Direct Membrane Binding by Bacterial Actin MreB. Molecular Cell. Elsevier Inc; 2011 Aug 5;43(3):478–87.

87. Divakaruni AV, Baida C, White CL, Gober JW. The cell shape proteins MreB and MreC control cell morphogenesis by positioning cell wall synthetic complexes. Mol Microbiol. 2007 Oct;66(1):174–88.

88. White CL, Kitich A, Gober JW. Positioning cell wall synthetic complexes by the bacterial morphogenetic proteins MreB and MreD. Mol Microbiol. 2010 Mar 10;76(3):616–33.

89. Bendezú FO, Hale CA, Bernhardt TG, de Boer PAJ. RodZ (YfgA) is required for proper assembly of the MreB actin cytoskeleton and cell shape in E. coli. EMBO J. 2008 Dec 11;28(3):193–204.

90. van den Ent F, Johnson CM, Persons L, de Boer P, we JLO. Bacterial actin MreB assembles in complex with cell shape protein RodZ. EMBO J. Nature Publishing Group; 2010 Feb 18;29(6):1081–90.

91. Morgenstein RM, Bratton BP, Nguyen JP, Ouzounov N, Shaevitz JW, Gitai Z. RodZ links MreB to cell wall synthesis to mediate MreB rotation and robust morphogenesis. Proc Natl Acad Sci USA. 2015 Oct 6;112(40):12510–5.

92. Domínguez-Escobar J, Chastanet A, Crevenna AH, Fromion V, Wedlich-Söldner R, Carballido-Lopez R. Processive movement of MreB-associated cell wall biosynthetic complexes in bacteria. Science. 2011 Jul 8;333(6039):225–8.

93. Fenton AK, Gerdes K. Direct interaction of FtsZ and MreB is required for septum synthesis and cell division in Escherichia coli. EMBO J. 2013 Jun 11;32(13):1953–65.

94. Cordell SC, Robinson EJH, Lowe J. Crystal structure of the SOS cell division inhibitor SulA and in complex with FtsZ. Proc Natl Acad Sci USA. 2003 Jun 24;100(13):7889–94.

95. Chen Y, Milam SL, Erickson HP. SulA Inhibits Assembly of FtsZ by a Simple Sequestration Mechanism. Biochemistry. 2012 Apr 10;51(14):3100–9.

96. IWAI N, NAGAI K, Wachi M. Novel S-benzylisothiourea compound that induces spherical cells in Escherichia coli probably by acting on a rod-shape-determining protein(s) other than penicillin-binding protein 2. Biosci Biotechnol Biochem. 2002 Dec;66(12):2658–62.

97. Gitai Z, Dye NA, Reisenauer A, Wachi M, Shapiro L. MreB Actin-Mediated Segregation of a Specific Region of a Bacterial Chromosome. Cell. 2005 Feb;120(3):329–41.

98. Kruse T, Bork-Jensen J, Gerdes K. The morphogenetic MreBCD proteins of Escherichia coli form an essential membrane-bound complex. Mol Microbiol. 2004 Oct 6;55(1):78–89.

99. Bendezu FO, de Boer PAJ. Conditional Lethality, Division Defects, Membrane Involution, and

Endocytosis in mre and mrd Shape Mutants of Escherichia coli. J Bacteriol. 2008 Feb 20;190(5):1792–811.

100. Leplae R, Geeraerts D, Hallez R, Guglielmini J, Drèze P, Van Melderen L. Diversity of bacterial type II toxin-antitoxin systems: a comprehensive search and functional analysis of novel families. Nucleic Acids Research. 2011 Jul;39(13):5513–25.

101. Varma A, de Pedro MA, Young KD. FtsZ directs a second mode of peptidoglycan synthesis in Escherichia coli. J Bacteriol. 2007 Aug;189(15):5692–704.

102. Baba T, Ara T, Hasegawa M, Takai Y, Okumura Y, Baba M, et al. Construction of Escherichia coli K-12 in-frame, single-gene knockout mutants: the Keio collection. Mol Syst Biol. 2006 Feb 21;2.

103. Arbing MA, Handelman SK, Kuzin AP, Verdon G, Wang C, Su M, et al. Crystal structures of Phd-Doc, HigA, and YeeU establish multiple evolutionary links between microbial growth-regulating toxin-antitoxin systems. Structure. 2010 Aug 11;18(8):996–1010.

Chapter 2: The CbtA toxin mediates a simultaneous block of cell division and cell elongation via independent interactions with both FtsZ and MreB

Attributions: I wrote this chapter in its entirety with helpful editing advice from my advisor, Ann Hochschild. Ann Hochschild and Mrinalini Tavag conceptualized the development of the bacterial two-hybrid system as a genetic system to dissect the interactions of CbtA. Mrinalini Tavag generated and initially tested several important constructs for the two-hybrid and morphology studies presented in this chapter (designated in Table A2.2 at the end of this chapter) and performed the genetic selection that led to the isolation of the YpjF-F65S variant. I conducted the rest of the experimental work presented in this chapter with major conceptual contributions from Ann Hochschild. I would like to thank Tom Bernhardt and members of the Bernhardt lab for the NP1 strain and for helpful technical advice related to the ZapA-GFP imaging study.

Chapter 2.1: The CbtA toxin of *E. coli* alters cell shape and interacts with the bacterial cytoskeleton

Prokaryotic toxin-antitoxin (TA) systems are genetic modules consisting of a stable toxin protein that mediates growth inhibition or cell death in the cell in which it is produced, coupled with an antitoxin that neutralizes this toxicity. While the molecular nature of antitoxins can vary, typically they are more labile than their cognate toxin, requiring consistent production to block toxicity (reviewed in (1-4)). In most cases, TA gene pairs are found in an operon, with the antitoxin gene directly upstream of the toxin gene; transcription of the toxin-antitoxin genes is typically negatively auto-regulated by binding of the antitoxin (often in complex with the toxin) within the promoter region (4). First discovered in the context of plasmid-based addiction modules (5,6), work in recent decades has shown these systems also to be well represented on bacterial chromosomes (7). Mining of all sequenced bacterial genomes for homologs of previously characterized TA families led to the discovery that bacterial genomes can harbor anywhere from zero to greater than 50 TA systems (8). Characterization of many of these TA systems has revealed that the toxins have evolved the ability to target a diverse set of essential cellular processes ranging from translation to DNA replication, to membrane integrity (3).

As described in Chapter 1 of this dissertation, Brown and Shaw identified a family of three prophage-encoded TA systems in the *E. coli* K-12 genome (9). Their work indicated that the toxin components of these systems (CbtA, YpjF, and YkfI) are potent growth inhibitors (9). Subsequent work by Tan et al. demonstrated that overproduction of the CbtA toxin from a multi-copy plasmid in *E. coli* results in a loss of rod shape and the formation of lemon-shaped cells which eventually lyse (10). As work by Varma et al. established, lemon-like morphology can be achieved in *E. coli* through dual disruption of cell division and cell elongation pathways (11). Interestingly, Tan et al. detected interactions between the CbtA toxin and both FtsZ and MreB *in vivo* (by yeast two-hybrid) and *in vitro* (by pull-down assay) (10). They also demonstrated that His_6-CbtA reduces the sedimentation efficiencies of purified MreB and FtsZ and inhibits FtsZ GTPase activity (10). Taken together, their data suggest that CbtA may block cell division and cell elongation through simultaneous inhibition of FtsZ and MreB.

CbtA is a small protein, consisting of only 124 amino acids, and its two cytoskeletal targets, FtsZ and MreB, share no sequence or structural homology. Thus, it seems remarkable that such a small protein would be capable of potently inhibiting two distinct proteins through independent physical interaction. In their discussion, Tan et al. acknowledged that simultaneous inhibition of cell division and cell elongation may be a consequence of CbtA only physically interacting with FtsZ, thereby blocking some important interaction between FtsZ and MreB (10). To support this, they cited the observation made by multiple groups that prior to cytokinesis, MreB and other members of the cell elongation complex assemble into mid-cell ring structures flanking the Z ring (12-14). The observed MreB ring structures were shown to require advance assembly of FtsZ at mid-cell (13).

While some MreB cytological structures have since been shown to be artifacts caused by certain fluorescent protein tags (especially those at the N-terminus of MreB) (15), Fenton et al. recently provided compelling evidence that MreB and FtsZ directly interact in a manner that is essential for *E. coli* cell division (16). In this study, the authors observed early recruitment of MreB to the Z ring; this recruitment was dependent on a direct interaction between MreB and FtsZ, which was detectable both by bacterial two-hybrid analysis and crosslinking pull-downs. A strain producing an MreB mutant (MreB-D285A) incapable of interaction with FtsZ, had a pronounced division defect, leading to filamented cells with locked Z ring structures. Interestingly, single amino acid substitutions in FtsZ restored interaction with this MreB variant and allowed for normal division to occur. Further characterization of the locked Z rings produced by disruption of the MreB-FtsZ interaction led to the model that direct interaction of these two cytoskeletal proteins is needed to hand-off essential synthetic enzymes during the switch from cell elongation to cell division (16).

This recent demonstration of the direct coordination between cell elongation and cell division pathways necessitates further characterization of the mechanism by which CbtA inhibits growth. While Tan et al. provided compelling evidence that CbtA interacts with the bacterial cytoskeleton, it has not previously been determined whether this small protein can mediate direct and independent interactions with both FtsZ and MreB. Furthermore, up until now, it has not been confirmed whether the interactions detected by Tan et al. are functionally relevant and contribute to the overexpression phenotypes observed. In their 2011 paper, Tan et al., attempted to dissect CbtA function by making truncations at the N- and C-terminal ends of the protein. They found that overproduction of a truncated variant missing the last 52 residues of CbtA resulted in modest cell filamentation rather than formation of lemons; however, they reported that this was likely due to destabilization of the protein rather than disruption of the MreB-CbtA interaction (10).

A major goal of the work presented in this dissertation was to genetically dissect the interactions between the CbtA toxin and its two proposed cytoskeletal targets in order to determine whether or not direct and independent interaction of CbtA with both targets is necessary for CbtA-mediated toxicity. In this chapter, I describe the discovery and characterization of CbtA variants that interact with only a single cytoskeletal target. Based on the characterization of these variants, we conclude that CbtA does indeed interact independently with both FtsZ and MreB; furthermore, we provide compelling evidence indicating these interactions directly contribute to the lemon-shape phenotype and growth inhibition previously described.

Chapter 2.2: Results

CbtA interacts with FtsZ and MreB and produces lemon-shaped cells

Consistent with previous reports, we observed that overexpression of *his_6-cbtA-gfp* from the *pT5-lac* promoter on a multi-copy plasmid (pMT139) in *E. coli* BW27785 resulted in a severe decrease in viability (Figure 2.1A). Furthermore, time-lapse microscopy confirmed that upon overexpression of *his_6-cbtA-gfp,* cells failed to divide, forming swollen lemons that eventually lysed (Figure 2.1B). Observation of GFP fluorescence in this strain revealed no obvious localization phenotype; His_6-CbtA-GFP was distributed diffusely throughout the entire bloated cell (Figure 2.1C). Importantly, we also found that overproduction of untagged CbtA yielded an identical lemon phenotype (Figure 2.1D). As the various images in Figure 2 illustrate, while we observed drastic morphological change in basically all cells observed, the individual lemons displayed striking heterogeneity. Many cells formed smooth lemons, while others had pronounced tubular projections at one or both poles; bi-lobed lemons (such as the one shown in panel C) were seen by time-lapse microscopy to form from pre-constricted cells (see the top panel of Figure 2.4F later in this chapter). These morphologies are consistent with the varied cell shapes observed by Varma et al. with combined FtsZ and MreB inhibition (11).

Tan et al. observed interaction between CbtA and its proposed cytoskeletal targets in a yeast two-hybrid system (10). Similarly, we were able to detect interactions between CbtA and both FtsZ and MreB in a bacterial two-hybrid system developed in our lab (17,18). As shown in Figure 2.2A, in this two-hybrid assay, a protein domain of interest is fused to the N-terminal domain of the α subunit of *E. coli* RNA polymerase and its partner domain is fused to the λCI-DNA binding protein. Contact between these two protein domains activates transcription of a *lacZ* reporter gene under the control of a test promoter bearing an upstream λCI binding site. Our two-hybrid strain contains two compatible plasmids encoding our two fusion proteins and a single copy episome containing the *lacZ* reporter. A two-hybrid interaction can be visualized as blue colonies on indicator plates containing X-gal or can be measured quantitatively using a liquid β-galactosidase assay. Having wild-type FtsZ and wild-type CbtA in our two-hybrid assay results in a 15 to 25-fold increase of *lacZ* expression as measured by beta-galactosidase assay (Figure 2.2B), while having wild-type MreB and wild-type CbtA results in a 3-fold increase of *lacZ* expression. The detection of these interactions in our two-hybrid assay is consistent with CbtA interacting with both MreB

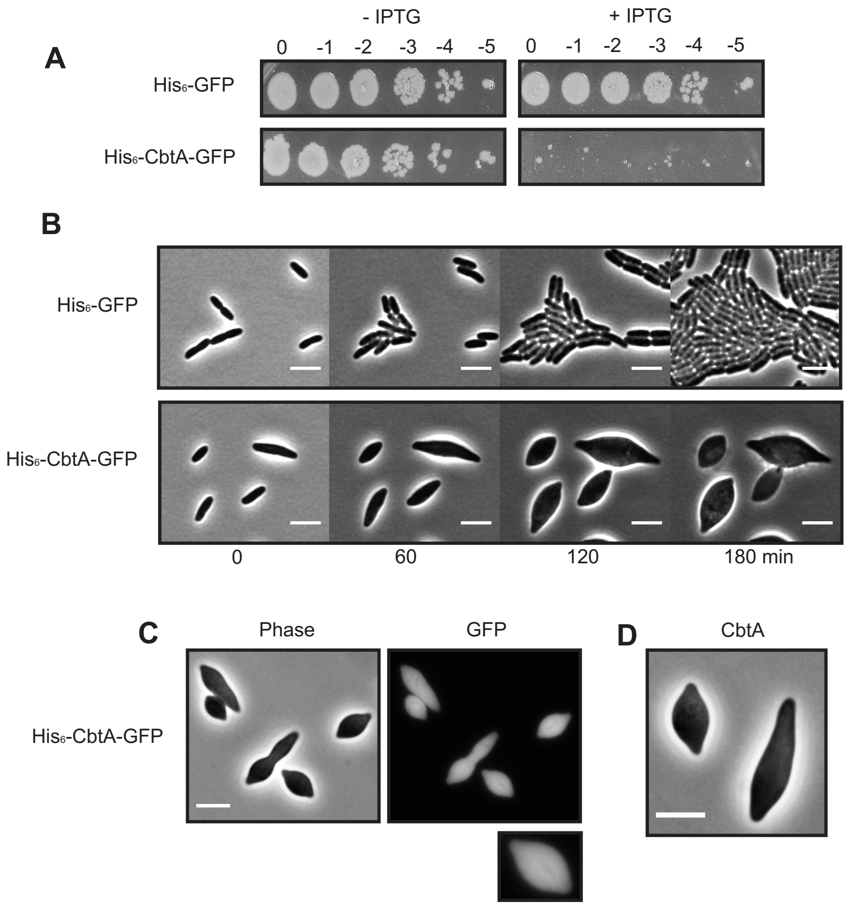
A
- IPTG
+ IPTG
0 -1 -2 -3 -4 -5
0 -1 -2 -3 -4 -5
His6-GFP
His6-CbtA-GFP
B
His6-GFP
His6-CbtA-GFP
0
60
120
180 min
C
Phase
GFP
His6-CbtA-GFP
D
CbtA

Figure 2.1: Overproduction of CbtA causes lemon-like morphology. A) Spot dilution assay indicates that expression of *his*$_6$*-cbtA-gfp* from $P_{T5\text{-}lac}$ on the multi-copy plasmid pMT139 causes a decrease in the viability of *E. coli* BW27785. The same strain expressing *his*$_6$*-gfp* from pMT136 is shown for comparison. For this experiment, all growth steps were done at 37 ºC. Late-log cultures were spotted on LB (Cm) with or without added IPTG (100 µM). B) Cells of strains BW27785/pMT136 and BW27785/pMT139 were imaged every 3 min for 3 hrs at 30 ºC on 2% agarose pads containing LB and 100 µM IPTG. Images taken after 0, 60, 120, and 180 min are shown. C) GFP fluorescence imaging of BW27785/ pMT139 induced with 100 µM IPTG for 2 hrs at 30 ºC shows that His$_6$-CbtA-GFP is diffuse throughout the cell. D) Overexpression of *cbtA* (untagged allele) from the pSG360-derived plasmid, pDH325, in BW27785 yields a similar lemon-like morphology. Expression was induced with 200 µM IPTG for 2 hrs at 30 ºC. For all panels, scale bars represent 5 µm.

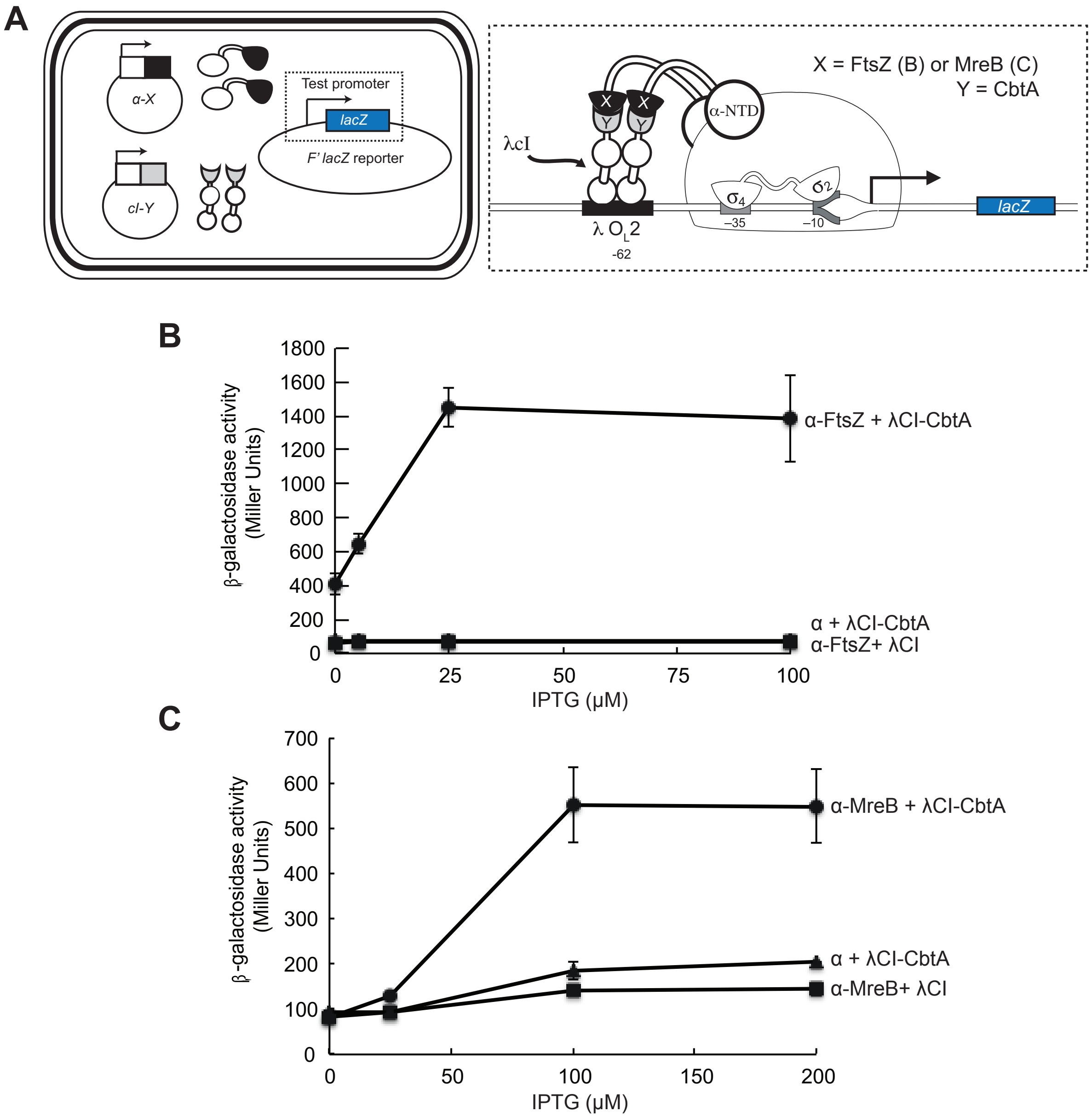

Figure 2.2: Detection of CbtA interaction with FtsZ and MreB in a transcription-based bacterial two-hybrid system. A) In order to detect an interaction of interest, the two-hybrid strain FW102 O_L2-62 is transformed with two compatible plasmids: one encoding a protein of interest fused to the N-terminal domain of the α subunit of *E. coli* RNA polymerase and one encoding a second protein fused to the λCI DNA-binding protein. The expression of both fusion genes is under the control of IPTG-inducible promoters. This strain also bears an F' episome with *lacI*^{q} and the two-hybrid *lacZ* reporter construct. As

Figure 2.2 (Continued)

shown in the panel on the right, this reporter construct contains a λCI operator positioned 62 bp upstream of the transcription start site. B, C) The two-hybrid interactions of α-FtsZ and α-MreB with λCI-CbtA are shown in panels B and C, respectively. β-galactosidase activity was measured at multiple induction levels (0, 5, 25 and 100 μM IPTG for B; 0, 25, 100, and 200 μM IPTG for C). Each point represents the average of triplicate values; error bars represent standard deviation.

and FtsZ (though it does not exclude the possibility that endogenous FtsZ may be bridging the apparent interaction between CbtA and MreB).

Brown and Shaw reported that CbtA has two homologs in *E. coli,* YpjF and YkfI, that cause similar growth reduction when overproduced (9). However, it had not previously been established whether these toxin homologs also yield a simultaneous block of cell elongation and cell division. As shown in Figure 2.3, we found that indeed this is the case. Overexpression of *his*$_6$*-ypjF-gfp* and *his*$_6$*-ykfI-gfp* from the *pT5-lac* promoter on multi-copy plasmids (pMT138 and p3-37, respectively) in *E. coli* BW27785 resulted in a decrease in viability (Figure 2.3A) and led to the formation of lemon-shaped cells (Figure 2.3B). We were also able to detect strong interactions between both toxins and FtsZ, and between YpjF and MreB in our bacterial two-hybrid system (Figure 2.3C). Although YkfI is ~80% identical to YpjF and blocks cell elongation when overproduce (Figure 2.3B), we were unable to detect an interaction between YkfI and MreB in our bacterial two-hybrid system (Figure 2.3C).

Our microscopic observations and two-hybrid data support the model that CbtA binds both FtsZ and MreB; however, in order to determine if CbtA can interact independently with each target and to examine whether these interactions are contributing directly to the observed toxicity, we sought to isolate mutations that specifically disrupt each of the interactions. Through methods described below, we were able to isolate a CbtA variant, CbtA-F65S, which is only able to interact with MreB (Figure 2.4A and B); we also identified a second variant, CbtA-R15C, which is severely decreased for interaction with MreB but maintains interaction with FtsZ (Figure 2.5A and B). Whereas this latter variant was found by means of a two-hybrid screening approach, the F65S variant was isolated in a more fortuitous manner.

Identification of a CbtA variant that interacts only with MreB

Our lab is interested in the identification of endogenous bacterial amyloid-forming proteins, and CbtA and its homologs, YpjF and YkfI, were initially of interest to us because of their propensity to form intracellular SDS-resistant aggregates (data not shown). Prior to the report of CbtA being a cytoskeletal inhibitor (10), we had sought to determine whether aggregation of this family of proteins was connected to their toxicity. A dual selection/screen strategy was employed in order to identify variants with reduced toxicity. The *cbtA*, *ypjF,* and *ykfI* genes were amplified by error-prone PCR and cloned into the same

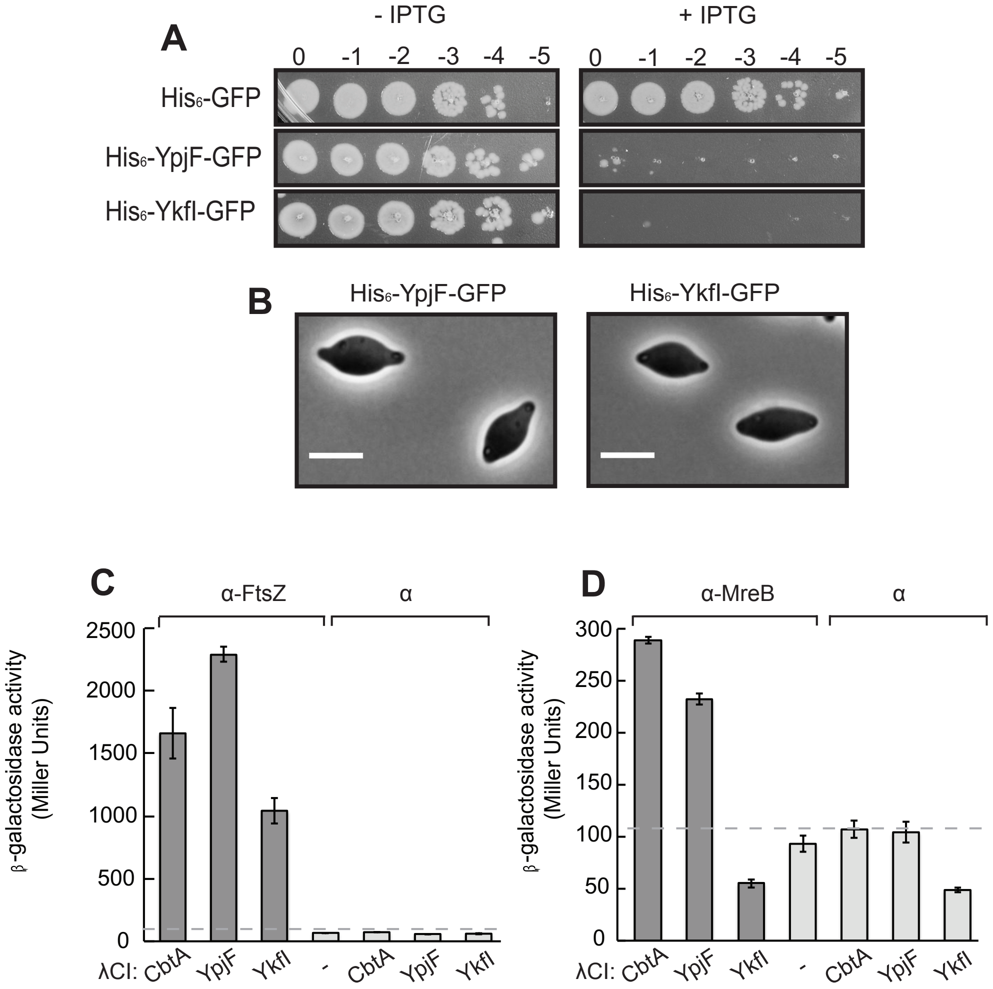

Figure 2.3: YpjF and YkfI cause lemon-like morphology. A) As seen by spot dilution analysis, overexpression of *his$_6$-ypjF-gfp* and *his$_6$-ykfI-gfp* from plasmids pMT138 and p3-37, respectively, is toxic. Overnight cultures of BW27785/pMT136, BW27785/pMT138, and BW27785/p3-37 were back diluted to a starting OD600 of 0.05 in fresh LB (Cm) and grown until late-log phase at 37 ºC. Cultures were normalized, serially diluted, and spotted on LB (Cm) with or without 100 µM IPTG. Plates were incubated at 37 ºC overnight. B) Strains BW27785/pMT138 and BW27785/p3-37 were imaged after 1.5 hr induction at 37 ºC with 100 µM IPTG. Scale bar represents 5 µm. Two-hybrid interactions of α-FtsZ (C) and α-MreB (D) with λCI-YpjF and λCI-YkfI are shown. λCI-CbtA interactions from the same experiments are included for comparison. The experiment shown in C was done with 25 µM IPTG induction; the experiment shown

Figure 2.3 (Continued)

in D was done with 100 µM IPTG induction. Bars represent the average Miller unit values for triplicate cultures; error bars represent standard deviation.

vectors used for the expression studies shown in Figures 2.1 and 2.3. The mutagenized alleles all contained an N-terminal His$_6$ tag and a C-terminal GFP fusion and were under the control of the *pT5-lac* IPTG-inducible promoter. These mutant libraries were transformed into *E. coli* BW27785 and plated on a high concentration of IPTG (500 μM), thus selecting for toxin variants with lowered toxicity. These surviving colonies were then screened for green colony color and fluorescence to indicate that the GFP-fusion protein was still being produced to roughly comparable levels. Although many other selected variants were found to have decreased stability as compared to the wild-type proteins, a stable YpjF variant, YpjF-F65S, was isolated.

After learning of the reported interactions between CbtA and the bacterial cytoskeleton and successfully demonstrating that these interactions could be detected in our bacterial two-hybrid system (Figure 2.2), we wondered if the F65S substitution would have any effect on these CbtA cytoskeletal interactions. As shown in Figure 1.2, the F65 residue is conserved in all three toxins. When the F65S substitution was introduced into CbtA, the resulting variant was still toxic upon overproduction, as was the YpjF-F65S variant, though to a slightly lesser degree (Figure 2.4C). However, interestingly, when we assayed the interaction between λCI-CbtA-F65S and both α-FtsZ and α-MreB by bacterial two-hybrid analysis, we observed that this variant maintained interaction with α-MreB (Figure 2.4B) but failed to interact with α-FtsZ (Figure 2.4A). Morphological observation was consistent with this result; upon overproduction of His$_6$-CbtA-F65S-GFP to levels comparable to that of the wild-type protein (Figure 2.4D), cells adopted a spherical rather than lemon morphology (Figure 2.4E). As seen by time-lapse microscopy (Figure 2.4F), over the course of a three-hour induction period, cells producing His$_6$-CbtA-F65S-GFP lose their rod-shape, becoming spheres. These spherical cells continue to divide for 1-2 generations, gradually increasing in diameter until they lyse. This striking phenotype is very similar to that observed upon depletion of MreB (19,20), thus demonstrating that CbtA-F65S is able to interact with MreB and mediate a block in cell elongation even in the absence of an FtsZ interaction.

We tested the F65S substitution in the context of YkfI and also re-examined the YpjF-F65S-encoding plasmid originally isolated in our screen. We saw that like with the CbtA-F65S mutant, overproduction of these toxin variants yielded spherical rather than lemon-shaped cells (Figure 2.4E). Furthermore, we found that λCI-YpjF-F65S and λCI-YkfI-F65S were both severely decreased for their

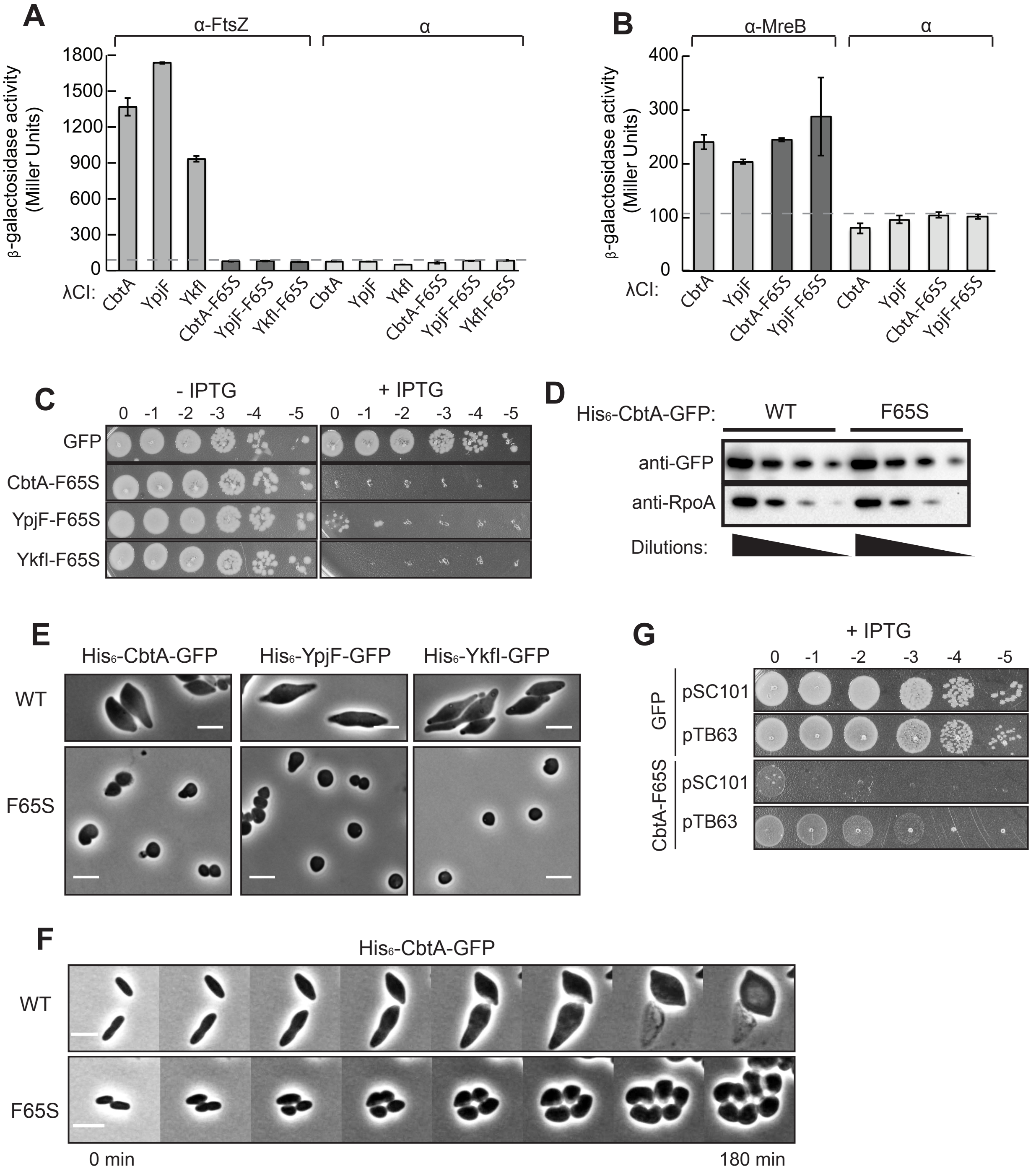

Figure 2.4: Toxin variants containing the F65S substitution interact only with MreB. β-galactosidase assays were performed to measure the interaction between α-FtsZ (A) and α-MreB (B) and the toxin variants, λCI-CbtA-F65S, λCI-YpjF-F65S, and λCI-YkfI-F65S. β-galactosidase activity was measured at 25 μM IPTG in A and 100 μM IPTG in B; bars represent averages of triplicate values and error bars

Figure 2.4 (Continued)

represent standard deviation. C) Late log cultures of BW27785/pMT136, BW27785/pMT144 (*his*$_6$*-ykfI-F65S-gfp*), BW27785/pMT146 (*his*$_6$*-cbtA-F65S-gfp*), and BW27785/pMT188 (*his*$_6$*-ypjF-F65S-gfp*) grown without induction, were spotted on LB (Cm) plates with or without 100 μM IPTG; plates were incubated at 37 ºC overnight. D) Western blot analysis using a GFP antibody to detect His$_6$-CbtA-GFP levels indicates that the F65S substitution does not obviously destabilize the CbtA-GFP fusion protein. Cells were harvested and lysed after 2 hr induction with 100 μM IPTG at 30 ºC. Several dilutions (1:2, 1:10, 1:30, and 1:90) are shown. RpoA was detected on a separate blot using an antibody that specifically binds the C-terminal domain; this serves as a loading control. E) BW27785 strains transformed with the appropriate pCA24N-derived plasmid were imaged after 1.5 hr induction with 100 μM IPTG at 37 ºC. F) Time-lapse microscopy of BW27785/pMT139 and BW27785/pMT146 was performed for 3 hrs at 30 ºC. Cells were imaged on 2% agarose pads containing LB and 100 μM IPTG. Scale bars represent 5 μm. G) BW27785 was co-transformed with pMT136 or pMT146, and pSC101 (empty vector) or pTB63 (*ftsQAZ*). Overnight cultures were back diluted in LB (CmTet) and grown at 30 ºC until they reached mid-log phase. Cultures were normalized, serially diluted, and spotted on LB (CmTet) with or without 100 μM IPTG. Plates were incubated at 30 ºC overnight.

interaction with α-FtsZ (Figure 2.4A), but λCI-YpjF-F65S maintained a strong interaction with α-MreB (Figure 2.4B). These analyses suggest that the FtsZ interaction determinants for all three toxins are conserved and further highlights that the cytoskeletal interactions of this family of toxins can be genetically parsed. Importantly, the morphology data also suggest that toxin interaction with FtsZ contributes to the striking lemon-shape phenotype.

The CbtA-F65S, YpjF-F65S, and YkfI-F65S variants are all still very toxic at high induction levels (Figure 2.4C) and are not obviously destabilized (Figure 2.4D and data not shown); we speculate that the ability of the original isolate expressing the *his*$_6$*-ypjF-F65S-gfp* allele to grow in the presence of 500 µM IPTG, may have been the result of an extragenic suppressor. The lethality of a defect in cell elongation can be overcome by slower growth rate or increased expression of *ftsZ*, and such mutations occur at a relatively high frequency (19-21). Indeed, we observed that increased expression of *ftsZ* from the pTB63 plasmid partially rescued viability when His$_6$-CbtA-F65S was overproduced (Figure 2.4G). In addition to suggesting a possible explanation for the discovery of the F65S variant (although we cannot know for certain), this result indicates that lethal CbtA-F65S-mediated block of cell elongation can be similarly suppressed by increased *ftsZ* levels.

Identification of a CbtA variant that interacts only with FtsZ

To further investigate the phenotypic contributions of both cytoskeletal interactions, we sought to identify a CbtA variant with the opposite interaction profile: strong FtsZ interaction and abrogated MreB interaction. To do this, we used a two-hybrid-based screening strategy. As mentioned previously, our bacterial two-hybrid system allows for the visual representation of a protein-protein interaction, yielding blue colonies when cells are plated on indicator medium supplemented with X-gal. This clear visualization makes the two-hybrid system an effective genetic screening platform that can be used to identify substitutions in either binding partner that disrupt the detected interaction of interest. Mutagenized libraries of either fusion construct can be rapidly generated and screened; mutant proteins that fail to interact with their binding partner yield white or pale blue colonies on X-gal indicator medium. When performing a genetic analysis, our aim is to identify mutations that specifically disrupt the interaction of interest; however, it is not possible to distinguish these specific mutants from uninformative destabilized or truncated mutants based on white colony color alone. Thus, to distinguish between these informative and uninformative mutants, we perform two-hybrid counterscreens with other known interacting proteins and demand that a mutant of interest maintain this secondary interaction. This two-hybrid screening platform served as an essential genetic tool for much of the work described in this dissertation.

Because the MreB-CbtA two-hybrid interaction is relatively weak (yielding a ~3-fold increase in *lacZ* levels), we had difficulty finding suitable blue-white screening conditions using our standard two-hybrid *lacZ* reporter construct (shown in Figure 2.2A). Although several alternative strategies were attempted, we were finally able to identify appropriate screening conditions using a modified two-hybrid reporter construct. In this reporter, the λCI operator is positioned 20 bp closer to the transcription start site[c], which allows for an additional stabilizing contact between λCI and region 4 of σ^{70} bound to the -35 promoter element. This stabilization results in a boosted level of *lacZ* expression[d] and for our purposes, provided a greater color range for blue-white screening.

We generated a library of PCR-mutagenized *cbtA* alleles fused to λCI and transformed the resulting plasmid library into the modified two-hybrid reporter strain (BN30) containing the *α-mreB* plasmid. “Down” candidates that formed paler colonies (as compared to the wild-type interaction positive control) on indicator plates containing IPTG and X-gal were pooled and counter-screened for their interaction with α-FtsZ. Those that yielded dark blue colonies in this context were investigated further. Among these, we identified a variant (λCI-CbtA-R15C) that exhibited a decreased interaction with α-MreB but maintained a very strong interaction with α-FtsZ (Figure 2.5A and B). Consistent with these two-hybrid data, induction of His_6-CbtA-R15C-GFP production with 50 μM IPTG resulted in filamentation of cells rather than the formation of lemons as seen with comparable levels of the wild-type protein (Figure 2.5C and D). This morphology strongly suggests that the CbtA-R15C variant does not fully inhibit MreB, allowing cell elongation to proceed; however, this variant still binds FtsZ, leading to a block in cell division and filamentation. With 100 μM IPTG, cells do increase in width, forming fat, elongated, snake-like cells, similar to those seen by Varma et al. (11) with simultaneous *sulA* expression and lower A22

---

[c] In the standard two-hybrid reporter, the λCI operator is positioned 62 bp upstream of the transcription start site (-62); in the modified reporter it is at position -42 (17,22).

[d] Note that this boost in *lacZ* levels is independent of the specific two-hybrid interaction. Indeed, in this system, the empty vector control basal levels are also elevated such that the normalized fold-change value is the same.

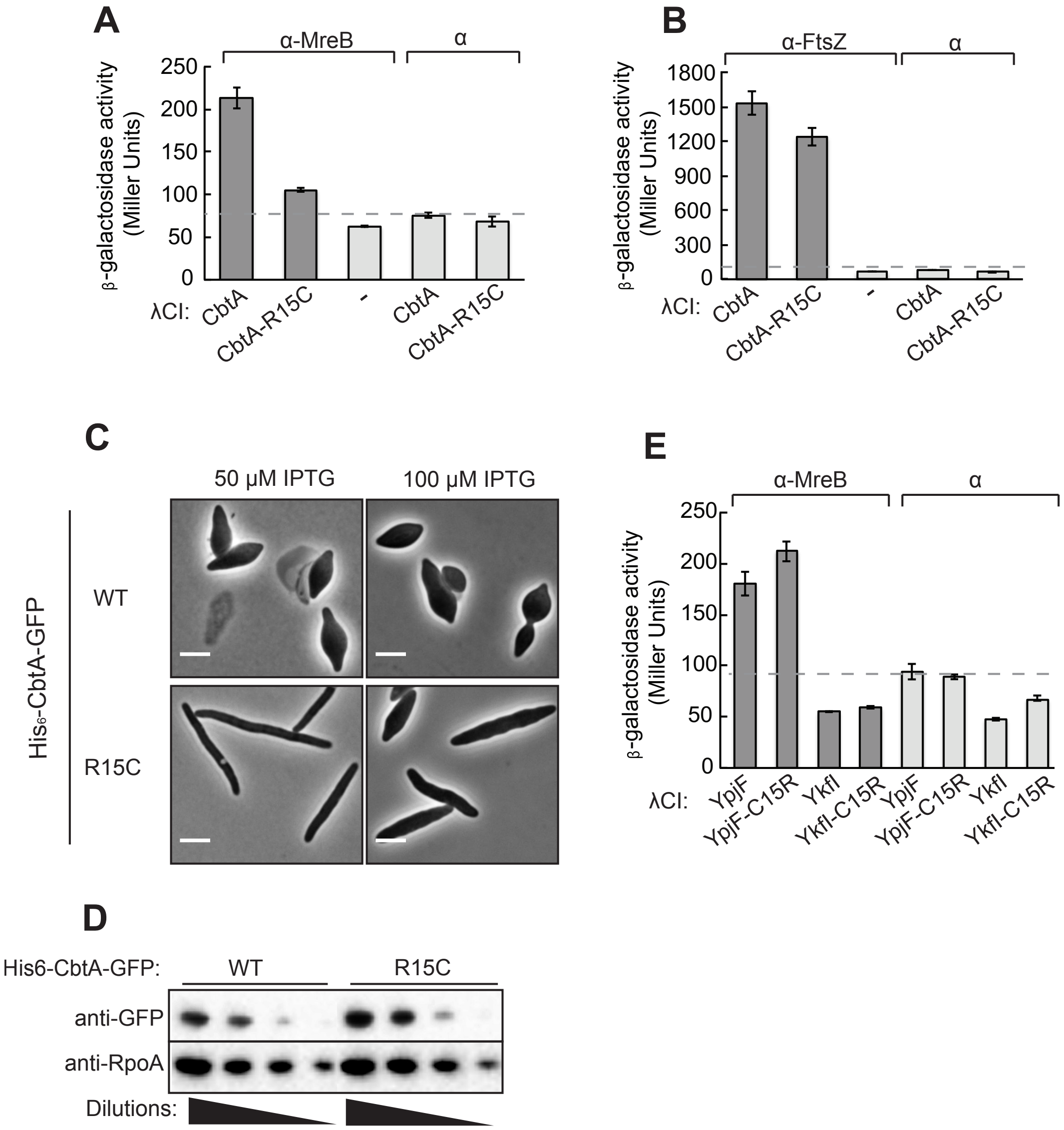

Figure 2.5: CbtA-R15C inhibits cell division. Two-hybrid analysis shows that λCI-CbtA-R15C is decreased for interaction with α-MreB (A) but still maintains strong interaction with α-FtsZ (B). Experiments were performed with 100 μM IPTG and 25 μM IPTG, respectively. C) Overnight cultures of BW27785/pMT139 or BW27785/pDH253 (*his$_6$-cbtA-R15C-gfp)* were back diluted in fresh LB (Cm), grown for 1 hr at 30 ºC, then induced with either 50 μM IPTG (left panels) or 100 μM IPTG (right panels). Images were taken after 2 hrs of induction at 30 ºC. Scale bars represent 5 μm. D) Western blot analysis indicates that His$_6$-CbtA-R15C accumulates to comparable levels as the wild-type protein within the cell. Cells were harvested and lysed after 2 hr induction with 100 μM IPTG at 30 ºC. Several dilutions (1:2,

Figure 2.5 (Continued)

1:10, 1:30, and 1:90) are shown. Toxin levels were detected using an anti-GFP antibody. RpoA was detected on a separate blot using an antibody that specifically binds the C-terminal domain; this serves as a loading control. E) Two-hybrid analysis shows that the C15R substitution has only a slight effect on the interaction between α-MreB and λCI-YpjF and does not result in a detectable interaction between α-MreB and λCI-YkfI. This experiment was performed at 100 μM IPTG. For A, B, and E, bars represent the average Miller unit values of triplicate cultures; error bars represent standard deviation.

concentration. Clearly with higher levels, the R15C variant is able to mediate a partial block of cell elongation, but importantly this still produces a distinct morphology characteristic of relaxed MreB inhibition. Our ability to disrupt the CbtA-MreB interaction while maintaining the CbtA-FtsZ interaction with only a single amino acid substitution strongly suggests that CbtA is able to interact independently with MreB and FtsZ. Furthermore, the formation of cell filaments when the interaction with MreB is disrupted indicates that the CbtA-MreB interaction is necessary for the inhibition of cell elongation.

Interestingly, R15 is not a conserved residue. As shown in the alignment in Figure 1.2, YpjF and YkfI both have a cysteine at this position. Since mutation of R15C decreased the interaction between CbtA-MreB, we wondered if the reverse substitution (C15R) in YpjF would increase its interaction with MreB, and in the case of YkfI, might allow for a detectable interaction. We found that this substitution made no difference in either case (Figure 2.5E). Thus, the genetic determinants that allow for YpjF- and YkfI-mediated inhibition of cell elongation remain unknown.

The CbtA-R15C/F65S variant exhibits reduced toxicity

As summarized in Figure 2.6A, we were able to identify two CbtA variants, each of which interacts with a single cytoskeletal target. CbtA-F65S interacts only with MreB in our two-hybrid system and inhibits cell elongation, resulting in spherical cells. CbtA-R15C, on the other hand, interacts only with FtsZ in the two-hybrid system and produces cell filaments that are blocked for cell division. As the observed morphologies would suggest, overexpression of either *his_6-cbtA-F65S* or *his6-cbtA-R15C* is still lethal (Figure 2.6B). However, we found that overproduction of the His_6-CbtA-R15C/F65S double mutant variant, which accumulates to comparable levels as the wild-type protein (Figure 2.6C), does not result in decreased viability (Figure 2.6B). Furthermore, cells producing this variant maintain their rod-shape, exhibiting only minor morphological perturbations (Figure 2.6A). These results indicate that the interactions between CbtA and both MreB and FtsZ are functionally relevant and together contribute to the lemon-like morphology and the viability defects we observe.

Figure 2.6: CbtA-R15C/F65S has reduced toxicity and does not affect ZapA-GFP localization. A) All BW27785 strains transformed with the relevant plasmids (pMT136, pMT139, pMT146, pDH253, and pDH262, from left to right) were imaged after 2 hr induction with 50 µM IPTG at 30 ºC. B) The same strains as described in A were grown without induction until they reached mid to late-log phase. Cultures were normalized, serially diluted, and spotted on LB (Cm) with or without 50 µM IPTG. Plates were incubated overnight at 30 ºC. C) Western blot analysis was done essentially as described in Figure 2.6D. D) Strain NP1 was transformed with pSG360 (empty vector), pDH325 (*placUV5*-*cbtA*), pDH326 (*placUV5*-*cbtF65S),* pDH327 (*placUV5*-*cbtA-R15C),* or pDH328 (*placUV5*-*cbtA-R15C/F65S).* Overnight cultures were back diluted to a starting OD600 of 0.03 in fresh LB (SpecStrep), grown for 1 hr at 30 ºC, then induced for toxin expression with 200 µM IPTG for 2 hrs at 30 ºC. Cultures were in mid-log phase at the time of imaging. Magenta arrows in the CbtA-F65S panel highlight points of constriction in spherical cells. Scale bars represent 5 µm.

Figure 2.6 (Continued)

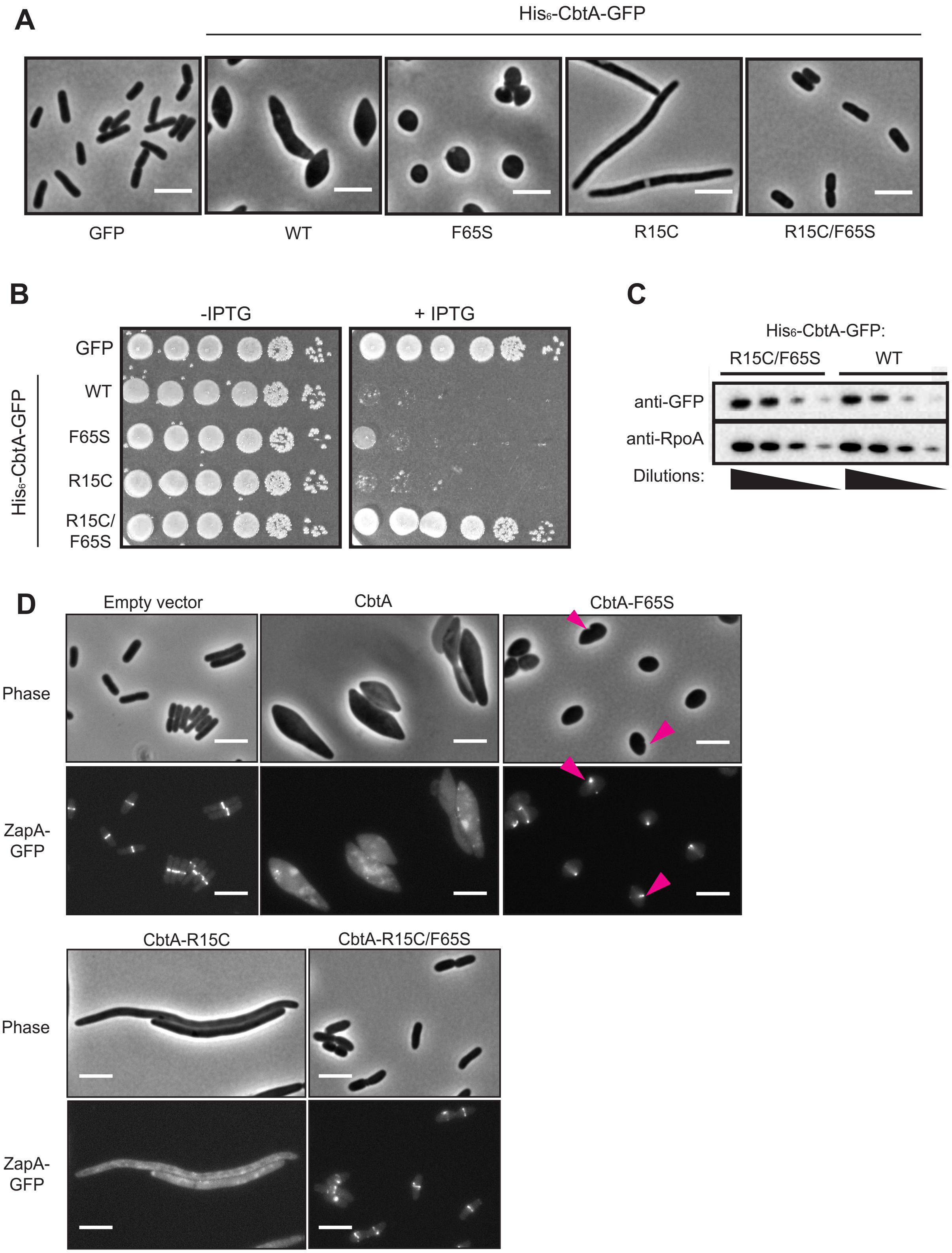
A
His6-CbtA-GFP
GFP
WT
F65S
R15C
R15C/F65S
B
-IPTG
+ IPTG
GFP
WT
F65S
R15C
R15C/
F65S
His6-CbtA-GFP
C
His6-CbtA-GFP:
R15C/F65S
WT
anti-GFP
anti-RpoA
Dilutions:
D
Empty vector
CbtA
CbtA-F65S
Phase
ZapA-
GFP
CbtA-R15C
CbtA-R15C/F65S
Phase
ZapA-
GFP

CbtA-R15C disrupts Z rings

As an additional readout of the physiological perturbations caused by each of our CbtA variants, we observed Z ring formation in cells producing the untagged mutant proteins. We used a strain, NP1, which constitutively produces a ZapA-GFP fusion from its native locus (23). ZapA is a nonessential component of the division complex that is recruited to mid-cell early on in division via interaction with FtsZ (24). ZapA-GFP forms fluorescent ring structures that require proper assembly of the FtsZ ring, and thus it serves as a proxy for FtsZ localization (23,25). As seen in Figure 2.6, when NP1 is transformed with the pSG360 empty vector, fluorescent ZapA-GFP bands can be observed at mid cell in the majority of cells. After two hours of *cbtA* expression, ZapA-GFP exhibited diffuse (patchy) localization throughout the resulting lemon-shaped cells, suggesting disruption of Z ring formation. When ZapA-GFP localization was observed in cells producing CbtA-R15C, the majority of cell filaments did not contain visible ring structures, whereas in cells producing CbtA-F65S, aberrant ring structures were observed in many of the spherical cells, especially at sites of obvious constriction (Figure 2.6D, fluorescence images). This is consistent with a previous report by Bendezú et al., where it was noted that in cells depleted for MreB, FtsZ forms anomalous assemblies including bright foci and patches and rings that fail to span the entire cell diameter (20). In cells overproducing the less toxic CbtA-R15C/F65S variant, rod-shape was maintained and ZapA-GFP rings were observed in most cells. Importantly, overproduction of the untagged CbtA variants in these experiments resulted in identical morphologies to those observed with the His_6/GFP constructs (compare Figure 2.6D, phase contrast images with those shown in Figure 2.6A). Thus, ZapA-GFP localization suggests that wild-type CbtA and CbtA-R15C are able to disrupt FtsZ assembly and localization, blocking cell division, while the double mutant variant does not. Although CbtA-F65S causes aberrant ring assemblies, these are characteristic of a block in MreB inhibition. This molecular view of cell division is consistent with our model that CbtA is able to independently inhibit cell division and cell elongation.

Chapter 2.3: Discussion

The CbtA toxin of *E. coli* is a potent growth inhibitor. As described above, we observe that upon overproduction of this toxin, bacterial growth is severely inhibited, and cells adopt a distinctive lemon-like morphology (Figure 2.1). We also report that we can detect robust interactions between CbtA and two bacterial cytoskeletal elements, FtsZ and MreB, by means of a transcription-based bacterial two-hybrid assay (Figure 2.2). These observations are consistent with those made previously by both Brown and Shaw and Tan et al. (9,10). Importantly, in this chapter, we build upon previously published observations, providing the first reported genetic dissection of CbtA toxicity.

We were able to identify a single amino acid substitution, F65S, which in the bacterial two-hybrid system, eliminates the CbtA-FtsZ interaction but has no effect on the CbtA-MreB interaction. Overproduction of the CbtA-F65S variant leads to a lethal block in cell elongation, causing cells to form spheres rather than lemons (Figure 2.4). We observed that these spheres display aberrant Z ring structures (Figure 2.6D), and toxicity of this variant can be partially suppressed with increased expression of *ftsZ* (Figure 2.4G). These observations are all analogous to those seen with other methods of cell elongation inhibition, including depletion of MreB (19,20). Furthermore, we see by time-lapse microscopy, that whereas production of wild-type CbtA leads to a complete block in cell division even in cells with obvious pre-formed constrictions, cells producing CbtA-F65S are able to complete 1-2 more rounds of cell division. These spheres appear to divide from cleavage furrows that are enriched for ZapA-GFP (and likely FtsZ) (Figure 2.4F and Figure 2.6D magenta arrows). Thus, together, these data strongly suggest that CbtA-F65S mediates a complete block of cell elongation via interaction with MreB, preventing maintenance of rod-shape; however, this variant does not interact with FtsZ or block cell division.

We isolated the CbtA-R15C variant in a two-hybrid screen for CbtA mutants decreased for interaction with MreB. The R15C substitution does not disrupt interaction between CbtA and FtsZ but leads to a pronounced decrease in the CbtA-MreB two-hybrid interaction (Figure 2.5A and B). In support of this observation, CbtA-R15C was found to primarily inhibit cell division, allowing for the continued elongation of cells into filaments (Figure 2.5C). These filamented cells exhibit patchy to diffuse ZapA-GFP localization, suggesting that CbtA-R15C disrupts FtsZ assembly and blocks Z ring formation.

Together, these two variants indicate that the cytoskeletal interactions and morphological phenotype of CbtA can be genetically parsed, leading us to conclude that CbtA i) interacts independently with both FtsZ and MreB and ii) induces lemon shape in cells through interaction with both targets. The loss of toxicity upon introduction of both substitutions further confirms that interaction with both FtsZ and

MreB is the mechanism by which CbtA blocks bacterial growth. It remains to be seen still whether a single toxin molecule is able to simultaneously interact with both MreB and FtsZ or if instead combined inhibition in the cell is mediated by subsets of toxin molecules interacting with a single target. The structure of CbtA is unknown, but based on its small size it seems more likely that the binding determinants of each interaction are at least partially overlapping.

Additionally, we report our findings that two CbtA paralogs, YpjF and YkfI, also disrupt cell division and cell elongation, suggesting a common mechanism of growth inhibition for this family of toxins. Whereas all three toxins require residue F65 for their interaction with FtsZ, the genetic determinants of cell elongation inhibition by these two homologs are less clear. In the future, it would be interesting to use our two-hybrid screening platform to attempt to identify YpjF variants with decreased MreB interaction. Nonetheless, the exclusive disruption of cell elongation by YpjF-F65S and YkfI-F65S implies that these toxins also have separable inhibitory functions.

The ability of CbtA to inhibit two distinct pathways through interaction with two unrelated proteins is compelling for multiple reasons. First, the work presented in this chapter confirms that CbtA is the first characterized toxin component of a TA system found to have more than one cellular target. Similarly, although small molecule and protein inhibitors of each cytoskeletal element have been previously reported, CbtA is the first described inhibitor capable of independently interacting with and disrupting both MreB and FtsZ. However, recent work has revealed two interesting parallels. The same group that first reported the interaction between CbtA and the cytoskeleton discovered an inner membrane-bound protein, YgfX, which also induces lemon-shape in *E. coli* cells (26). This putative toxin was able to pull-down both FtsZ and MreB, but it remains to be seen if it can physically interact with each protein separately. Another group did not observe YgfX toxicity upon overproduction, but did report the ability of YgfX to interact with FtsZ and MreB in a bacterial two-hybrid assay (27). Moreover, characterization of T7 phage-encoded growth inhibitors in two separate studies revealed that a pair of genes found adjacent to one another in the T7 genome encode two separate cytoskeletal inhibitors: Gp0.4, which inhibits FtsZ function, and Gp0.6, which inhibits MreB function (28,29). Inhibition of cell division by Gp0.4 was found to confer a fitness advantage to T7 phage (28), and the authors of both studies speculate that cytoskeletal inhibition may be an effective strategy to both prevent dilution of essential phage components during early infection and aid in cell lysis and release of virions (28,29).

The physiological function of the CbtA toxin and its homologs remains to be seen. Since all three TA systems are encoded on prophage elements it is likely that they evolved to perform some phage-related function, perhaps similar to that proposed for the T7-encoded inhibitors. Like other chromosomal TA modules found in bacteria, these systems may also contribute in some way to the bacterial stress response. However, regardless of their specific biological function, further study of the detailed mechanisms by which CbtA and its homologs can inhibit both FtsZ and MreB is an important endeavor that may potentially reveal information on how these cytoskeletal elements function individually and together. Due to their essentiality and conservation amongst bacteria, FtsZ and MreB have recently been considered as a potential antimicrobial drug targets (30-34); thus, identifying the inhibitory surfaces utilized by CbtA is of special interest. In the next two chapters of this dissertation, I describe our work to uncover the CbtA-inhibitory surfaces on both FtsZ and MreB. Chapter 3 details our discovery of the H6/H7 loop of FtsZ as a site of direct CbtA interaction, and Chapter 4 describes our characterization of several MreB variants with altered CbtA binding.

Chapter 2.4: Materials and Methods

Strains, plasmids, and growth conditions

A complete list of the bacterial strains used in this chapter is provided in Table 2.1 (shown at the end of this section). Additionally, lists of the plasmids and oligonucleotides used in this chapter can be found in Tables 2.2 and 2.3 (shown at the end of this section), respectively. NEB5-α F’I^q (New England Biolabs) was used as the cloning strain for all plasmid constructions outlined below. Two-hybrid studies were performed in FW102 O_L2-6 (35) or BN30 (22). Morphology observations were made primarily in strain BW27785. This strain also served as template for all colony PCRs. *E. coli* strains were grown in LB (1% NaCl) broth at 37 ºC or 30 ºC or on LB plates supplemented with appropriate antibiotics at the following concentrations (unless otherwise noted): carbenicillin (Carb), 100 μg/mL; chloramphenicol (Cm), 25 μg/mL; kanamycin (Kan), 50 μg/mL; spectinomycin (Spec), 50 μg/mL, tetracycline (Tet), 5 μg/mL.

Construction of toxin expression vectors

p3-37 is a derivative of the ASKA overexpression vector, pCA24N, encoding His$_6$-YkfI-GFP under the control of the *pT5-lac* promoter. It was first isolated from an ASKA-library screen to identify proteins that formed SDS-resistant intracellular aggregates upon overproduction. In this construct, *his$_6$-ykfI-gfp* contains two SfI sites flanking the *ykfI* sequence. Empty vector plasmid pMT136 encoding His$_6$-GFP was made by cloning in a linker sequence composed of annealed oligonucleotides, oSG623 and oSG624, into SfI-digested p3-37. This linker sequence contains ClaI and XbaI sites and encodes for the additional residues "IDAAASR" in between the SfI sites in the His$_6$-GFP sequence. To construct plasmids pMT138 (encoding His$_6$-YpjF-GFP) and pMT139 (encoding His$_6$-CbtA-GFP), colony PCR products generated using primer pairs oSG639/oSG640 and oSG641/oSG642, respectively, were digested with AclI and XbaI and ligated into pMT136 digested with ClaI and XbaI. Plasmids pMT144 (encoding His$_6$-YkfI-F65S-GFP) and pMT146 (encoding His$_6$-CbtA-F65S-GFP) were generated by ligation of AclI/XbaI-digested overlap PCR products amplified with internal mutagenic primers (oSG663/oSG664 and oSG667/oSG668) and outside primers (oSG659/oSG660 and oSG641/oSG642) into ClaI/XbaI-digested pMT136 backbone. To clone plasmid pDH253, the *cbtA-R15C* allele was amplified from the two-hybrid construct pDH246 using primers oSG641 and oSG642, digested with AclI and XbaI, and ligated into pMT136 ClaI/XbaI backbone. Plasmid pDH262 (encoding His$_6$-CbtA-R15C/F65S-GFP) was cloned in the same manner as pMT146 except using pDH253 as PCR template.

To generate plasmids pDH325, pDH326, pDH327, and pDH328 encoding untagged CbtA variants, the relevant allele was amplified from the appropriate construct described above using primers oDH446 and oDH447, digested with EcoRI/HindIII, and ligated into pSG360 (EcoRI/HindIII) backbone.

Construction of plasmids used in the bacterial two-hybrid system

All α fusion constructs were cloned by restriction digest into the parent plasmid pBRα-β flap; all λCI constructs were cloned by restriction digest into the parent plasmid pACλCI-β flap. Briefly, the parent plasmids were digested with NotI and BamHI to generate backbone. These backbones were ligated to relevant inserts generated by NotI/BamHI digestion of PCR products amplified using a NotI-containing forward primer and BamHI-containing reverse primer. Forward primers all contain an extra "A" base after the NotI site to maintain the reading frame. Reverse primers all encode a stop codon preceding the BamHI site. PCR template for these constructs was a single colony of *E. coli* BW27785. Plasmids encoding F65S variants fused to λCI were cloned from PCR products amplified using gene-specific primers from template plasmids pMT144, pMT146, or pMT188. Inserts for plasmids pDH266 and pDH267 were generated using mutagenic forward primers oDH344 and ODH345, respectively. Oligonucleotides pBRα_F, pBRα_R, pACλCI_F, and pACλCI_R were used to sequence all two-hybrid constructs.

β-galactosidase assays

FW102 O_L2-62 was co-transformed with plasmids encoding the relevant α and λCI fusions. Cultures inoculated with transformants were grown in 1 mL LB (KanCmCarb) in deep-well 96-well plates at 37 ºC, 900 rpm, 90% humidity in a Multitron incubation shaker (Infors HT) overnight. Overnight cultures were back diluted 1:100 in LB (KanCmCarb) supplemented with the appropriate concentration of IPTG in sterile microtitre plates (total volume of 200 µL); subcultures were grown, shaking at 37 ºC until they reached mid-log phase (OD600 0.4- 0.8). A 100 µL aliquot of subculture was lysed by addition of 10 µL PopCulture reagent (Novagen) supplemented with rlysozyme (400 mU/µL). LacZ levels were determined by β-galactosidase assay performed in microtitre plates with a microtitre plate reader, as described in (36). All assays were done in triplicate and were repeated independently at least twice. All values shown in this chapter are from a single representative experiment and represent averages of triplicate measurements. Fold-change values were calculated by normalizing to the highest relevant empty vector control.

Genetic screen to identify toxin variants with reduced toxicity

The *cbtA*, *ypjF,* and *ykfI* gene fragments were amplified from plasmids pM139, pMT138, and p3-37, respectively, using outside sequencing primers oSG625 and oSG626 by error-prone *Taq* PCR. PCR products as well as the p3-37, pMT138, and pMT139 parent plasmids were digested with SfiI; the *cbtA* mutagenized PCR insert was ligated into the pMT139 backbone, the *ypjF* mutagenized PCR insert was ligated into the pMT138 backbone, and the *ykfI* mutagenized PCR insert was ligated into the p3-37 backbone. The resulting plasmid libraries encoding the mutant toxins (bearing an N-terminal His_6 tag and

C-terminal GFP moiety) were transformed into *E. coli* BW27785 and plated on LB (Cm) supplemented with IPTG (500 µM IPTG). After growth overnight at 37 ºC, surviving colonies were patched onto the same medium, and GFP fluorescence was monitored the following day using a Typhoon fluorescence scanner (GE). Plasmids were isolated from those candidates that were as fluorescent as a control strain transformed with pMT136 and sent for sequencing with primers oSG625 and oSG626. The stability of isolated variants was assessed by Western blot analysis via a protocol very similar to that described below.

Genetic screen to identify amino acid substitutions in CbtA that decrease the MreB-CbtA interaction

The *cbtA* gene fragment (found on pMT154) was mutagenized by error-prone PCR using *Taq* polymerase and the outside primers pACλCI_F and pACλCI_R. The mutagenized alleles were cloned into the λCI expression vector by the method described above. The modified two-hybrid reporter strain (BN30) bearing pBRα-MreB was transformed with this mutant library; transformants were plated on LB (KanCarbCm) indicator medium containing IPTG (25 µM) and X-gal (40 µg/mL). Plates were incubated overnight at 30 ºC and refrigerated (4 ºC) for an additional 8-16 hrs. Several thousand colonies were screened to identify those exhibiting lower *lacZ* expression (white or light blue color) as compared to the dark blue colonies producing wild-type α-MreB and λCI-CbtA fusions. Paler candidate colonies were pooled into a single overnight culture, grown at 30 ºC. In order to identify those candidates that maintained interaction with α-FtsZ, a pooled plasmid prep generated from this overnight culture was transformed into FW102 O_L2-62/pBRα-FtsZ. Transformants were plated on LB (KanCarbCm) indicator medium supplemented with 5 µM IPTG, 40 µg/mL, and 250 µM TPEG (a competitive inhibitor of β-galactosidase); dark blue candidates were selected and the pACλCI-CbtA plasmids were isolated and sequenced. The interaction between λCI-CbtA mutants and both α-FtsZ and α-MreB fusions was assayed by liquid β-galactosidase assay.

Microscopic observation of CbtA-mediated cell morphology changes

To observe cells producing a specific toxin variant, BW27785 was transformed with the relevant plasmid, and transformants were selected for on LB containing appropriate antibiotic. For most experiments, all growth incubation steps were done at 30 ºC. Overnight cultures were back diluted to a starting OD600 of 0.02-0.05, grown without induction for 1 hr (cultures had reached an OD600 of ~0.1), and then induced for toxin expression with the addition of IPTG. For pCA24N-derived vectors, either 50 or 100 µM IPTG was used; for pSG360-derived vectors, 200 µM IPTG was used. When the experiment was done with growth at 30 ºC, cultures were imaged after 2 hrs induction; when the experiment was done at 37 ºC, cultures were imaged after 1.5 hrs. All cultures were typically in an OD600 range of 0.4-1 at the time of imaging.

To observe ZapA-GFP localization, the NP1 (TB28 *zapA-gfp frt*) strain was transformed with pSG360-derived vectors, and transformants were selected for on LB containing a mixture of Spec (50 µg/mL) and Strep (25 µg/mL). Overnight cultures were back diluted to a starting OD600 of 0.020-0.03, grown for 1 hr in LB (SpecStrep), then induced by addition of 200 µM IPTG. Cultures were imaged by fluorescence light microscopy after 2 hr induction. Cells were mounted on 2% agarose pads, and microscopic observation of all strains was performed using an Olympus BX61 microscope (objective UplanF1 100x). Images were captured with a monochrome CoolSnapHQ digital camera (Photometrics) using Metamorph software version 6.1 (Universal Imaging). Images were aligned in Metamorph; cropping and minimal adjustment was performed with ImageJ (37).

For time-lapse imaging of CbtA-induced morphology changes, pMT136, pMT139, and pMT146 were individually transformed into BW27785. Overnight cultures were back diluted to a starting OD600 of 0.05 and grown at 30 ºC for 1 hr without induction. Cells were concentrated 5x, and 2 µL was spotted on the bottom of a glass-bottomed dish (Willco dish HBSt-5040; Willco Wells). A 2% agarose pad containing LB growth medium supplemented with 100 µM IPTG was placed on top of the culture aliquot. Cells were imaged on a Well Plate Holder stage (TI-SH-W; Nikon) equipped with a humid, temperature-controlled incubator (TC-MIS; Bioscience Tools). The objective was heated to ~30 ºC using a Bioptechs objective heater system. Images were acquired every 3 min for 3 hrs. Image analysis was performed in FIJI and ImageJ.

Spot dilution assays

E. coli BW27785 was transformed with the appropriate plasmid(s); transformants were selected on LB supplemented with appropriate antibiotic at 30 ºC or 37 ºC. Overnight cultures were back diluted in fresh LB + antibiotics to a starting OD600 of 0.05 and grown at the indicated temperature until cultures reached an OD600 of 0.5-1. Cultures were normalized by OD600 value and 1:10 serial dilutions were made in fresh LB. 5 μL of each culture were spotted on LB plates containing the appropriate antibiotics with or without the indicated level of IPTG.

Western blot analysis

To compare levels of the His_6-CbtA-GFP variants, 2 mL of each culture used for microscopic observation was pelleted and resuspended in BugBuster lysis buffer (EMD) supplemented with rlysozyme and Omnicleave. Pellets were resuspended in varying amounts of lysis buffer to normalize by OD600 value and lysed at room temperature for 30 min. Total protein concentration was measured by Bradford assay, and lysate volumes were adjusted using lysis buffer such that all samples contained equivalent amounts of protein. Lysates were diluted 1:2 in 2x Laemmli buffer; further dilutions were made in 1x Laemmli buffer. Standard SDS-PAGE and transfer procedures were used; duplicate gels were run and transferred. His_6-CbtA-GFP proteins were detected on one blot using an anti-GFP primary antibody (Roche) at a concentration of 1:5,000; RpoA levels were detected on the second blot using an anti-RpoA antibody (Neoclone) at a concentration of 1:5,000. Secondary anti-mouse antibody was used at a concentration of 1:10,000 for both. The anti-RpoA blot served as a loading control to ensure equivalent amounts of protein were loaded.

Table 2.1: Strains used in this study

Strain	Description	Reference/ Source
NEB5-α F’I^q	DH5-α derivative containing an F’ (Tet resistant) bearing *lacI*^{q}	New England Biolabs
BW27785	Δ(*araB-araD*)*567* Δ*lacZ4787*(::*rrnB-3*) LAM-Δ(*araH-araF*)570(::FRT) *ΔaraEp-532*::FRT φ(*Pcp18-araE534*) Δ(*rhaB-rhaD*)*568 hsdR514*	(39)
FW102 O$_L$2-62	FW102 (38) containing an F’ (Kan resistant) bearing the *plac*OL$_2$–62-*lacZ* fusion in which the λCI operator is centered at position –62 upstream of the *lac* promoter	(35)
BN30 (FW102 O$_L$2-42)	FW102 (38) containing an F’ (Kan resistant) bearing the *plac*OL$_2$–42-*lacZ* fusion in which the λCI operator is centered at position –42 upstream of the *lac* promoter	(22); Bryce Nickels
NP1 (TB28 *zapA-gfp frt)*	TB28 (MG1655 Δ*lacIZYA*::*frt*) encoding ZapA-GFP from the native chromosomal locus. Linked *cat* cassette has been removed by FLP recombinase.	(23); Generous gift of T. Bernhardt

Table 2.2: Plasmids used in this study

Plasmid	Description	Reference/ Source
pBRα	Encodes the full-length α subunit of RNAP under the control of tandem p*lacUV5* and p*lpp* promoters; confers resistance to Carb	(17)
pACλCI	Encodes λCI (residues 1-236) under the control of *lacUV5* promoter; confers resistance to Cm	(17)
pBRα-FtsZ (pMT153)	Encodes residues 1-248 of α fused by a three-alanine linker to full-length *E. coli* FtsZ under the control of tandem p*lacUV5* and p*lpp* promoters; confers resistance to Carb	This study; M. Tavag
pBRα-MreB (pMT151)	Encodes residues 1-248 of α fused by a three-alanine linker to full-length *E. coli* MreB under the control of tandem p*lacUV5* and p*lpp* promoters; confers resistance to Carb	This study; M. Tavag
pACλCI-CbtA (pMT155)	Encodes λCI fused by a three-alanine linker to full-length CbtA under the control of *lacUV5* promoter; confers resistance to Cm	This study; M. Tavag
pACλCI-YkfI (pMT169)	Encodes λCI fused by a three-alanine linker to YkfI under the control of *lacUV5* promoter; confers resistance to Cm	This study; M. Tavag
pACλCI-YpjF (pMT170)	Encodes λCI fused by a three-alanine linker to YpjF under the control of *lacUV5* promoter; confers resistance to Cm	This study; M. Tavag
pACλCI-CbtA-F65S (pMT180)	Encodes λCI fused by a three-alanine linker to CbtA-F65S under the control of *lacUV5* promoter; confers resistance to Cm	This study; M. Tavag
pACλCI-YkfI-F65S (pDH206)	Encodes λCI fused by a three-alanine linker to YkfI-F65S under the control of *lacUV5* promoter; confers resistance to Cm	This study
pACλCI-YpjF-F65S (pMT192)	Encodes λCI fused by a three-alanine linker to YpjF-F65S under the control of *lacUV5* promoter; confers resistance to Cm	This study; M. Tavag
pACλCI-CbtA-R15C (pDH246)	Encodes λCI fused by a three-alanine linker to CbtA-R15C under the control of *lacUV5* promoter; isolated in a λCI-CbtA mutant screen; confers resistance to Cm	This study
pACλCI-YkfI-C15R (pDH266)	Encodes λCI fused by a three-alanine linker to YkfI-C15R under the control of *lacUV5* promoter; confers resistance to Cm	This study

Table 2.2 (Continued)

Plasmid	Description	Reference/Source
pACλCI-YpjF-C15R (pDH267)	Encodes λCI fused by a three-alanine linker to YpjF-C15R under the control of *lacUV5* promoter; confers resistance to Cm	This study
p3-37	Derivative of pCA24N; Encodes full-length His_6-YkfI-GFP under the control of *pT5-lac* promoter; pBR origin and confers resistance to Cm	(40); This study
pMT136	Derivative of pCA24N; Empty vector control plasmid encoding full-length His_6- GFP under the control of *pT5-lac* promoter; pBR origin and confers resistance to Cm	This study; M. Tavag
pMT138	Derivative of pCA24N; Encodes full-length His_6-YpjF-GFP under the control of *pT5-lac* promoter; pBR origin and confers resistance to Cm	This study; M. Tavag
pMT139	Derivative of pCA24N; Encodes full-length His_6-CbtA-GFP under the control of *pT5-lac* promoter; pBR origin and confers resistance to Cm	This study; M. Tavag
pMT144	Derivative of pCA24N; Encodes full-length His_6-YkfI-F65S-GFP under the control of *pT5-lac* promoter; pBR origin and confers resistance to Cm	This study; M. Tavag
pMT146	Derivative of pCA24N; Encodes full-length His_6-CbtA-F65S-GFP under the control of *pT5-lac* promoter; pBR origin and confers resistance to Cm	This study; M. Tavag
pMT188	Derivative of pCA24N; Encodes full-length His_6-YpjF-F65S-GFP under the control of *pT5-lac* promoter; pBR origin and confers resistance to Cm	This study; M. Tavag
pDH253	Derivative of pCA24N; Encodes full-length His_6-CbtA-R15C-GFP under the control of *pT5-lac* promoter; pBR origin and confers resistance to Cm	This study
pDH262	Derivative of pCA24N; Encodes full-length His_6-CbtA-R15C/F65S-GFP under the control of *pT5-lac* promoter; pBR origin and confers resistance to Cm	This study
pSG360	Empty vector used for cloning genes downstream of a p*lacUV5* promoter with an additional *lacO* site; pCDF origin; confers resistance to Spec; *lacI^q*	Seth Goldman
pDH325	pSG360 derivative encoding untagged CbtA*;* confers resistance to Spec	This study
pDH326	pSG360 derivative encoding untagged CbtA-F65S*;* confers resistance to Spec	This study

Table 2.2 (Continued)

Plasmid	Description	Reference/Source
pDH327	pSG360 derivative encoding untagged CbtA-R15C*;* confers resistance to Spec	This study
pDH328	pSG360 derivative encoding untagged CbtA-R15C/F65S*;* confers resistance to Spec	This study
pSC101	Low copy plasmid; confers resistance to Tet	Generous gift of T. Bernhardt
pTB63	pSC101 derivative; *ftsQAZ*; confers resistance to Tet	(41); Generous gift of T. Bernhardt

Table 2.3: Important DNA oligonucleotides used in this study

Name	Sequence (5' to 3')	Description
pBRα_F	GAACAGCGTACCGACCTGGAC	Sequencing primer for all pBRα fusion constructs
pBRα_R	CCTATATCGCCGACATCACC	Sequencing primer for all pBRα fusion constructs
pACλCI_F	GATCAGGGATAGCGGTCAGG	Sequencing primer for all λCI fusion constructs
pACλCI_R	CCTACATCTGTATTAACGAAGC	Sequencing primer for all λCI fusion constructs
oSG623	GGGCCATCGATGCCGCGGCATCTAGAGGCCTATG	Annealed with oSG624 to form in-frame linker with MCS for pMT136
oSG624	AGGCCTCTAGATGCCGCGGCATCGATGGCCCTCA	Annealed with oSG623 to form in-frame linker with MCS for pMT136
oSG625	AGGAGAAATTAACTATGAGAG	Sequencing primer for pCA24N-derived plasmids
oSG626	AACATCACCATCTAATTCAACAAG	Sequencing primer for pCA24N-derived plasmids
oSG639	GGGGACAAGTTTGTACAAAAAAGCAGGCTTCAACG TTAACACTCTACCTGCTACAATTTC	Amplifies *ypjF* sequence (no start codon); contains AclI site
oSG640	GGGGACAAGTTTGTACAAAAAAGCAGGCTTCAACG TTAACACTCTACCTGCTACAATTTC	Amplifies *ypjF* sequence (no stop codon); contains XbaI site
oSG641	GGGGACAAGTTTGTACAAAAAAGCAGGCTTCAACG TTAAAACATTACCTGTATTACCCG	Amplifies *cbtA* sequence (no start codon); contains AclI site
oSG642	GGGGACCACTTTGTACAAGAAAGCTGGGTCTCTAG ATTTCGCCTCCGGATACTTAC	Amplifies *cbtA* sequence (no stop codon); contains XbaI site
oSG659	GGGGACAAGTTTGTACAAAAAAGCAGGCTTCAACG TTAAAACTTTACCTGCAATAACTCAGCGG	Amplifies *ykfI* sequence (no start codon); contains AclI site
oSG660	GGGGACCACTTTGTACAAGAAAGCTGGGTCTCTAG ATCGTACTACGTTGTTACGGC	Amplifies *ykfI* sequence (no stop codon); contains XbaI site
oSG663	CCCTAGCCGATGCCGTGAATTCTCTGGTAGAAAAA TACGAGCTGG	Internal mutagenic primer to introduce F65S into *ykfI* sequence
oSG664	CCAGCTCGTATTTTTCTACCAGAGAATTCACGGCA TCGGCTAGGG	Internal mutagenic primer to introduce F65S into *ykfI* sequence
oSG667	TCACTGTGTGATGCGGTGAACTCTCTCGTGGAAAA ATACGCGCTGGTGCG	Internal mutagenic primer to introduce F65S into *cbtA* sequence

Table 2.3 (Continued)

Name	Sequence (5' to 3')	Description
oSG668	CGCACCAGCGCGTATTTTTCCACGAGAGAGTTCAC CGCATCACACAGTGA	Internal mutagenic primer to introduce F65S into *cbtA* sequence
oSG723	GGGGACAAGTTTGTACAAAAAAGCAGGCTTCGCG GCCGCATTGAAAAAATTTCGTGGCATGTTTTCC	Forward primer for amplification of *mreB;* contains a NotI site
oSG724	GGGGACCACTTTGTACAAGAAAGCTGGGTCGGAT CCTTACTCTTCGCTGAACAGGTCGCC	Reverse primer for amplification of *mreB*; contains BamHI site
oSG727	GGGGACAAGTTTGTACAAAAAAGCAGGCTTCGCG GCCGCAAAAACATTACCTGTATTACCCGGG	Forward primer for amplification of *cbtA;* contains a NotI site
oSG728	GGGGACCACTTTGTACAAGAAAGCTGGGTCGGAT CCTTATTTCGCCTCCGGATACTTACC	Reverse primer for amplification of *cbtA*; contains BamHI site
oSG729	GGGGACAAGTTTGTACAAAAAAGCAGGCTTCGCG GCCGCAAAAACTTTACCTGCAATAACTCAGCGG	Forward primer for amplification of *ykfI;* contains a NotI site
oSG730	GGGGACCACTTTGTACAAGAAAGCTGGGTCGGAT CCTTATCGTACTACGTTGTTACGGC	Reverse primer for amplification of *ykfI*; contains BamHI site
oSG731	GGGGACAAGTTTGTACAAAAAAGCAGGCTTCGCG GCCGCAAACACTCTACCTGCTACAATTTCGC	Forward primer for amplification of *ypjF;* contains a NotI site
oSG732	GGGGACCACTTTGTACAAGAAAGCTGGGTCGGAT CCTTATTTCACATTAGTTTTTAGCAAGCCGG	Reverse primer for amplification of *ypjF*; contains BamHI site
oDH70	TATATAGCGGCCGCATTTGAACCAATGGAAC	Forward primer for amplification of *ftsZ;* contains a NotI site
oDH71	TATATAGGATCCTTAATCAGCTTGCTTACGC	Reverse primer for amplification of *ftsZ*; contains BamHI site
oDH344	ATATATGCGGCCGCAAAAACTTTACCTGCAATAACT CAGCGGGCGGTGAAGCCCCGTCTGTCACCCGTGG CTG	Forward mutagenic primer to introduce C15R into *ykfI*; contains NotI site
oDH345	ATATATGCGGCCGCAAACACTCTACCTGCTACAAT TTCGCAGGCGGCGAAGCCCCGCCTGTCGCCAGTG GCTG	Forward mutagenic primer to introduce C15R into *ypjF*; contains NotI site
oDH446	ATATATGAATTCAAGGAGATATACCATGAAAACATT ACCTGTATTACCCG	Forward primer to clone *cbtA* variants into pSG360; contains EcoRI site; includes RBS
oDH447	ATATATAAGCTTTCATTTCGCCTCCGGATACTTACC CAG	Reverse primer to clone *cbtA* variants into pSG360; contains HindIII site

Chapter 2.5: References

1. Gerdes K, Christensen SK, Løbner-Olesen A. Prokaryotic toxin–antitoxin stress response loci. Nat Rev Micro. 2005 May;3(5):371–82.

2. Yamaguchi Y, Inouye M. Regulation of growth and death in Escherichia coli by toxin–antitoxin systems. Nat Rev Micro. 2011 Sep 19;9(11):779–90.

3. Yamaguchi Y, Park J-H, Inouye M. Toxin-Antitoxin Systems in Bacteria and Archaea. Annu Rev Genet. 2011 Dec 15;45(1):61–79.

4. Page R, Peti W. Toxin-antitoxin systems in bacterial growth arrest and persistence. Nature Chemical Biology. 2016 Mar 18;12(4):208–14.

5. Ogura T, Hiraga S. Mini-F plasmid genes that couple host cell division to plasmid proliferation. Proc Natl Acad Sci USA. 1983 Aug;80(15):4784–8.

6. Gerdes K, Bech FW, Jørgensen ST, Løbner-Olesen A, Rasmussen PB, Atlung T, et al. Mechanism of postsegregational killing by the hok gene product of the parB system of plasmid R1 and its homology with the relF gene product of the E. coli relB operon. EMBO J. 1986 Aug;5(8):2023–9.

7. Shao Y, Harrison EM, Bi D, Tai C, He X, Ou HY, et al. TADB: a web-based resource for Type 2 toxin-antitoxin loci in bacteria and archaea. Nucleic Acids Research. 2010 Dec 22;39(Database):D606–11.

8. Pandey DP. Toxin-antitoxin loci are highly abundant in free-living but lost from host-associated prokaryotes. Nucleic Acids Research. 2005 Feb 18;33(3):966–76.

9. Brown JM, Shaw KJ. A novel family of Escherichia coli toxin-antitoxin gene pairs. J Bacteriol. 2003 Nov;185(22):6600–8.

10. Tan Q, Awano N, Inouye M. YeeV is an Escherichia coli toxin that inhibits cell division by targeting the cytoskeleton proteins, FtsZ and MreB. Mol Microbiol. 2011 Jan;79(1):109–18.

11. Varma A, de Pedro MA, Young KD. FtsZ directs a second mode of peptidoglycan synthesis in Escherichia coli. J Bacteriol. 2007 Aug;189(15):5692–704.

12. Figge RM, Divakaruni AV, Gober JW. MreB, the cell shape-determining bacterial actin homologue, co-ordinates cell wall morphogenesis in Caulobacter crescentus. Mol Microbiol. 2004 Mar;51(5):1321–32.

13. Vats P, Rothfield L. Duplication and segregation of the actin (MreB) cytoskeleton during the

prokaryotic cell cycle. Proc Natl Acad Sci USA. 2007 Nov 6;104(45):17795–800.

14. Vats P, Shih Y-L, Rothfield L. Assembly of the MreB-associated cytoskeletal ring of Escherichia coli. Mol Microbiol. 2009 Mar 19;72(1):170–82.

15. Swulius MT, Jensen GJ. The Helical MreB Cytoskeleton in Escherichia coli MC1000/pLE7 Is an Artifact of the N-Terminal Yellow Fluorescent Protein Tag. J Bacteriol. 2012 Nov 9;194(23):6382–6.

16. Fenton AK, Gerdes K. Direct interaction of FtsZ and MreB is required for septum synthesis and cell division in Escherichia coli. EMBO J. 2013 Jun 11;32(13):1953–65.

17. Dove SL, Joung JK, Hochschild A. Activation of prokaryotic transcription through arbitrary protein-protein contacts. Nature. 1997 Apr 10;386(6625):627–30.

18. Dove SL, Hochschild A. A bacterial two-hybrid system based on transcription activation. Methods Mol Biol. 2004;261:231–46.

19. Kruse T, Bork-Jensen J, Gerdes K. The morphogenetic MreBCD proteins of Escherichia coli form an essential membrane-bound complex. Mol Microbiol. 2004 Oct 6;55(1):78–89.

20. Bendezu FO, de Boer PAJ. Conditional Lethality, Division Defects, Membrane Involution, and Endocytosis in mre and mrd Shape Mutants of Escherichia coli. J Bacteriol. 2008 Feb 20;190(5):1792–811.

21. Bendezú FO, Hale CA, Bernhardt TG, de Boer PAJ. RodZ (YfgA) is required for proper assembly of the MreB actin cytoskeleton and cell shape in E. coli. EMBO J. 2008 Dec 11;28(3):193–204.

22. Castang S, Dove SL. High-order oligomerization is required for the function of the H-NS family member MvaT in Pseudomonas aeruginosa. Mol Microbiol. 2010 Nov;78(4):916–31.

23. Peters NT, Dinh T, Bernhardt TG. A Fail-Safe Mechanism in the Septal Ring Assembly Pathway Generated by the Sequential Recruitment of Cell Separation Amidases and Their Activators. J Bacteriol. 2011 Aug 25;193(18):4973–83.

24. Huang KH, Durand-Heredia J, Janakiraman A. FtsZ Ring Stability: of Bundles, Tubules, Crosslinks, and Curves. J Bacteriol. 2013 Apr 9;195(9):1859–68.

25. Galli E, Gerdes K. Spatial resolution of two bacterial cell division proteins: ZapA recruits ZapB to the inner face of the Z-ring. Mol Microbiol. 2010 Apr 1;76(6):1514–26.

26. Masuda H, Tan Q, Awano N, Yamaguchi Y, Inouye M. A novel membrane-bound toxin for cell

division, CptA (YgfX), inhibits polymerization of cytoskeleton proteins, FtsZ and MreB, in Escherichia coli. FEMS Microbiol Lett. 2012 Jan 30;328(2):174–81.

27. McNeil MB, Iglesias-Cans MC, Clulow JS, Fineran PC. YgfX (CptA) is a multimeric membrane protein that interacts with the succinate dehydrogenase assembly factor SdhE (YgfY). Microbiology. 2013 Jul 2;159(Pt_7):1352–65.

28. Kiro R, Molshanski-Mor S, Yosef I, Milam SL, Erickson HP, Qimron U. Gene product 0.4 increases bacteriophage T7 competitiveness by inhibiting host cell division. Proc Natl Acad Sci USA. 2013 Nov 26;110(48):19549–54.

29. Molshanski-Mor S, Yosef I, Kiro R, Edgar R, Manor M, Gershovits M, et al. Revealing bacterial targets of growth inhibitors encoded by bacteriophage T7. Proc Natl Acad Sci USA. 2014 Dec 15;:201413271.

30. Haydon DJ, Stokes NR, Ure R, Galbraith G, Bennett JM, Brown DR, et al. An Inhibitor of FtsZ with Potent and Selective Anti-Staphylococcal Activity. Science. 2008 Sep 19;321(5896):1673–5.

31. IWAI N, NAGAI K, Wachi M. Novel S-benzylisothiourea compound that induces spherical cells in Escherichia coli probably by acting on a rod-shape-determining protein(s) other than penicillin-binding protein 2. Biosci Biotechnol Biochem. 2002 Dec;66(12):2658–62.

32. Adams DW, Wu LJ, Errington J. A benzamide-dependent ftsZmutant reveals residues crucial for Z-ring assembly. Mol Microbiol. 2015 Nov;:n/a–n/a.

33. Vollmer W. The prokaryotic cytoskeleton: a putative target for inhibitors and antibiotics? Appl Microbiol Biotechnol. 2006 Oct 6;73(1):37–47.

34. Li X, Ma S. European Journal of Medicinal Chemistry. European Journal of Medicinal Chemistry. Elsevier Masson SAS; 2015 May 5;95(C):1–15.

35. Deaconescu AM, Chambers AL, Smith AJ, Nickels BE, Hochschild A, Savery NJ, et al. Structural Basis for Bacterial Transcription-Coupled DNA Repair. Cell. 2006 Feb;124(3):507–20.

36. Thibodeau SA, Fang R, Joung JK. High-throughput beta-galactosidase assay for bacterial cell-based reporter systems. BioTechniques. 2004 Mar;36(3):410–5.

37. Schneider CA, Rasband WS, Eliceiri KW. NIH Image to ImageJ: 25 years of image analysis. Nat Meth. Nature Publishing Group; 2012 Jul 1;9(7):671–5.

38. Whipple FW. Genetic analysis of prokaryotic and eukaryotic DNA-binding proteins in Escherichia coli. Nucleic Acids Research. 1998 Aug 15;26(16):3700–6.

39. Khlebnikov A, Datsenko KA, Skaug T. Homogeneous expression of the PBAD promoter in Escherichia coli by constitutive expression of the low-affinity high-capacity AraE transporter. …. 2001.

40. Kitagawa M, Ara T, Arifuzzaman M, Ioka-Nakamichi T, Inamoto E, Toyonaga H, et al. Complete

set of ORF clones of Escherichia coli ASKA library (a complete set of E. coli K-12 ORF archive): unique resources for biological research. DNA Res. 2005;12(5):291–9.

41. Bernhardt TG, de Boer PAJ. Screening for synthetic lethal mutants in Escherichia coli and identification of EnvC (YibP) as a periplasmic septal ring factor with murein hydrolase activity. Mol Microbiol. 2004 Apr 19;52(5):1255–69.

Chapter 3: CbtA interacts directly with the H6/H7 loop of *E. coli* FtsZ

Attributions: I wrote this chapter in its entirety with helpful editing advice from my advisor, Ann Hochschild. I conducted the majority of the experimental work presented in this chapter under the guidance of Ann Hochschild. Mrinalini Tavag initiated the genetic screen to identify α-FtsZ variants with decreased CbtA interaction; I performed all subsequent characterization of isolated variants. I would like to acknowledge David Rudner and Alexander Meeske for helpful technical advice and reagents used in the *B. subtilis* experiments performed in this chapter, as well as Tom Bernhardt and Hongbaek Cho for useful reagents and strategies used in the *E. coli* FtsZ studies.

Chapter 3.1: Introduction to the regulated assembly of FtsZ filaments

Cytokinesis in bacteria proceeds in three general stages (reviewed in 1-4). In the first step of cell division, the bacterial tubulin homolog FtsZ polymerizes into dynamic filaments that coalesce into a contractile ring structure (referred to as the Z ring) at mid-cell, perpendicular to the long axis of rod-shaped bacteria such as *E. coli* and *B. subtilis.* This Z ring structure marks the site of cell division and orchestrates the final two steps of cytokinesis: the maturation of the division site via recruitment and scaffolding of several essential and nonessential divisome factors, and finally, the activation and coordination of inner membrane constriction, septal peptidoglycan synthesis, and outer membrane invagination. These final two stages of cell division are absolutely dependent on the proper assembly and localization of FtsZ established in the first stage, earning FtsZ the title of master division regulator (5). Cells that are unable to properly assemble this division complex fail to divide and grow as filaments.

FtsZ levels are constant throughout the bacterial cell cycle (6,7), indicating that cell division is governed by the dynamics and positioning of FtsZ assembly. The precise spatial and temporal control of FtsZ polymerization is determined by essential structural and biochemical features of the FtsZ subunit and polymer together with the coordinated activity of several modulatory proteins. This chapter takes an FtsZ-centric view of bacterial cell division and highlights some of the key factors involved in the regulation of FtsZ assembly. Main consideration is given to the model organism *E. coli*. Furthermore, after reviewing some of the known strategies employed by FtsZ inhibitors, this chapter presents our genetic characterization of the interaction between *E. coli* FtsZ and the recently described cell division inhibitor, CbtA.

The FtsZ subunit

The essentiality of FtsZ in cell division is underscored by the fact that this tubulin homolog is found ubiquitously throughout bacterial and archaeal species, with 40-50% sequence identity between even the most divergent species (8-10). In contrast, FtsZ has only 10% amino acid identity with eukaryotic tubulins. Despite this low sequence similarity, structural data from several species indicate that bacterial FtsZs have many highly conserved structural features of tubulins, suggesting that FtsZ may be the ancestral tubulin protein (8,9).[e]

Like tubulin, FtsZ has a globular core (encompassing *E. coli* residues 10-316) comprised of two self-folding domains separated by a central helix (H7[f] labeled in Figure 3.1A). The N-terminal domain exhibits a Rossmann fold and contains a highly-conserved tubulin GTP-binding motif (GGGTG[S/T]G); the C-terminal domain includes the GTP-contacting synergy loop (the T7 loop labeled in Figure 3.1A, and shown in orange in Figure 3.1B) with the highly conserved tubulin motif (NxDxx[E/D]) essential for monomer assembly and GTP hydrolysis (3,8,11,12). There is some debate as to the exact cut off between these two globular domains, but for the purpose of this discussion we will consider the border proposed by Osawa and Erickson (13). They found that truncated FtsZ proteins containing just the N-terminal domain (terminating at *E. coli* residue 195) or C-terminal domain (*E. coli* residues 195-383) were both produced as soluble proteins in *E. coli.* Furthermore, they argue that this border, unlike the division at residue 179 proposed by Oliva et al. (11), allows for the inclusion of conserved GTP-contacting residues F182 and N186 in the N-terminal GTP-binding domain (11,13).

In addition to these two core domains, the FtsZ monomer contains two unstructured domains that are unresolved in a number of FtsZ crystal structures. Proximal to the N-terminal core domain is a poorly conserved N-terminal extension (residues 1-9 in *E. coli* FtsZ) that varies in length and amino acid

---

[e] For this discussion, *E. coli* residue designations will be used.

[f] H, S, and T designations used when discussing regions of the FtsZ structure stand for helix, sheet, and turn, respectively.

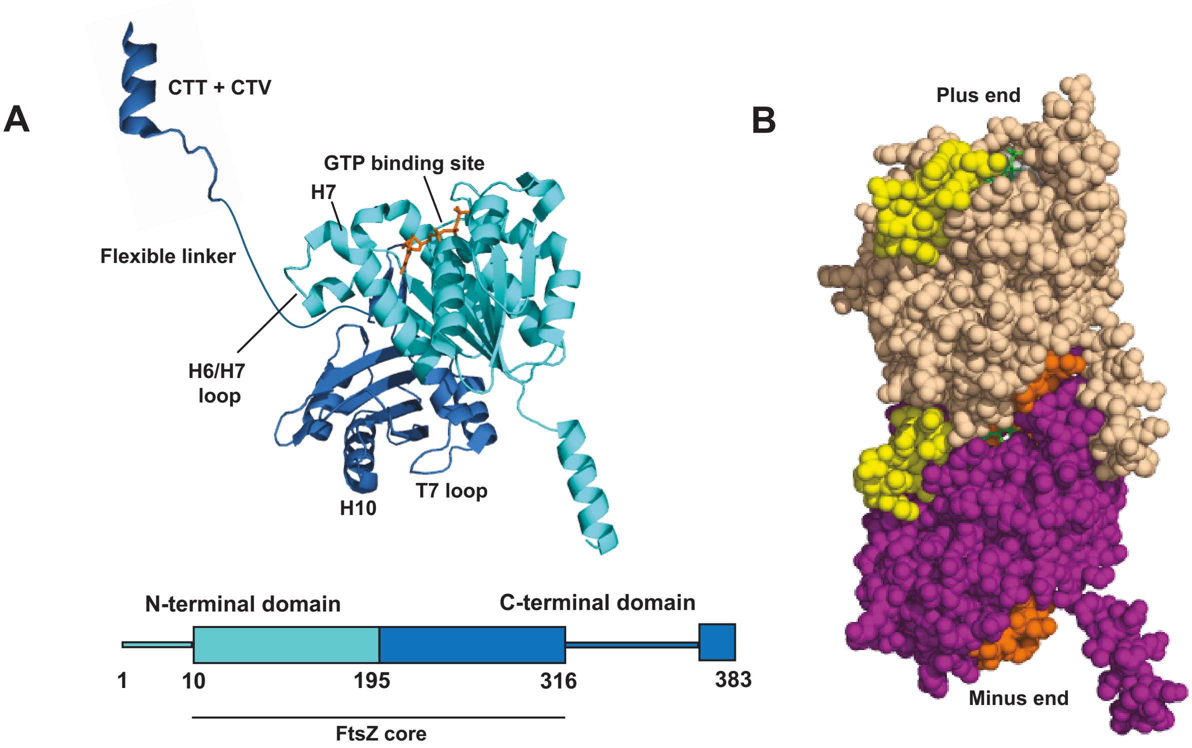
A
CTT + CTV
GTP binding site
H7
Flexible linker
H6/H7
loop
H10
T7 loop
N-terminal domain
C-terminal domain
1
10
195
316
383
FtsZ core
B
Plus end
Minus end

Figure 3.1: The FtsZ subunit and protofilament. Crystal structures of the *Methanococcus jannaschii* FtsZ monomer (A) and space-filled protofilament (B) (PDB 1W5B (11)). A) The globular core of FtsZ is made up of the GTP-binding N-terminal domain (shown in cyan), and the C-terminal domain (shown in sky blue). A line representing the unstructured C-terminal linker has been drawn to connect the FtsZ core to the structured C-terminal peptide containing both the conserved ~15-17aa CTT and the variable ~4-6aa CTV. The C-terminal peptide is shown in the conformation it adopts when bound to ZipA (PDB 1F47 (14)). The bound GTP is shown in orange. In the bottom domain diagram, *E. coli* residue designations are shown. B) Two space-filled FtsZ monomers (wheat and purple) are shown in head-to-tail arrangement. The T7 loop (shown in orange) contacts the GTP nucleotide (green) bound to the GTP-binding pocket (gray). The loop formed by helix 6 and helix 7 (H6/H7 loop) is shown in yellow.

composition amongst different bacterial species (10,12). Furthermore, the C-terminal core domain (ending at *E. coli* residue 316) is followed by a C-terminal tail domain that is composed of an intrinsically disordered peptide linker ranging in length from approximately 50 residues in *E. coli* and *B. subtilis* to 300 residues in some bacterial species, and a highly conserved extreme C-terminal segment (15-17 aa) (10,15,16). This conserved C-terminal tail (CTT) is a regulatory hub that mediates important interactions between FtsZ and its anchoring proteins, FtsA and ZipA in *E. coli*, the SepF protein of *B. subtilis*, and several negative regulators of assembly (discussed below), such as MinC and SlmA (14,17-19). Co-crystal structures of this C-terminal peptide fragment indicate that it adopts different conformations, depending on the accessory protein to which it is bound (14,20,21). At the extreme C-terminus of FtsZ, adjacent to this conserved peptide, is a set of residues (four aa in *E. coli*) that are highly variable between different species (CTV) (22).

Recent work by both the Erickson and Levin groups indicates that the unstructured C-terminal linker is necessary for FtsZ assembly *in vitro* and function *in vivo,* and that length, not sequence is the most important determinant of function (15,16,23). They postulated that this unstructured linker forms a flexible tether between the FtsZ globular core and the inner membrane that allows FtsZ filaments to assemble in the proper conformation for cell division to occur (15,16,23).

FtsZ polymerization and *in vitro* assembly

In vitro, FtsZ polymerizes with a critical concentration of 1 μM into single-stranded filaments ranging from 120 to 200 nm long (3,24). These FtsZ polymers are composed of 30-50 FtsZ subunits stacked vertically in a head-to-tail fashion, similar to the manner in which eukaryotic tubulins polymerize. (3,7,11,25,26). As revealed by crystal structures of the FtsZ protofilament from multiple bacterial species (the *M. jannaschii* structure is shown in Figure 3.1B), this vertical stacking of monomers allows for the T7 loop of the top subunit to reach into the GTP binding pocket of the bottom subunit, positioning critical catalytic residues (N207, N209, D212) near the GTP molecule and allowing for GTP hydrolysis (11,26,27). Thus, as in tubulin, GTP hydrolysis is self-activating and requires FtsZ polymerization (3,11). Similar to microtubule designations, the end of the FtsZ polymer with exposed nucleotide is designated the “plus end”, while the opposite end of the polymer containing the T7 loop is designated the “minus end.”

There is disagreement amongst different structures as to the exact residues involved in longitudinal contact between FtsZ monomers; however, it is generally accepted that in addition to the insertion of the T7 loop into the GTP-binding site, the protofilament interface is formed by contact between residues in helices H0, H8, H9, and H10 of the C-terminal core domain of the top subunit and H2, S3, T3, and the loop formed between helices H6 and H7 in the N-terminal domain of the bottom subunit (11,28-30). Most contacts are between highly conserved residues, with the notable exception of the contact formed by helix H10 of the top subunit and the H6/H7 loop of the bottom subunit (30). With the exception of residue F182, these regions of FtsZ are very poorly conserved across bacteria, suggesting that specific contacts may not be needed to form this stabilizing longitudinal interaction (30). Mutational analyses have confirmed the importance of these contacts in filament formation both *in vivo* and *in vitro* (26,27,31).

Biochemical studies have suggested that GTP binding and hydrolysis are not essential for FtsZ assembly; Huecas et al. found that nucleotide-free *M. jannaschii* FtsZ was able to assemble as well as FtsZ bound to GTP and that addition of GDP destabilized nucleotide-free filaments (32). Their observations agreed with electron microscopy studies suggesting that FtsZ polymers may undergo a nucleotide-dependent conformational switch (32-34). EM images show GDP-bound polymers adopt a more relaxed, curved conformation, while FtsZ-GTP polymers tend to be straight and rigid. Initial crystal structures, however, showed no obvious conformational difference between FtsZ monomers or protofilaments bound to different nucleotides (11). More recently, molecular simulation and structural studies have suggested that this conformational change may be mediated by shifts in the core helix H7, the GTP-contacting T7 loop, and the H6/H7 loop, resulting in weaker monomer-monomer contact in the curved, GDP-bound filament (27,29,30,35,36). Li et al. suggested based on their *Mycobacterium tuberculousis* protofilament structure that this hydrolysis-dependent straight-to-curved transition is further mediated by a hinge-opening of the T3 loop; in their structure the inter-subunit interface is mostly preserved in both conformations and acts as a pivot-point for filament curving (26). Taken together, these recent data align nicely with earlier observations and suggest that nucleotide-driven conformational changes may contribute to constriction of the Z-ring during cytokinesis, and they further imply that GTP hydrolysis may be an important driver of FtsZ turnover (3,26,30,32,34).

Although in *in vitro* assembly reactions single filaments seem to predominate, higher order assemblies of FtsZ filament including bundles, rings, and spirals have also been observed (37). The formation of these structures seems to be dependent on the buffer conditions, the species from which the FtsZ protein originated, and the presence of modulatory proteins (such as ZipA and Zaps) (reviewed in (3,4)). The physiological relevance of these *in vitro* structures and if and how they correlate with *in vivo* Z ring observations is still a topic of debate in the field (3).

In vivo observation of the Z ring

There are approximately 5,000-15,000 molecules of FtsZ per *E. coli* cell, about 40% of which are thought to reside in the Z ring, a structure first visualized via immunoelectron microscopy by Bi and Lutkenhaus in 1991 (3,31,38-40). Observation of fluorescently tagged FtsZ in *E. coli* and *B. subtilis* by conventional fluorescence microscopy shows a dynamic, closed ring at mid-cell that transitions throughout the cell cycle from expanded helical structures, to a transverse fluorescent band, and finally to a fully constricted focus (41-44). FRAP (fluorescence recovery after photobleaching) analyses have shown that turnover of FtsZ subunits in the Z ring proceeds with a half time of about 8-10 s (3,38,45).

In recent years, super-resolution light microscopy has provided striking insight into the arrangement of individual protofilaments in the Z ring. Imaging of the Z ring from multiple species using techniques such as PALM (photoactivated localization microscopy) and 3D-SIM (3D structured illumination microscopy) has suggested that it is not a continuous ring structure, but is instead composed of loose clusters of overlapping filaments separated by filament-free gaps resembling a bead-like arrangement (46-50). Polarized fluorescence microscopy similarly suggests that in *E. coli*, the Z ring is a disordered arrangement of FtsZ filaments that lacks significant order throughout the cell cycle (51). The pool of free FtsZ not associated with the mid-cell Z ring consists of a mixture of dynamic monomers and oligomers (3,50).

Modulation of FtsZ assembly by positive and negative regulators

In addition to the inherent biochemical properties of the FtsZ polymer, Z ring assembly, maintenance, and disassembly are influenced by a diverse set of modulatory proteins throughout the cell cycle. The functions of these endogenous factors can be broadly divided into four categories: i) membrane anchoring ii) stabilization of the Z ring iii) division site selection and iv) response to environmental cues. Additionally, several exogenous inhibitors of FtsZ, including phage-encoded proteins and small molecule inhibitors have been described. Each category is discussed briefly below.

FtsA and ZipA anchor *E. coli* FtsZ in the inner membrane

Electron cryotomography of the Z ring shows that it lies in close proximity to the inner membrane (52). In *E. coli,* this membrane localization is a result of direct interaction between distinct sites on the conserved C-terminal peptide of FtsZ and two collaborating membrane anchor proteins: FtsA and ZipA (14,17,25,53-56). ZipA and FtsA co-localize with the Z ring (44), and both are essential for cell division in *E. coli*. Disruption of either (in the context of a temperature sensitive allele) results in filamented cells that contain regularly spaced Z rings but fail to divide; disruption of both eliminates any observable Z rings (25,53). Despite this partially redundant FtsZ-anchoring role, there is very little similarity between FtsA and ZipA. FtsA is a member of the actin/Hsp70/sugar kinase family that is broadly conserved across bacteria (25); in addition to a slightly modified actin-fold (57), FtsA contains a membrane-targeting amphipathic helix at its extreme C-terminus that is essential for its role in division (56). ZipA, on the other hand, is found only in the gammaproteobacteria and is a bitopic protein composed of an N-terminal trans-membrane domain and a cytoplasmic FtsZ-interacting C-terminal domain that are separated by a proline-glutamine rich linker (54,58). It has been found that a single amino acid substitution in FtsA (*ftsA**) is sufficient for bypass of ZipA essentiality (59). The finding that *ftsA** exhibits decreased self-interaction has suggested that ZipA may be required, in part, in order to modulate FtsA assembly (60).

Z ring stabilization

Combined genetic and biochemical evidence suggests that ZipA may also play a role in stabilizing the membrane-tethered Z ring. RayChaudhuri found that increased expression of *zipA* was able to suppress the assembly defect of the temperature-sensitive *ftsZ84* allele *in vivo*, and that addition of ZipA to FtsZ assembly reactions resulted in the formation of large filament bundles and sheets (61). Several other Z ring associated proteins, or Zaps, are thought to act as positive regulators of the Z ring by promoting lateral interaction between protofilaments (reviewed in (4)). The ZapABCD proteins of *E. coli* are not essential for viability; deletion of any single *zap* gene causes slight defects in Z ring assembly and division. However, deletion of multiple *zap* genes or combining individual *zap* deletions with other divisome perturbations is synergistic, revealing pronounced synthetic sick phenotypes (4). These proteins promote formation of large FtsZ bundles *in vitro* (62-64). Despite this apparent overlap in function, the Zaps share no sequence similarity, and with the exception of ZapA and ZapB (65), do not interact with each other. ZapACD interact directly with FtsZ; ZapD is thought to interact with the conserved C-terminal tail of FtsZ (62). The Gram-positive FtsZ regulator, SepF, similarly promotes FtsZ bundling and was also found to interact with the conserved C-terminal tail region (4,19). Interestingly, super-resolution imaging of the Z ring in a strain lacking both *zapA* and *zapB*, did not show marked difference in the *in vivo* formation of multi-filament FtsZ clusters (66). It was noticed, though, that these filament clusters did not align as efficiently at mid-cell as in a wild-type strain, suggesting that rather than playing a vital role in FtsZ bundling, ZapA and ZapB may primarily function in spatial organization of the Z ring (66).

Although several lines of evidence suggest that the formation of lateral interactions stabilizes FtsZ assembly, the specific FtsZ-FtsZ contacts involved in lateral interaction have not been well established. Notably, *B. subtilis* FtsZ has a higher propensity to form bundles than FtsZ from *E. coli* (22). Buske and Levin recently found that swapping the extreme C-terminal residues (the CTV) of *E. coli* and *B. subtilis* FtsZs led to the reciprocal observation, suggesting that this region is sufficient to promote lateral interactions (22). Furthermore, mutation of two residues in the H6/H7 loop has been found to alter the bundling properties of *E. coli* FtsZ. The R174D substitution was shown to decrease FtsZ bundling *in vitro* (67), while recent work by the Margolin group has shown that the L169R substitution enhances bundling of FtsZ, resulting in increased resistance to negative regulators of assembly and allowing for the bypass of the proposed stabilizer ZipA (68). However, it remains to be seen precisely how these various residues interact with monomers in an adjacent filament.

Division site selection

The precise positioning of the Z ring is determined by collaboration of two partially redundant systems, the Min and nucleoid occlusion systems, both of which employ negative regulators to restrict the assembly of FtsZ filaments to mid-cell. The Min system of *E. coli* prevents Z-ring assembly at the cell poles and consists of three proteins: 1) MinC, an FtsZ antagonist 2) MinD, a ParA family ATPase that when bound to ATP dimerizes and is targeted to the inner membrane in a complex with MinC, and 3) MinE, a membrane-bound protein that activates MinD ATPase activity and positions the MinCD complex at the cell poles (2,69). Extensive *in vitro*, *in vivo*, and *in silico* work has illustrated that these Min proteins rapidly oscillate from cell pole to cell pole, ensuring that on average, over time they are most often found at the ends of cell and absent from the mid-cell zone (70,71). Disruption of the Min system results in aberrant Z ring localization and the formation of a mixture of anucleate mini-cells and elongated, multinucleate cells (72).

MinC has two inhibitory domains, both of which interfere with FtsZ assembly. The C-terminal domain of MinC interacts with the conserved C-terminal tail of FtsZ and is thought to displace FtsA and ZipA from this site in the context of assembled Z rings (73). Additional work by Shen and Lutkenhaus showed that mutation of residues in the H10 helix at the longitudinal interface of the FtsZ protofilament, conferred resistance to the N-terminal domain of MinC both *in vivo* and in *in vitro* assembly reactions (74). Their observations, combined with earlier work showing that MinC does not block *in vitro* polymerization or GTPase activity of FtsZ but does lead to the shortening of filaments (75), led them to suggest the following model. They propose that MinC inhibition is a two-pronged mechanism in which the CTD of MinC first binds the C-terminal tail of FtsZ, disrupting membrane anchoring; the NTD of MinC then attacks the intra-protofilament interface, breaking apart FtsZ polymers (74). They specify that the NTD of MinC is likely able to access the H10 helix only when filaments are in the curved, GDP-bound state (74).

Nucleoid occlusion ensures that Z ring assembly and cytokinesis do not occur until the segregation of nucleoids is successfully completed and thus serves to maintain genomic integrity (76). In *B. subtilis*, nucleoid occlusion is mediated by the Noc effector (77), which appears to block Z ring assembly not by interaction with FtsZ, but by recruitment of DNA to the cell membrane to form large nucleoprotein complexes (78). It has been proposed that these large complexes may crowd the mid-cell region, physically blocking Z ring formation (78). In *E. coli,* the nucleoid occlusion factor is SlmA, which was first identified through a screen to find factors synthetically lethal with loss of the Min system (79). In contrast to Noc, SlmA directly binds to the conserved C-terminal peptide of FtsZ to disrupt assembly; SlmA antagonism also requires sequence-specific binding to the DNA (18,21,79,80). Strikingly, a recent co-crystal structure of SlmA bound to DNA and to the FtsZ CTD shows that the C-terminal peptide adopted an extended conformation quite distinct from that formed when in complex with either FtsA or ZipA (14,20,21). This finding reveals the remarkable conformational flexibility of the FtsZ C-terminal peptide, a characteristic that allows it to interact with a diverse group of unrelated accessory proteins.

Inhibition of FtsZ assembly in response to the environment

In addition to being regulated by these "house-keeping" proteins throughout the typical cell cycle, FtsZ is also the target of several inhibitors that block its assembly in response to specific environmental cues. FtsZ assembly is a logical node of regulation as its inhibition can lead to a rapid block in cell division. Here, two examples with unique mechanisms are considered. Cell division is halted during the SOS response; DNA damage in *E. coli* leads to the RecA-mediated inactivation of LexA, resulting in a drastic increase in production of the SulA division inhibitor (81). SulA, the most well-characterized negative regulator of FtsZ, has been shown by co-crystal structure to bind the T7 loop of the C-terminal core domain, completely occluding the top surface of the longitudinal interface (Figure 3.1B) (82). *In vivo*, this interaction results in cell filamentation and disruption of Z rings (83), whereas *in vitro,* addition of SulA disrupts FtsZ GTPase activity and assembly and causes an increase in the critical concentration of FtsZ assembly by an amount equivalent to the concentration of added inhibitor (84-86). Taken together, these observations suggest that SulA sequesters FtsZ subunits, preventing them from participating in assembly (86).

Interestingly, SulA exhibits decreased toxicity when GTPase activity of FtsZ is reduced; several mutations that confer resistance to *sulA* expression do not map to the T7 loop interaction surface (but instead attenuate GTPase activity (82,87). Furthermore, FtsZ assembly *in vitro* is less sensitive to SulA inhibition in the presence of nonhydrolyzable GTP analogs (84,86). This evidence suggests that SulA requires filament turnover in order to disrupt FtsZ function, an interesting parallel to the N-terminal domain of the MinC inhibitor (74,75). Despite using distinct inhibitory mechanisms, both inhibitors apparently exploit the dynamic nature of FtsZ filaments to exert their activities.

MciZ, a 40 aa peptide produced in *B. subtilis* during sporulation, employs another notable mechanism to inhibit FtsZ assembly in the mother cell (88,89). Recent structural data indicate that MciZ binds to helix H10 of the C-terminal FtsZ core (89); this site overlaps with the MinC-NTD interaction surface suggested by Shen and Lutkenhaus (74) and is in close proximity to the T7 loop that binds SulA. Indeed, in the MciZ-FtsZ co-crystal, the T7 loop was found to be displaced by MciZ binding (89). Observation that MciZ shortens FtsZ polymers *in vitro* and prevents Z ring formation *in vivo*, both at substoichiometric levels, is highly suggestive of a capping mechanism (89). This mechanism of action was elegantly confirmed by fusion of MciZ to the flexible C-terminal tail of FtsZ; addition of this covalently linked FtsZ-MciZ complex to wild-type FtsZ assembly reactions still led to shortened filaments *in vitro,* ruling out the possibility of a simple sequestration model (since in the sequestration model, MciZ pre-complexed with FtsZ should have no effect on FtsZ assembly) (89). This demonstration of capping of FtsZ filaments on the C-terminal face (minus end) revealed a notable difference between FtsZ polymers and microtubules. Microtubules exhibit treadmilling, i.e. addition of subunits to the plus end and disassociation of subunits from the minus end (24). While capping of the minus end of microtubules is typically stabilizing, MciZ markedly destabilizes FtsZ, implying that FtsZ polymers may not exhibit treadmilling in the same manner as eukaryotic tubulins (89). Instead, Bisson-Filho et al. propose that the fragmentation and annealing of polymers may play an important role in assembly. Thus, interaction with the FtsZ H10/T7 region can inhibit FtsZ function via three distinct mechanisms: capping (89), sequestration (86), and polymer breaking (74).

As inhibition of FtsZ is such a potent method of preventing cell division, it is unsurprising that several bacteriophages encode their own negative regulators of this essential protein. The Kil protein encoded by λ phage (and homologous prophage elements) and Gp0.4 from T7 phage have both been shown to directly inhibit FtsZ assembly (90-92). In the case of the latter, Gp0.4-mediated inhibition of FtsZ during infection conferred a fitness advantage for T7 phage, suggesting that block of cell division aids in successful infection (92).

Motivation for the current study

As evidenced by the many factors so far discussed in this chapter, bacteria (as well as the phages that target them) have evolved a wide range of mechanisms to control cell division through interaction with the division regulator FtsZ. Elucidation of these mechanisms has provided important insight into numerous aspects of FtsZ dynamics and cytokinesis. It has also helped to motivate the development of FtsZ as a druggable anti-bacterial target (93,94). The benzamides, a class of synthetic compounds that target FtsZ, exhibit potent antibacterial activity against several Gram-positive organisms, including multi-drug resistant *Staphylococcus aureus* (25,95). Isolation of resistance mutants in helix H7 and a recent co-crystal structure indicate that this compound binds to this central core helix, likely restricting the flexibility needed to transition between relaxed GDP-bound and straight GTP-bound polymer states (35,95,96). In addition to their exciting promise for the treatment of infections, these compounds will likely serve as important tools to further study FtsZ dynamics.

If the recent surge in our understanding of diverse FtsZ inhibitory mechanisms is any indication, it seems likely that there are yet unidentified ways to mediate a block of cell division. In the following study, we describe our efforts to elucidate the mechanism employed by the CbtA protein of *E. coli* to block cell division. CbtA, the toxin component of a prophage-encoded chromosomal toxin-antitoxin system, mediates a simultaneous block of cell division and cell elongation when overproduced in *E. coli* ((97) and our work). Work described in Chapter 2 of this dissertation demonstrates that CbtA interacts independently with both FtsZ and MreB and illustrates that these interactions are necessary for CbtA-mediated toxicity. In this chapter, I perform a more detailed analysis of the interaction between CbtA and FtsZ and in Chapter 4 I focus on the interaction between CbtA and MreB.

As mentioned previously, Tan et al. demonstrated that His-tagged CbtA is able to pull down both MreB and FtsZ from an *E. coli* cell lysate, and using a yeast two-hybrid system they were able detect interactions between CbtA and FtsZ, CbtA and MreB, and MreB and FtsZ (97). In an attempt to characterize the region of FtsZ responsible for the detected CbtA-FtsZ interaction, they tested two FtsZ truncations. They found that removal of either the first 32 amino acids or the last 66 amino acids of the FtsZ protein eliminated the yeast two-hybrid interaction detected between CbtA and FtsZ as well as the interaction between MreB and FtsZ (97). As the last 66 residues of *E. coli* FtsZ form the C-terminal tail domain, which, as described above, is a site of interaction for several known FtsZ-modulatory proteins, Tan et al. concluded that this was a likely site of CbtA interaction.

Using our bacterial two-hybrid system and a variety of genetic approaches, we sought to further characterize the interaction between the CbtA toxin and *E. coli* FtsZ to determine whether CbtA does in fact interact with this C-terminal regulatory hub or an alternative surface. By identifying the FtsZ binding site of CbtA, we hoped to shed light on the inhibitory mechanism employed by this potent cytoskeletal inhibitor and potentially learn additional information about the assembly and function of FtsZ. The following study outlines our findings that the CbtA toxin and its homologs interact directly with the H6/H7 loop of *E. coli* FtsZ. We believe this represents a new FtsZ inhibitory interaction.

Chapter 3.2: Results

E. coli FtsZ interacts with CbtA, ZipA, and itself in a transcription-based bacterial two-hybrid system

By means of our transcription-based bacterial two-hybrid assay, we can detect a strong interaction between wild-type CbtA and *E. coli* FtsZ (resulting in a 20-fold increase in *lacZ* transcription) (shown previously in Figure 2.2). As shown in Figure 3.2 panel A, we can also detect a strong interaction (resulting in a 7- to 9-fold increase in *lacZ* expression) between *E. coli* FtsZ and a truncated variant of the membrane anchoring protein, ZipA. In this ZipA two-hybrid construct, the λCI protein is fused to the cytoplasmic C-terminal domain of ZipA (residues 186-328); the N-terminal trans-membrane segment and unstructured linker are not included (58). An interaction between the cytoplasmic portion of ZipA and FtsZ in the yeast two-hybrid system was previously reported by both the Lutkenhaus and de Boer groups (98,99). In the yeast two-hybrid system, both mutation of residue 373 in the conserved C-terminus of FtsZ from aspartate to glycine (D373G) (98) and deletion of 63 residues at the C-terminus of FtsZ were found to severely diminish the interaction between ZipA and FtsZ (99). These results align with structural data indicating that the cytoplasmic C-terminal domain of ZipA binds the C-terminus of FtsZ (14). We were able to replicate these results in our bacterial two-hybrid system; the ZipA-FtsZ interaction was disrupted both by removal of the C-terminal 66 residues of the FtsZ moiety and by introduction of the D373G substitution (Figure 3.2 panel A). These results strongly suggest that we are detecting a biologically relevant ZipA-FtsZ interaction in our bacterial two-hybrid system.

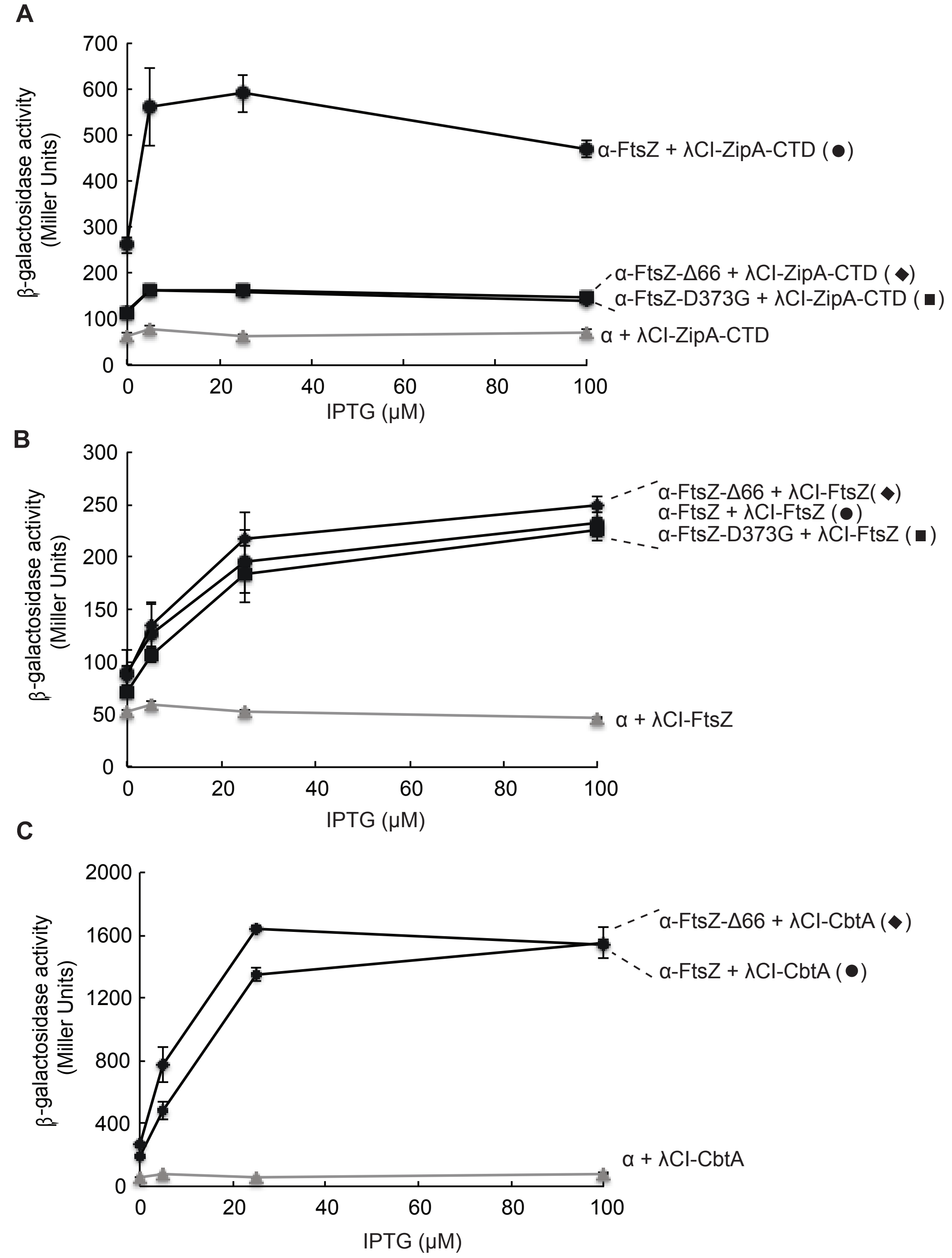

Figure 3.2: FtsZΔ66 interaction with ZipA-CTD, FtsZ, and CbtA. Two-hybrid interactions of α-FtsZΔ-66 and α-FtsZ-D373G with λCI-ZipA-CTD (residues 186-328) and λCI-FtsZ are shown in A and B, respectively. Two-hybrid interaction of α-FtsZΔ-66 and λCI-CbtA is shown in C. β-galactosidase activity was measured at multiple induction levels (0, 5, 25 and 100 µM IPTG) for all interactions. Each point represents the average of triplicate values; error bars represent standard deviation.

Importantly, these FtsZ variants (FtsZ-D373G and FtsZ-∆66, each fused to the α subunit of RNA polymerase) still maintained an interaction with wild-type λCI-FtsZ, yielding approximately a 4-fold increase in *lacZ* expression (Figure 3.2, panel B). The genetic determinants of this FtsZ self-interaction are not known, but a similar interaction was previously reported in the context of the yeast two-hybrid system. In this system, similar results to ours were observed, indicating that removal of the last ~60 aa of FtsZ does not play a role in this detected FtsZ self-interaction (55).

CbtA maintains interaction with an FtsZ variant lacking the C-terminal tail domain

Based on the yeast two-hybrid result previously reported by Tan et al., we predicted that deletion of the C-terminal tail domain of FtsZ would eliminate its interaction with the CbtA toxin. Surprisingly, we found that while this FtsZ-Δ66 was decreased for interaction with ZipA, it maintained an interaction with CbtA comparable to that of the wild-type protein, across several induction levels (Figure 3.2, panel C). We were unable to detect an interaction between wild-type FtsZ and *E. coli* MreB in our two-hybrid system and thus could not determine whether or not this C-terminal truncation had any effect on that reported interaction (data not shown). Since, in our bacterial two-hybrid system, the last 66 residues of FsZ do not appear to mediate the interaction with CbtA, we sought to identify substitutions in FtsZ that specifically disrupt its interaction with CbtA. In order to do this, we took an unbiased genetic approach, using our two-hybrid system as a blue-white screening platform.

Substitutions in the H6/H7 loop of FtsZ disrupt the FtsZ-CbtA interaction

A two-hybrid mutant library was constructed by cloning PCR mutagenized *ftsZ* into the α vector of our bacterial two-hybrid system. This library was transformed into our two-hybrid reporter strain containing CbtA fused to λCI, and candidate variants with lowered CbtA interaction were identified as light blue or white colonies on medium containing 5 µM IPTG and 40 µg/µL X-gal. Approximately 100 α-FtsZ mutant clones were found to have lowered interaction with λCI-CbtA. In order to identify mutants specifically deficient for interaction with CbtA, these candidates were counter-screened to identify those that maintained the FtsZ-FtsZ self-interaction; 24 candidates with a self-interaction that was comparable to wild-type and at least a 50% decrease in the λCI-CbtA interaction were sequenced. We found that the most promising of these sequenced candidates, specifically those that maintained a self-interaction of at least ~75% and resulted in at least a ~60% decrease in the λCI-CbtA interaction as compared to wild-type α-FtsZ, all had mutations affecting residues 169-182 (Figure 3.3A). These α-FtsZ mutants also maintained strong interaction with the C-terminal domain of ZipA (Figure 3.3A). FtsZ residues 168-182 form the H6/H7 loop found in the core GTP-binding N-terminal domain of FtsZ. This loop (shown in yellow in figure 3.1B) is on the opposite end of the central core helix from the T7 synergy loop. As discussed above, FtsZ protofilament structures from multiple species indicate that this H6/H7 loop, which has low sequence conservation across different species, is located at the interface of two FtsZ monomers (11,26). Additional mutants identified in this screen are discussed in Appendix I (Figure A1.1).

To further evaluate whether the mutated loop residues identified in our screen are important for the CbtA-FtsZ interaction, we wanted to test whether *cbtA* overexpression in an *E. coli* strain bearing one of these H6/H7 loop mutations at the endogenous *ftsZ* locus resulted in the formation of lemon-shaped cells (indicative of a simultaneous block of cell division and cell elongation) or spherical cells (indicative of MreB inhibition only). Three mutant *ftsZ* alleles (*ftsZ-L169P*, *ftsZ-S177P*, and *ftsZ-D180N*) were found to complement growth of an *ftsZ* depletion strain when expressed from a multi-copy plasmid; however, only *ftsZ-L169P* was able to support growth when introduced into the chromosomal *ftsZ* locus (shown in supplementary figure A1.2A). We observed that this strain does not fully support division in fast-growth conditions (LB at 37 ºC) as we see a subset of filamented cells and notable heterogeneity in cell length (supplementary Figure A1.2B). This division defect can be partially rescued by slower growth in LB at 30 ºC and fully rescued by growth in M9 minimal medium (supplemented with 0.4% maltose and 0.01% casamino acids) at 30 ºC (supplementary Figure A1.2B). Indeed, in minimal medium, we observed comparable cell lengths for the wild-type (2.0 ± 0.5 μm) and *ftsZ-L169P* (2.4 ± 0.7 μm) strains.[g]

We found that when wild-type *cbtA* was overexpressed from the multi-copy plasmid pMT139 (*pT5-lac-his*$_6$*-cbtA-gfp*) in this *ftsZ-L169P* strain (DH73), in M9 maltose, cells lost their rod-shape, but formed spherical or sphere-like cells rather than lemons (Figure 3.3B). Quantification of these data shows a more pronounced increase in cell roundness (width divided by length) upon *cbtA* overexpression in the

---

[g] Reported values are mean ± standard deviation. Cell length measurements were made of BW27785/ pMT139 (*n*=725) and DH73/pMT139 (*n*=739) strains in the absence of IPTG from three independent experiments.

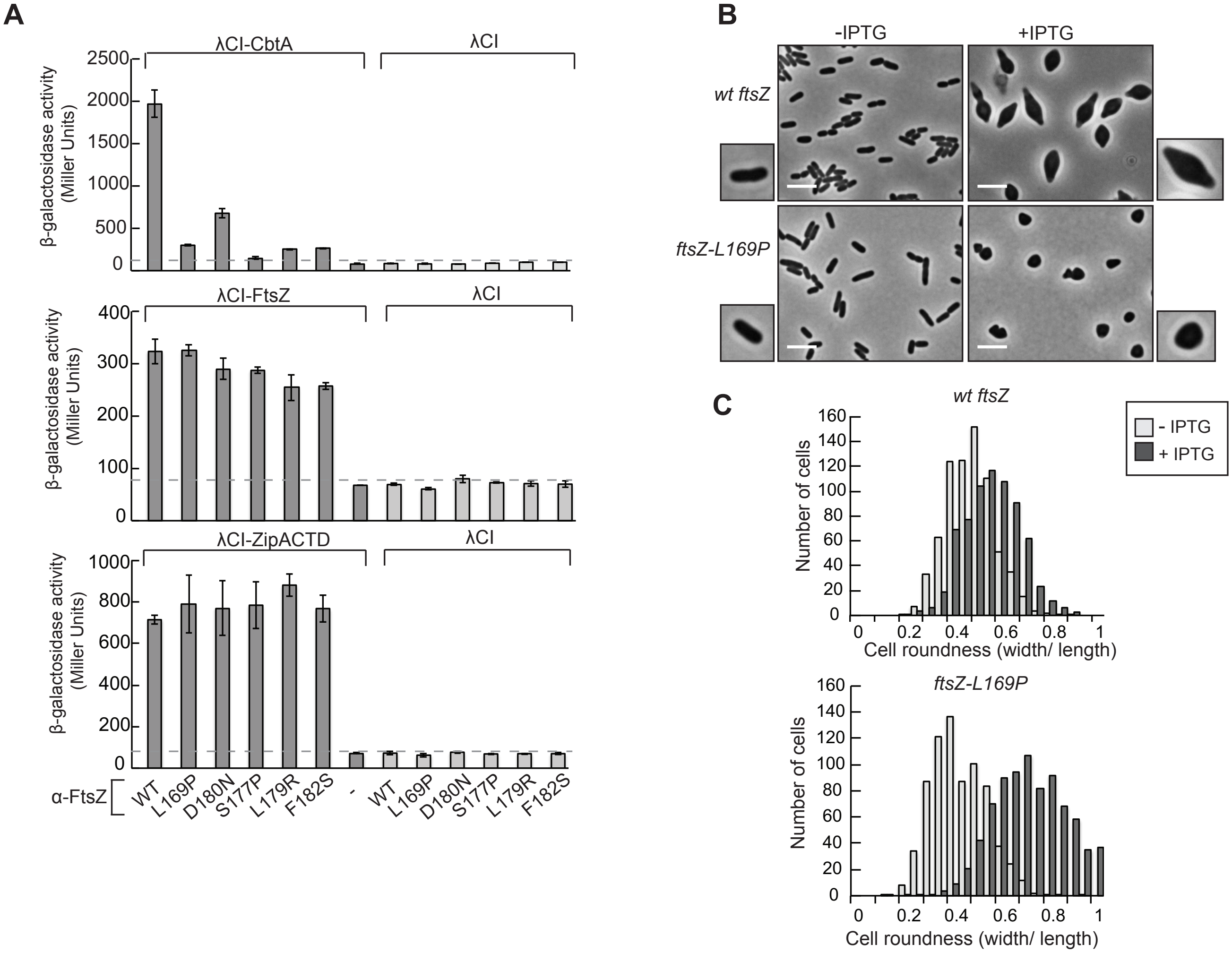

Figure 3.3: Residues in the H6/H7 loop are necessary for CbtA-FtsZ interaction. A) These graphs represent the interactions between the α-FtsZ H6/H7 loop mutants and cI-CbtA, cI-FtsZ, and cI-ZipA-CTD (from top to bottom). The bars represent the average β-galactosidase activity from three independent measurements. Error bars represent standard deviations. Experiments were done with 100 μM, 100 μM, and 25 μM IPTG, from top to bottom. B) Phase contrast images were taken of either wild-type BW27785 or BW27785 *ftsZ-L169P* cells overproducing His$_6$-CbtA-GFP (encoded on plasmid pMT139). Overnight cultures grown at 30 ºC in M9 maltose (0.4% maltose, 1mM MgSO4, 0.01% casamino acids) were back-diluted 1:3,000 into fresh medium and grown at 30 ºC for ~14 hrs until they reached an OD600 of 0.3. Cultures were then induced with 100μM IPTG and grown for 8hrs at 30 ºC. Scale bar represents 5 μm. C) Quantification of cell roundness (cell width/ cell length) from cells in B. Histograms include compiled measurements from three-independent experiments (*n*= 725, wild-type without IPTG; *n*=706, wild-type +

Figure 3.3 (Continued)

IPTG; *n*=739, L169P without IPTG; *n*=813, L169P +IPTG). Width and length measurements were made manually in ImageJ.

ftsZ-L169P strain than in the wild-type strain (shown in Figure 3.3C). In the wild-type strain, *cbtA* expression increased cell roundness only slightly (from 0.45 ± 0.1 to 0.53 ± 0.1) while in the L169P strain, cell roundness shifted more drastically (from about 0.41 ± 0.1 to 0.68 ± 0.2).[h][i] The combined two-hybrid and morphology data suggest that this loop region is critical for the FtsZ-CbtA interaction.

CbtA interacts directly with the H6/H7 loop of FtsZ

We next sought to determine whether CbtA interacts directly with the H6/H7 loop of FtsZ. As a first approach, we aimed to identify compensatory substitutions in CbtA that restore its interaction with FtsZ H6/H7 loop mutants through use of our two-hybrid screening platform. We made a *cbtA* mutant library fused to λCI by PCR mutagenesis, transformed this into our two-hybrid strain containing a particular α-*ftsZ* mutant plasmid, and screened for dark blue "up" mutants on plates supplemented with IPTG, X-gal, and TPEG (a competitive inhibitor of β-galactosidase). We pooled these candidate suppressor mutants and then counter-screened them against wild-type FtsZ to identify those substitutions that enabled CbtA to interact with a specific mutant FtsZ but not wild-type FtsZ. As charge reversal mutations are often the easiest types of mutations with which to identify allele-specific interactions, we took advantage of an aspartic acid residue within the H6/H7 loop of *E. coli* FtsZ. As shown in Figure 3.4, an aspartic acid to lysine charge reversal substitution at residue 180 almost completely eliminates the interaction between FtsZ and CbtA. We were able to identify a substitution in CbtA, V48E, which partially restores the interaction between CbtA and FtsZ-D180K (resulting in a 9-fold increase in *lacZ* expression). This interaction is allele-specific, as CbtA-V48E is unable to interact with wild-type FtsZ or any of the other H6/H7 loop mutants identified (L169P, S177P, D180N[j]) (Figure 3.4).

---

[h] Reported values are mean ± standard deviation.

[i] Previous reports have measured the cell roundness of wild-type, rod-shaped *E. coli* as about 0.6.(100,101) The cell roundness ratios for both the wild-type and *ftsZ-L169P* strains (without *cbtA* expression) in our experiment were slightly lower (between 0.4 and 0.5). We speculate that this may be due to strain or growth condition differences, as previous measurements were made in rich LB medium whereas ours were made in M9 minimal medium supplemented with 0.4% maltose and 0.01% casamino acids (102).

[j] It is interesting to note that λCI-CbtA-V48E seems to be able to discriminate between wild-type α-FtsZ and the H6/H7 mutants, α-FtsZ-L169P and α-FtsZ-S177P, but not between wildtype α-FtsZ and α-FtsZ-D180N. As shown in Figure 3.4, introduction of the L169P and S177P substitutions causes a decrease in

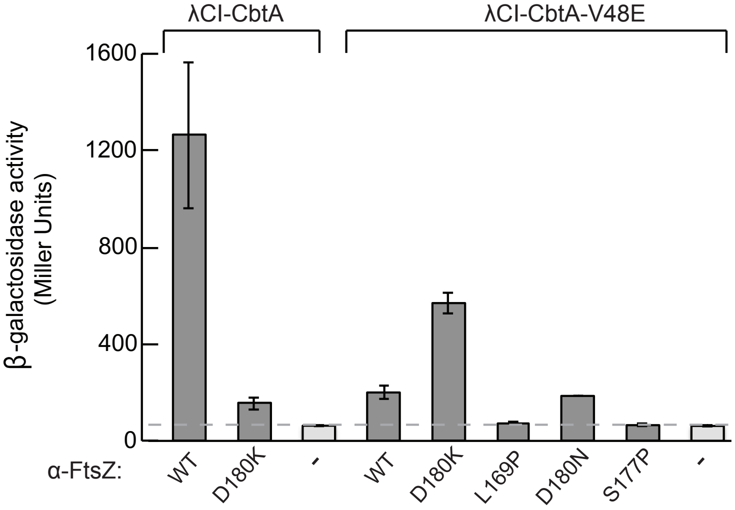

Figure 3.4: CbtA-V48E and FtsZ-D180K interact in an allele-specific manner. Two-hybrid analysis shows that the CbtA-V48E substitution partially restores the CbtA-FtsZ (D180K) interaction, but disrupts the interaction with wild-type FtsZ. The bars represent the average β-galactosidase activity from three independent measurements. Error bars represent standard deviations. Experiment was done with 25 μM IPTG.

To further investigate whether CbtA interacts directly with the H6/H7 loop, we developed a *B. subtilis* heterologous system in which to investigate the FtsZ amino acid requirements for CbtA toxicity. Although there is ~47% amino acid identity between *E. coli* and *B. subtilis* FtsZ proteins, the H6/H7 loop has several non-conservative amino acid differences (Figure 3.5A). Thus, we predicted that if the H6/H7 loop is the primary CbtA interaction surface, there should be no detectable interaction between the CbtA toxin and BsFtsZ. As shown in Figure 3.5B, CbtA is unable to interact with BsFtsZ by two-hybrid analysis; however, replacement of the *B. subtilis* H6/H7 loop with the *E. coli* loop allowed for a strong interaction between BsFtsZ and CbtA. To test whether this interaction would allow for CbtA toxicity in *B. subtilis,* we

---

the already compromised α-FtsZ/λCI-CbtA-V48E interaction; introduction of the D180N substitution does not further abrogate this interaction. Although subtle, this loss of specificity upon alteration of residue D180 further suggests that CbtA-V48E interacts directly with this residue in an allele-specific manner.

constructed strains with either the wild-type or chimeric *ftsZ* (linked to *spec*) at the endogenous locus and either *gfp*, wild-type *cbtA* or *cbtA-F65S* (both alleles encode an N-terminal His_6 tag preceding *cbtA* followed by a C-terminal GFP moiety) at the *ycgO* locus under the control of the *pHYPERSPANK* promoter. The chimeric *ftsZ* allele caused a slight growth defect as illustrated by the reduced colony size in Figure 3.5C and decreased growth rate in Figure 3.5D, and microscopic analysis indicated that cells form filaments (see Appendix I, Figure A1.3, for a complete discussion of microscopic phenotypes). Overproduction of wild-type CbtA in the chimera strain caused a severe growth defect both on plates (shown in Figure 3.5C) and in liquid (shown in Figure 3.5D), but overproduction of CbtA-F65S to comparable levels (Figure 3.5E) did not. Thus, the allele-specific interaction between CbtA-V48E and FtsZ-D180K and the *B. subtilis* studies provide strong support for our hypothesis that CbtA is interacting directly with the H6/H7 loop of FtsZ. Furthermore, the CbtA-dependent toxicity observed in the *B. subtilis* chimera strain indicates that this interaction contributes to the toxicity of CbtA[k].

CbtA homologs, YpjF and YkfI, also interact with the H6/H7 loop of FtsZ

CbtA has two homologs in *E. coli*: the YkfI toxin of the YkfI/YafW toxin-antitoxin system, and the YpjF toxin of the YpjF/YfjZ toxin-antitoxin system (103). The three toxins are encoded on different cryptic prophage elements within the *E. coli* genome, and have high amino acid sequence identity (58% identity between CbtA and YkfI, 62% identity between CbtA and YpjF, 78% identity between YpjF and YkfI) (103). As shown in Chapter 2 (Figure 2.3B), using our bacterial two-hybrid assay we can detect strong interactions between FtsZ and YpjF and also between FtsZ and YkfI (20-fold increase in *lacZ* expression and 13-fold increase in *lacZ* expression, respectively). Indeed, when we assayed their interactions with the BsFtsZ chimeras, we found that neither YkfI nor YpjF interacted with wild-type *B. subtilis* FtsZ, but both toxins interacted very strongly with the BsFtsZ chimera containing the H6/H7 loop of *E. coli* (Figure 3.6). Thus, we believe that all three toxin homologs interact directly with the H6/H7 loop of *E. coli*.

---

[k] The lack of CbtA-mediated toxicity in the wild-type strain suggests that the CbtA toxin does not noticeably disrupt cell elongation in *B. subtilis*.

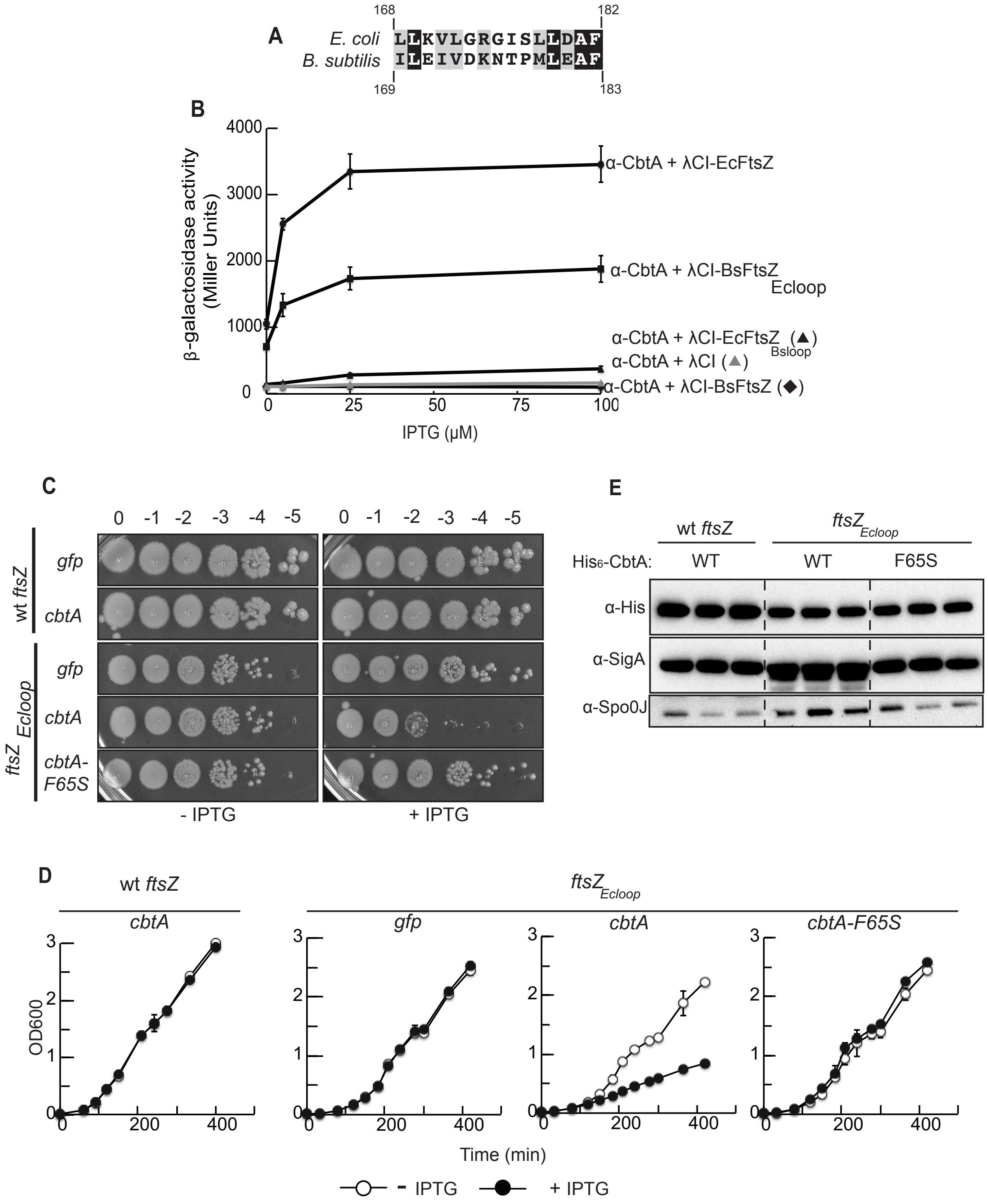

Figure 3.5: CbtA interacts with chimeric BsFtsZ containing the E. coli H6/H7 loop. A) An alignment of the H6/H7 loop sequences from *E. coli* and *B. subtilis* is shown. Identical residues are shown in black; similar residues are shown in gray. Alignment was prepared using Boxshade. B) Two-hybrid analysis

Figure 3.5 (Continued)

shows that a BsFtsZ chimera containing the H6/H7 loop from *E. coli* FtsZ (residues 169-183 of BsFtsZ are replaced with residues 168-182 of EcFtsZ) can interact with CbtA. β-galactosidase activity was measured at multiple induction levels (0, 5, 25 and 100 μM IPTG). Points represent the average β-galactosidase activity from three independent measurements; error bars represent standard deviations. Experiment was done with 25 μM IPTG. C) A spot dilution assay was used to measure CbtA toxicity in *B. subtilis* strains containing the indicated *ftsZ* and *cbtA* alleles. A single colony of each strain was grown in LB at 37 ºC until late-log phase. All cultures were normalized to the same OD600 value, 1:10 serial dilutions were made, and cultures were spotted on LB plates with or without 1mM IPTG. Plates were incubated at 37 ºC overnight. D) Growth curve analysis was performed on *B. subtilis* strains containing the indicated *ftsZ* and *cbtA* alleles. Strains were grown in LB ± 1 mM IPTG at 37 ºC over several hours. Each point represents the average of triplicate values; error bars represent standard deviation. E) His_6-CbtA-GFP and His_6-CbtA-F65S-GFP levels from a growth curve experiment similar to that described in D were assayed by Western blot, in triplicate using an anti-His_6 antibody. Samples were taken after 4 hrs growth. SigA and Spo0J levels were also measured and serve as loading controls.

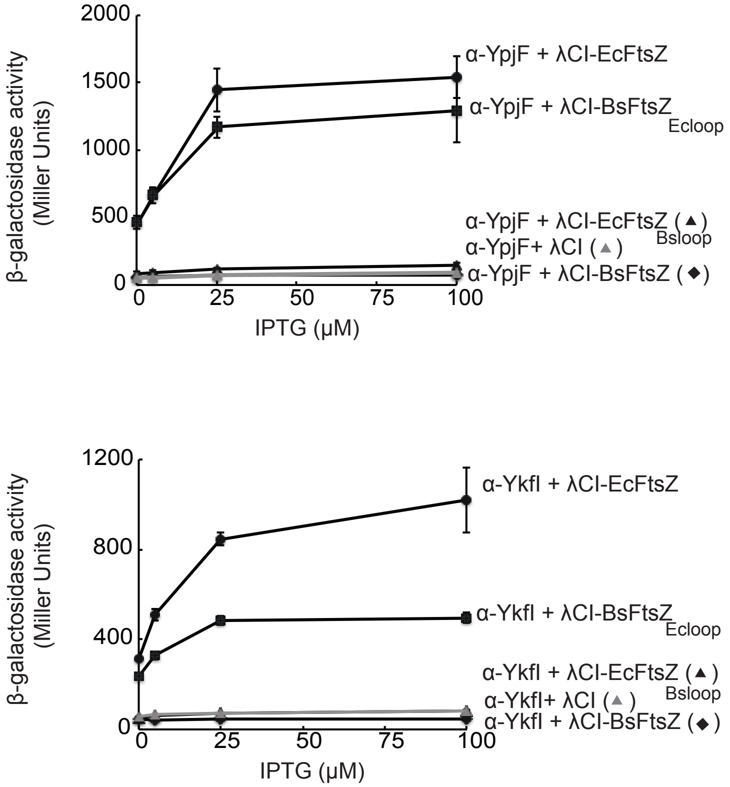

Figure 3.6: YkfI and YpjF interact with chimeric BsFtsZ containing the E. coli H6/H7 loop. Two-hybrid analysis indicates that the BsFtsZ chimera containing the H6/H7 loop from *E. coli* FtsZ interacts strongly with both the YkfI and YpjF toxins. β-galactosidase activity was measured at multiple induction levels (0, 5, 25 and 100 μM IPTG). Points represent the average β-galactosidase activity from three independent measurements; error bars represent standard deviations.

Chapter 3.3: Discussion

CbtA interacts directly with the H6/H7 loop of *E. coli* FtsZ

CbtA is a potent inhibitor of both cell elongation and cell division. When the wild-type toxin is produced, cells become bloated lemons; when a variant that interacts only with FtsZ (CbtA-R15C) is produced, cells fail to divide and form filaments lacking functional Z rings (see Chapter 2 of this dissertation). Here, we show that the CbtA toxin interacts directly with the H6/H7 loop of *E. coli* FtsZ. Our argument that CbtA exerts its inhibitory effect on cell division via direct interaction with the H6/H7 loop is based on the following observations. First, mutation of residues in the H6/H7 loop disrupts the CbtA-FtsZ interaction detected by bacterial two-hybrid analysis, and expression of *cbtA* in a strain harboring one of these mutant alleles does not result in the formation of lemon-shaped cells, but instead yields sphere-like cells indicative of a reduction in FtsZ-inhibition. Second, we identified an allele-specific interaction between CbtA-V48E and FtsZ-D180K, which suggests that CbtA is directly interacting with residues in the H6/H7 loop. Finally, through use of our *B. subtilis* heterologous system, we found that replacement of the *B. subtilis* H6/H7 loop with the *E. coli* loop sequence allows for toxic interaction between CbtA and BsFtsZ, confirming a direct interaction. Additionally, our two-hybrid data indicate that the H6/H7 loop is the likely interaction surface of two homologous toxins, YkfI and YpjF.

Our findings do not align with those previously reported by Tan et al (97). They saw that removal of the C-terminal tail of FtsZ eliminated interaction between CbtA and FtsZ in their yeast two-hybrid system; this FtsZ variant was also unable to interact with MreB. In our two-hybrid system, removal of this tail domain had no effect on the CbtA-FtsZ interaction. We believe that FtsZ-Δ66 is behaving in a physiologically relevant manner in our two-hybrid system, as the truncation was found to decrease the interaction with ZipA-CTD, a protein known to bind the C-terminal tail of FtsZ (14). We were unable to determine whether this FtsZ variant can interact with MreB; however, recent work by Fenton et al. suggests that MreB interacts with an alternative surface of FtsZ (104). In that work, the authors present an allele-specific interaction between MreB-D285A and FtsZ-P203Q, suggesting that MreB likely interacts with the globular C-terminal domain of FtsZ (104). Based on our strong genetic evidence, we conclude that the H6/H7 loop and not the C-terminal tail is the primary CbtA interaction surface.

Genetic insight into the mechanism of CbtA-mediated cell division inhibition

Structural studies have shown that the H6/H7 loop contacts the H10 helix in the FtsZ protofilament interface; mutation of residues L178, A181, and F182 in this loop has previously been shown to block FtsZ polymerization and cell division (26,31). Additionally, this loop is connected to the H7 central core helix, which is thought to play an important role in nucleotide-dependent conformational changes (27). Based on the positioning of the H6/H7 loop at the protofilament interface, we propose that CbtA bound to the H6/H7 loop may act as a steric block of polymerization, preventing the addition of monomers to a growing FtsZ filament. This mechanism is consistent with published biochemical data showing that CbtA decreases GTPase activity and sedimentation of FtsZ (97). Residues in this loop region (L169 and R174) have also been implicated in FtsZ lateral interactions and bundling (67,68). Thus, it is also possible that the binding of CbtA to this loop may prevent the formation of stabilizing lateral interactions. Interestingly, it was recently proposed that the cognate antitoxin of CbtA, CbeA (or YeeU), neutralizes CbtA-mediated toxicity by promoting bundling of FtsZ filaments (105). However, one might predict that simply preventing bundling would make FtsZ protofilaments more dynamic, a model that does not fully agree with the reported GTPase activity decrease. Further *in vivo* and *in vitro* work is needed to elucidate the exact mechanism of CbtA-mediated inhibition of FtsZ. It would be especially interesting to monitor the appearance of FtsZ polymers *in vitro* with or without the addition of CbtA. The previously reported biochemical data and our suggested binding site at the longitudinal interface suggests that CbtA may abolish filament formation altogether. Assessment of whether or not CbtA inhibition requires GTP hydrolysis, as has been observed for MinC (75) and SulA (84), would also be informative. The H6/H7 loop is buried at the longitudinal interface and thus, CbtA may be able access this site only when FtsZ is a free monomer or in a relaxed, GDP-bound polymer. In addition to *in vitro* assembly experiments, another way to investigate whether GTP hydrolysis is necessary *in vivo* would be to assess the inhibitory effect of CbtA-R15C (which yields filamented cells when overproduced) in strains containing complementing *ftsZ* alleles with reduced GTPase activity. Several such alleles have been studied and are resistant to SulA and MinC (3).

Despite its importance in the formation of longitudinal, and potentially lateral, FtsZ interactions, the H6/H7 loop sequence is quite variable across different bacterial species (30).This low sequence similarity suggests that CbtA inhibition of cell division is limited to a very narrow species range, which correlates with its own limited distribution across bacterial taxa (CbtA is found only in species closely related to *E. coli*). Indeed, we found that CbtA was unable to interact with wild-type *B. subtilis* FtsZ. It would be an interesting exercise to use our bacterial two-hybrid system to assess CbtA-binding to a broader range of bacterial FtsZ proteins and further, to see if CbtA could be engineered to interact with additional FtsZ proteins. This could potentially allow for further refinement of our understanding of the sequence determinants involved in the CbtA-FtsZ interaction.

The H6/H7 loop represents a new inhibitory surface on FtsZ

As outlined in the introduction to this chapter, there are several known negative regulators of FtsZ, and several inhibitory interactions have been previously characterized (73,74,82,89). Based on genetic and structural studies, there seem to be two main FtsZ surfaces that are exploited by inhibitors: the conserved C-terminal (CTT) regulatory hub, which binds the C-terminal domain of MinC and SlmA (as well as several positive regulators), and the T7 loop/ H10 polymerization surface of the C-terminal domain. We believe the findings presented here represent the first description of a protein inhibitor binding within the N-terminal domain of FtsZ. While the exact mechanism of CbtA inhibition is not known, it is clear that binding to this new inhibitory surface leads to a potent block of cell division.

An active area of research in the FtsZ field is the elucidation of the roles played by the plus and minus ends of FtsZ polymers in assembly and disassembly. Redick et al. attempted to create FtsZ cappers by mutating residues in the plus end (near the GTP-binding site) and minus end (near the T7 loop) (31). They found that mutation of residues at the plus end was far less debilitating than mutation of residues at the minus end, suggesting polymer polarity opposite to that of microtubules (with FtsZ subunits primarily being added to the minus end of polymers and disassociation occurring at the plus end) (31). This model disagrees with that recently proposed in the MciZ study, which despite diverging from the eukaryotic paradigm, still designated the plus end as the major site of polymer assembly (89). Further study of how CbtA binding to the H6/H7 loop, which is located at the plus end of the polymer, affects FtsZ polymer assembly and disassembly could provide important insight into this polarity issue.

Chapter 3.4: Materials and Methods

Strains, plasmids, and growth conditions

A complete list of the bacterial strains used in this chapter is provided in Table A1.1 in Appendix I of this dissertation. Additionally, lists of the plasmids and oligonucleotides used in this chapter can be found in Tables A1.2 and A1.3 in Appendix I, respectively. All *B. subtilis* strains are derived from the prototrophic strain PY79 (106). NEB5-α F'I^q (New England Biolabs) was used as the cloning strain for all plasmid constructions outlined below. All two-hybrid studies were performed in FW102 O_L2-62 (107). *E. coli* strains were grown in LB (1% NaCl) broth at 37 ºC or 30 ºC or on LB plates supplemented with appropriate antibiotics at the following concentrations (unless otherwise noted): carbenicillin (Carb), 100 µg/mL; chloramphenicol (Cm), 25 µg/mL; kanamycin (Kan), 50 µg/mL; spectinomycin (Spec), 50 µg/mL. For microscopic observation, the *ftsZ-L169P* mutant was grown in M9 minimal medium (1 mM $MgSO_4$) supplemented with 0.4% maltose and 0.01% casamino acids at 30 ºC. *B. subtilis* strains were grown at 37 ºC in LB (0.5% or 1% NaCl) broth without antibiotic or on LB plates supplemented with spectinomycin (100 µg/mL) or MLS (mixture of 1 µg/mL erythromycin and 25 µg/mL lincomycin).

Construction of plasmids used in the bacterial two-hybrid system

All α fusion constructs were cloned by restriction digest into the parent plasmid pBRα-β flap; all λCI constructs were cloned by restriction digest into the parent plasmid pACλCI-β flap. Briefly, the parent plasmids were digested with NotI and BamHI to generate backbone. These backbones were ligated to relevant inserts generated by NotI/BamHI digestion of PCR products amplified using a NotI-containing forward primer and BamHI-containing reverse primer. Forward primers all contain an extra "A" base after the NotI site to maintain the reading frame. Reverse primers all encode a stop codon preceding the BamHI site. PCR template for these constructs was either a single colony of *E. coli* BW27785 or *B. subtilis* PY79 genomic DNA. Single point mutants (e.g. pBRα-FtsZ-D180K) were generated by overlap PCR with internal mutagenic primers (oDH239_F, oDH240_R) and NotI/BamHI-containing flanking primers (oDH70_F, oDH71_R). pBRα-FtsZΔ-66 and pBRα-FtsZ-D373G were generated from inserts amplified with forward primer oDH70_F and with reverse primers oDH279_R and oDH278_R, respectively. The insert of pACλCI-EcFtsZ$_{Bsloop}$ (pDH59) was generated by overlap PCR with internal primers (oDH84_R and oDH85_F) introducing BsFtsZ residues 169-183, and flanking primers oDH70_F and oDH71_R. The insert of pACλCI-BsFtsZ$_{Ecloop}$ (pDH66) was generated by overlap PCR with internal primers (oDH101_R and oDH102_F) introducing EcFtsZ residues 168-182, and flanking primers oDH86_F and oDH87_R. Oligonucleotides pBRα_F, pBRα_R, pACλCI_F, and pACλCI_R were used to sequence all two-hybrid constructs.

β-galactosidase assays

FW102 O$_L$2-62 was co-transformed with plasmids encoding the relevant α and λCI fusions. Cultures inoculated with transformants were grown in 1 mL LB (KanCmCarb) in deep-well 96-well plates at 37 ºC, 900 rpm, 90% humidity in a Multitron incubation shaker (Infors HT) overnight. Overnight cultures were back diluted 1:100 in LB (KanCmCarb) supplemented with the appropriate concentration of IPTG in sterile microtitre plates (total volume of 200 µL); subcultures were grown, shaking at 37 ºC until they reached mid-log phase (OD600 0.4- 0.8). A 100 µL aliquot of subculture was lysed by addition of 10 µL PopCulture reagent (Novagen) supplemented with rlysozyme (400 mU/µL). LacZ levels were determined by β-galactosidase assay performed in microtitre plates with a microtitre plate reader, as described in (108). All assays were done in triplicate and were repeated independently at least twice. All values shown in this chapter are from a single representative experiment and represent averages of triplicate measurements. Fold-change values were calculated by normalizing to the highest relevant empty vector control.

Genetic screen to identify amino acid substitutions in FtsZ that decrease the FtsZ-CbtA interaction

The E. coli *ftsZ* gene fragment was randomly mutagenized by PCR amplification of pBRα-FtsZ (pMT151) using*Taq* polymerase and the outside primers pBRα_F and pBRα_R. FW102 O$_L$2-62/ pACλCI-CbtA (pMT154) was transformed with a pool of plasmids encoding the resulting α-FtsZ mutants; transformants were plated on LB (KanCarbCm) indicator medium containing IPTG (5 µM) and X-gal (40 µg/mL). Plates were incubated overnight at 37 ºC. Several thousand colonies were screened to identify those exhibiting lower *lacZ* expression (white or light blue color) as compared to the dark blue colonies producing wild-type α-FtsZ and λCI-CbtA fusions; approximately 100 candidates were identified. The pBRα-FtsZ plasmid was isolated from these candidates and transformed into FW102 O_L2-62/ pACλCI-CbtA and FW102 O_L2-62/ pACλCI-FtsZ for assessment of their CbtA- and self-interactions by liquid β-galactosidase assay. Those candidates that exhibited at least a 60% decrease in interaction with CbtA but maintained greater than 75% self-interaction were sequenced and further assayed for their interaction with λCI-ZipA-CTD by liquid β-galactosidase assay.

Genetic screen to identify compensatory substitutions in CbtA that restore interaction with FtsZ-D180K

The *cbtA* gene (encoded on pACλCI-CbtA) was randomly mutagenized by PCR amplification with *Taq* polymerase using the outside primers pACλCI_F and pACλCI_R. A pool of plasmids encoding the resulting plasmids was transformed into FW102 O_L2-62 pre-transformed with pBRα-FtsZ-D180K, and transformants were plated on LB (KanCmCarb) indicator medium supplemented with IPTG (5 μM), X-gal (40 μg/mL), and TPEG (250 μM). Plates were incubated at 30 ºC overnight. Several thousand colonies were screened in order to identify those that exhibited increased *lacZ* expression as compared to the pale blue control colonies producing wild-type λCI-CbtA and α-FtsZ-D180K. Dark blue candidate colonies were pooled into a single overnight culture, grown at 30 ºC. In order to identify those candidates that specifically interact with α-FtsZ-D180K, a pooled plasmid prep generated from this overnight culture was transformed into FW102 O_L2-62/pBRα-FtsZ. Transformants were plated on the same indicator medium as before; pale blue candidates were selected and the pACλCI-CbtA plasmids were isolated and sequenced. The interaction between λCI-CbtA-V48E and all relevant α-FtsZ fusions was assayed by liquid β-galactosidase assay.

Integration of *ftsZ-L169P* at chromosomal *ftsZ* locus

The *ftsZ-L169P*, *ftsZ-D180N*, *ftsZ-S177P* alleles were cloned into pCX41 (digested with HindIII/ClaI) in place of wild-type *ftsZ* by restriction digest (HindIII/ClaI) and ligation of overlap PCR products generated using wild-type pCX41 as template, internal mutagenic primers (oDH34_F and oDH35_R for L169P) and flanking primers oDH36_F, oDH37_R, which anneal within *ftsA* and *lpxC*, respectively. This generated plasmids pDH35 (L169P), pDH33 (D180N), and pDH34 (S177P), replication of which is controlled by a temperature-sensitive origin of replication. Plasmid is maintained at 30 ºC and lost at 42 ºC. Attempted integration of these mutant alleles into the endogenous chromosomal locus was performed essentially as described in (109). Briefly, these plasmids were transformed into *E. coli* strain BW27785 in parallel with a pCX41 derivative encoding FtsZ-F268C (generous gift of H. Cho and T. Bernhardt). *ftsZ-F268C* is a known complementing allele and thus serves as a control for chromosomal integration. Transformants were plated on LB agar supplemented with Cm (10 µg/mL) and incubated overnight at 30 ºC. Several colonies were restreaked onto LB (Cm) and incubated at 42 ºC overnight in order to identify single crossover integrants. After an additional round of restreaking on LB (Cm) at the nonpermissive temperature, candidates were streaked onto LB (Cm) and incubated at 30 ºC overnight. Firing of the plasmid origin of replication on the chromosome causes a severe growth defect, and double crossover integrants that had looped out the plasmid were identified as healthy revertants within poorly growing streaks. These candidates were purified by restreaking, and were cured of plasmid by growth on LB (without Cm) at 42 ºC. The *ftsZ* locus was PCR amplified and sequenced (using sequencing primers generously provided by H. Cho and T. Bernhardt) from Cm-sensitive candidates in order to identify those in which allelic replacement occurred. Only *ftsZ-L169P* (as well as the *ftsZ-F286C* control) was successfully obtained. All subsequent propagation of this strain was done at RT or 30 ºC to minimize growth defects. Multiple isolates of this strain exhibited identical phenotypes.

Construction of *B. subtilis ftsZ* chimera strains

B. subtilis strains were generated by directly transforming a PY79 derivative with either a linearized plasmid containing homology to the chromosomal locus where integration was desired or a PCR fragment containing chromosomal homology. In order to generate *B. subtilis* strains with *gfp* or various *cbtA* alleles integrated into the chromosome, plasmids pDH84 (*pHYPERSPANK-his*$_6$*-gfp*), pDH85 (*pHYPERSPANK -his*$_6$*-cbtA-gfp),* and pDH102 (*pHYPERSPANK -his*$_6$*-cbtA-F65S-gfp)* were constructed. These plasmids were generated by restriction digest (HindIII/NheI) and ligation of PCR products amplified from pMT136 (see Chapter 2), pMT139, or pMT146 (see Chapter 2) using primers oDH108_R and oDH116_F into QER167 (generous gift of D. Rudner) HindIII/NheI digested backbone. These plasmids all contain homology to the *ycgO* locus flanking the insert. Plasmids were linearized by digestion with ScaI. DH84 (*ycgO:: pHYPERSPANK -his*$_6$*-gfp erm*), DH85 (*ycgO:: pHYPERSPANK -his*$_6$*-cbtA-gfp erm*), and

DH104 (*ycgO:: pHYPERSPANK -his$_6$-cbtA-F65S-gfp erm)* were generated by transformation of linearized plasmids pDH84, pDH85, and pDH102, respectively, into PY79 *ycgO::spec.* Transformants were selected on LB supplemented with MLS.

The wild-type *ftsZ* allele linked to a spec resistance cassette was assembled by Gibson assembly (110) of three PCR products with >20bp of overlapping homology: 1) part of the *ftsA* locus and the entire *ftsZ* locus amplified from PY79 genomic DNA using oligos oDH130_F and oDH131_R, 2) amplification of *spec* from pDR111 using oDH132_F and oDH133_R, and 3) 2 kb chromosomal sequence downstream of the *ftsZ* locus amplified from PY79 genomic DNA using oligos oDH134_F and oDH135_R. This assembled PCR product was transformed directly into PY79 to generate strain DH98. Transformants were selected for on LB (Spec).

The chimeric *ftsZ* allele (containing *E. coli ftsZ* residues 169-182) linked to a spec resistance cassette, was assembled by Gibson assembly of three PCR products (all with at least 20 bp of overlapping homology: 1) 2 kb upstream of *ftsZ* amplified from PY79 genomic DNA using oligos ODH141 and ODH142, 2) the *ftsZ* chimeric allele amplified from pDH69 (Ecloop chimera) using oligos oDH143_F and oDH131_R 3) 2 kb downstream of *ftsZ*, including *spec*, amplified from DH98 genomic DNA using oDH132_F. This assembled PCR product was transformed directly into PY79 to generate strain DH99. Transformants were selected for on LB (Spec). The *ftsZ* loci from DH98 and DH99 were PCR amplified (using oDH167_F and oDH168_R) and sequenced using oDH127_F, oDH172_F, and oDH173_F. oDH124_F and oDH125, which anneal inside the *ftsZ* ORF were also used for PCR and sequencing; in some instances it was found that candidate DH99 isolates had maintained a second wild-type copy of *ftsZ* somewhere on the chromosome. These could be distinguished from correct isolates by the appearance of double peaks on oDH124/oDH125 sequencing reads.

Strains DH100, DH101, and DH105 were generated by direct transformation of DH98 genomic DNA into strains DH84, DH85, and DH104, respectively. Strains DH102, DH103, and DH106 were generated by direct transformation of DH99 genomic DNA into DH84, DH85, and DH104, respectively. Transformants were selected on LB (Spec) and patched on LB (MLS) to ensure the *ycgO* locus was unchanged. The *ftsZ* loci were re-sequenced after transformation. Strains DH99, DH102, DH103, and DH106 were quite sick compared to the other *B. subtilis* strains. Colony size was greatly reduced and cells grown in broth tended to form large clumps. Growth at lower temperature did not seem to rescue these growth defects.

Microscopic observation of CbtA-mediated morphology changes in *ftsZ-L169P*

pMT139 was transformed into either wild-type BW27785 or DH73 (*ftsZ-L169P*); transformants were plated on LB (Cm) and incubated overnight at 30 ºC. Overnight cultures were set up in M9 maltose supplemented with Cm and incubated at 30 ºC. Once these cultures reached an OD600 ~2 (about 24 hrs), a 1:3,000 back dilution was made into fresh M9 medium; cultures were incubated at 30 ºC for 14-16 hrs, resulting in a typical OD600 of 0.1. *cbtA* expression was induced with 100 µM IPTG at 30 ºC for 8 hrs. After 8 hrs, cells were mounted on 2% agarose pads, and phase contrast microscopy was performed using an Olympus BX61 microscope (objective UplanF1 100x). Images were captured with a monochrome CoolSnapHQ digital camera (Photometrics) using Metamorph software version 6.1 (Universal Imaging). Images were cropped and adjusted in ImageJ (111). Cell roundness quantification was done manually in ImageJ with the ObjectJ plugin. Briefly, the length of the cell was measured along the long axis, and the width was measured as the axis roughly perpendicular to the long axis. Angle measurements were spot-checked to ensure the axes intersected at an angle close to 90º. Cell roundness data were compiled from three independent experiments; 200-300 cells of each strain from each independent experiment were measured.

Assessment of CbtA toxicity in *B. subtilis*

For spot dilution analysis, relevant strains were streaked from glycerol stocks onto LB supplemented with 100 µg/mL spectinomycin and incubated at 37 ºC overnight followed by additional overnight incubation at RT. LB cultures were inoculated with single colonies, which were grown at 37 ºC until they reached an OD600 ~1. Cultures were normalized by OD600 value, and 1:10 serial dilutions were made in fresh LB in a microtitre plate. 5 µL of each dilution was spotted on LB agar supplemented with 100 µg/mL spectinomycin and LB agar supplemented with 100 µg/mL spectinomycin and 1 mM IPTG. Plates were incubated overnight at 37 ºC. Spot dilution analysis was done on both LB Miller (1% NaCl) and LB Lennox (0.5%) agar with identical results.

For growth curves, 5 mL LB cultures were inoculated with single colonies of relevant strains. Several dilutions of these cultures were made and grown with shaking at RT overnight. The next day, cultures that were in early to mid-log phase were back diluted to a starting OD600 of 0.01 in 5 mL fresh LB medium supplemented with 1 mM IPTG. Growth was monitored by taking OD600 measurements using a plate reader roughly every 30-60 min. All growth curves were done in triplicate and repeated independently several times.

Western blot analysis was performed on whole-cell lysates generated from growth curve cultures. Briefly, cultures were resuspended in lysis buffer (20 mM Tris-HCl pH 7.5, 50 mM EDTA, 100 mM NaCl) supplemented with 1 μL rlysozyme (30 kU/μL) and 1 μL Omnicleave (200 U/μL) to normalize for OD600 (OD600 of 1 = 100 μL lysis buffer) and lysed for 30 min at 37 ºC. An equal volume of 2x Laemmli dye was added to the lysates; any additional dilutions were made in 1x Laemmli dye. Standard SDS-PAGE and Western blot techniques were used. An anti-His_6 (Genscript) antibody was used to detect His_6-CbtA-GFP, and SigA and Spo0J (detected with anti-SigA and anti-Spo0J antibodies, respectively; generous gifts of D. Rudner) were used as loading controls. Spo0J and His_6-CbtA-GFP were blotted for on the same membrane; thus Spo0J serves as an especially relevant internal loading control.

Chapter 3.5: References

1. Lutkenhaus J, Pichoff S, Du S. Bacterial cytokinesis: From Z ring to divisome. Robinson DN, Bement WM, Balasubramanian MK, Sanger JW, editors. Cytoskeleton. 2012 Aug 30;69(10):778–90.

2. de Boer PA. Advances in understanding E. coli cell fission. Current Opinion in Microbiology. 2010 Dec;13(6):730–7.

3. Erickson HP, Anderson DE, Osawa M. FtsZ in Bacterial Cytokinesis: Cytoskeleton and Force Generator All in One. Microbiology and Molecular Biology Reviews. 2010 Nov 30;74(4):504–28.

4. Huang KH, Durand-Heredia J, Janakiraman A. FtsZ Ring Stability: of Bundles, Tubules, Crosslinks, and Curves. J Bacteriol. 2013 Apr 9;195(9):1859–68.

5. Typas A, Banzhaf M, Gross CA, Vollmer W. From the regulation of peptidoglycansynthesis to bacterial growth andmorphology. Nat Rev Micro. Nature Publishing Group; 2011 Dec 28;10(2):123–36.

6. Weart RB, Levin PA. Growth Rate-Dependent Regulation of Medial FtsZ Ring Formation. J Bacteriol. 2003 May 1;185(9):2826–34.

7. Romberg L, Levin PA. A SSEMBLYD YNAMICS OF THEB ACTERIALC ELLD IVISIONP ROTEINF TSZ: Poised at the Edge of Stability. Annu Rev Microbiol. 2003 Oct;57(1):125–54.

8. Nogales E, Downing KH, Amos LA, Löwe J. Tubulin and FtsZ form a distinct family of GTPases. Nat Struct Biol. 1998 Jun;5(6):451–8.

9. Erickson HP. Evolution of the cytoskeleton. Bioessays. 2007;29(7):668–77.

10. Vaughan S, Wickstead B, Gull K, Addinall SG. Molecular Evolution of FtsZ Protein Sequences Encoded Within the Genomes of Archaea, Bacteria, and Eukaryota. Journal of Molecular Evolution. 2004 Jan 1;58(1):19–29.

11. Oliva MA, Cordell SC, Lowe J. Structural insights into FtsZ protofilament formation. Nat Struct Mol Biol. 2004 Nov 21;11(12):1243–50.

12. Löwe J, Amos LA. Crystal structure of the bacterial cell-division protein FtsZ. Nature. 1998.

13. Osawa M. Probing the domain structure of FtsZ by random truncation and insertion of GFP. Microbiology. 2005 Dec 1;151(12):4033–43.

14. Mosyak L, Zhang Y, Glasfeld E, Haney S, Stahl M, Seehra J, et al. The bacterial cell-division protein ZipA and its interaction with an FtsZ fragment revealed by X-ray crystallography. EMBO J. 2000 Jul 3;19(13):3179–91.

15. Buske PJ, Levin PA. A flexible C-terminal linker is required for proper FtsZ assembly in vitroand cytokinetic ring formation in vivo. Mol Microbiol. 2013 Jun 10;89(2):249–63.

16. Gardner KAJA, Moore DA, Erickson HP. The C-terminal linker of Escherichia coli FtsZ functions as an intrinsically disordered peptide. Mol Microbiol. 2013 Jun 17;89(2):264–75.

17. Szwedziak P, Wang Q, Freund SM, we JLO. FtsA forms actin-like protofilaments. EMBO J. Nature Publishing Group; 2012 Mar 30;31(10):2249–60.

18. Du S, Lutkenhaus J. SlmA Antagonism of FtsZ Assembly Employs a Two-pronged Mechanism like MinCD. Søgaard-Andersen L, editor. PLoS Genet. 2014 Jul 31;10(7):e1004460.

19. Król E, van Kessel SP, van Bezouwen LS, Kumar N, Boekema EJ, Scheffers D-J. Bacillus subtilis SepF binds to the C-terminus of FtsZ. PLoS ONE. 2012;7(8):e43293.

20. Szwedziak P, Wang Q, Freund SM, we JLO. FtsA forms actin-like protofilaments. EMBO J. Nature Publishing Group; 2012 Mar 30;31(10):2249–60.

21. Schumacher MA, Zeng W. Structures of the nucleoid occlusion protein SlmA bound to DNA and the C-terminal domain of the cytoskeletal protein FtsZ. Proc Natl Acad Sci USA. 2016 May 3;113(18):4988–93.

22. Buske PJ, Levin PA. Extreme C terminus of bacterial cytoskeletal protein FtsZ plays fundamental role in assembly independent of modulatory proteins. Journal of Biological Chemistry. 2012 Mar 30;287(14):10945–57.

23. Buske PJ, Mittal A, Pappu RV, Levin PA. Seminars in Cell & Developmental Biology. Seminars in Cell and Developmental Biology. Elsevier Ltd; 2015 Jan 1;37:3–10.

24. Romberg L, Simon M, Erickson HP. Polymerization of FtsZ, a Bacterial Homolog of Tubulin. IS ASSEMBLY COOPERATIVE? Journal of Biological Chemistry. 2001 Jan 4;276(15):11743–53.

25. Adams DW, Errington J. Bacterial cell division: assembly, maintenance and disassembly of the Z ring. Nat Rev Micro. 2009 Sep;7(9):642–53.

26. Li Y, Hsin J, Zhao L, Cheng Y, Shang W, Huang KC, et al. FtsZ protofilaments use a hinge-opening mechanism for constrictive force generation. Science. American Association for the Advancement of Science; 2013;341(6144):392–5.

27. Matsui T, Han X, Yu J, Yao M, Tanaka I. Structural Change in FtsZ Induced by Intermolecular Interactions between Bound GTP and the T7 Loop. Journal of Biological Chemistry. 2014 Feb 7;289(6):3501–9.

28. Li Y, Hsin J, Zhao L, Cheng Y, Shang W, Huang KC, et al. FtsZ Protofilaments Use a Hinge-Opening Mechanism for Constrictive Force Generation. Science. 2013 Jul 25;341(6144):392–5.

29. Matsui T, Yamane J, Mogi N, Yamaguchi H, Takemoto H, Yao M, et al. Structural reorganization of the bacterial cell-division protein FtsZ from Staphylococcus aureus. Acta Crystallogr D Biol Crystallogr. 2012 Sep;68(Pt 9):1175–88.

30. Hsin J, Gopinathan A. Nucleotide-dependent conformations of FtsZ dimers and force generation observed through molecular dynamics simulations. 2012.

31. Redick SD, Stricker J, Briscoe G, Erickson HP. Mutants of FtsZ Targeting the Protofilament Interface: Effects on Cell Division and GTPase Activity. J Bacteriol. 2005 Apr 1;187(8):2727–36.

32. Huecas S, Andreu JM. Polymerization of nucleotide-free, GDP- and GTP-bound cell division protein FtsZ: GDP makes the difference. FEBS Letters. 2004 Jun 7;569(1-3):43–8.

33. Lu C, Reedy M, Erickson HP. Straight and curved conformations of FtsZ are regulated by GTP hydrolysis. J Bacteriol. 2000 Jan;182(1):164–70.

34. Huecas S, Andreu JM. Energetics of the Cooperative Assembly of Cell Division Protein FtsZ and the Nucleotide Hydrolysis Switch. Journal of Biological Chemistry. 2003 Nov 14;278(46):46146–54.

35. Tan CM, Therien AG, Lu J, Lee SH, Caron A, Gill CJ, et al. Restoring methicillin-resistant Staphylococcus aureus susceptibility to β-lactam antibiotics. Sci Transl Med. 2012 Mar 21;4(126):126ra35.

36. Martin-Galiano AJ, Buey RM, Cabezas M, Andreu JM. Mapping Flexibility and the Assembly Switch of Cell Division Protein FtsZ by Computational and Mutational Approaches. Journal of Biological Chemistry. 2010 Jul 9;285(29):22554–65.

37. Erickson HP, Taylor DW, Taylor KA, Bramhill D. Bacterial cell division protein FtsZ assembles into protofilament sheets and minirings, structural homologs of tubulin polymers. Proc Natl Acad Sci USA. 1996 Jan 9;93(1):519–23.

38. Geissler B, Shiomi D, Margolin W. The ftsA* gain-of-function allele of Escherichia coli and its effects on the stability and dynamics of the Z ring. Microbiology. 2007 Mar 1;153(3):814–25.

39. Mohammadi T, Ploeger GEJ, Verheul J, Comvalius AD, Martos A, Alfonso C, et al. The GTPase

Activity of Escherichia coliFtsZ Determines the Magnitude of the FtsZ Polymer Bundling by ZapA in Vitro. Biochemistry. 2009 Nov 24;48(46):11056–66.

40. Bi E, Lutkenhaus J. FtsZ ring structure associated with division in Escherichia coli. Nature. 1991.

41. Ben-Yehuda S, Losick R. Asymmetric cell division in B. subtilis involves a spiral-like intermediate of the cytokinetic protein FtsZ. Cell. 2002.

42. Thanedar S, Margolin W. FtsZ Exhibits Rapid Movement and Oscillation Waves in Helix-like Patterns in Escherichia coli. Current Biology. 2004 Jul;14(13):1167–73.

43. Peters PC, Migocki MD, Thoni C, Harry EJ. A new assembly pathway for the cytokinetic Z ring from a dynamic helical structure in vegetatively growing cells of Bacillus subtilis. Mol Microbiol. 2007 Apr 17;64(2):487–99.

44. Ma X, Ehrhardt DW, Margolin W. Colocalization of cell division proteins FtsZ and FtsA to cytoskeletal structures in living Escherichia coli cells by using green fluorescent protein. Proc Natl Acad Sci USA. 1996 Nov 12;93(23):12998–3003.

45. Anderson DE, Gueiros-Filho FJ, Erickson HP. Assembly Dynamics of FtsZ Rings in Bacillus subtilis and Escherichia coli and Effects of FtsZ-Regulating Proteins. J Bacteriol. 2004 Aug 18;186(17):5775–81.

46. Meier EL, Goley ED. ScienceDirectForm and function of the bacterial cytokinetic ring. Current Opinion in Cell Biology. Elsevier Ltd; 2014 Feb 1;26:19–27.

47. Biteen JS, Goley ED, Shapiro L, Moerner WE. Three-Dimensional Super-Resolution Imaging of the Midplane Protein FtsZ in Live Caulobacter crescentusCells Using Astigmatism. ChemPhysChem. 2012 Jan 20;13(4):1007–12.

48. Strauss MP, Liew ATF, Turnbull L, Whitchurch CB, Monahan LG, Harry EJ. 3D-SIM Super Resolution Microscopy Reveals a Bead-Like Arrangement for FtsZ and the Division Machinery: Implications for Triggering Cytokinesis. Amos L, editor. PLoS Biol. 2012 Sep 11;10(9):e1001389.

49. Fu G, Huang T, Buss J, Coltharp C, Hensel Z, Xiao J. In Vivo Structure of the E. coli FtsZ-ring Revealed by Photoactivated Localization Microscopy (PALM). Polymenis M, editor. PLoS ONE. 2010 Sep 13;5(9):e12680.

50. Rowlett VW, Margolin W. Biophysical Letter. Biophysj. Biophysical Society; 2014 Oct 21;107(8):L17–L20.

51. Si F, Busiek K, Margolin W, Sun SX. Organization of FtsZ Filaments in the Bacterial Division Ring Measuredfrom Polarized Fluorescence Microscopy. Biophysj. Biophysical Society; 2013

Nov 5;105(9):1976–86.

52. Li Z, Trimble MJ, Brun YV, Jensen GJ. The structure of FtsZ filaments in vivo suggests a force-generating role in cell division. EMBO J. 2007 Nov 14;26(22):4694–708.

53. Pichoff S, Lutkenhaus J. Unique and overlapping roles for ZipA and FtsA in septal ring assembly in Escherichia coli. EMBO J. 2002 Feb 15;21(4):685–93.

54. Hale CA, de Boer PA. Direct binding of FtsZ to ZipA, an essential component of the septal ring structure that mediates cell division in E. coli. Cell. 1997 Jan 24;88(2):175–85.

55. Wang X, Huang J, Mukherjee A, Cao C, Lutkenhaus J. Analysis of the interaction of FtsZ with itself, GTP, and FtsA. J Bacteriol. 1997 Sep;179(17):5551–9.

56. Pichoff S, Lutkenhaus J. Tethering the Z ring to the membrane through a conserved membrane targeting sequence in FtsA. Mol Microbiol. 2005 Feb 4;55(6):1722–34.

57. van den Ent F, Löwe J. Crystal structure of the cell division protein FtsA from Thermotoga maritima. EMBO J. 2000 Oct 16;19(20):5300–7.

58. Ohashi T, Hale CA, de Boer PAJ, Erickson HP. Structural Evidence that the P/Q Domain of ZipA Is an Unstructured, Flexible Tether between the Membrane and the C-Terminal FtsZ-Binding Domain. J Bacteriol. 2002 Aug 1;184(15):4313–5.

59. Geissler B, Elraheb D, Margolin W. A gain-of-function mutation in ftsA bypasses the requirement for the essential cell division gene zipA in Escherichia coli. Proc Natl Acad Sci USA. 2003 Apr 1;100(7):4197–202.

60. Pichoff S, Shen B, Sullivan B, Lutkenhaus J. FtsA mutants impaired for self-interaction bypass ZipA suggesting a model in which FtsA's self-interaction competes with its ability to recruit downstream division proteins. Mol Microbiol. 2011 Nov 29;83(1):151–67.

61. RayChaudhuri D. ZipA is a MAP–Tau homolog and is essential for structural integrity of the cytokinetic FtsZ ring during bacterial cell division. EMBO J. 1999.

62. Durand-Heredia J, Rivkin E, Fan G, Morales J, Janakiraman A. Identification of ZapD as a Cell Division Factor That Promotes the Assembly of FtsZ in Escherichia coli. J Bacteriol. 2012 May 24;194(12):3189–98.

63. Schumacher MA, Zeng W, Huang K-H, Tchorzewski L, Janakiraman A. Structural and Functional Analyses Reveal Insights into the Molecular Properties of the Escherichia coliZ Ring Stabilizing Protein, ZapC. Journal of Biological Chemistry. 2016 Jan 29;291(5):2485–98.

64. Dajkovic A, Pichoff S, Lutkenhaus J, Wirtz D. Cross-linking FtsZ polymers into coherent Z rings. Mol Microbiol. 2010 Sep 20;78(3):651–68.

65. Galli E, Gerdes K. FtsZ-ZapA-ZapB Interactome of Escherichia coli. J Bacteriol. 2011 Dec 29;194(2):292–302.

66. Buss J, Coltharp C, Huang T, Pohlmeyer C, Wang S-C, Hatem C, et al. In vivoorganization of the FtsZ-ring by ZapA and ZapB revealed by quantitative super-resolution microscopy. Mol Microbiol. 2013 Aug 14;89(6):1099–120.

67. Koppelman C-M, Aarsman MEG, Postmus J, Pas E, Muijsers AO, Scheffers D-J, et al. R174 of Escherichia coli FtsZ is involved in membrane interaction and protofilament bundling, and is essential for cell division. Mol Microbiol. 2003 Dec 16;51(3):645–57.

68. Haeusser DP, Rowlett VW, Margolin W. A mutation in Escherichia coli ftsZbypasses the requirement for the essential division gene zipAand confers resistance to FtsZ assembly inhibitors by stabilizing protofilament bundling. Mol Microbiol. 2015 Jul 4;:n/a–n/a.

69. Lutkenhaus J. Assembly Dynamics of the Bacterial MinCDE System and Spatial Regulation of the Z Ring. Annu Rev Biochem. 2007 Jun 7;76(1):539–62.

70. Raskin DM, de Boer PA. Rapid pole-to-pole oscillation of a protein required for directing division to the middle of Escherichia coli. Proc Natl Acad Sci USA. 1999 Apr 27;96(9):4971–6.

71. Ivanov V, Mizuuchi K. Multiple modes of interconverting dynamic pattern formation by bacterial cell division proteins. Proc Natl Acad Sci USA. 2010 May 4;107(18):8071–8.

72. de Boer PA, Crossley RE, Rothfield LI. Isolation and properties of minB, a complex genetic locus involved in correct placement of the division site in Escherichia coli. J Bacteriol. 1988 May;170(5):2106–12.

73. Shen B, Lutkenhaus J. The conserved C-terminal tail of FtsZ is required for the septal localization and division inhibitory activity of MinC(C)/MinD. Mol Microbiol. 2009 Apr;72(2):410–24.

74. Shen B, Lutkenhaus J. Examination of the interaction between FtsZ and MinC Nin E. colisuggests how MinC disrupts Z rings. Mol Microbiol. 2010 Mar;75(5):1285–98.

75. Dajkovic A, Lan G, Sun SX, Wirtz D, Lutkenhaus J. MinC Spatially Controls Bacterial Cytokinesis by Antagonizing the Scaffolding Function of FtsZ. Current Biology. 2008 Feb;18(4):235–44.

76. Jaffé A, Boye E, D'Ari R. Rule governing the division pattern in Escherichia coli minB and wild-type filaments. J Bacteriol. 1990 Jun;172(6):3500–2.

77. Wu LJ, Errington J. Coordination of cell division and chromosome segregation by a nucleoid occlusion protein in Bacillus subtilis. Cell. 2004 Jun 25;117(7):915–25.

78. Adams DW, Wu LJ, Errington J. Nucleoid occlusion protein Noc recruits DNA to the bacterial cell membrane. EMBO J. 2015 Feb 11;34(4):491–501.

79. Bernhardt TG, de Boer PAJ. SlmA, a Nucleoid-Associated, FtsZ Binding Protein Required for Blocking Septal Ring Assembly over Chromosomes in E. coli. Molecular Cell. 2005 May;18(5):555–64.

80. Cho H, McManus HR, Dove SL, Bernhardt TG. Nucleoid occlusion factor SlmA is a DNA-activated FtsZ polymerization antagonist. Proc Natl Acad Sci USA. 2011 Mar 1;108(9):3773–8.

81. Huisman O, D'Ari R, Gottesman S. Cell-division control in Escherichia coli: specific induction of the SOS function SfiA protein is sufficient to block septation. Proc Natl Acad Sci USA. 1984 Jul;81(14):4490–4.

82. Cordell SC, Robinson EJH, Lowe J. Crystal structure of the SOS cell division inhibitor SulA and in complex with FtsZ. Proc Natl Acad Sci USA. 2003 Jun 24;100(13):7889–94.

83. Bi E, Lutkenhaus J. Cell division inhibitors SulA and MinCD prevent formation of the FtsZ ring. J Bacteriol. 1993 Feb;175(4):1118–25.

84. Dajkovic A, Mukherjee A, Lutkenhaus J. Investigation of Regulation of FtsZ Assembly by SulA and Development of a Model for FtsZ Polymerization. J Bacteriol. 2008 Mar 16;190(7):2513–26.

85. Trusca D, Scott S, Thompson C, Bramhill D. Bacterial SOS checkpoint protein SulA inhibits polymerization of purified FtsZ cell division protein. J Bacteriol. 1998 Aug;180(15):3946–53.

86. Chen Y, Milam SL, Erickson HP. SulA Inhibits Assembly of FtsZ by a Simple Sequestration Mechanism. Biochemistry. 2012 Apr 10;51(14):3100–9.

87. Dai K, Mukherjee A, Xu Y, Lutkenhaus J. Mutations in ftsZ that confer resistance to SulA affect the interaction of FtsZ with GTP. J Bacteriol. 1994 Jan;176(1):130–6.

88. Handler AA, Lim JE, Losick R. Peptide inhibitor of cytokinesis during sporulation in Bacillus subtilis. Mol Microbiol. 2008 May;68(3):588–99.

89. Bisson-Filho AW, Discola KF, Castellen P, Blasios V, Martins A, Sforça ML, et al. FtsZ filament capping by MciZ, a developmental regulator of bacterial division. Proc Natl Acad Sci USA. 2015 Apr 6;:201414242.

90. Hernandez-Rocamora VM, Alfonso C, Margolin W, Zorrilla S, Rivas G. Evidence that bacteriophage λ Kil peptide inhibits bacterial cell division by disrupting FtsZ protofilaments and sequestering protein subunits. Journal of Biological Chemistry. 2015 Jun 29;:jbc.M115.653329.

91. Haeusser DP, Hoashi M, Weaver A, Brown N, Pan J, Sawitzke JA, et al. The Kil Peptide of Bacteriophage λ Blocks Escherichia coli Cytokinesis via ZipA-Dependent Inhibition of FtsZ Assembly. Kearns DB, editor. PLoS Genet. 2014 Mar 20;10(3):e1004217.

92. Kiro R, Molshanski-Mor S, Yosef I, Milam SL, Erickson HP, Qimron U. Gene product 0.4 increases bacteriophage T7 competitiveness by inhibiting host cell division. Proc Natl Acad Sci USA. 2013 Nov 26;110(48):19549–54.

93. Sass P, Brötz-Oesterhelt H. Bacterial cell division as a target for new antibiotics. Current Opinion in Microbiology. Elsevier Ltd; 2013 Oct 1;16(5):522–30.

94. Li X, Ma S. European Journal of Medicinal Chemistry. European Journal of Medicinal Chemistry. Elsevier Masson SAS; 2015 May 5;95(C):1–15.

95. Haydon DJ, Stokes NR, Ure R, Galbraith G, Bennett JM, Brown DR, et al. An Inhibitor of FtsZ with Potent and Selective Anti-Staphylococcal Activity. Science. 2008 Sep 19;321(5896):1673–5.

96. Adams DW, Wu LJ, Errington J. A benzamide-dependent ftsZmutant reveals residues crucial for Z-ring assembly. Mol Microbiol. 2015 Nov;:n/a–n/a.

97. Tan Q, Awano N, Inouye M. YeeV is an Escherichia coli toxin that inhibits cell division by targeting the cytoskeleton proteins, FtsZ and MreB. Mol Microbiol. 2011 Jan;79(1):109–18.

98. Haney SA, Glasfeld E, Hale C, Keeney D, He Z, de Boer P. Genetic Analysis of the Escherichia coli FtsZ{middle dot}ZipA Interaction in the Yeast Two-hybrid System. CHARACTERIZATION OF FtsZ RESIDUES ESSENTIAL FOR THE INTERACTIONS WITH ZipA AND WITH FtsA. Journal of Biological Chemistry. 2001 Jan 16;276(15):11980–7.

99. Liu Z, Mukherjee A, Lutkenhaus J. Recruitment of ZipA to the division site by interaction with FtsZ. Mol Microbiol. 1999 Mar;31(6):1853–61.

100. van den Ent F, Izoré T, Bharat TA, Johnson CM, Lowe J. Bacterial actin MreB forms antiparallel double filaments. eLife. 2014;3:e02634.

101. Salje J, van den Ent F, de Boer P, Lowe J. Direct Membrane Binding by Bacterial Actin MreB. Molecular Cell. Elsevier Inc; 2011 Aug 5;43(3):478–87.

102. Volkmer B, Heinemann M. Condition-Dependent Cell Volume and Concentration of Escherichia

coli to Facilitate Data Conversion for Systems Biology Modeling. Langowski J, editor. PLoS ONE. 2011 Jul 29;6(7):e23126.

103. Brown JM, Shaw KJ. A novel family of Escherichia coli toxin-antitoxin gene pairs. J Bacteriol. 2003 Nov;185(22):6600–8.

104. Fenton AK, Gerdes K. Direct interaction of FtsZ and MreB is required for septum synthesis and cell division in Escherichia coli. EMBO J. 2013 Jun 11;32(13):1953–65.

105. Masuda H, Tan Q, Awano N, Wu K-P, Inouye M. YeeU enhances the bundling of cytoskeletal polymers of MreB and FtsZ, antagonizing the CbtA (YeeV) toxicity in Escherichia coli. Mol Microbiol. 2012 May 17;84(5):979–89.

106. Youngman PJ, Perkins JB, Losick R. Genetic transposition and insertional mutagenesis in Bacillus subtilis with Streptococcus faecalis transposon Tn917. Proc Natl Acad Sci USA. 1983 Apr;80(8):2305–9.

107. Deaconescu AM, Chambers AL, Smith AJ, Nickels BE, Hochschild A, Savery NJ, et al. Structural Basis for Bacterial Transcription-Coupled DNA Repair. Cell. 2006 Feb;124(3):507–20.

108. Thibodeau SA, Fang R, Joung JK. High-throughput beta-galactosidase assay for bacterial cell-based reporter systems. BioTechniques. 2004 Mar;36(3):410–5.

109. Wang XD, de Boer P, Rothfield LI. A factor that positively regulates cell division by activating transcription of the major cluster of essential cell division genes of Escherichia coli. EMBO J. 1991.

110. Gibson DG, Young L, Chuang R-Y, Venter JC, Hutchison CA, Smith HO. Enzymatic assembly of DNA molecules up to several hundred kilobases. Nat Meth. 2009 Apr 12;6(5):343–5.

111. Schneider CA, Rasband WS, Eliceiri KW. NIH Image to ImageJ: 25 years of image analysis. Nat Meth. Nature Publishing Group; 2012 Jul 1;9(7):671–5.

Chapter 4: Genetic evidence suggests CbtA may interact with the MreB double filament interface

Attributions: I conducted all experimental work presented in this chapter under the guidance of my advisor, Ann Hochschild. I wrote this chapter in its entirety with editorial assistance from Ann Hochschild. I would like to thank Tom Bernhardt and members of the Bernhardt lab for several strains and constructs used in this chapter.

Chapter 4.1: The enigmatic MreB filament and its role in cell elongation

In the vast majority of bacteria, cell shape is determined by a rigid sacculus composed of peptidoglycan strands crosslinked by short peptides (1). The ability of this mesh-like structure to provide cells with mechanical stability while still allowing for dynamic cell growth and faithful propagation requires the precise spatiotemporal coordination of a diverse set of enzymes across multiple layers of the cell envelope. In rod-shaped organisms, such as *E. coli*, *B. subtilis*, and *C. crescentus*, sacculus growth is the result of two distinct modes of cell wall synthesis: elongation of the cylindrical sidewall by incorporation of newly synthesized peptidoglycan strands at multiple sites, followed by construction of the septal wall, which allows for separation of daughter cells (reviewed in (2,3)). As discussed in Chapter 3 of this dissertation, this latter process is controlled by the tubulin homolog, FtsZ, which acts as a scaffold for the enzymes required for synthesis of the septum (reviewed in (4-6)). Elongation of the sidewall, on the other hand, requires MreB. This actin-like protein has been shown to associate with essential components of the cell wall synthesis machinery (7,8) as well as conserved membrane-spanning proteins (RodZ, RodA, MreC, and MreD) (9-11) to direct organized insertion of lateral cell wall material and ensure the maintenance of rod-shape (12-14).

MreB was first proposed as a factor involved in bacterial morphogenesis after discovery that mutations within *mreB* genes cause a dramatic change in cell shape in *E. coli* and *B. subtilis* (15-18). Similar to morphological changes seen with disruption of the cell wall machinery (19,20), genetic disruption or depletion of MreB as well as inactivation by the MreB-specific antibiotic A22 cause cells to become round (12,15,17,21,22). Under conditions that promote fast growth, these round cells continue to expand until they lyse, but, certain growth conditions can suppress this lethality; in *E. coli,* growth in minimal medium or increased levels of FtsZ allow MreB- cells to propagate as small spheres (9,23), whereas addition of magnesium to the growth medium suppresses the defects associated with disruption of MreB homologs in *B. subtilis* (24,25).

The pivotal role of MreB in rod-shape determination is further underscored by its distribution throughout the bacterial lineage. At least one *mreB* homolog is found in most rod-shaped bacteria, with the notable exception of those species that elongate via polar tip extension rather than sidewall expansion (e.g. *Rhizobium* and *Agrobacterium* species) (26). The rod-shaped model organisms *E. coli* and *C. crescentus* both possess a single *mreB* gene within their genomes, whereas the *B. subtilis* genome encodes three homologs (MreB, Mbl, and MreBH) that perform partially redundant functions (25). However, *mreB* homologs are conspicuously missing in cocci species, such as *Staphylococcus aureus* (26). In these spherical cells, new cell wall synthesis occurs chiefly at the division site in an FtsZ-dependent manner (27). Interestingly, it has been observed that in *E. coli* cells where lethal disruption of MreB has been suppressed, these small spheres divide via cleavage furrows in alternating perpendicular planes, a mechanism closely resembling that employed by cocci species lacking *mreB* (2,23,27,28).

Early cell biology (12) and structural (29) studies revealed striking similarities between MreB proteins and eukaryotic actin. This led to the widespread view that this cell shape determinant may form a bona fide cytoskeleton, polymerizing into actin-like cables capable of scaffolding cell wall synthesis and other cellular functions (21,26). However, several structural and imaging studies in the past five years have called this view into question, instead presenting a model with few parallels to the actin paradigm (13,14). In this chapter, I briefly summarize the evolution of our current understanding of the role of MreB in rod-shape morphogenesis, especially highlighting the recent discovery that MreB forms antiparallel filament pairs (30). I then describe our work to characterize the MreB inhibitory surface bound by the CbtA toxin, one of the few known inhibitors of this essential cell shape factor.

The original model: the bacterial actin MreB forms helical filaments

The MreB protein was first proposed to be a member of the actin superfamily after its identification in a sequence-based search for specific actin-like sequence motifs involved in ATP binding (31). Two studies published in 2001 provided seemingly complementary evidence that MreB does indeed exhibit actin-like behavior. In their 2001 report, Jones et al. performed the first MreB cellular localization studies, observing by fluorescence light microscopy that in *B. subtilis*, both MreB and Mbl formed extended helical structures that span the entire long axis of the cell and sit very close to the inner face of the cytoplasmic membrane (12). Subsequent studies using both immunofluorescence and fluorescent protein tags described similar localization patterns in both *E. coli* and *C. crescentus* (32-35). Based on these observations, it was proposed that MreB polymerizes into actin-like cables that provide long-range spatial organization of the cell wall machinery. This model was supported both by the helical pattern of peptidoglycan insertion seen in *B. subtilis* (26,36) and by the colocalization of several MreB-interacting proteins in similar helical structures (10,37).

Soon after the first description of this extended MreB helix (12), van den Ent et al. demonstrated both biochemically and structurally that MreB is able to polymerize into actin-like filaments (29). These authors observed by electron microscopy that an MreB protein purified from the thermophilic bacterium *Thermatoga maritima* (TmMreB) polymerized in an ATP-dependent manner into double protofilament structures as well as higher order sheet assemblies similar to those formed by eukaryotic F-actin (29,38). Determination of the TmMreB crystral structure revealed that the MreB subunit exhibits a canonical actin core consisting of two domains (I and II) that can be further divided into subdomains (IA, IB, IIA, and IIB); the ATP moiety binds within a cleft formed by domains I and II (Figure 4.1) (29). While many members of the actin super-family display a diverse array of structural modifications in domains IB and IIB (for example, the prokaryotic division protein FtsA contains a unique domain in place of IB (39)), the MreB domain topology was found to be almost identical to that of actin.

Despite the tendency of TmMreB to form double protofilaments in *in vitro* assembly reactions, the *T. maritima* crystral structure contained only linear, single-stranded protofilaments, characterized by a flat surface on one side, and a contoured surface on the opposite side (29). The longitudinal intra-protofilament interface was formed by contact between hydrophobic residues in subdomains IIA and IA of the top subunit and subdomains IIB and IB of the bottom subunit. Although the regions involved in longitudinal contact resemble those of F-actin, the specific residues involved are not well-conserved (29).

The MreB-specific antibiotic A22, which was first discovered based on its deformation of *E. coli* cell morphology (22), binds within the ATP-binding pocket of MreB and disrupts normal filament

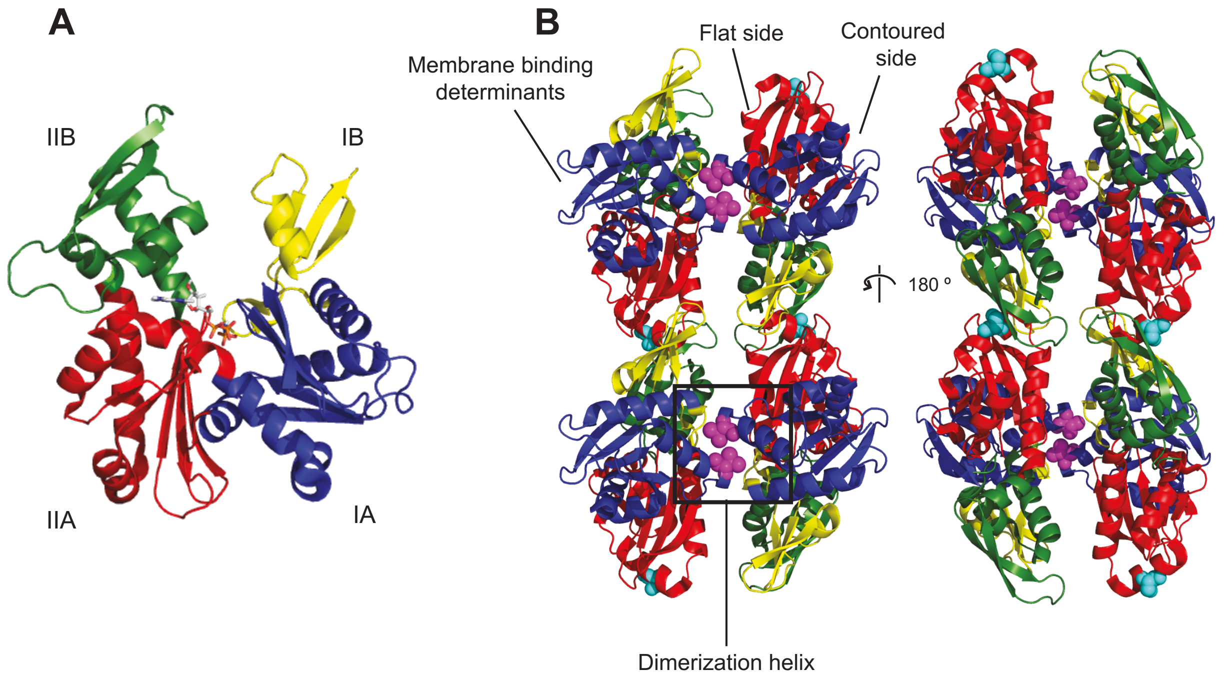

Figure 4.1: The bacterial actin MreB forms antiparallel filament pairs. A) MreB proteins are structurally related to eukaryotic actin. Shown is the ribbon structure of a modified MreB variant from *C. crescentus* (PDB 4czm (30)). Canonical actin domains IA, IIA, IB, and IIB are shown in blue, red, yellow, and green, respectively. The AMPPNP moiety (gray) binds within a cleft formed by domains I and II. B) Two antiparallel CcMreB protofilaments interact via their flat surfaces to form a double filament. Shown is the nucleotide-free double filament (PDB 4cze, (30)) arranged with the dimerization helix containing the critical V118 residue (magenta sphere) in the front (left) or rotated 180 ºC with this helix in the back (right). The same domain coloring as shown in A is used. Residue S283 (cyan sphere) is shown to highlight the MreB intra-protofilament interface. Although this CcMreB variant is lacking the N-terminal amphipathic helix, the MreB face that mediates membrane-binding is indicated.

architecture (described in more detail below) (21,30,40). Gitai et al. showed that A22 treatment of *C. crescentus* results in the dissolution of MreB helical structures and induces morphological change, suggesting that nucleotide-dependent assembly was necessary for formation of observed cytological structures (21). *In vivo* observation of MreB helical structures showed these extended filaments to be dynamic, displaying continuous remodeling and growth towards and away from the cell poles (41-43). However, *in vitro* studies suggested that these cellular dynamics were not likely the result of ATP hydrolysis; only modest differences were seen in assembly reactions using ATP versus ADP (44,45). Thus, despite the striking structural similarities between MreB and eukaryotic actin, it seemed unlikely that MreB filaments are capable of actin-like treadmilling, which is driven by nucleotide hydrolysis.

The updated model: disconnected complexes and a unique double filament architecture

For a decade, the model of MreB function was dominated by the view that MreB polymerizes into an actin-like cytoskeleton that orchestrates cell wall synthesis throughout the entire rod cell. However, since 2011, several studies have called this view into question, and a new model has emerged that paints MreB as a more decentralized figure. In this section, several recent advances in the MreB field are considered, providing a reexamination of the cytological and structural nature of MreB filaments.

Membrane-bound MreB patches display circumferential rotation

In 2011, Salje et al. demonstrated that unlike eukaryotic actin, bacterial MreB proteins contain one or two additional structural elements that allow for binding of MreB filaments to the inner membrane. The authors of this study observed that many MreB proteins from Gram-negative species contain a short N-terminal extension (7-9 amino acids); it was subsequently demonstrated that these additional residues form an amphipathic helix that directs MreB binding to the inner membrane (46). Membrane binding in *E. coli* was found to be essential for MreB function, as deletion of this amphipathic helix disrupted rod shape. A hydrophobic loop in domain IA, which is broadly conserved in Gram-positive and Gram-negative bacteria but is not found in actin, also aids in MreB membrane localization. A TmMreB mutant bearing substitutions in residues L93 and F94 within this hydrophobic loop was unable to assemble on lipid monolayers *in vitro* in contrast with the wild-type protein (46). Interestingly, elucidation of the MreB membrane-binding determinants by Salje et al. provided explanation for a technical challenge that had been encountered by many in the MreB field. MreB from *T. maritima* had been the primary protein used for *in vitro* MreB research since MreB proteins from other bacteria, especially Gram negative species, are notoriously difficult to purify (46,47). Salje et al. demonstrated that removal of the amphipathic helix allowed for purification of soluble *E. coli* MreB; this observation has enabled subsequent *in vitro* analyses of additional MreB proteins (30,46,47).

The discovery that MreB binds the inner membrane also raised concern about the use of fluorescently tagged proteins in *in vivo* localization studies. Many N and C-terminal MreB fusions are not fully functional, which, as Salje et al. suggested, may be the result of bulky fluorescent tags interfering with typical membrane association (46). This concern was compounded by several reports that questioned the physiological relevance of the MreB helix. Using electron cryotomography, Swulius et al. were unable to identify MreB filaments greater than 80 nm in length in various species in which extended helices had been observed by fluorescence light microscopy (48). A later report by the same group revealed that overexpression of *yfp-mreB* in *E. coli* (using a strain commonly used for MreB localization studies (32)) did yield extensive helical filaments, but these were found to be artifacts caused by the N-terminal YFP tag; overproduction of untagged MreB or a variant harboring an internal fluorescent tag (MreB-RFP^{SW}) did not produce visible helices (49).

The observations by Swulius et al. were consistent with work done by three separate groups describing the motion of MreB complexes in both *B. subtilis* and *E. coli* (50-52). Measurement of MreB dynamics revealed that small patches of MreB filaments move radially around the cell in a circumferential (as in, perpendicular to the long axis) rather than helical pattern. There is some discrepancy as to the length of these mobile MreB assemblies; some studies have suggested these small "patches" can actually extend up to 1-3 μM in length (53,54). However, importantly, across all studies, these dynamic MreB complexes are disconnected, exhibiting bidirectional movement around the cell, with no spatial coordination between even closely positioned patches (13,50).

Strikingly, MreB motion does not seem to be driven by polymerization dynamics; inhibition of ATP hydrolysis by mutation of residues in the *B. subtilis* nucleotide-binding site (50) or with addition of A22 to

E. coli cells (52) had no observable effect on the velocity of MreB complexes[I]. However, MreB motion was shown to be dependent on active cell wall synthesis. In *B. subtilis*, depletion of essential components of the cell wall machinery (RodA, RodZ, PBP2A) or treatment with cell wall-specific antibiotics halted MreB dynamics (50,51); a similar result was observed with several cell wall perturbations in *E. coli* (52). Consistent with peptidoglycan insertion acting as a motor for MreB dynamics, several components of the cell wall elongation complex, including MreC, MreD, RodZ, and *B. subtilis* PBP2a, have been observed to display similar motion (50,51,55).

Very recently, Morgenstein et al. reported that in *E. coli*, MreB motion requires RodZ, a conserved transmembrane protein that directly binds MreB (11), coupling it to the RodA/PBP2 complex (55). They also reported the surprising result that processive, circumferential rotation of *E. coli* MreB is not essential for rod-shape maintenance under normal growth conditions; a single amino acid substitution in MreB (MreB-S14A) allowed for rod-shaped growth in a *ΔrodZ* strain despite a continued lack of processive motion (55). Morgenstein et al. do report though that rotation of MreB increases resistance to osmotic and cell wall stresses (55). Together, these recent descriptions of disconnected, dynamic filaments strongly suggest a model in which MreB creates cell shape locally, not synchronously across the entire cell length. This is consistent with the observation that MreB preferentially localizes to regions of negative curvature, promoting cell wall synthesis to fix local perturbations (56). It remains unclear what role the processive motion of MreB plays in rod-shape growth.

MreB forms an antiparallel double protofilament

Although *in vitro* studies over the past decade have consistently demonstrated the tendency of MreB to assemble into bundles of two or more protofilaments (29,46,47,57), the structural basis for these MreB lateral interactions was only recently described. Based on cryotomography images of assembled TmMreB double filaments, Salje et al. predicted that TmMreB protofilaments paired along their flat surfaces with the opposite contoured surface facing outwards (46). The crystal structure of a modified

---

[I] Although the velocity of mobile complexes was unchanged, addition of A22 did decrease the number of mobile MreB patches in imaged *E. coli* cells suggesting that it was depolymerizing MreB structures (52).

MreB protein purified from *C. crescentus* (CcMreB)[m] was solved by van den Ent and colleagues in 2014, providing confirmation of this orientation (30). In contrast to the single protofilaments observed in crystals obtained for TmMreB (29), CcMreB protofilaments were observed as doublets formed by interaction of two antiparallel single protofilaments along the length of their flat surfaces (Figure 4.1B). Mutation of residue V118 on the flat face of CcMreB prevented the formation of filament doublets, yielding only single filaments *in vitro* (30).

van den Ent et al. used two genetic strategies to demonstrate the biological relevance of this antiparallel double filament. First, they tested the ability of two MreB variants harboring disruptive substitutions at either the intra (S284D)- or inter-protofilament interface (V121E, which is the *E. coli* equivalent of CcMreB V118E) to support rod-shape in *E. coli.* (CcMreB residues S283 and V118 are shown as cyan and magenta spheres, respectively, in Figure 4.1B) When these variants were produced as the sole source of MreB in an *E. coli* strain bearing a deletion of chromosomal *mreB*[n], cells displayed spherical morphology. This result confirms the importance of MreB longitudinal polymerization in rod-shape maintenance in *E. coli* and also indicates that formation of double filaments via an intact flat surface is necessary for MreB *in vivo* function (30).

In their second strategy, van den Ent et al. used an *in vivo* cross-linking assay to validate the predicted antiparallel orientation of the double filament. Cysteine substitutions were introduced at specific residues inside and outside of the inter-protofilament interface, and again these cysteine variants were produced as the exclusive source of MreB in *E. coli*[o]. It was predicted that if protofilaments are indeed organized in an antiparallel fashion in *E. coli*, then the symmetry should allow for the covalent cross-linking of equivalent cysteine residues on adjacent filaments found within ~8Å of each other. Cysteine residues outside of this interface should not be able to access each other; furthermore, other protofilament configurations should not allow for cross-linking of cysteine residues on the flat surface of MreB. After exposing each of the *mreB* mutant strains to a thiol-reactive crosslinker, Van den Ent et al. were able to detect MreB cross-linked dimers (by Western blotting with an MreB-specific antibody) only when a cysteine residue was present at the predicted double protofilament interface, thus confirming the antiparallel arrangement of protofilaments *in vivo* (30).

---

[m] The CcMreB variant used in (30) is lacking the N-terminal amphipathic helix and bears two substitutions within the hydrophobic membrane insertion loop region.

[n] To assess complementation by these MreB variants a complex genetic setup was used. Strain FB17 (*ΔmreBCD*) was transformed with three plasmids: i) a construct constitutively expressing *sdiA* which leads to increased *ftsZ* transcription; ii) a plasmid encoding wild-type MreC and MreD; and iii) a plasmid encoding the *mreB* allele of interest under the control of the *plac* promoter. Increased FtsZ levels allow this strain to survive and propagate as small spheres even in the absence of functional MreB. Thus, complementation is not measured by growth, but instead of spherical versus rod-shaped morphology (30).

[o] Wild-type MreB has three cysteine residues (C113, C278, C324). These three residues were mutated to serines to ensure that cross-linking occurred only at the cysteine residue of interest.

This antiparallel architecture is unique amongst known actin homologs. In eukaryotes, actin filaments pair in the same direction, establishing two polar ends that display differential assembly and disassembly properties (38). The lack of polarity in antiparallel MreB filament pairs suggests that unlike actin, MreB filament ends are indistinguishable; this prediction is consistent with the bidirectional movement of MreB filament patches observed *in vivo* (30,50) and is consistent with the evidence suggesting that MreB filaments do not exhibit treadmilling. Importantly, this antiparallel orientation allows for extensive contact between the N-terminal amphipathic helix and the membrane and ensures binding of MreB to its transmembrane interaction partners (e.g. RodZ) (30,46).

Although it remains to be determined exactly how this filament architecture influences MreB assembly dynamics and dictates cell-shape maintenance, work by van den Ent et al. establishes that the formation of the double filament is essential for MreB function. In addition to the genetic assay described above, they also present structural evidence that the inhibitor A22 blocks MreB function by disrupting formation of the double filament (30). Co-crystallization of an A22 analog (MP265) bound to CcMreB revealed simultaneous binding of the drug and either ATP or ADP within the nucleotide-binding site (30). This positioning likely blocks phosphate release upon nucleotide hydrolysis, but more strikingly, MP265 distorts the inter-protofilament interface, drawing the main dimerization helix away from the adjacent filament; consistent with this observation, all crystals generated in the presence of inhibitor contained single filaments (30). van den Ent et al. postulate that inter-protofilament contact stabilizes filaments and disruption of the double filament could lead to disassembly of single filaments as had been previously observed in the presence of A22 (40).

Motivation for the current study

Unlike its division-specific counterpart FtsZ, very few protein modulators of MreB function are known. In *C. crescentus*, overproduction of the MbiA protein phenocopies a loss of MreB, which can be suppressed by mutation of residues near the RodZ interface (58). Recently, Duan et al. reported the discovery of two sporulation-specific factors in *B. subtilis* (YodL and YisK) that genetically interact with *mreB* and *mbl* to alter cell shape when expressed during vegetative growth (59). Furthermore, the lytic *E. coli* T7 phage encodes an MreB inhibitor (gp0.6) that induces morphological change upon ectopic expression (60). In all the cases listed above, the molecular mechanisms and physiological relevance of inhibition are unknown, but these regulators could provide important tools with which to study MreB function. As illustrated in Chapter 2 of this dissertation, the CbtA toxin of *E. coli,* which was the first endogenous MreB inhibitor to be discovered (61), interacts with MreB to block cell elongation. In this chapter, I report genetic evidence suggesting that this MreB inhibitor may interact with the MreB face involved in double filament formation.

Chapter 4.2: Results

Substitutions in MreB that decrease CbtA interaction map to the double filament interface

In an attempt to identify the MreB surface utilized by CbtA to mediate a block in cell elongation, we sought to isolate MreB variants reduced for their interaction with CbtA in our bacterial two-hybrid system. However, before undertaking this two-hybrid screen, it was necessary to first identify a two-hybrid counter-screen that could be used to assess the specificity of any isolated MreB variants. It had been previously demonstrated that the cytoplasmic N-terminal domain (NTD) of the *E. coli* cell wall elongation component RodZ can detectably interact with full-length MreB in a bacterial two-hybrid system (10). Similarly, we found that in our two-hybrid system, fusion of the RodZ NTD (residues 2-84) to λCI resulted in a 3 to 4- fold increase in *lacZ* expression when α-MreB was present (Figure 4.2A). An α-MreB variant with a charge reversal substitution (E319K in *E. coli* MreB, corresponding to E309K in TmMreB) at the MreB-RodZ interface (11) is greatly reduced for its interaction with λCI-RodZ$_{\mathrm{NTD}}$ (Figure 4.2A), but maintains full interaction with λCI-CbtA (Figure 4.2B); this suggests that we are detecting a biologically relevant interaction between these two essential elongation factors.

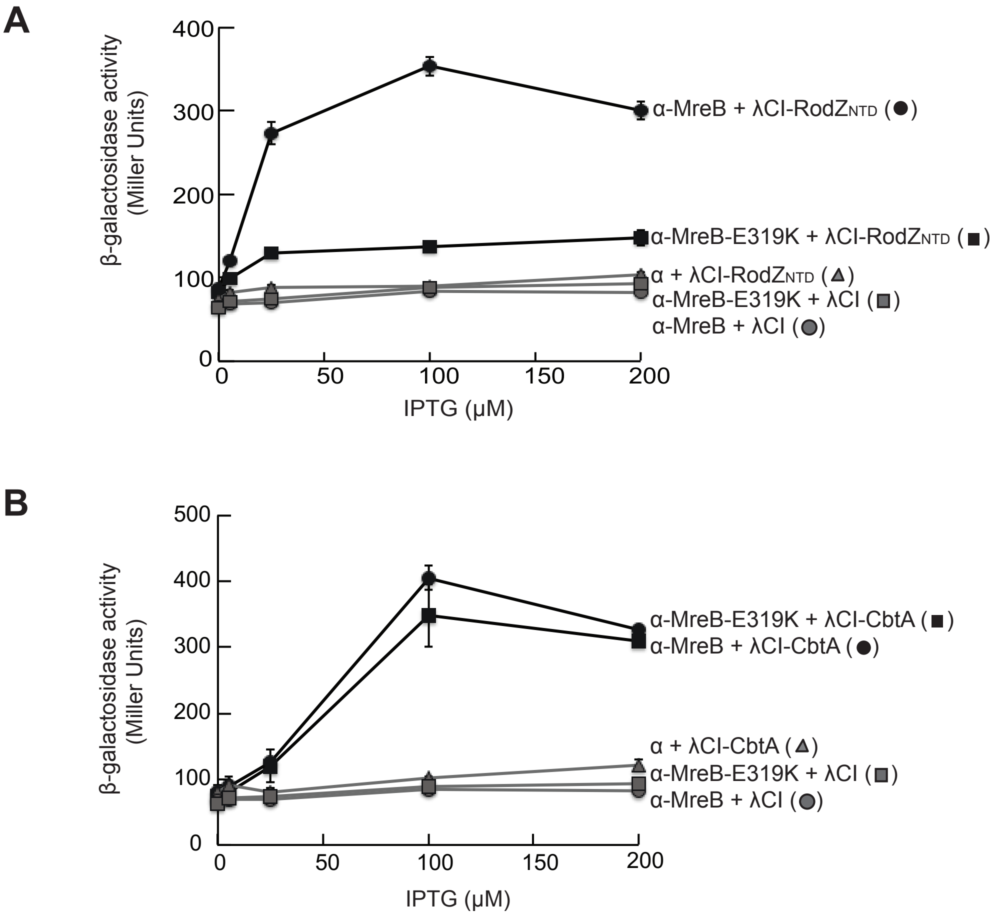

Figure 4.2: MreB interacts with the N-terminal domain of RodZ in a transcription-based bacterial two-hybrid system. Two-hybrid interactions of wild-type α-MreB and α-MreB-E319K with λCI-RodZ$_{NTD}$ (residues 2-84) and λCI-CbtA are shown in A and B, respectively. β-galactosidase activity was measured at multiple induction levels (0, 25, 100, and 200 μM IPTG) for both interactions. Each point represents the average of triplicate values; error bars represent standard deviation.

To identify MreB variants specifically abrogated for interaction with CbtA, we decided to use our modified two-hybrid screening platform, which had allowed for the isolation of the CbtA-R15C variant. As explained in Chapter 2, in this setup, the test promoter controlling *lacZ* expression bears a λCI operator positioned such that the λCI DNA-binding protein is able to make secondary contact with σ^{70} (62,63). This additional stabilizing contact allows for a boost in *lacZ* expression and enhanced colony color resolution. We generated a library of PCR-mutagenized *mreB* alleles fused to the N-terminal domain of the α subunit and transformed the resulting plasmid library into our modified two-hybrid strain (BN30) containing the λCI-CbtA-encoding plasmid. We screened several thousand colonies on indicator plates (25 μM IPTG and 40 μg/mL X-gal) for those that displayed paler blue color as compared to a control strain producing the wild-type fusion proteins. Plasmids from ~60 candidates were isolated and individually transformed into our counter-screen strain (FW102 O_L2-62) containing the λCI-RodZ$_{NTD}$-encoding plasmid. The abilities of these α-MreB mutants to interact with λCI-RodZ$_{NTD}$ was assessed by liquid β-galactosidase assay. We identified four MreB variants (I126V, V173A, E196G, and E262G) that were severely compromised in their abilities to interact with CbtA but maintained 60-90% of their interaction with RodZ (Figure 4.3A and Table 4.1; mutants labeled with *).

When these residues are mapped onto the CcMreB double filament structure (30), an interesting pattern can be observed (Figure 4.4). Two of the residues identified in our screen (E196 and E262) map to the surface of the flat side of the CcMreB protofilament (*C. crescentus* residues E193 and E261, respectively). As shown in Figure 4.1, two antiparallel protofilaments interact via these flat sides to form the MreB double filament structure; residues E196 and E262 are found within this inter-protofilament interface (Figure 4.4). In their *in vivo* site-specific crosslinking experiment (described above), van den Ent et al. observed that introduction of a cysteine at position 262 in EcMreB enabled crosslinking of the double filament, verifying its position at this interface. Although residues I126 (Cc I123) and V173 (Cc V170) are buried within the MreB subunit, they also reside near the inter-protofilament interface; residue I126 is part of the main dimerization helix that contains critical residue V121, and residue V173 is found in the beta-sheet-rich portion of domain IIA (Figure 4.4) (30).

As van den Ent et al. demonstrated, lateral interaction of MreB filaments via their flat sides is necessary for proper MreB function in *E. coli* (30); thus, if CbtA is indeed interacting with the flat side of

Figure 4.3: Substitutions in the MreB double filament interface alter CbtA interaction. A) Shown are the two-hybrid interactions of λCI-CbtA (top panel) and λCI-RodZ$_{NTD}$ (bottom panel) with several α-MreB inter-protofilament interface mutants. For both experiments, β-galactosidase activity was measured at 100 μM IPTG induction; bars represent the average Miller unit values of biological triplicates, and error bars represent standard deviation. * denotes variants identified in our original two-hybrid screen. B) To compare the two-hybrid interactions of α-MreB and α-MreB-S269F with λCI-CbtA (left panel) and λCI-RodZ$_{NTD}$ (right panel), fold-change values are shown across multiple induction levels (left panel- 0, 25, 100, and 200 μM IPTG; right panel- 0, 5, 25, 100 μM IPTG). These fold-change values were calculated by dividing the average Miller unit value for the strain producing both fusions of interest (e.g. α-MreB and λCI-CbtA) by the average Miller unit value for the relevant empty vector control with the highest β-galactosidase activity (e.g. α + λCI-CbtA). Average Miller unit values were calculated from biological triplicates from a single representative experiment. Similar results were obtained from multiple independent experiments. C) α-MreB-S269F is increased for interaction with both λCI-CbtA and λCI-CbtA-F65S. β-galactosidase activity was measured at 100 μM IPTG induction; bars represent the average Miller unit values of biological triplicates, and error bars represent standard deviation.

Figure 4.3 (Continued)

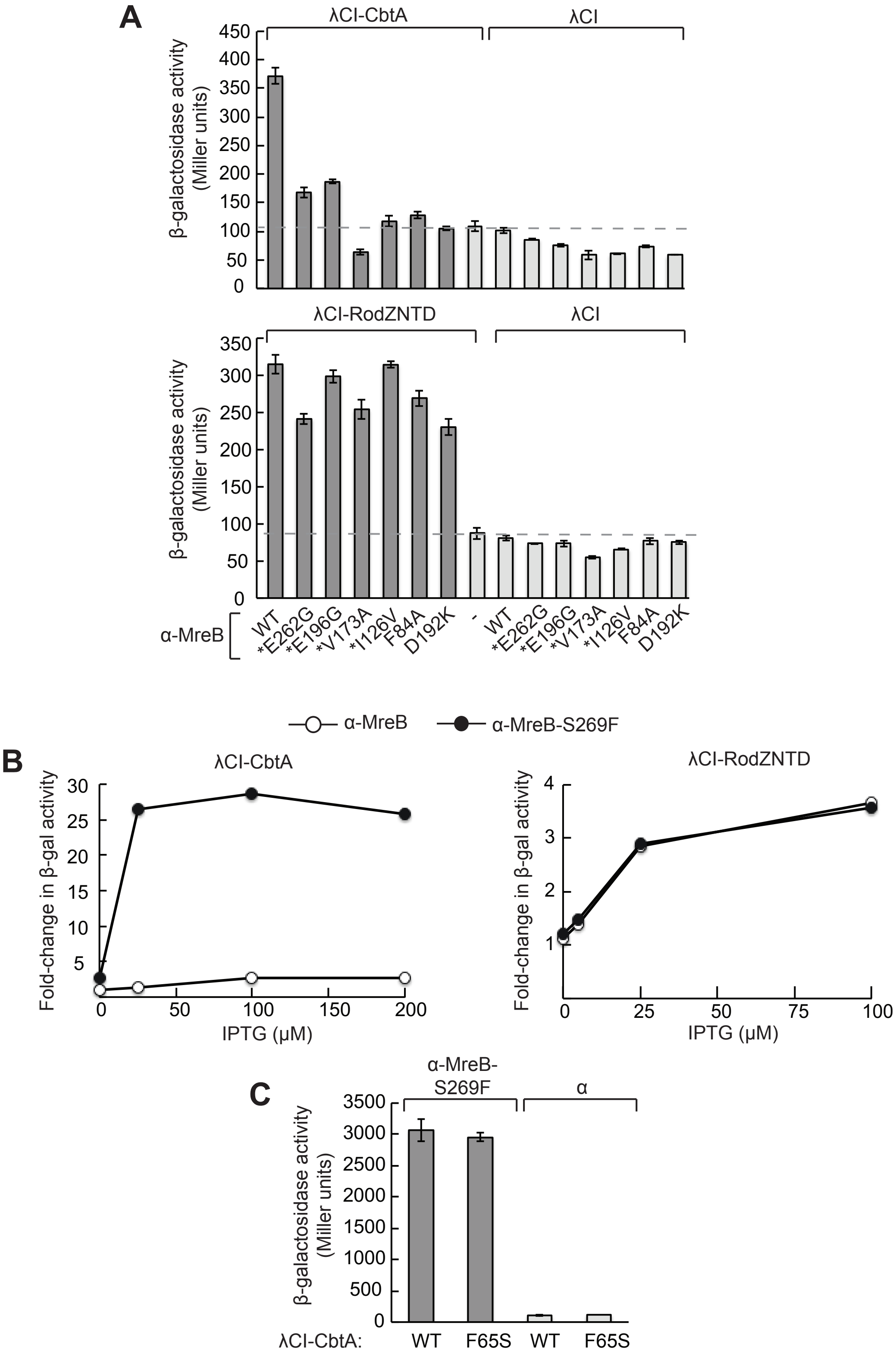

Table 4.1: Summary of two-hybrid interactions of α-MreB mutants

	α-MreB mutant	λCI-CbtA✚	λCI-RodZ$_{NTD}$❖
Inter-protofilament interface mutants	WT	+++	+++
	K77D	++	++
	D78K	++	+++
	F84A	-	++
	V121E	+++	+++
	R124D	++	+++
	A125D	++	++
	I126V*	-	+++
	R127D	+	-
	E128K	+++	+++
	V173A*	-	++`
	R188D	+++	+++
	D192K	-	++
	E196G*	+	++
	E196K	+	+++
	N200A	+++	+++
	E262G*	-	++
	E262K	+	+++
	G266E	+++	+++
	S269F	+++++	+++
	S269K	+	++
	V273E	+++	+++
Cysteine mutants	C113S	+	+++
	C278S	+++	+++
	C324S	++	+++
	C113S/C278S/C324S	+	+++

+++ 90-100% of wild-type interaction; ++ 60-90% of wild-type interaction; + 40-60% of wild-type interaction; - less than 40% of wild-type interaction; +++++ > 200% of wild-type interaction

✚λCI-CbtA interactions were assessed at 100 µM IPTG

❖λCI-RodZ$_{NTD}$ interactions were assessed at 25 µM IPTG

* These mutants were identified in our original two-hybrid screen

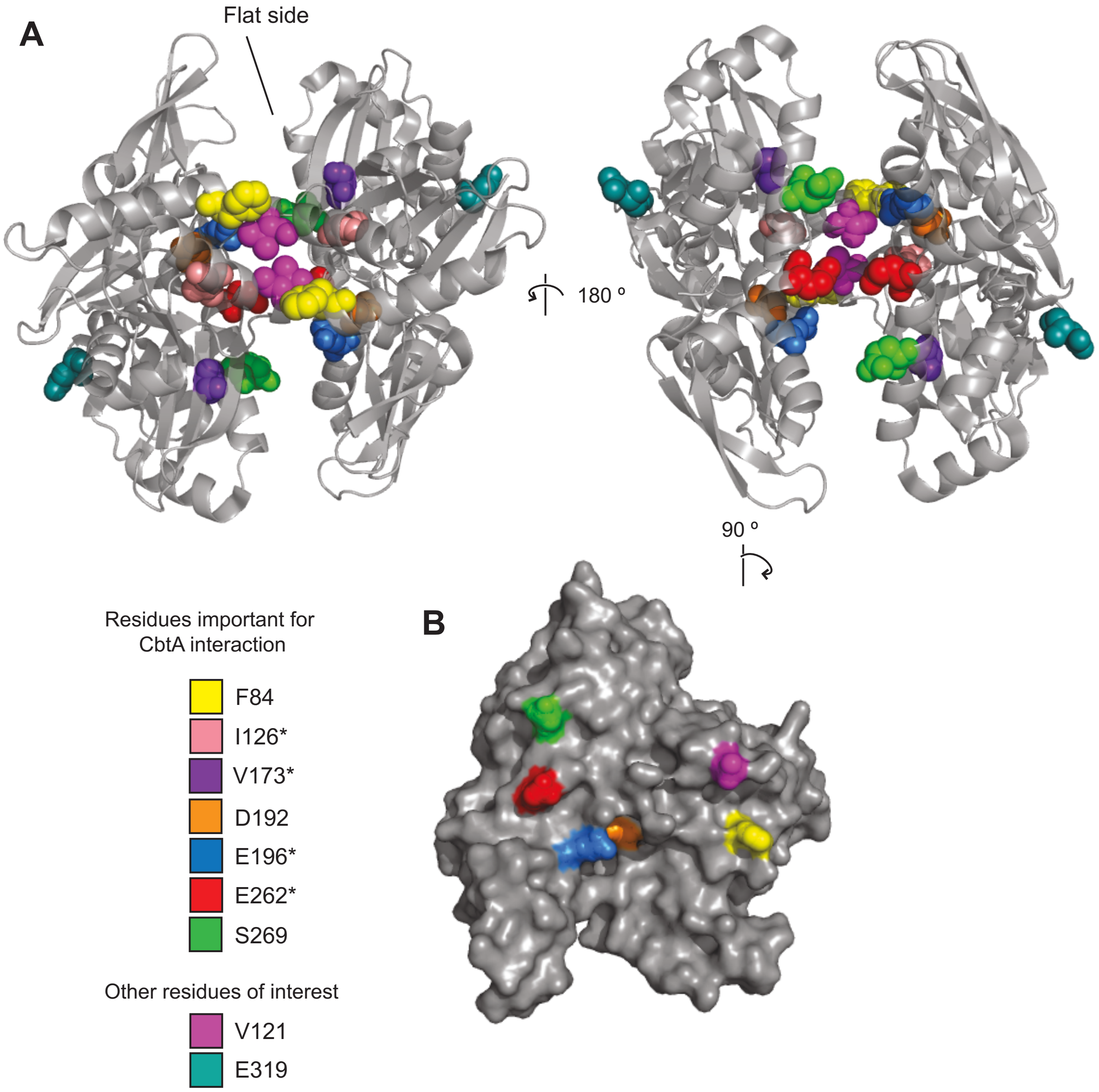
A
Flat side
180 °
90 °
B
Residues important for CbtA interaction
🟨 F84
I126*
V173*
D192
E196*
🟥 E262*
🟩 S269
Other residues of interest
V121
E319

Figure 4.4: Substitutions that alter CbtA binding cluster to the inter-protofilament interface of MreB. Residues found to influence the MreB-CbtA two-hybrid interaction are mapped onto the CcMreB double filament interface (PDB 4cze (30)). Front and back views of the ribbon structure are shown in A; the surface rendered model of a single subunit rotated 90 ° such that the flat surface is facing forward is shown in B. Residues are color coded as shown in the inset box. Although the V121E substitution did not

Figure 4.4 (Continued)

affect the ability of MreB to interact with CbtA via two-hybrid analysis, the corresponding CcMreB residue, V118 is shown in magenta to highlight the location of the dimerization helix shown in (30) to be critical for double filament formation. Residue E319 is shown in teal to illustrate the MreB surface bound by RodZ (11). * denotes variants identified in our original two-hybrid screen.

MreB, it may be blocking MreB function by preventing the formation of the essential double filament. To further probe the ability of CbtA to interact with this MreB surface, we performed a targeted mutagenesis of the flat side of the MreB subunit. Charge reversal substitutions were introduced at several positions containing charged residues (e.g. D192K); non-conservative changes were made at additional positions (e.g. F84A). The ability of each MreB mutant (bearing a single amino acid substitution) to interact with both CbtA and RodZ_{NTD} was assessed in our two-hybrid system. Table A4.1 summarizes the two-hybrid interaction profiles of the complete set of MreB variants that were tested. Among those α-MreB mutants tested, we identified three additional inter-protofilament interface mutants with altered CbtA-binding. The mutants α-MreB-F84A and α-MreB-D192K are unable to interact with λCI-CbtA, but maintain strong interaction with λCI-RodZ_{NTD} (Figure 4.3A). Conversely, the α-MreB-S269F variant is greatly increased in its ability to interact with λCI-CbtA, yielding a 25-30-fold increase in *lacZ* expression as compared to the highest empty vector control (Figure 4.3B). This fold-change value is ~10 times higher than the 3-fold *lacZ* increase consistently measured with wild-type α-MreB and λCI-CbtA. Importantly, this S269F-dependent boost in interaction is specific to CbtA; α-MreB-S269F yielded a λCI-RodZ_{NTD} interaction profile identical to that of wild-type α-MreB across multiple induction levels (Figure 4.3B). Since MreB and CbtA are both known to interact with FtsZ (64), we considered the possibility that the S269F substitution may actually promote interaction between α-MreB and FtsZ; enhanced bridging of α-MreB-S269F and λCI-CbtA by endogenous FtsZ molecules could potentially lead to an apparent increase in the MreB-CbtA interaction. However, this explanation seems unlikely as α-MreB-S269F is similarly boosted for interaction with the λCI-CbtA-F65S variant, which is unable to interact with FtsZ (Figure 4.3C).

MreB residue E262 is necessary for CbtA and YpjF inhibition of cell elongation

As Figure 4.4 illustrates, single amino acid substitutions at various positions along the flat side of MreB (including several in residues found directly at the double filament interface) alter its interaction with CbtA in the context of our two-hybrid system. These data suggest that the MreB inter-protfilament interface may be the binding surface utilized by CbtA to inhibit cell elongation. To further assess whether the MreB interface residues identified in our two-hybrid analyses are critical for the toxic block in cell elongation mediated by CbtA, we aimed to overexpress *cbtA-F65S* in *E. coli* strains producing the various mutants as the exclusive source of endogenous MreB. As was demonstrated in Chapter 2, overproduction of CbtA-F65S results in a lethal loss of rod shape, causing cells to become spherical. We predicted that in strains bearing substitutions that disrupt the CbtA-MreB interaction, overproduction of CbtA-F65S would be less toxic and would not induce spherical morphology. Importantly, this strategy required the use of an MreB variant capable of supporting rod-shaped growth.

To identify an appropriate MreB variant to use in this analysis, we tested the abilities of several of our isolated mutants to complement the growth and morphology of an *mreBCD* depletion strain. Briefly, this depletion strain (FB30/pFB174) harbors a kanamycin resistance cassette in place of the chromosomal *mreBCD* operon, which is instead provided on the multi-copy plasmid pFB174 downstream of the *pBAD* promoter (23). Thus, this depletion strain requires arabinose for robust rod-shaped growth. Each of the *mreB* alleles shown in Figure 4.5 was cloned along with *mreC* and *mreD* downstream of the *plac* promoter on the ColE1 plasmid pFB149 (*plac-mreBCD*) (23). Growth and cell morphology phenotypes for FB30/pFB174 transformed with each of the pFB149 derivatives were assessed in medium containing IPTG or arabinose. When cells were plated on LB supplemented with 0.5% arabinose, all strains grew well; when cells were plated on LB supplemented with 250 μM IPTG, only *mreB-E262G* and *mreB-S269F* were able to support growth to the same extent as wild-type *mreB* (Figure 4.5B). The cell morphology phenotypes were consistent with the plate-based results; only cells expressing *mreB-E262G* or *mreB-S269F* maintained a rod-shape comparable to that of the wild-type *mreB*-expressing strain in M9 maltose supplemented with 250 μM IPTG (Figure 4.5C).

Because MreB-E262G is able to support rod-shaped growth in cells but is severely decreased for CbtA interaction in our bacterial two-hybrid system, we decided to assess CbtA-F65S toxicity in this genetic context. Plasmids *plac-mreBCD* (pFB149) and *plac-mreB-E262G mreCD* (pDH278) were transformed in parallel into *E. coli* strain BW27785; the *mreBCD* knockout allele was transferred from strain FB30/pFB174 into both strains via P1 transduction. The resulting transductants exhibited IPTG-dependent rod-shaped growth in either LB or M9 maltose. It was observed that in both strains, about 5% of cells failed to grow as rods, forming large spheres (yellow arrows in Figure 4.6A); this is likely the result of *plac-mreBCD* plasmid loss. We transformed both strains with either pBAD33 or pBAD33-*cbtA-F65S* (pDH212) and observed growth and morphology in the presence of arabinose. As shown in Figure 4.6A,

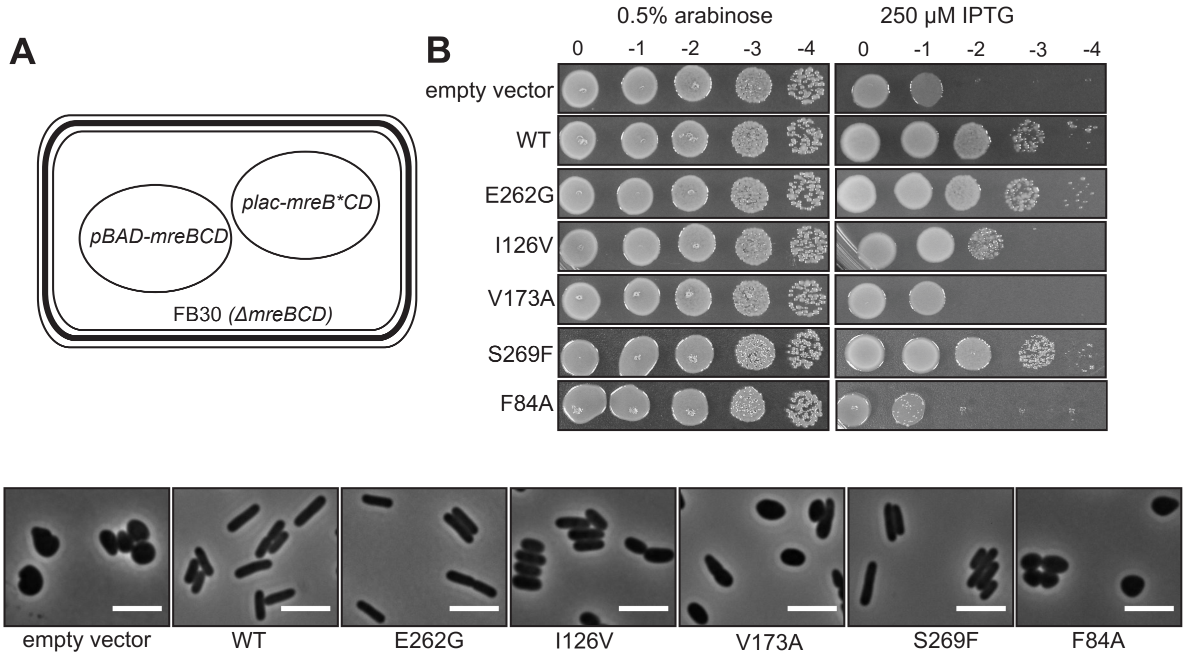
A
B
0.5% arabinose
250 µM IPTG
0
-1
-2
-3
-4
0
-1
-2
-3
-4
empty vector
WT
E262G
I126V
V173A
S269F
F84A
plac-mreB*CD
pBAD-mreBCD
FB30 (ΔmreBCD)
empty vector
WT
E262G
I126V
V173A
S269F
F84A

Figure 4.5: Assessment of the ability of MreB interface mutants to support rod-shaped growth. Our complementation strategy is diagrammed in A. Depletion strain FB30/pFB174 (*mreBCD::kan^R/pBAD-mreBCD)* was transformed with either an empty vector control (pMLB1113) or a plasmid derived from pFB149 (*plac-mreBCD*) expressing wild-type *mreB* (pFB149), *mreB-E262G* (pDH279), *mreB-V173A* (pDH280), *mreB-I126V* (pDH281), *mreB-S269F* (pDH332), or *mreB-F84A* (pDH333). B) To assess the ability of each *mreB* allele to support growth on plates, overnight cultures were grown in M9 maltose (0.2% maltose, 0.2% casamino acids, 1 mM $MgSO_4$) supplemented with 0.5% arabinose at 37 ºC. The following morning, cultures were back-diluted 1:100 in fresh M9 maltose + 0.5% arabinose and grown at 37 ºC for several hours until they reached late log phase. Cultures were normalized to the same OD600 value, several 1:10 serial dilutions were made in sterile phosphate buffered saline (PBS), and 5 µL of each culture was spotted on LB plates supplemented with either 0.5% arabinose or 250 µM IPTG. Plates were incubated overnight at 37 ºC. C) To observe the morphology phenotypes of these strains, aliquots from the same overnight cultures described in B were washed once and resuspended in fresh M9 maltose (without arabinose). These washed aliquots were used as inoculum for M9 maltose cultures

Figure 4.5 (Continued)

supplemented with 250 μM IPTG. All cultures were grown at 37 ºC until the MreB$^-$ phenotype was observed in the empty vector control strain, indicating MreB levels had been depleted (approximately 5 hrs). Cultures were back diluted to remain in log-phase during this period. After 5 hrs, strains were imaged.

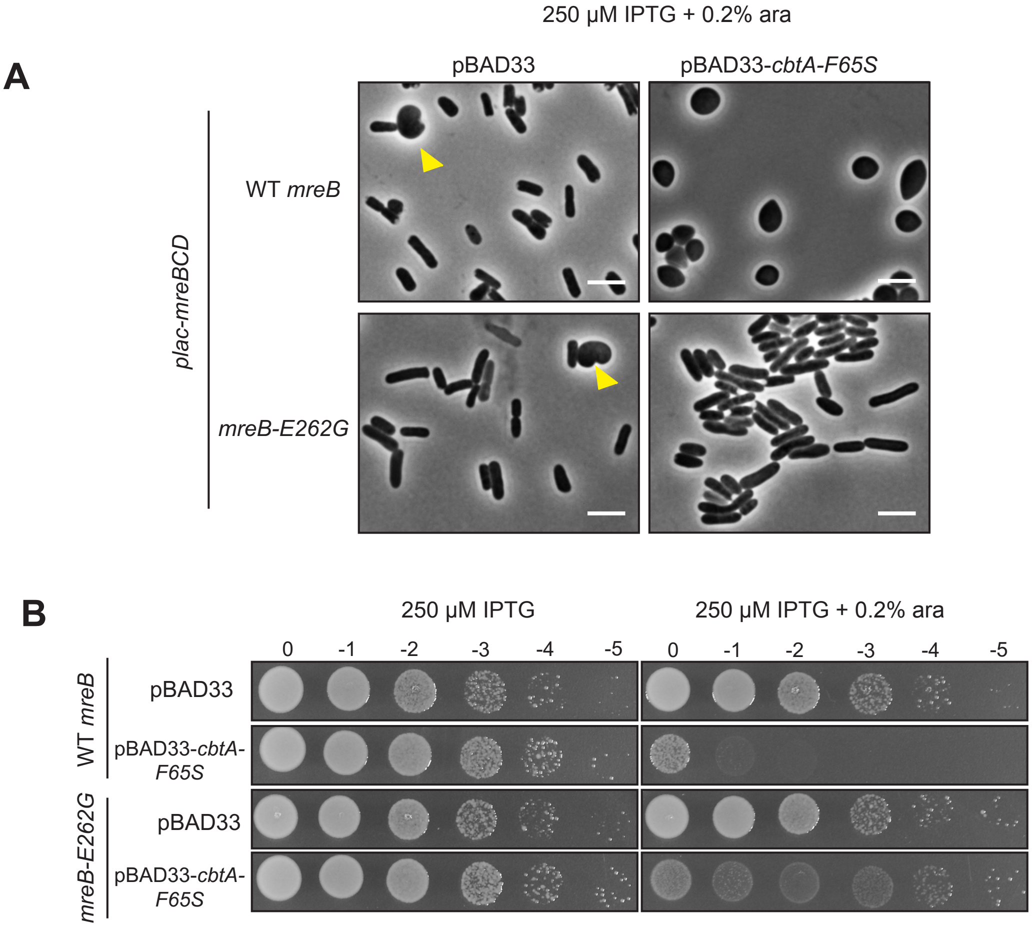
250 µM IPTG + 0.2% ara
A
pBAD33
pBAD33-*cbtA-F65S*
WT *mreB*
plac-mreBCD
mreB-E262G
B
250 µM IPTG
250 µM IPTG + 0.2% ara
0
-1
-2
-3
-4
-5
0
-1
-2
-3
-4
-5
WT *mreB*
pBAD33
pBAD33-*cbtA-F65S*
mreB-E262G
pBAD33
pBAD33-*cbtA-F65S*

Figure 4.6: MreB residue E262 is necessary for CbtA-F65S toxicity and cell elongation inhibition. Strains DH118/pFB149 (BW27785 *mreBCD::*kan^R/ *plac-mreBCD*) and DH118/pDH278 (BW27785 *mreBCD::*kan^R/ *plac-mreB-E262G mreCD*) were transformed with either the empty vector pBAD33 control plasmid or pBAD33-*cbtA-F65S* (pDH212). Transformants were selected on M9 maltose (0.2% maltose 0.2% casamino acids 1 mM $MgSO_4$) plates supplemented with appropriate antibiotics and 250 µM IPTG at 30 ºC. Overnight cultures were grown in M9 maltose + 250 µM IPTG at 30 ºC. In B, these overnight cultures were back diluted to a starting OD600 of 0.03 in LB (CmCarb) supplemented with 250 µM IPTG, and grown for 1 hr at 30 ºC (reaching an OD600 ~0.08). Cultures were induced by addition of 0.2% arabinose and grown for an additional 2 hrs at 30 ºC, at which point microscopic analysis was performed. In C, overnight cultures were back diluted 1:100 in M9 maltose + 250 µM IPTG and grown at 30 ºC for

Figure 4.6 (Continued)

~5 hrs (until cultures had reached an OD600 of ~0.7). Cultures were normalized to the same OD600 value, several 1:10 serial dilutions were made in sterile phosphate buffered saline (PBS), and 5 μL of each culture was spotted on LB plates supplemented with 250 μM IPTG ± 0.2% arabinose. Plates were incubated for 48 hrs at RT.

both strains bearing the pBAD33 empty vector maintain rod-shape in the presence of IPTG and arabinose (left panels), and, as expected, cells containing wild-type *mreB* and pBAD33-*cbtA-F65S* become spherical within 2 hrs of arabinose addition. However, importantly, cells expressing the *mreB-E262G* allele do not become round, maintaining rod-like shape after 2 hrs of *cbtA-F65S* expression; CbtA-F65S-dependent growth inhibition is also reduced in the *mreB-E262G* strain (Figure 4.6B). Thus, this result indicates that residue E262, which is found within the MreB double filament interface, is necessary for MreB-CbtA interaction and for cell elongation inhibition by CbtA-F65S.

As described in Chapter 2 of this dissertation, the CbtA homolog, YpjF, also inhibits cell elongation, and we can detect interaction between α-MreB and λCI-YpjF in our two-hybrid system (resulting in a 2-fold increase in *lacZ* levels). As was seen with λCI-CbtA, several single amino acid substitutions in the flat side of α-MreB alter λCI-YpjF binding. The four substitutions originally isolated in our two-hybrid screen (E262G, E196G, V173A, and I126V) disrupt the MreB-YpjF interaction (Figure 4.7A), whereas the S269F substitution more than doubles the detected interaction (Figure 4.7B). Likewise, it was observed that a strain harboring the *mreB-E262G* allele was less susceptible to YpjF-F65S-induced morphological change (Figure 4.7C), suggesting that CbtA and YpjF both require residues within the inter-protofilament interface for MreB inhibition.

Chapter 4.3: Discussion

The flat surface of the MreB subunit represents a putative CbtA-binding site

As described in Chapter 2 of this dissertation, the CbtA toxin of *E. coli* is able to mediate simultaneous inhibition of both cell division and cell elongation through independent interaction with FtsZ and MreB. Here, I report our findings that residues found in the double protofilament interface of MreB are necessary for CbtA binding and cell elongation perturbation. Two-hybrid analyses indicate that several amino acid changes at positions along the flat side of the MreB subunit alter the ability of MreB to bind CbtA (Figure 4.3 and Table 4.1). We identified six MreB mutants (F84A, I126V, V173A, D192K, E196G, E262G) that are specifically reduced in their ability to interact with CbtA; residues F84, E196, and E262 are surface-exposed, suggesting that they may participate directly in protein-protein interaction with CbtA. Residue D192 is found within a small pocket beneath residue E196 (see the orange and sky blue

Figure 4.7: Residues at the MreB inter-protofilament interface are necessary for the YpjF-MreB interaction. The two-hybrid interactions of λCI-YpjF and the indicated α-MreB variants are shown in A and B. For the experiment in A, β-galactosidase activity was measured at 100 μM IPTG induction; bars represent the average Miller unit values of biological triplicates, and error bars represent standard deviation. * denotes variants identified in our original two-hybrid screen. For the experiment in B, β-galactosidase activity was measured at 0, 25, 100, and 200 μM IPTG induction; points represent the average Miller unit values of biological triplicates, and error bars represent standard deviation. C) Strains DH118/pFB149 (BW27785 *mreBCD::kan*^{R}/ *plac-mreBCD*) and DH118/pDH278 (BW27785 *mreBCD::kan*^{R}/ *plac-mreB-E262G mreCD*) were transformed with either the empty vector pBAD33 control plasmid or pBAD33-*ypjF-F65S* (pDH289). Transformants were selected on M9 maltose (0.2% maltose 0.2% casamino acids 1 mM $MgSO_4$) plates supplemented with appropriate antibiotics and 250 μM IPTG at 30 ºC. Overnight cultures were grown in M9 maltose + 250 μM IPTG at 30 ºC. The next morning, cultures were back diluted to a starting OD600 of 0.03 in LB (CmCarb) supplemented with 250 μM IPTG, and grown for 1 hr at 30 ºC (reaching an OD600 ~0.08). Cultures were induced by addition of 0.2% arabinose and grown for an additional 2 hrs at 30 ºC, at which point microscopic analysis was performed.

Figure 4.7 (Continued)

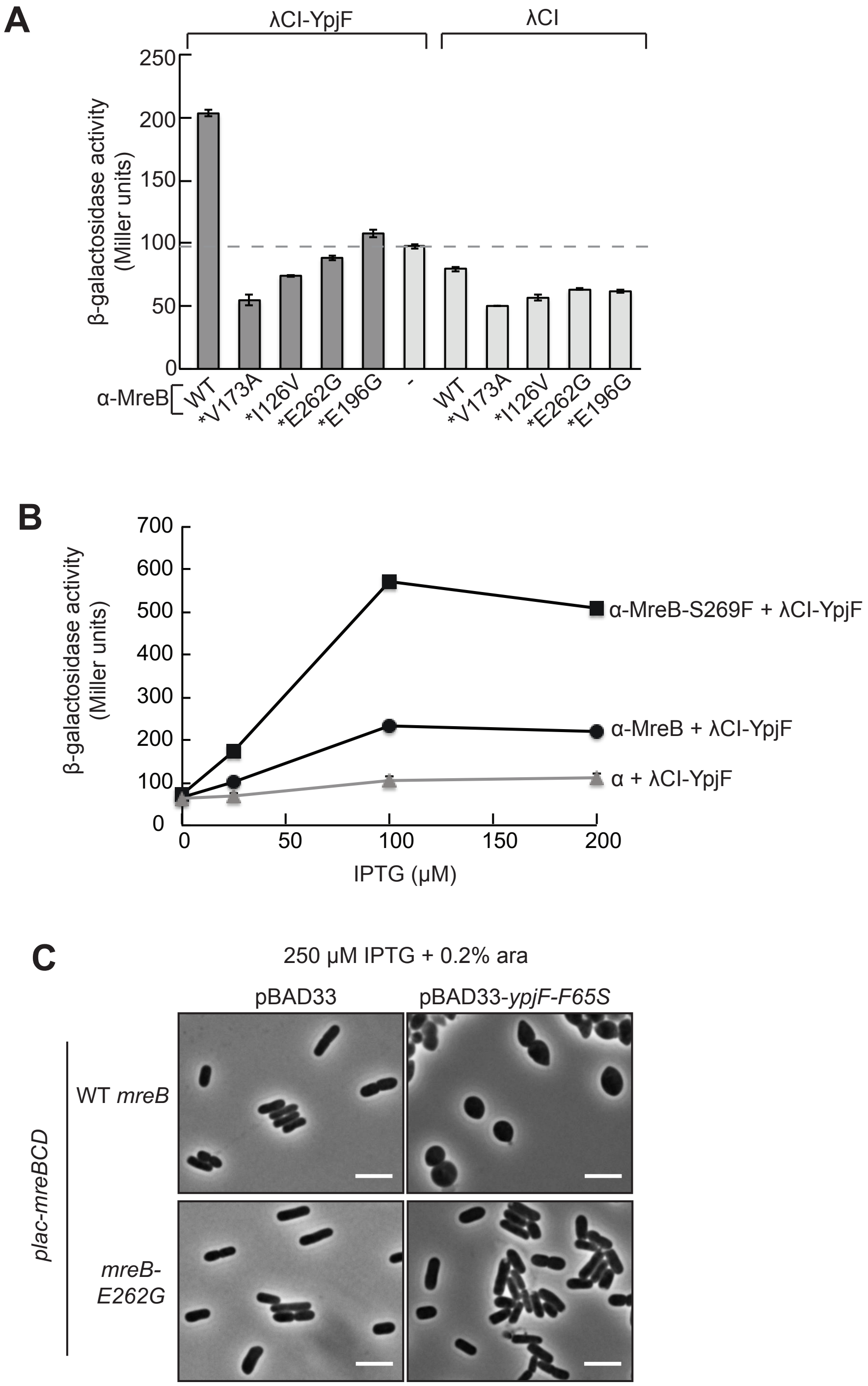

residues in Figure 4.4B); we speculate that the introduction of a positively charged lysine in this pocket may alter the position of the surface-exposed residue E196, indirectly deforming the putative CbtA-binding surface.

Additionally, we found that the introduction of a hydrophobic phenylalanine at surface residue S269 (which is very close to residue E262) led to an impressive increase in CbtA binding (going from a 3-fold to a 30-fold increase in reporter gene expression in the two-hybrid system) (Figure 4.3B). This substitution caused no alteration of the MreB-RodZ interaction, suggesting that its effects are specific to CbtA-binding. Furthermore, this substitution does not appear to indirectly increase the MreB-CbtA interaction by facilitating a bridging interaction with chromosomally encoded FtsZ, based on the fact that the F65S substitution in λCI-CbtA does not abrogate the effect of the S269F substitution in α-MreB (Figure 4.3C). The ability of a single amino acid change to cause such a pronounced increase in interaction provides further support for the idea that CbtA binds directly to the flat side of MreB.

As shown in Table A4.1, lysine substitutions at positions E196 and E262 also decrease the MreB-CbtA interaction. In an effort to confirm that the surface residues identified in our two-hybrid analyses directly bind CbtA, we attempted to identify compensatory substitutions in CbtA that restore an interaction with either of these MreB charge-reversal variants; we were unfortunately unable to identify CbtA variants that interacted with these MreB mutants in an allele-specific manner (data not shown). The MreB-S269K variant is also reduced in its ability to interact with CbtA (Table A4.1), making it a good candidate for future attempts to isolate a mutant suppressor pair.

We observed that overproduction of the CbtA-F65S variant, which causes a pronounced spherical morphology in a wild-type *mreB* strain, does not result in a loss of rod shape in a strain bearing the functional mutant allele *mreB-E262G* (Figure 4.6A). The viability defect mediated by CbtA-F65S overproduction is also abrogated in the *mreB-E262G* mutant background (Figure 4.6B). Thus, alteration of residue E262 prevents CbtA-F65S-dependent inhibition of cell elongation. It is possible that this E262G substitution prevents CbtA interference in a more indirect manner (for example, increasing the stability of MreB filaments by enhancing lateral interaction or increasing protein levels); however, our observation that MreB-E262G does not interact with CbtA by two-hybrid analysis and is resistant to inhibition by CbtA-F65S, is consistent with a model in which CbtA binding to the flat surface of MreB is responsible for inhibition of cell elongation. Amino acid substitutions on the flat side of MreB similarly affect the MreB-YpjF two-hybrid interaction, and residue E262 was also found to be necessary for cell elongation inhibition by YpjF-F65S (Figure 4.7). This suggests that these homologous toxins may target the same MreB surface.

In our complementation system, we saw that MreB-S269F was also able to support rod-shaped growth (Figure 4.5). It would be interesting to assess whether in the *mreB-S269F* background, CbtA-F65S toxicity is increased, as would be predicted by the two-hybrid data. Specifically, we would like to test whether the level of cell elongation inhibition that is seen with high expression of *cbtA-F65S* in a wild-type strain (i.e. spherical morphology and severe viability defects, Figure 4.6) can be achieved with normally sub-inhibitory levels of *cbtA-F65S* expression in the *mreB-S269F* strain. As expression from the *pBAD* promoter is not very tunable, this will require the construction of an alternative expression system.

Genetic insight into the CbtA mechanism of cell elongation inhibition

As van den Ent et al. recently demonstrated, the formation of the MreB antiparallel double filament is necessary for the maintenance of rod-shape in *E. coli*. Their structural evidence indicates that this essential architecture is mediated by the pairing of two adjacent MreB filaments along their flat sides (30). As described above, we believe that this flat side of MreB may serve as the inhibitory surface bound by both CbtA and YpjF. As illustrated in Figure 4.4, several of the residues found to be necessary for CbtA binding are found directly within the inter-protofilament filament interface, suggesting that CbtA may inhibit MreB function by competing for sites needed for formation of the double filament. This potential mechanism is consistent with two previously published observations. First, Tan et al. observed that *in vitro*, CbtA decreased the sedimentation efficiency of purified *E. coli* MreB but did not affect MreB ATPase activity (61). MreB requires ATP for polymerization and only hydrolyzes ATP in its polymerized state (29,44). Although (to the best of my knowledge) it has not been absolutely determined what if any influence double filament formation has on ATP hydrolysis, a possible explanation for the result observed by Tan et al. is that in the presence of CbtA, MreB still polymerizes into single filaments capable of nucleotide hydrolysis but cannot form more sedimentation-prone paired filaments. In further support of this proposed mechanism, Masuda et al. reported that the cognate antitoxin of CbtA (CbeA) enhances sedimentation of *E. coli* MreB *in vitro* (by a proposed bundling mechanism) and prevents morphological perturbations caused by *cbtA* overexpression and A22 treatment when expressed *in vivo* (65). This suggests that like A22 (30), CbtA may disrupt double filament formation which can be overcome by enhanced bundling by CbeA.

As one way to test whether CbtA can indeed prevent double filament formation *in vivo*, we hoped to develop a modified cross-linking strategy similar to the one employed by van den Ent et al. (30). Our aim was to identify a cysteine substitution within the inter-protofilament interface that mediated cross-linking of the double filament but did not disrupt the MreB-CbtA two-hybrid interaction. We then planned to assess cross-linking of this MreB cysteine variant *in vivo* with or without overproduction of CbtA-F65S. As a first step to establish this system, we generated an MreB variant with all three naturally occurring cysteine residues mutated to serine (MreB-C113S/C278S/C324S). Unfortunately, we found that this variant is specifically decreased for interaction with CbtA in our two-hybrid assay; further dissection of this variant revealed that the C113S substitution is responsible for the decrease in MreB-CbtA interaction (Table 4.1). Interestingly, in the MreB structure, residue C113 is found very close to residue I126, which resides in the main dimerization helix of MreB and is necessary for the MreB-CbtA two-hybrid interaction. At any rate, the development of a suitable *in vivo* cross-linking strategy is unlikely to be straightforward. As a complementary approach to investigate the molecular details of CbtA inhibition, it would be informative to observe the *in vitro* architecture of MreB filaments in the presence of CbtA by electron microscopy. As MreB from *E. coli* is notoriously difficult to work with *in vitro* (47), this strategy may not be completely straightforward either. It would be interesting to assess whether CbtA is capable of interaction with the CcMreB variant used by van den Ent et al. in their structural studies. If so, this may facilitate biochemical and structural study of the CbtA mechanism of MreB inhibition.

In summary, we believe that CbtA interacts with the flat side of MreB, potentially perturbing MreB double filament formation. Although additional *in vivo* and *in vitro* work is needed to confirm this putative inhibitory mechanism, our findings suggest that disruption of the double protofilament interface may be a common strategy employed by MreB inhibitors. Structural evidence shows that A22 interrupts pairing of MreB filaments by dislocating the main dimerization helix (30). Furthermore, Duan et al. found that a lysine substitution at residue E250 of *B. subtilis* Mbl (which is equivalent to E262 in *E. coli* MreB) suppressed morphological defects caused by the sporulation factors, YodL and YisK (59). As far as we know, it has not yet been established whether Mbl adopts a similar filament architecture, but if so, the effect of the E250K substitution on YodL and YisK activity may suggest that these regulators disrupt cell shape through targeting of this inter-protofilament interface. Further elucidation of the mechanistic details by which CbtA and these other regulators inhibit MreB function may provide important insight into the involvement of MreB assembly and filament architecture in cell elongation and rod-shape maintenance.

Chapter 4.4: Materials and Methods

Strains, plasmids, and growth conditions

A complete list of the bacterial strains used in this chapter is provided in Table A4.2 (shown at the end of this section). Additionally, lists of the plasmids and oligonucleotides used in this chapter can be found in Tables A4.3 and A4.4 (shown at the end of this section), respectively. NEB5-α F'I^q (New England Biolabs) was used as the cloning strain for all plasmid constructions outlined below. All two-hybrid studies were performed in either FW102 O_L2-62 (63,66) or BN30 (FW102 O_L2-42) (62). Strains were grown in either LB (1% NaCl) broth at 37 ºC or 30 ºC or on LB plates supplemented with appropriate antibiotics at the following concentrations (unless otherwise noted): carbenicillin (Carb), 100 µg/mL; chloramphenicol (Cm), 25 µg/mL; kanamycin (Kan), 50 µg/mL; spectinomycin (Spec), 50 µg/mL. Where noted, strains were grown in M9 minimal medium (1 mM $MgSO_4$) supplemented with 0.2% maltose and 0.2% casamino acids.

All two-hybrid constructs were cloned as described in Chapter 2 of this dissertation. A single colony of *E. coli* BW27785 was used as template to amplify the *rodZ* locus using primer pair oDH236/oDH237 for construct pACλCI-RodZ$_{NTD}$ (pDH238). To generate the pBRα-MreB-C113S/C278S/C324S construct (pDH287), the triple mutant *mreB* allele was synthesized (gBlock; IDT). This gene product was amplified using oDH298 (NotI site) and oDH299 (BamHI) site, NotI/BamHI digested, and cloned into the pBRα backbone. To construct all pBRα-MreB single mutants, the allele of interest was generated by overlap PCR (using pMT151 as template) with outside primers oDH298/oDH299 and specific internal mutagenic primers; this PCR product was digested with NotI/BamHI and ligated into similarly digested vector backbone. Oligonucleotides pBRα_F, pBRα_R, pACλCI_F, and pACλCI_R were used to sequence all two-hybrid constructs (see Chapter 2 for sequences).

To construct *cbtA-F65S* and *ypjF-F65S* arabinose-inducible overexpression vectors (pDH212 and pDH289), alleles were amplified from pMT146 and pMT188 (see Chapter 2 for descriptions) using primer pair oDH285/oDH286 or oDH380/381, respectively. PCR products were digested with NdeI/XbaI and ligated into the pBAD33 (NdeI/XbaI) backbone.

Sequencing of plasmid pFB149 (*plac-mreBCD*; generous gift of T. Bernhardt) revealed two missense mutations within the *mreB* gene. To generate a construct with the wild-type *mreB* sequence, the entire *mreB* and *mreC* genes, and part of the *mreD* gene sequence were amplified from a single *E. coli* BW27785 colony with primers oDH372_F (anneals to the beginning of the *mreB* sequence and contains an XbaI restriction site) and oDH369_R (anneals within the *mreD* sequence). There is a naturally occurring BamHI site within *mreD* that is unique on plasmid pFB149; both the *mreBCD* PCR product and pFB149 were digested with XbaI/BamHI and ligated together. The entire *mreBCD* locus was verified by sequencing using primers oDH355, oDH369, oDH373, oDH374, and oDH375. In this dissertation, all references to pFB149 refer to this corrected plasmid. To construct pFB149-derivatives for MreB mutant expression studies, *mreB* mutant alleles were generated by overlap PCR using corrected pFB149 as template, outside primers oDH372/oDH369, and allele-specific internal mutagenic primers. PCR products were digested with XbaI/BamHI and ligated into the pFB149 (XbaI/BamHI) backbone. All pFB149-derivatives were verified by sequencing using primers oDH355, oDH369, oDH373, oDH374, and oDH375.

To construct strains DH118/pFB149 and DH118/pDH278, plasmids pFB149 and pDH278 were transformed into strain BW27785. To introduce the *mreBCD::kan* deletion, a P1 lysate was grown on strain FB30/pFB174 and used to infect each recipient strain. Transductants were selected on M9 maltose plates (0.2% maltose, 0.2% casamino acids, 1 mM $MgSO_4$) supplemented with 5 mM sodium citrate and 250 µM IPTG (for expression of *mreBCD*). Growth on minimal medium is known to suppress *mreBCD* defects and was used to prevent acquisition of suppressor mutations. Strains were checked for proper *kan* insertion by colony PCR using primers oDH289 and oDH307.

Genetic screen to identify substitutions in MreB that disrupt the MreB-CbtA interaction

The *mreB* gene fragment (found on pMT151) was mutagenized by error-prone PCR using *Taq* polymerase and the outside primers pBRα_F and pBRα_R. The mutagenized alleles were cloned into the α expression vector by the method described in Chapter 2. The modified two-hybrid reporter strain (BN30) bearing pACλCI-CbtA (pMT154) was transformed with this mutant library; transformants were plated on LB (KanCarbCm) indicator medium containing IPTG (25 μM) and X-gal (40 μg/mL). Plates were incubated overnight at 30 ºC and refrigerated (4 ºC) for an additional 8-16 hrs. Several thousand colonies were screened to identify those exhibiting lower *lacZ* expression (white or light blue color) as compared to the dark blue colonies producing wild-type α-MreB and λCI-CbtA fusions. Individual overnight cultures of ~60 candidate colonies were grown in LB supplemented with Carb (to select for only the pBRα-MreB plasmid) at 30 ºC. Plasmids were prepped from these cultures, most likely generating a mixed prep of α and λCI plasmids. In order to confirm the loss of interaction with λCI-CbtA and to identify those candidates that maintained interaction with α-RodZ$_{NTD}$, mixed preps were used to transform FW102 O$_L$2-62 strains containing either pACλCI-CbtA or pACλCI-RodZ$_{NTD}$ (pDH238). Transformants were selected on LB (CmCarbKan). β-galactosidase assays were used to measure interaction between each α-MreB mutant and λCI-CbtA at 100 μM IPTG and λCI-RodZ$_{NTD}$ at 25 μM IPTG. pBRα-MreB plasmids were isolated from candidates that were down for λCI-CbtA interaction but maintained >60% λCI-RodZ$_{NTD}$, sequenced, and re-tested by β-galactosidase assay.

All β-galactosidase assays were performed in microtitre plates with a microtitre plate reader as described in Chapter 2 of this dissertation and in (67). All assays were done in triplicate and most were repeated independently at least twice. For some α-MreB mutants shown in Table 4.1 that had no effect on λCI-CbtA interaction (V121E, R188D, N200A, G266E, V273E) the experiment was done only once in triplicate; however most mutants shown in Table 4.1 were assayed at least twice. All values shown in this chapter are from a single representative experiment and represent averages of triplicate measurements. Fold-change values were calculated by normalizing to the highest relevant empty vector control. "+" and "-" designations in Table 4.1 were assigned based on % interaction as compared to the interaction of wild-type α-MreB. The normalized fold-change value for each mutant interaction was divided by the fold-change value for the wild-type interaction and multiplied by 100.

Complementation studies with *mreB* mutant alleles

Strain FB30/pFB174 was found to support robust rod-shaped growth in M9 minimal medium supplemented with 0.2-0.5% arabinose at 37 ºC. FB30/pFB174 was transformed with pMLB1113, corrected pFB149, pDH278, pDH280, pDH281, pDH332, and pDH333; transformants were selected on M9 plates (0.2% arabinose, 0.2% casamino acids, 1 mM $MgSO_4$) and grown overnight at 37 ºC. Overnight cultures were grown in M9 medium (0.2% maltose, 0.2% casamino acids, 0.5% arabinose, 1 mM $MgSO_4$) at 37 ºC. The following morning, cells were harvested by centrifugation to remove overnight medium, and resuspended in M9 maltose (0.2% maltose, 0.2% casamino acids). This resuspended culture was used as inoculum for subculturing. 5 mL M9 maltose cultures supplemented with 0.5% arabinose, 250 µM IPTG, or 0.1% glucose were inoculated to a starting OD600 of 0.03-0.05. All cultures were grown in test tubes at 37 ºC. It took ~5 hrs hours for MreBCD depletion to occur in strains with 0.1% glucose and in FB30/pFB174/pMLB1113 with 250 µM IPTG. All cultures were back-diluted 1:3 in the same medium after 3 hrs of growth to keep them in mid log phase for imaging. After 5 hrs, cells were mounted on 2% agarose pads and imaged as described in Chapter 2. In Figure 4.5, only cells grown in the presence of IPTG are shown. All cells grown in arabinose maintained rod-shape; all cells grown in glucose became spherical. Cells also became spherical just in the absence of arabinose (see pMLB1113 in Figure 4.5), indicating glucose is not necessary for depletion.

The same cultures described above grown in the presence of 0.5% arabinose were used for spot dilution assay. Once cultures had reached an OD600 of ~0.7-0.8, cells were harvested by centrifugation, and resuspended in M9 maltose without arabinose. Cultures were normalized to the same OD600 value, several 1:10 serial dilutions were made in sterile phosphate buffered saline (PBS), and 5 µL of each culture was spotted on LB (KanCmCarb) plates supplemented with 0.5% arabinose, 0.1% glucose, or 250 µM IPTG. Plates were incubated overnight at 37 ºC. All cultures were unable to grow on 0.1% glucose and are not shown in Figure 4.5.

Assessing CbtA-F65S and YpjF-F65S-mediated cell morphology changes

Strains DH118/pFB149 and DH118/pDH278 were transformed with plasmids pBAD33, pDH212, or pDH289. Transformants were selected on M9 maltose plates supplemented with Kan, Carb, Cam, and 250 μM IPTG, grown for 24-40 hrs at 30 ºC. Overnight cultures were grown in 3 mL M9 maltose supplemented with Kan, Carb, Cam, and 250 μM IPTG at 30 ºC for ~16 hrs. The next morning, overnight cultures were back diluted to a starting OD600 of 0.03 into LB supplemented with Cm, Carb, and 250 μM IPTG and grown for 1 hr at 30 ºC (until reaching an OD600 ~0.08). Cultures were then induced with 0.2% arabinose for 2 hrs at 30 ºC. After 2 hrs, cells were mounted on 2% agarose pads and imaged as described in Chapter 2.

For the spot dilution assay shown in Figure 4.6, the same M9 maltose overnight cultures described above were back diluted 1:100 into fresh M9 maltose supplemented with Cm, Carb, and 250 μM IPTG. Cultures were grown at 30 ºC for 5 hrs until reaching an OD600 of ~0.7. Cultures were normalized to the same OD600 value, several 1:10 serial dilutions were made in sterile phosphate buffered saline (PBS), and 5 μL of each culture was spotted on LB plates supplemented with Kan, Cm, Carb, and 250 μM IPTG, with or without 0.2% arabinose. Plates were incubated at room temperature for two nights.

Table 4.2: Strains used in this study

Strain	Description	Reference/ Source
NEB5-α F'I^q	DH5-α derivative containing an F' (Tet^R) bearing *lacI^q*	New England Biolabs
BW27785	Δ(*araB-araD*)*567* Δ*lacZ4787*(::*rrnB-3*) LAM-Δ(*araH-araF*)570(::FRT) *ΔaraEp-532*::FRT φ(*Pcp18-araE534*) Δ(*rhaB-rhaD*)*568 hsdR514*	(69)
FW102 O$_L$2-62	FW102 (68) containing an F' (Kan^R) bearing the p*lac*OL$_2$–62-*lacZ* fusion in which the λCI operator is centered at position –62 upstream of the *lac* promoter	(66)
BN30 (FW102 O$_L$2-42)	FW102 (68) containing an F' (Kan^R) bearing the p*lac*OL$_2$–42-*lacZ* fusion in which the λCI operator is centered at position –42 upstream of the *lac* promoter	(62,63); Bryce Nickels
FB30/pFB174	TB28 (MG1655 Δ*lacIZYA*::*frt*) *ΔmreBCD::kan* transformed with Cm^R plasmid pFB174 (*pBAD-mreBCD-LE)*	(23) ;Generous gift of T. Bernhardt
DH118/pFB149	BW27785 *ΔmreBCD::kan* transformed with Carb^R plasmid pFB149 (*plac-mreBCD-LE)*	This study
DH118/pDH278	BW27785 *ΔmreBCD::kan* transformed with Carb^R plasmid pDH278 (*plac-mreB-E262G mreCD-LE)*	This study

Table 4.3: Plasmids used in this study

Plasmid	Description	Reference/ Source
pBRα	Encodes the full-length α subunit of RNAP under the control of tandem p*lacUV5* and p*lpp* promoters; confers $Carb^R$	(63)
pACλCI	Encodes λCI (residues 1-236) under the control of *lacUV5* promoter; confers Cm^R	(63)
pACλCI-CbtA (pMT154)	Encodes λCI fused by a three-alanine linker to full-length CbtA under the control of *lacUV5* promoter; confers Cm^R	This study; M. Tavag
pACλCI-CbtA-F65S (pMT180)	Encodes λCI fused by a three-alanine linker to CbtA-F65S under the control of *lacUV5* promoter; confers Cm^R	This study; M. Tavag
pACλCI-YpjF (pMT170)	Encodes λCI fused by a three-alanine linker to YpjF under the control of *lacUV5* promoter; confers Cm^R	This study; M. Tavag
pACλCI-$RodZ_{NTD}$ (pDH238)	Encodes λCI fused by a three-alanine linker to the NTD of RodZ (residues 2-84) under the control of *lacUV5* promoter; confers Cm^R	This study
pBRα-MreB (pMT151)	Encodes residues 1-248 of α fused by a three-alanine linker to full-length *E. coli* MreB under the control of tandem p*lacUV5* and p*lpp* promoters; confers $Carb^R$	This study; M. Tavag
pBRα-MreB mutant plasmids isolated in two-hybrid screen: V173A (pDH256) I126V (pDH257) E262G (pDH258) E196G (pDH259)	All plasmids encode residues 1-248 of α fused by a three-alanine linker to full-length *E. coli* MreB mutant indicated under the control of tandem p*lacUV5* and p*lpp* promoters; confers $Carb^R$	This study
Additional pBRα-MreB mutant plasmids: E196K (pDH271) E262K (pDH272) C113S/C278S/C324S (pDH287) C113S (pDH290) C278S (pDH291) C324S (pDH292) V121E (pDH293) R127D (pDH294) E128K (pDH295) R124D (pDH298) A125D (pDH299) F84A (pDH300)	All plasmids encode residues 1-248 of α fused by a three-alanine linker to full-length *E. coli* MreB mutant indicated under the control of tandem p*lacUV5* and p*lpp* promoters; confers $Carb^R$	This study

Table 4.3 (Continued)

Plasmid	Description	Reference/ Source
Additional pBRα-MreB mutant plasmids: K77D (pDH301) D78K (pDH302) D192K (pDH303) S269F (pDH305) R204D (pDH306) R188D (pDH307) G266V (pDH308) N200A (pDH309) V273E (pDH310) E319K (pDH318) S269K (pDH330)	All plasmids encode residues 1-248 of α fused by a three-alanine linker to full-length *E. coli* MreB mutant indicated under the control of tandem p*lacUV5* and p*lpp* promoters; confers Carb^R	This study
pFB149	ColE1 origin; Encodes wild-type MreBCD under the control of the *lac* promoter. Residues LE are appended to the end of the MreD sequence; *lacI*^{q}; confers Carb^R; was re-cloned to remove mutations	(23)
pMLB1113	ColE1 origin; Encodes *lacZ* under the control of the *lac* promoter; *lacI*^{q}; confers Carb^R	(70)
pDH278	ColE1 origin; Encodes MreB-E262G and MreCD under the control of the *lac* promoter. Residues LE are appended to the end of the MreD sequence; *lacI*^{q}; confers Carb^R	This study
pDH280	ColE1 origin; Encodes MreB-V173A and MreCD under the control of the *lac* promoter. Residues LE are appended to the end of the MreD sequence; *lacI*^{q}; confers Carb^R	This study
pDH281	ColE1 origin; Encodes MreB-I126V and MreCD under the control of the *lac* promoter. Residues LE are appended to the end of the MreD sequence; *lacI*^{q}; confers Carb^R	This study
pDH332	ColE1 origin; Encodes MreB-S269F and MreCD under the control of the *lac* promoter. Residues LE are appended to the end of the MreD sequence; *lacI*^{q}; confers Carb^R	This study
pDH333	ColE1 origin; Encodes MreB-F84A and MreCD under the control of the *lac* promoter. Residues LE are appended to the end of the MreD sequence; *lacI*^{q}; confers Carb^R	This study

Table 4.3 (Continued):

Plasmid	Description	Reference/ Source
pBAD33	*araC*; pACYC 184 origin; *pBAD* promoter with no insert; confers Cm^R	(71)
pDH212	*araC*; pACYC 184 origin; *pBAD-cbtA-F65S*; confers Cm^R	This study
pDH289	*araC*; pACYC 184 origin; *pBAD-ypjF-F65S*; confers Cm^R	This study

Table 4.4: Important oligonucleotides used in this study

Name	Sequence (5' to 3')	Description
oDH285	ATATATTCTAGATTATTTCGCCTCCGGATACTTAC	Reverse primer used to amplify *cbtA* for pBAD33; contains XbaI site
oDH286	ATATATCATATGAAAACATTACCTGTATTACCCGGG	Forward primer used to amplify *cbtA* for pBAD33; contains NdeI site
oDH289	AATTTCCTGCAGAATACCG	Anneals downstream of chromosomal *mreD*; used for PCR verification of *ΔmreBCD*
oDH298	ATATATGCGGCCGCATTGAAAAAATTTCGTGGCATG	Forward primer for amplification of *mreB*; contains NotI site
oDH299	ATATATGGATCCTTACTCTTCGCTGAACAGG	Reverse primer for amplification of *mreB*; contains BamHI site
oDH307	AAGTAAGCGGATTTTCTTTTCC	Anneals upstream of chromosomal *mreB*; used for PCR verification of *ΔmreBCD*
oDH336	ATATATGCGGCCGCAAATACTGAAGCCACGCACG	Forward primer for amplification of *rodZ*$_{NTD}$; contains NotI site
oDH337	ATATATGGATCCTTATTCCAGCCCTGGCAGCAG	Reverse primer for amplification of *rodZ*$_{NTD}$; contains BamHI site
oDH346F	GGTGGTGACCGTTTCGACAAAGCTATCATCAACTATGTG	*mreB* mutagenic primer; E196K
oDH347R	CACATAGTTGATGATAGCTTTGTCGAAACGGTCACCACC	*mreB* mutagenic primer; E196K
oDH348F	ATCCTCGAAGCACTGCAGAAACCGCTGACCGGTATTGTG	*mreB* mutagenic primer; E262K
oDH349R	CACAATACCGGTCAGCGGTTTCTGCAGTGCTTCGAGGAT	*mreB* mutagenic primer; E262K
oDH355	AAGTTATGCGTATTCTCG	Anneals between *mreB* and *mreC*; used to sequence pFB149
oDH357F	GGTGGTACCACTGAAGCTGCTGTTATCTCCTTG	*mreB* mutagenic primer; V173A
oDH358R	CAAGGAGATAACAGCAGCTTCAGTGGTACCACC	*mreB* mutagenic primer; V173A
oDH359F	GTTGAACGCCGCGCAGTTCGTGAATCCGCG	*mreB* mutagenic primer; I126V
oDH360R	CGCGGATTCACGAACTGCGCGGCGTTCAAC	*mreB* mutagenic primer; I126V
oDH361F	GTGGTGACCGTTTCGACGGAGCTATCATCAACTATG	*mreB* mutagenic primer; E196G

Table 4.4 (Continued)

Name	Sequence (5' to 3')	Description
oDH362R	CATAGTTGATGATAGCTCCGTCGAAACGGTCACCAC	*mreB* mutagenic primer; E196G
oDH363F	CTCGAAGCACTGCAGGGACCGCTGACCGGTATTG	*mreB* mutagenic primer; E262G
oDH364R	CAATACCGGTCAGCGGTCCCTGCAGTGCTTCGAG	*mreB* mutagenic primer; E262G
oDH369	GCGTCGAGCCGCTGATCAG	Anneals within *mreD* sequence downstream of BamHI site
oDH372	ATATATTCTAGACAGCTTTCAGGATTATCCCTTAGTATGTTGAAAAAATTTCGTG	Forward primer to amplify *mreB* sequence for pFB149 derivatives; contains XbaI site
oDH373	CAGGAAACAGCTATGACCATG	Sequencing primer for pFB149 derivatives; anneals upstream of *mreB* and XbaI site
oDH374	TGTGCTGCAAGGCGATTAAG	Sequencing primer for pFB149 derivatives; anneals downstream of *mreD*
oDH375	CGGCGGCGACCTGTTCAG	Sequencing primer for pFB149 derivatives; anneals upstream of *mreC*
oDH380	ATATATCATATGAACACTCTACCTGCTACAATTTCG	Forward primer used to amplify *ypjF* for pBAD33; contains NdeI site
oDH381	ATATATTCTAGATTATTTCACATTAGTTTTTAG	Reverse primer used to amplify *cbtA* for pBAD33; contains XbaI site
oDH382F	GCCCGCGCGTTCTGGTTAGCGTGCCGGTTGGCGCGACCCAG	*mreB* mutagenic primer; C113S
oDH383R	CTGGGTCGCGCCAACCGGCACGCTAACCAGAACGCGCGGGC	*mreB* mutagenic primer; C113S
oDH384F	GGTTGCACTGGAACAGAGCCCGCCGGAACTGGCTTCCG	*mreB* mutagenic primer; C278S
oDH385R	CGGAAGCCAGTTCCGGCGGGCTCTGTTCCAGTGCAACC	*mreB* mutagenic primer; C278S
oDH386F	GCTGAAGACCCGCTGACCAGCGTGGCGCGCGGTGGCGGC	*mreB* mutagenic primer; C324S
oDH387R	GCCGCCACCGCGCGCCACGCTGGTCAGCGGGTCTTCAGC	*mreB* mutagenic primer; C324S

Table 4.4 (Continued)

Name	Sequence (5' to 3')	Description
oDH388F	GCCGGTTGGCGCGACCCAGGAAGAACGCCGCGCAATTCG	*mreB* mutagenic primer; V121E
oDH389R	CGAATTGCGCGGCGTTCTTCCTGGGTCGCGCCAACCGGC	*mreB* mutagenic primer; V121E
oDH390F	CCCAGGTTGAACGCCGCGCAGACCGTGAATCCGCGCAGGG	*mreB* mutagenic primer; R127D
oDH391R	CCCTGCGCGGATTCACGGTCTGCGCGGCGTTCAACCTGGG	*mreB* mutagenic primer; R127D
oDH392F	GAACGCCGCGCAATTCGTAAATCCGCGCAGGGCGCTGG	*mreB* mutagenic primer; E128K
oDH393R	CCAGCGCCCTGCGCGGATTTACGAATTGCGCGGCGTTC	*mreB* mutagenic primer; E128K
oDH399F	CGACCCAGGTTGAACGCGACGCAATTCGTGAATCCGCG	*mreB* mutagenic primer; R124D
oDH400R	CGCGGATTCACGAATTGCGTCGCGTTCAACCTGGGTCG	*mreB* mutagenic primer; R124D
oDH401F	GACCCAGGTTGAACGCCGCGACATTCGTGAATCCGCGCAG	*mreB* mutagenic primer; A125D
oDH402R	CTGCGCGGATTCACGAATGTCGCGGCGTTCAACCTGGGTC	*mreB* mutagenic primer; A125D
oDH403F	GACGGCGTTATCGCCGACGCCTTCGTGACTGAAAAAATG	*mreB* mutagenic primer; F84A
oDH404R	CATTTTTTCAGTCACGAAGGCGTCGGCGATAACGCCGTC	*mreB* mutagenic primer; F84A
oDH405F	GCTGCCATTCGCCCAATGGACGACGGCGTTATCGCCGAC	*mreB* mutagenic primer; K77D
oDH406R	GTCGGCGATAACGCCGTCGTCCATTGGGCGAATGGCAGC	*mreB* mutagenic primer; K77D
oDH407F	GCCATTCGCCCAATGAAAAAAGGCGTTATCGCCGACTTC	*mreB* mutagenic primer; D78K
oDH408R	GAAGTCGGCGATAACGCCTTTTTTCATTGGGCGAATGGC	*mreB* mutagenic primer; D78K
oDH409F	CTGTGCGCATTGGTGGTAAACGTTTCGACGAAGCTATC	*mreB* mutagenic primer; D192K

Table 4.4 (Continued)

Name	Sequence (5' to 3')	Description
oDH410R	GATAGCTTCGTCGAAACGTTTACCACCAATGCGCACAG	*mreB* mutagenic primer; D192K
oDH413F	CGCTGACCGGTATTGTGTTCGCGGTAATGGTTGCACTG	*mreB* mutagenic primer; S269F
oDH414R	CAGTGCAACCATTACCGCGAACACAATACCGGTCAGCG	*mreB* mutagenic primer; S269F
oDH415F	CATCAACTATGTGCGTGATAATTACGGTTCTCTGATCG	*mreB* mutagenic primer; R204D
oDH416R	CGATCAGAGAACCGTAATTATCACGCACATAGTTGATG	*mreB* mutagenic primer; R204D
oDH417F	GTTTACTCCTCTTCTGTGGACATTGGTGGTGACCGTTTCG	*mreB* mutagenic primer; R188D
oDH418R	CGAAACGGTCACCACCAATGTCCACAGAAGAGGAGTAAAC	*mreB* mutagenic primer; R188D
oDH419F	CTGCAGGAACCGCTGACCGAAATTGTGAGCGCGGTAATG	*mreB* mutagenic primer; G266E
oDH420R	CATTACCGCGCTCACAATTTCGGTCAGCGGTTCCTGCAG	*mreB* mutagenic primer; G266E
oDH421F	GTTTCGACGAAGCTATCATCGCATATGTGCGTCGTAATTACG	*mreB* mutagenic primer; N200A
oDH422R	CGTAATTACGACGCACATATGCGATGATAGCTTCGTCGAAAC	*mreB* mutagenic primer; N200A
oDH423F	GTATTGTGAGCGCGGTAATGGAAGCACTGGAACAGTGCCCG	*mreB* mutagenic primer; V273E
oDH424R	CGGGCACTGTTCCAGTGCTTCCATTACCGCGCTCACAATAC	*mreB* mutagenic primer; V273E
oDH438F	CCGGCATTCCAGTCGTTGTTGCTAAAGACCCGCTGACCTGTGTGG	*mreB* mutagenic primer; E319K
oDH439R	CCACACAGGTCAGCGGGTCTTTAGCAACAACGACTGGAATGCCGG	*mreB* mutagenic primer; E319K
oDH452F	CCGCTGACCGGTATTGTGAAAGCGGTAATGGTTGCACTG	*mreB* mutagenic primer; S269K
oDH453R	CAGTGCAACCATTACCGCTTTCACAATACCGGTCAGCGG	*mreB* mutagenic primer; S269K

Chapter 4.5: References

1. Höltje JV. Growth of the stress-bearing and shape-maintaining murein sacculus of Escherichia coli. Microbiology and Molecular Biology Reviews. 1998 Mar;62(1):181–203.

2. Margolin W. Sculpting the Bacterial Cell. Curr Biol. Elsevier Ltd; 2009 Sep 15;19(17):R812–22.

3. Typas A, Banzhaf M, Gross CA, Vollmer W. From the regulation of peptidoglycansynthesis to bacterial growth andmorphology. Nat Rev Micro. Nature Publishing Group; 2011 Dec 28;10(2):123–36.

4. de Boer PA. Advances in understanding E. coli cell fission. Current Opinion in Microbiology. 2010 Dec;13(6):730–7.

5. Lutkenhaus J, Pichoff S, Du S. Bacterial cytokinesis: From Z ring to divisome. Robinson DN, Bement WM, Balasubramanian MK, Sanger JW, editors. Cytoskeleton. 2012 Aug 30;69(10):778–90.

6. Erickson HP, Anderson DE, Osawa M. FtsZ in Bacterial Cytokinesis: Cytoskeleton and Force Generator All in One. Microbiology and Molecular Biology Reviews. 2010 Nov 30;74(4):504–28.

7. White CL, Kitich A, Gober JW. Positioning cell wall synthetic complexes by the bacterial morphogenetic proteins MreB and MreD. Mol Microbiol. 2010 Mar 10;76(3):616–33.

8. Kawai Y, Daniel RA, Errington J. Regulation of cell wall morphogenesis in Bacillus subtilisby recruitment of PBP1 to the MreB helix. Mol Microbiol. 2009 Mar;71(5):1131–44.

9. Kruse T, Bork-Jensen J, Gerdes K. The morphogenetic MreBCD proteins of Escherichia coli form an essential membrane-bound complex. Mol Microbiol. 2004 Oct 6;55(1):78–89.

10. Bendezú FO, Hale CA, Bernhardt TG, de Boer PAJ. RodZ (YfgA) is required for proper assembly of the MreB actin cytoskeleton and cell shape in E. coli. EMBO J. 2008 Dec 11;28(3):193–204.

11. van den Ent F, Johnson CM, Persons L, de Boer P, we JLO. Bacterial actin MreB assembles in complex with cell shape protein RodZ. EMBO J. Nature Publishing Group; 2010 Feb 18;29(6):1081–90.

12. Jones L, Carballido-Lopez R, Errington J. Control of cell shape in bacteria: helical, actin-like filaments in Bacillus subtilis. Cell. 2001.

13. Eun Y-J, Kapoor M, Hussain S, Garner EC. Bacterial Filament Systems: Toward Understanding Their Emergent Behavior and Cellular Functions. Journal of Biological Chemistry. 2015 Jul 9;290(28):17181–9.

14. Chastanet A, Carballido-Lopez R. The actin-like MreB proteins in Bacillus subtilis: a new turn. Front Biosci (Schol Ed). 2012;4:1582–606.

15. Wachi M, Doi M, Tamaki S, Park W, Nakajima-Iijima S, Matsuhashi M. Mutant isolation and molecular cloning of mre genes, which determine cell shape, sensitivity to mecillinam, and amount of penicillin-binding proteins in Escherichia coli. J Bacteriol. 1987 Nov;169(11):4935–40.

16. Doi M, Wachi M, Ishino F, Tomioka S, Ito M, Sakagami Y, et al. Determinations of the DNA sequence of the mreB gene and of the gene products of the mre region that function in formation of the rod shape of Escherichia coli cells. J Bacteriol. 1988 Oct;170(10):4619–24.

17. Levin PA, Margolis PS, Setlow P, Losick R, Sun D. Identification of Bacillus subtilis genes for septum placement and shape determination. J Bacteriol. 1992 Nov;174(21):6717–28.

18. Abhayawardhane Y, Stewart GC. Bacillus subtilis possesses a second determinant with extensive sequence similarity to the Escherichia coli mreB morphogene. J Bacteriol. 1995 Feb;177(3):765–73.

19. Matsuzawa H, Hayakawa K, Sato T, Imahori K. Characterization and genetic analysis of a mutant of Escherichia coli K-12 with rounded morphology. J Bacteriol. 1973 Jul;115(1):436–42.

20. Waxman DJ, Strominger JL. Penicillin-binding proteins and the mechanism of action of beta-lactam antibiotics. Annu Rev Biochem. 1983;52:825–69.

21. Gitai Z, Dye NA, Reisenauer A, Wachi M, Shapiro L. MreB Actin-Mediated Segregation of a Specific Region of a Bacterial Chromosome. Cell. 2005 Feb;120(3):329–41.

22. IWAI N, NAGAI K, Wachi M. Novel S-benzylisothiourea compound that induces spherical cells in Escherichia coli probably by acting on a rod-shape-determining protein(s) other than penicillin-binding protein 2. Biosci Biotechnol Biochem. 2002 Dec;66(12):2658–62.

23. Bendezu FO, de Boer PAJ. Conditional Lethality, Division Defects, Membrane Involution, and Endocytosis in mre and mrd Shape Mutants of Escherichia coli. J Bacteriol. 2008 Feb 20;190(5):1792–811.

24. Formstone A, Errington J. A magnesium-dependent mreBnull mutant: implications for the role of mreBin Bacillus subtilis. Mol Microbiol. 2005 Jan 26;55(6):1646–57.

25. Kawai Y, Asai K, Errington J. Partial functional redundancy of MreB isoforms, MreB, Mbl and MreBH, in cell morphogenesis of Bacillus subtilis. Mol Microbiol. 2009 Aug;73(4):719–31.

26. Daniel RA, Errington J. Control of cell morphogenesis in bacteria: two distinct ways to make a rod-shaped cell. Cell. 2003 Jun 13;113(6):767–76.

27. Zapun A, Vernet T, Pinho MG. The different shapes of cocci. FEMS Microbiology Reviews. 2008 Mar 1;32(2):345–60.

28. Begg KJ, Donachie WD. Division planes alternate in spherical cells of Escherichia coli. J Bacteriol. 1998 May;180(9):2564–7.

29. van den Ent F, Amos LA, Löwe J. Prokaryotic origin of the actin cytoskeleton. Nature. 2001 Sep 6;413(6851):39–44.

30. van den Ent F, Izoré T, Bharat TA, Johnson CM, Lowe J. Bacterial actin MreB forms antiparallel double filaments. eLife. 2014;3:e02634.

31. Bork P, Sander C, Valencia A. An ATPase domain common to prokaryotic cell cycle proteins, sugar kinases, actin, and hsp70 heat shock proteins. Proc Natl Acad Sci USA. 1992 Aug 15;89(16):7290–4.

32. Shih Y-L, Le T, Rothfield L. Division site selection in Escherichia coli involves dynamic redistribution of Min proteins within coiled structures that extend between the two cell poles. Proc Natl Acad Sci USA. 2003 Jun 24;100(13):7865–70.

33. Figge RM, Divakaruni AV, Gober JW. MreB, the cell shape-determining bacterial actin homologue, co-ordinates cell wall morphogenesis in Caulobacter crescentus. Mol Microbiol. 2004 Mar;51(5):1321–32.

34. Gitai Z, Dye N, Shapiro L. An actin-like gene can determine cell polarity in bacteria. Proc Natl Acad Sci USA. 2004 Jun 8;101(23):8643–8.

35. Vats P, Rothfield L. Duplication and segregation of the actin (MreB) cytoskeleton during the prokaryotic cell cycle. Proc Natl Acad Sci USA. 2007 Nov 6;104(45):17795–800.

36. Tiyanont K, Doan T, Lazarus MB, Fang X, Rudner DZ, Walker S. Imaging peptidoglycan biosynthesis in Bacillus subtilis with fluorescent antibiotics. Proc Natl Acad Sci USA. 2006 Jul 18;103(29):11033–8.

37. Leaver M, Errington J. Roles for MreC and MreD proteins in helical growth of the cylindrical cell wall in Bacillus subtilis. Mol Microbiol. 2005 Jul 22;57(5):1196–209.

38. Bremer A, Aebi U. The structure of the F-actin filament and the actin molecule. Current Opinion in Cell Biology. 1992 Feb;4(1):20–6.

39. van den Ent F, Löwe J. Crystal structure of the cell division protein FtsA from Thermotoga maritima. EMBO J. 2000 Oct 16;19(20):5300–7.

40. Bean GJ, Flickinger ST, Westler WM, McCully ME, Sept D, Weibel DB, et al. A22 Disrupts the Bacterial Actin Cytoskeleton by Directly Binding and Inducing a Low-Affinity State in MreB. Biochemistry. 2009 Jun 9;48(22):4852–7.

41. Defeu Soufo HJ, Graumann PL. Dynamic movement of actin-like proteins within bacterial cells. EMBO Rep. 2004 Aug;5(8):789–94.

42. Carballido-Lopez R, Errington J. The bacterial cytoskeleton: in vivo dynamics of the actin-like protein Mbl of Bacillus subtilis. Dev Cell. 2003 Jan;4(1):19–28.

43. Kim SY, Gitai Z, Kinkhabwala A, Shapiro L, Moerner WE. Single molecules of the bacterial actin MreB undergo directed treadmilling motion in Caulobacter crescentus. Proc Natl Acad Sci USA. 2006 Jul 18;103(29):10929–34.

44. Bean GJ, Amann KJ. Polymerization Properties of the Thermotoga maritimaActin MreB: Roles of Temperature, Nucleotides, and Ions †. Biochemistry. 2008 Jan;47(2):826–35.

45. Mayer JA, Amann KJ. Assembly properties of the Bacillus subtilisactin, MreB. Cell Motil Cytoskeleton. 2009 Feb;66(2):109–18.

46. Salje J, van den Ent F, de Boer P, Lowe J. Direct Membrane Binding by Bacterial Actin MreB. Molecular Cell. Elsevier Inc; 2011 Aug 5;43(3):478–87.

47. Nurse P, Marians KJ. Purification and characterization of Escherichia coli MreB protein. Journal of Biological Chemistry. 2013 Feb 1;288(5):3469–75.

48. Swulius MT, Chen S, Ding HJ, Li Z, Briegel A, Pilhofer M, et al. Biochemical and Biophysical Research Communications. Biochemical and Biophysical Research Communications. Elsevier Inc; 2011 Apr 22;407(4):650–5.

49. Swulius MT, Jensen GJ. The Helical MreB Cytoskeleton in Escherichia coli MC1000/pLE7 Is an Artifact of the N-Terminal Yellow Fluorescent Protein Tag. J Bacteriol. 2012 Nov 9;194(23):6382–6.

50. Garner EC, Bernard R, Wang W, Zhuang X, Rudner DZ, Mitchison T. Coupled, Circumferential Motions of the Cell Wall Synthesis Machinery and MreB Filaments in B. subtilis. Science. 2011 Jul 7;333(6039):222–5.

51. Domínguez-Escobar J, Chastanet A, Crevenna AH, Fromion V, Wedlich-Söldner R, Carballido-Lopez R. Processive movement of MreB-associated cell wall biosynthetic complexes in bacteria. Science. 2011 Jul 8;333(6039):225–8.

52. van Teeffelen S, Wang S, Furchtgott L, Huang KC, Wingreen NS, Shaevitz JW, et al. The bacterial

actin MreB rotates, and rotation depends on cell-wall assembly. Proc Natl Acad Sci USA. 2011 Sep 20;108(38):15822–7.

53. Reimold C, Defeu Soufo HJ, Dempwolff F, Graumann PL. Motion of variable-length MreB filaments at the bacterial cell membrane influences cell morphology. Molecular Biology of the Cell. 2013 Jul 30;24(15):2340–9.

54. Olshausen von P, Soufo HJD, Wicker K, Heintzmann R, Graumann PL, Rohrbach A. Superresolution Imaging of Dynamic MreB Filaments in B. subtilis—A Multiple-Motor-Driven Transport? Biophysj. Biophysical Society; 2013 Sep 3;105(5):1171–81.

55. Morgenstein RM, Bratton BP, Nguyen JP, Ouzounov N, Shaevitz JW, Gitai Z. RodZ links MreB to cell wall synthesis to mediate MreB rotation and robust morphogenesis. Proc Natl Acad Sci USA. 2015 Oct 6;112(40):12510–5.

56. Ursell TS, Nguyen J, Monds RD, Colavin A, Billings G, Ouzounov N, et al. Rod-like bacterial shape is maintained by feedback between cell curvature and cytoskeletal localization. Proc Natl Acad Sci USA. 2014 Mar 18;111(11):E1025–34.

57. Popp D, Narita A, Maeda K, Fujisawa T, Ghoshdastider U, Iwasa M, et al. Filament structure, organization, and dynamics in MreB sheets. Journal of Biological Chemistry. 2010 May 21;285(21):15858–65.

58. Yakhnina AA, Gitai Z. The small protein MbiA interacts with MreB and modulates cell shape in Caulobacter crescentus. Mol Microbiol. 2012 Jul 25;85(6):1090–104.

59. Duan Y, Sperber AM, Herman JK. YodL and YisK possess shape-modifying activities that are suppressed by mutations in Bacillus subtilis mreBand mbl. J Bacteriol. 2016 May 23;:JB.00183–16.

60. Molshanski-Mor S, Yosef I, Kiro R, Edgar R, Manor M, Gershovits M, et al. Revealing bacterial targets of growth inhibitors encoded by bacteriophage T7. Proc Natl Acad Sci USA. 2014 Dec 15;:201413271.

61. Tan Q, Awano N, Inouye M. YeeV is an Escherichia coli toxin that inhibits cell division by targeting the cytoskeleton proteins, FtsZ and MreB. Mol Microbiol. 2011 Jan;79(1):109–18.

62. Castang S, Dove SL. High-order oligomerization is required for the function of the H-NS family member MvaT in Pseudomonas aeruginosa. Mol Microbiol. 2010 Nov;78(4):916–31.

63. Dove SL, Joung JK, Hochschild A. Activation of prokaryotic transcription through arbitrary protein-protein contacts. Nature. 1997 Apr 10;386(6625):627–30.

64. Fenton AK, Gerdes K. Direct interaction of FtsZ and MreB is required for septum synthesis and cell division in Escherichia coli. EMBO J. 2013 Jun 11;32(13):1953–65.

65. Masuda H, Tan Q, Awano N, Wu K-P, Inouye M. YeeU enhances the bundling of cytoskeletal polymers of MreB and FtsZ, antagonizing the CbtA (YeeV) toxicity in Escherichia coli. Mol Microbiol. 2012 May 17;84(5):979–89.

66. Deaconescu AM, Chambers AL, Smith AJ, Nickels BE, Hochschild A, Savery NJ, et al. Structural Basis for Bacterial Transcription-Coupled DNA Repair. Cell. 2006 Feb;124(3):507–20.

67. Thibodeau SA, Fang R, Joung JK. High-throughput beta-galactosidase assay for bacterial cell-based reporter systems. BioTechniques. 2004 Mar;36(3):410–5.

68. Whipple FW. Genetic analysis of prokaryotic and eukaryotic DNA-binding proteins in Escherichia coli. Nucleic Acids Research. 1998 Aug 15;26(16):3700–6.

69. Khlebnikov A, Datsenko KA, Skaug T. Homogeneous expression of the PBAD promoter in Escherichia coli by constitutive expression of the low-affinity high-capacity AraE transporter. …. 2001.

70. de Boer PA, Crossley RE, Rothfield LI. A division inhibitor and a topological specificity factor coded for by the minicell locus determine proper placement of the division septum in E. coli. Cell. 1989 Feb 24;56(4):641–9.

71. Guzman LM, Belin D, Carson MJ, Beckwith J. Tight regulation, modulation, and high-level expression by vectors containing the arabinose PBAD promoter. J Bacteriol. 1995 Jul;177(14):4121–30.

Chapter 5: Mechanistic insights and contextual unknowns

Attributions: I wrote this chapter in its entirety with helpful editing advice from my advisor, Ann Hochschild.

Chapter 5.1: Summary of our findings and mechanistic considerations

In this dissertation, I have presented a genetic dissection of the interactions between the CbtA toxin and its two cellular targets, FtsZ and MreB. Two methods were critical for our characterization of these two interactions. First, our transcription-based bacterial two-hybrid system served as an effective tool to detect and assay a variety of protein-protein interactions and to determine the specific effects of genetic modifications on these interactions. This system was also adapted as a versatile genetic screening platform, enabling the isolation of several variants with informative two-hybrid binding profiles. The second method that aided our genetic analysis was the microscopic observation of cellular morphology. The distinct morphological phenotypes produced by inhibition of cell division, cell elongation, or both allowed us to easily discern the physiological consequences of overproduction of multiple CbtA variants in assorted genetic backgrounds. The integration of these two strategies established important connections between CbtA binding and inhibitory function.

Prior to the genetic analysis shown here, it was known that overproduction of CbtA causes a distinctive lemon-like morphology (1) indicative of dual inhibition of cell division and cell elongation pathways (2); it had also been suggested that CbtA interacts with two bacterial cytoskeletal elements (1). Through concerted use of the two methods mentioned above, we have confirmed that CbtA mediates separable and functionally relevant interactions with FtsZ and MreB. As described in Chapter 2 of this dissertation, we identified two CbtA variants, CbtA-F65S and CbtA-R15C, both of which bind only a single target and produce morphologies consistent with exclusive inhibition of cell division and cell elongation pathways, respectively. Furthermore, as shown in Chapters 3 and 4 of this dissertation, our integrated approach revealed important determinants of CbtA-binding, allowing for the identification and validation of residues within both targets that are necessary for CbtA inhibition. Finally, the use of our two-hybrid assay in conjunction with microscopy enabled us to genetically dissect the toxicity of two CbtA homologs, YpjF and YkfI, providing the first demonstration that the three members of this toxin family inhibit growth in a conserved manner.

Altogether, the data presented in this dissertation support a model in which the CbtA toxin independently binds and inhibits the cell division regulator FtsZ and the cell elongation factor MreB. Our characterization of the CbtA-FtsZ interaction identified the H6/H7 loop of *E. coli* FtsZ as the inhibitory surface directly bound by CbtA. Similar genetic analyses identified the MreB double protofilament interface as the putative surface targeted by CbtA. The FtsZ H6/H7 loop and the flat side of MreB are necessary for CbtA-binding and inhibition of FtsZ and MreB, respectively. Both of these surfaces have also been shown previously to be important for the proper assembly and function of the associated bacterial cytoskeletal element. The H6/H7 loop is found at the intra-protofilament interface formed by FtsZ monomers and has been implicated both in the longitudinal assembly and lateral interactions of FtsZ filaments (3-5); formation of the MreB double filament via interaction of two adjacent filaments along their flat sides is required for MreB-directed cell elongation in *E. coli* (6). Thus, considering our genetic data and the essential functions of these surfaces, the H6/H7 loop of FtsZ and the double protofilament interface of MreB are highly plausible sites of CbtA inhibition. As discussed in Chapter 3, we believe that this work represents the first report of a negative FtsZ regulator binding within the N-terminal core domain of the FtsZ subunit and provides the first description of the H6/H7 loop as an important inhibitory surface. Additionally, although further evidence is needed to validate that CbtA directly binds the flat side of MreB, the work presented in Chapter 4 of this dissertation suggests that disruption of the MreB double filament, which is the mechanism employed by the MreB-specific antibiotic A22 (6), may be a common strategy for blocking cell elongation.

It is surprising that the small CbtA protein (124 amino acids) can so potently inhibit both FtsZ and MreB, especially considering the lack of sequence or structural homology shared by these two targets. One obvious feature FtsZ and MreB have in common is their propensity to polymerize into dynamic filaments. Our identification of these specific FtsZ and MreB inhibitory surfaces suggests that the CbtA toxin may exploit this commonality and in both cases act by disrupting filament architecture. Tan et al. measured the effects of purified CbtA on the sedimentation efficiency of both FtsZ and MreB and saw a noticeable reduction in both cases; they also observed that CbtA decreased the GTPase activity of FtsZ but had no effect on the ATPase activity of MreB (1). These biochemical observations combined with our genetic data are consistent with a model in which i) CbtA disrupts polymerization of FtsZ into single filaments (as longitudinal assembly of FtsZ subunits is required for GTP hydrolysis (3-5,7)) and ii) CbtA allows MreB to polymerize into single filaments but blocks pairing of these filaments. To test this model, it will be important to repeat these polymerization and nucleotide hydrolysis assays, using wild-type CbtA, as well as the mutant variants we characterized (CbtA-F65S and CbtA-R15C); it will also be informative to observe by electron microscopy the morphologies of FtsZ and MreB filaments assembled in the presence of wild-type or mutant CbtA. The model would predict a significant reduction in the length or number of FtsZ filaments and the exclusive formation of single MreB filaments. Subsequent determination of mechanistic details, such as whether CbtA binds and sequesters monomers of one or both proteins or acts upon pre-assembled filaments, will require additional biochemical analyses. As co-crystal structures have proven invaluable in elucidating the mechanisms of FtsZ (e.g. SulA (8) and MciZ (9)) and MreB (e.g. A22 (6)) inhibitors, it would be a useful endeavor to determine the structure of the CbtA toxin both by itself and bound to each target. This type of structural analysis may also potentially provide an answer to the open question of whether a single CbtA molecule can simultaneously bind both targets.

Chapter 5.2: CbtA in context

The genetic characterization of CbtA toxicity presented here sheds light on the molecular consequences of CbtA production; however, neither the regulation nor the physiological significance of CbtA activity is well understood. CbtA is the toxin component of the CbtA-CbeA chromosomal toxin-antitoxin system, an affiliation that may provide some functional context. There is some disagreement as to the mechanism by which the CbeA (formerly YeeU) antitoxin neutralizes CbtA-mediated toxicity. Brown et al. first reported that growth rescue by CbeA occurred only when both genes were co-expressed in *cis* and required the 68-bp UTR (1,10). This, combined with the structural revelation that CbeA contains a RelE-like nucleic acid binding domain (2,11), suggested that CbeA may act as a post-transcriptional regulator of *cbtA* expression. However, in 2012, Masuda et al. demonstrated that co-expression of *cbtA* and *cbeA* in *trans* without the 68-bp UTR was sufficient for neutralization of CbtA (1,12). These authors further demonstrated that the CbeA antitoxin acts as a bundling factor for both FtsZ and MreB filaments, promoting stabilizing lateral interactions between filaments to overcome the toxic effects mediated by CbtA. Interestingly, CbeA overproduction was also able to counteract the toxic effects of A22 treatment and SulA overexpression *in vivo*, suggesting it is a general stabilizer of both MreB and FtsZ rather than a specific neutralizer of CbtA (3-5,12). In both reports, interaction between CbeA and CbtA was not detected (6,10,12).

The proposed function of CbeA as a positive regulator of FtsZ and MreB assembly is intriguing. Characterization of this stabilizing function may offer important insight into the mechanistic details of CbtA inhibition. Furthermore, as CbeA is the first reported positive modulator of MreB function elucidation of the manner in which it promotes higher-order assembly will be broadly pertinent. Although the reasons for the discrepancy in the data supporting *cis* versus *trans* function for CbeA are unclear, it is possible that CbeA may act both as a bundling factor and as a regulator of *cbtA* expression. Indeed Type II protein antitoxins exhibit dual functionalities, binding both to their cognate toxins and to operator sequences within their promoter regions (6,13). To gain a fuller understanding of the regulation of this toxin-antitoxin system and the context in which CbtA is active, it will be important to investigate what, if any, transcriptional or post-transcriptional role CbeA plays and whether it, like Type II antitoxins, is specifically targeted for degradation by cellular proteases.

A rudimentary mining of available expression data does not yield any obvious clues as to the physiological role of the CbeA-CbtA TA system or its homologous systems. All three systems in this TA family are encoded on separate cryptic prophage elements in the *E. coli* chromosome; thus, it seems logical that these elements evolved in the context of phage fitness. The T7 lytic phage has recently been shown to encode separate inhibitors of FtsZ (gp0.4) and MreB (gp0.6), which are hypothesized to provide replicative benefits for the phage (1,14,15). Whether these prophage-encoded TA systems provide any advantages to their *E. coli* host remains to be seen; cryptic prophage elements have been implicated in bacterial stress physiology (7,16) as have toxin-antitoxin systems (8,13,17).

Whatever the biological function of the CbtA toxin may be, this unique cytoskeletal inhibitor has the exciting potential to reveal additional molecular details of FtsZ and MreB assembly and function and to provide insight into the methods by which they can be inhibited. We hope that the genetic tools described here will be useful in future studies of CbtA mechanism and regulation, studies that may shed new light on the functional organization of the bacterial cytoskeleton.

Chapter 5.3: References

1. Tan Q, Awano N, Inouye M. YeeV is an Escherichia coli toxin that inhibits cell division by targeting the cytoskeleton proteins, FtsZ and MreB. Mol Microbiol. 2011 Jan;79(1):109–18.

2. Varma A, de Pedro MA, Young KD. FtsZ directs a second mode of peptidoglycan synthesis in Escherichia coli. J Bacteriol. 2007 Aug;189(15):5692–704.

3. Li Y, Hsin J, Zhao L, Cheng Y, Shang W, Huang KC, et al. FtsZ Protofilaments Use a Hinge-Opening Mechanism for Constrictive Force Generation. Science. 2013 Jul 25;341(6144):392–5.

4. Koppelman C-M, Aarsman MEG, Postmus J, Pas E, Muijsers AO, Scheffers D-J, et al. R174 of Escherichia coli FtsZ is involved in membrane interaction and protofilament bundling, and is essential for cell division. Mol Microbiol. 2003 Dec 16;51(3):645–57.

5. Haeusser DP, Rowlett VW, Margolin W. A mutation in Escherichia coli ftsZbypasses the requirement for the essential division gene zipAand confers resistance to FtsZ assembly inhibitors by stabilizing protofilament bundling. Mol Microbiol. 2015 Jul 4;:n/a–n/a.

6. van den Ent F, Izoré T, Bharat TA, Johnson CM, Lowe J. Bacterial actin MreB forms antiparallel double filaments. eLife. 2014;3:e02634.

7. Oliva MA, Cordell SC, Lowe J. Structural insights into FtsZ protofilament formation. Nat Struct Mol Biol. 2004 Nov 21;11(12):1243–50.

8. Cordell SC, Robinson EJH, Lowe J. Crystal structure of the SOS cell division inhibitor SulA and in complex with FtsZ. Proc Natl Acad Sci USA. 2003 Jun 24;100(13):7889–94.

9. Bisson-Filho AW, Discola KF, Castellen P, Blasios V, Martins A, Sforça ML, et al. FtsZ filament capping by MciZ, a developmental regulator of bacterial division. Proc Natl Acad Sci USA. 2015 Apr 6;:201414242.

10. Brown JM, Shaw KJ. A novel family of Escherichia coli toxin-antitoxin gene pairs. J Bacteriol. 2003 Nov;185(22):6600–8.

11. Arbing MA, Handelman SK, Kuzin AP, Verdon G, Wang C, Su M, et al. Crystal structures of Phd-Doc, HigA, and YeeU establish multiple evolutionary links between microbial growth-regulating toxin-antitoxin systems. Structure. 2010 Aug 11;18(8):996–1010.

12. Masuda H, Tan Q, Awano N, Wu K-P, Inouye M. YeeU enhances the bundling of cytoskeletal polymers of MreB and FtsZ, antagonizing the CbtA (YeeV) toxicity in Escherichia coli. Mol Microbiol. 2012 May 17;84(5):979–89.

13. Gerdes K, Christensen SK, Løbner-Olesen A. Prokaryotic toxin–antitoxin stress response loci. Nat Rev Micro. 2005 May;3(5):371–82.

14. Kiro R, Molshanski-Mor S, Yosef I, Milam SL, Erickson HP, Qimron U. Gene product 0.4 increases bacteriophage T7 competitiveness by inhibiting host cell division. Proc Natl Acad Sci USA. 2013 Nov 26;110(48):19549–54.

15. Molshanski-Mor S, Yosef I, Kiro R, Edgar R, Manor M, Gershovits M, et al. Revealing bacterial targets of growth inhibitors encoded by bacteriophage T7. Proc Natl Acad Sci USA. 2014 Dec 15;:201413271.

16. Wang X, Kim Y, Ma Q, Hong SH, Pokusaeva K, Sturino JM, et al. Cryptic prophages help bacteria cope with adverse environments. Nat Comms. 2010 Dec;1(9):147.

17. Page R, Peti W. Toxin-antitoxin systems in bacterial growth arrest and persistence. Nature Chemical Biology. 2016 Mar 18;12(4):208–14.

Appendix 1: Supplemental results and methods for Chapter 3

Attributions: I wrote this appendix in its entirety with helpful editing advice from my advisor, Ann Hochschild. I conducted the majority of the experimental work presented in this appendix under the guidance of Ann Hochschild. Mrinalini Tavag initiated the genetic screen to identify α-FtsZ variants with decreased CbtA interaction; I performed all subsequent characterization of isolated variants. I would like to acknowledge David Rudner and Alexander Meeske for helpful technical advice and reagents used in the *B. subtilis* experiments performed in this chapter, as well as Tom Bernhardt and Hongbaek Cho for useful reagents and strategies used in the *E. coli* FtsZ studies.

Appendix 1.1: Supplemental results

Description of additional α-FtsZ mutants identified in genetic screen for decreased FtsZ-CbtA interaction

In our initial screen to identify α-FtsZ mutants with decreased CbtA interaction, in addition to the H6/H7 loop mutants described in Chapter 3, we identified another cluster of mutations (G19V, ΔG19, G22D) that decreased interaction with CbtA (Figure A1.1A). We did not pursue these α-FtsZ variants further as they also exhibited a substantial decrease in self-interaction (only 40-60% of the wild-type interaction was maintained). Interestingly, we later found that they maintained about 65-75% of the wild-type interaction with λCI-ZipA-CTD, suggesting that their decrease in CbtA and self-interaction may be specific. Indeed, Western blot analysis showed that these mutants accumulate to levels comparable to the wild-type α-FtsZ fusion (Figure A1.1B). Residues G19 and G22 (shown in magenta) cluster near the GTP binding pocket in the N-terminal domain of FtsZ, close to the H6/H7 loop, but are not surface-exposed (Figure A1.1C). It is unlikely that these residues mediate direct interaction with CbtA, but these substitutions may lead to local rearrangements in the N-terminal domain, thereby affecting CbtA binding.

ftsZ-L169P, *ftsZ-D180N*, and *ftsZ-S177P* complement growth of an *ftsZ* complementation strain

The complementation phenotypes of the H6/H7 loop mutant alleles identified in our two-hybrid screen were tested using an *ftsZ* depletion strain (CH45/pDB346). Briefly, this depletion strain harbors an *ftsZ*^{0} allele on the chromosome, which is complemented by a plasmid-encoded wild-type allele under the control of the λR promoter and the temperature sensitive repressor λCI857 (1). At the permissive

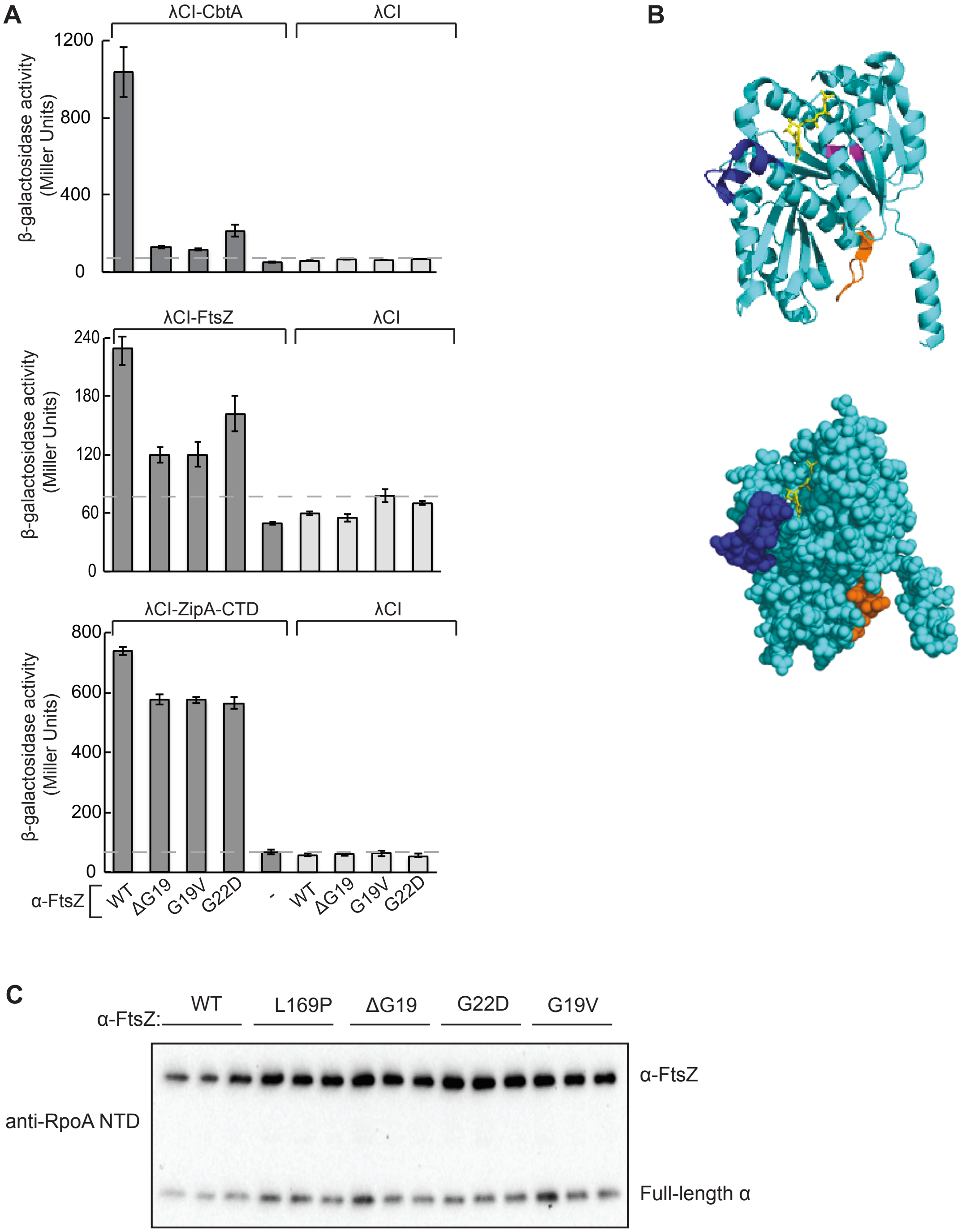

Figure A1.1: Mutation of FtsZ residues G19 and G22 decreases interaction with CbtA. A) Two-hybrid analysis shows that α-FtsZ-ΔG19, α-FtsZ-G19V, and α-FtsZ-G22D are substantially decreased for interaction with CbtA, modestly decreased for self-interaction, but maintain interaction with ZipA-CTD. The bars represent the average β-galactosidase activity from three independent measurements. Error

Figure A1.1 (Continued)

bars represent standard deviations. Experiments were done with 100 μM, 100 μM, and 25 μM IPTG, from top to bottom. B) Monomeric MjFtsZ (PDB 1W5B (1,2)) is shown in ribbon and space-filled renderings. The H6/H7 loop is shown in dark blue, the GTP moiety is shown in yellow, the T7 loop is shown in orange, and residues G19 and G22 are shown in magenta. C) Western blot analysis of α-FtsZ fusion levels was performed on lysates of cells expressing α-FtsZ fusions and wild-type λCI-CbtA (100 μM IPTG). The same lysates were used in the β-galactosidase assay shown in the top panel of A. Fusion proteins were detected using an antibody that binds the NTD of RpoA (α subunit of RNAP). This antibody also detects full-length RpoA, which serves as an internal loading control.

temperature (37 ºC), λCI857 is destabilized and wild-type *ftsZ* is expressed. When cells are shifted to the non-permissive temperature (30 ºC), λCI857 is properly folded and able to repress *ftsZ* expression from $P_{\lambda R}$. To assess complementation, our identified H6/H7 loop mutant alleles were cloned into the pDR3 plasmid under control of P_{lac} and transformed into the CH45/pDB346 depletion strain. We were unable to clone *ftsZ-L179R* into the pDR3 plasmid; thus it was excluded from this analysis. When cells were plated on LB without IPTG at 37 ºC, all strains grew well (Figure A1.2A); when cells were plated on LB with 100 µM IPTG at 30 ºC, *ftsZ-L169P*, *ftsZ-D180N*, and *ftsZ-S177P* strains grew as well as the strain expressing wild-type *ftsZ. ftsZ-F182S* did not support growth (Figure A1.2A).

As described in Chapter 3 of this dissertation, only *ftsZ-L169P* could be integrated into the chromosome at the endogenous *ftsZ* locus. The media and temperature-dependent growth phenotypes described previously are shown in Figure A1.2B.

Microscopic observation of *B. subtilis* strains

IPTG-inducible expression of *his$_6$-cbtA-gfp* from the *ycgO* locus in *B. subtilis* (strain DH85) had no appreciable effect on cell length or cell morphology as compared to an isogenic strain expressing *his$_6$-gfp* (strain DH84) (Figure A1.3). With the introduction of a genetically linked spectinomycin resistance cassette (*spec*) immediately downstream of the *ftsZ* ORF, cell length increased (Figure A1.3A). This may be due to alteration of normal transcription termination perhaps leading to a decrease in FtsZ levels. Although this was not tested here, it would be useful in the future to remake strains with *spec* positioned further downstream. Importantly, overexpression of *his$_6$-cbtA-gfp* in this background did not lead to further cell elongation or any other noticeable morphological change (Figure A1.3A). This observation is consistent with the lack of toxicity observed in Figure 3.5C and D.

Introduction of the chimeric $ftsZ_{ECloop}$ allele resulted in multiple division abnormalities (Figure A1.3B). All strains harboring this allele (DH102, DH103, and DH106) exhibited heterogeneous cell length, with a fraction of cells forming very long filaments. Careful quantification of cell length was very difficult as many cells were curved or even in some cases formed spirals, and therefore was not performed. Additionally, mini-cells, pre-mini-cell structures, and septa with abnormal appearance were observed frequently (Figure A1.3B and Figure A1.4). Thus, this chimeric allele is not able to fully support normal

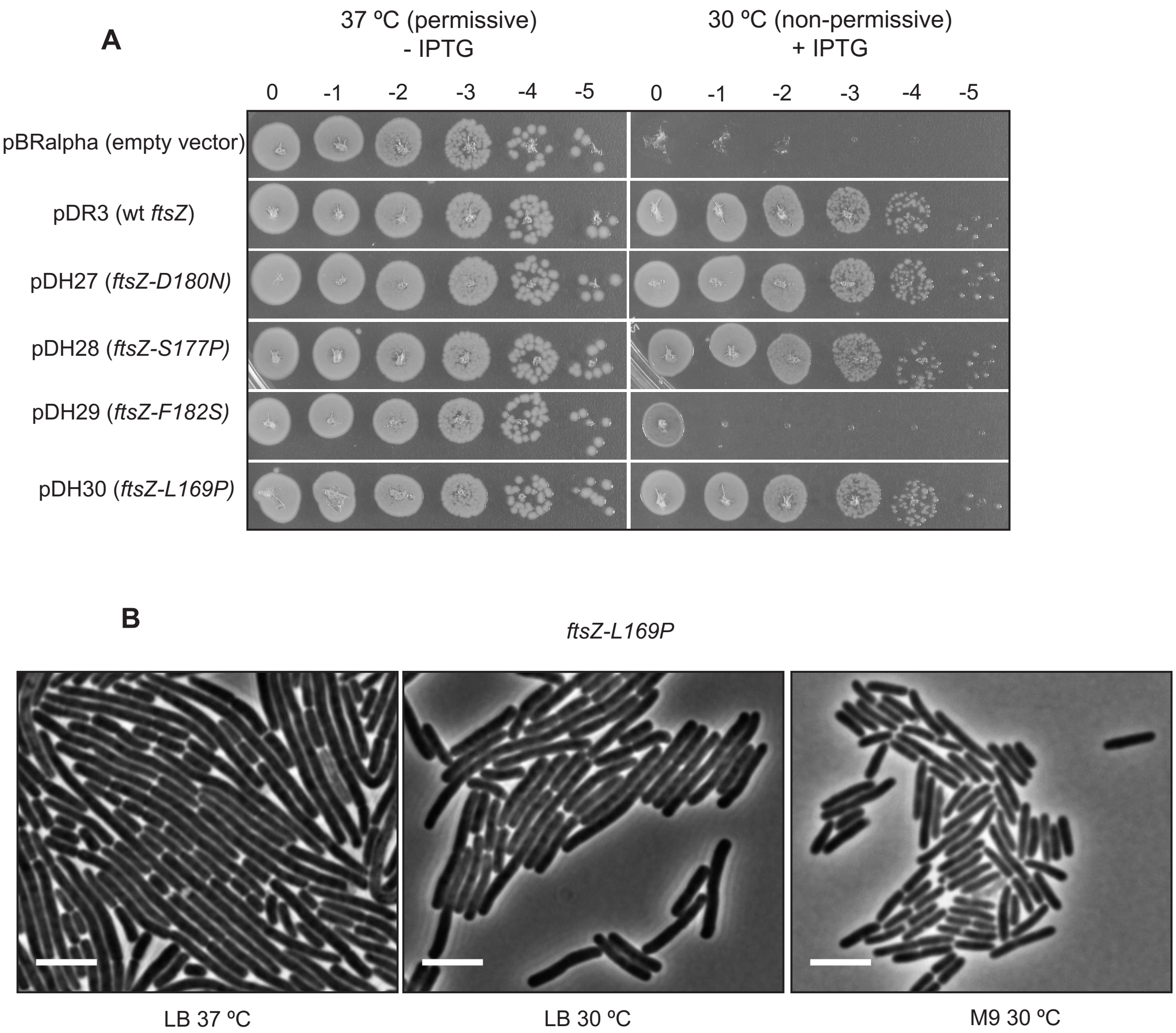
A
37 ºC (permissive)
- IPTG
30 ºC (non-permissive)
+ IPTG
0
-1
-2
-3
-4
-5
0
-1
-2
-3
-4
-5
pBRalpha (empty vector)
pDR3 (wt *ftsZ*)
pDH27 (*ftsZ-D180N)*
pDH28 (*ftsZ-S177P)*
pDH29 (*ftsZ-F182S)*
pDH30 (*ftsZ-L169P)*
B
ftsZ-L169P
LB 37 ºC
LB 30 ºC
M9 30 ºC

Figure A1.2: Complementation phenotypes of H6/H7 loop mutant alleles. A) The ability of *ftsZ* mutant alleles to complement growth of the CH45/pDB346 depletion strain was measured by spot dilution assay. Briefly, overnight cultures of CH45/pDB346 strains transformed with the indicated plasmids were back diluted to an OD600 of 0.05 in LB and grown at 37 ºC until they reached an OD600 of 1-1.5. Cultures were normalized to OD600, serially diluted in fresh LB, and spotted onto LB plates supplemented with the appropriate antibiotics, with or without 100 µM IPTG. Plates were incubated at the indicated temperature overnight. B) DH73 (BW27785 *ftsZ-L169P*) was grown from a single colony in either LB or M9 maltose (1 mM $MgSO_4$, 0.4% maltose, 0.01% casamino acids) at the indicated temperature until mid-log phase. Phase contrast images are shown. Scale bars represent 5 µm.

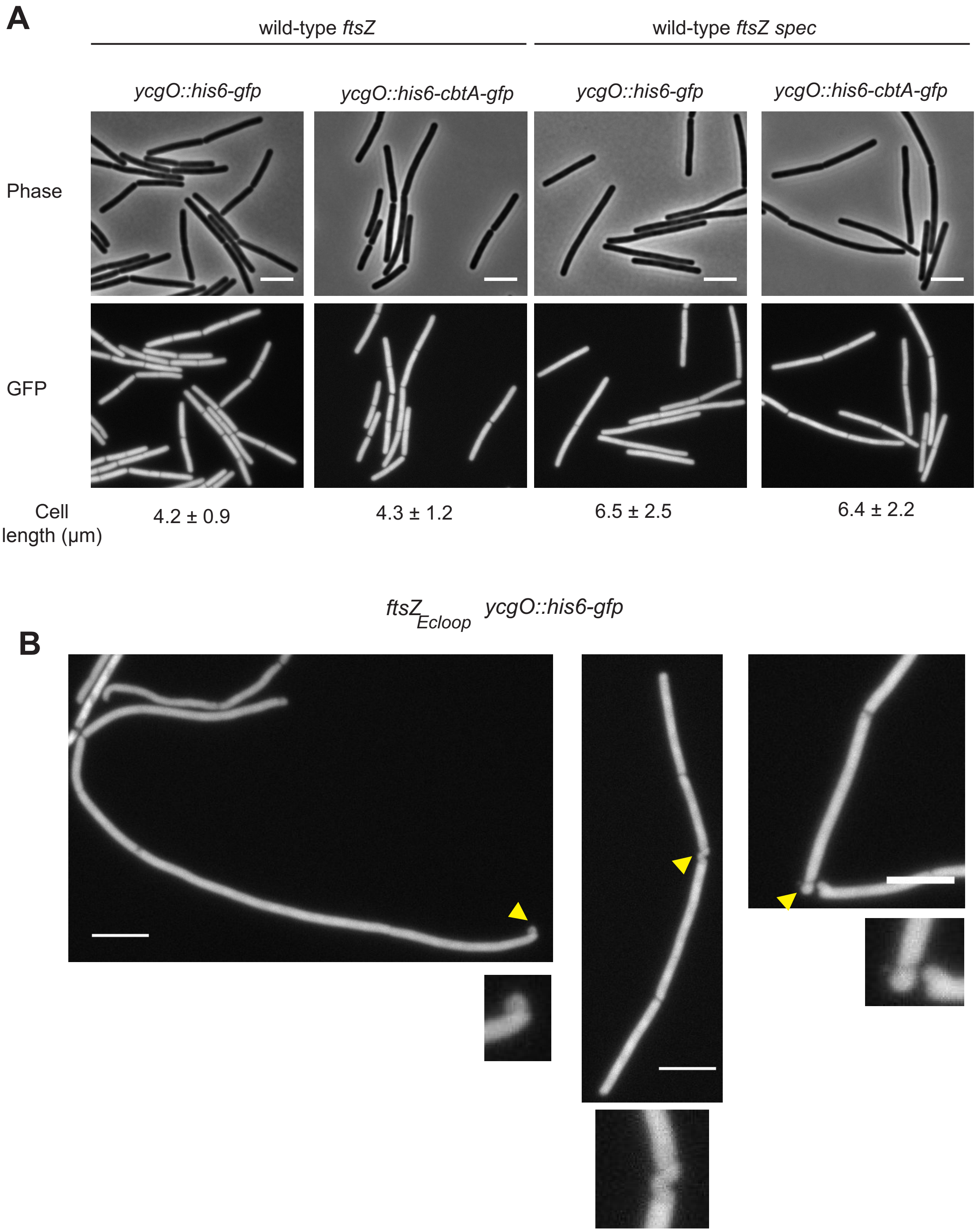
A
wild-type ftsZ
wild-type ftsZ spec
ycgO::his6-gfp
ycgO::his6-cbtA-gfp
ycgO::his6-gfp
ycgO::his6-cbtA-gfp
Phase
GFP
Cell length (µm)
4.2 ± 0.9
4.3 ± 1.2
6.5 ± 2.5
6.4 ± 2.2
ftsZ Ecloop ycgO::his6-gfp
B

Figure A1.3: CbtA is not toxic in strains with wild-type ftsZ. A) Strains with or without *spec* linked to the endogenous *ftsZ* locus and with *his*$_6$*-gfp* or *his*$_6$*-cbtA-gfp* expressed from *pHYPERSPANK* at the *ycgO* locus were imaged. Phase contrast and GFP fluorescence images are shown. Briefly, overnight cultures

Figure A1.3 (Continued)

grown in LB at 22 ºC were back diluted to a starting OD600 of 0.01 in LB supplemented with 1 mM IPTG. Cultures were grown at 37 ºC for 1.5 hrs until cultures reached an OD600 ~0.2. The cell length of ~200 cells was measured for each strain (*n*=200, *n*=200, *n*=203, *n*=205, from left to right). Measurements from a single representative experiment are shown. B) Strain DH102 with the chimeric *ftsZ*$_{ECloop}$ allele linked to *spec* and *his*$_6$*-gfp* expressed from *pHYPERSPANK* at the *ycgO* locus was imaged as described in A. GFP fluorescence images are shown. The mini-cells and abnormal septum pointed out by the yellow arrows are shown in the zoomed-in panels. For both A and B, scale bars represent 5 μm.

ftsZ$_{Ecloop}$ *ycgO::his6-gfp*

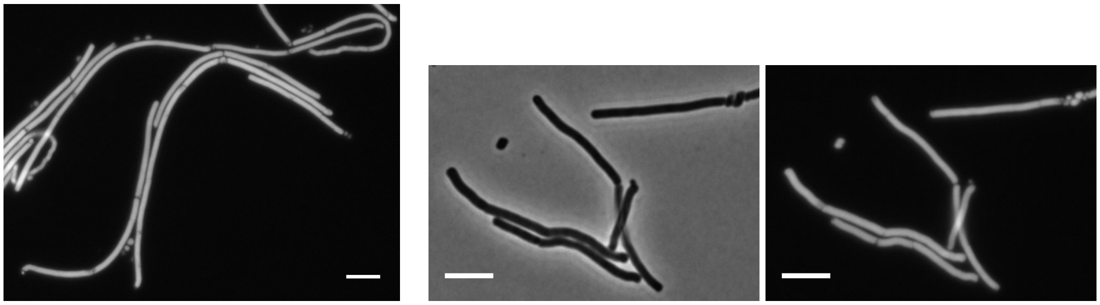

ftsZ$_{Ecloop}$ *ycgO::his6-cbtA-gfp*

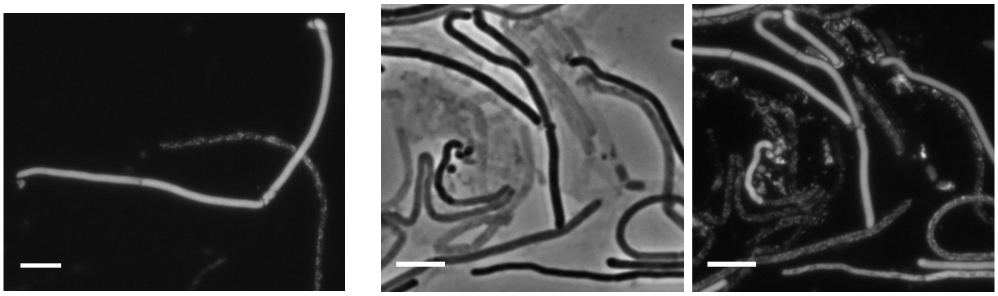

ftsZ$_{Ecloop}$ *ycgO::his6-cbtA-F65S-gfp*

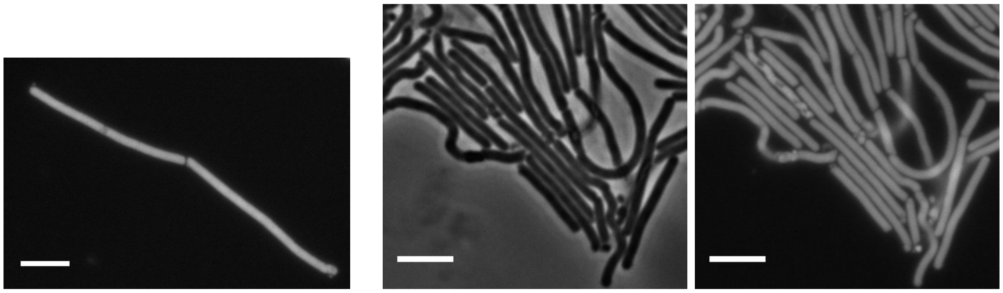

Figure A1.4: CbtA production leads to increased lysis in chimera strain. Shown are phase contrast (left panels, 200 min) and GFP fluorescence images (all panels, 130 min, right panels, 200 min) of strains DH102, DH103, and DH106 containing the chimeric *ftsZ*$_{ECloop}$ allele linked to *spec* and *his*$_6$*-gfp*, *his*$_6$*-cbtA-gfp*, and *his*$_6$*-cbtA-F65S-gfp* expressed from *pHYPERSPANK* at the *ycgO* locus, respectively. Briefly, overnight cultures grown in LB at 22 ºC were back diluted to a starting OD600 of 0.01 in LB supplemented with 1 mM IPTG. Cultures were grown at 37 ºC for several

Figure A1.4 (Continued)

hours. Images were taken at 130 min when all cultures were in mid-log phase, and at 200 min when DH102 and DH106 were at an OD600 ~1.2, and DH103 had only reached an OD600 of ~0.5.

cell division. The most obvious phenotype observed upon expression of *his_6-cbtA-gfp* in this background, was pronounced lysis (Figure A1.4). While some lysis was observed after 130 min, after induction of expression for 200 min, strain DH103 (*his_6-cbtA-gfp)* showed signs of copious lysis, while strains DH102 (*his_6-gfp)* and DH106 (*his_6-cbtA-F65S-gfp*) did not. This phenotype correlates with the cell growth defect observed in liquid culture (Figure 3.5D). In all strains imaged, His_6-CbtA-GFP displayed diffuse localization.

Appendix 1.2: Supplemental Methods

All general techniques were the same as described in Chapter 3 of this dissertation. Microscopic observation of *ftsZ-L169P* and *B. subtilis* strains was performed using an Olympus BX61 microscope (objective UplanF1 100x). Images were captured with a monochrome CoolSnapHQ digital camera (Photometrics) using Metamorph software version 6.1 (Universal Imaging). Images were cropped and adjusted in ImageJ, and cell length measurements were made using ObjectJ (3). GFP fluorescence images were used for cell length measurements for easier identification of cell septa.

All strains, plasmids, and DNA oligonucleotides used in this appendix as well as Chapter 3 are shown in Tables A1.1, A1.2, and A1.3, respectively. Plasmids used for the complementation assay (pDH27, pDH28, pDH29, pDH30) were constructed by restriction digest (XbaI/ HindIII) of PCR products amplified by primers opDR31_F and opDR32_R (using relevant pBRα-FtsZ plasmids as template). These inserts were ligated into backbone generated by XbaI/HindIII digest of pDR3.

Complementation studies with mutant *ftsZ* alleles

Plasmids (pDR3, pBRα, pDH27, pDH28, pDH29, pDH30) were transformed into CH45/pDB346, plated on LB (Spec Carb), and incubated at 37 ºC overnight. Overnight cultures grown in LB (Spec Carb) at 37 ºC were back diluted to an OD600 of 0.05 in fresh medium and grown until they reached a final OD600 of ~1. Cultures were normalized by OD600, 1:10 serial dilutions were made in fresh LB, and 5 µL of each culture was spotted on LB (Spec Carb) with or without 100 µM IPTG. Plates without IPTG were incubated at 37 ºC overnight; plates supplemented with IPTG were incubated at 30 ºC overnight.

Western blot analysis of α-FtsZ fusions

Lysates from a β-galactosidase assay measuring the interaction between the shown α-FtsZ mutants and λCI-CbtA (with 100 μM IPTG induction) were generated from triplicate cultures as described in Chapter 3. Total protein levels were measured by Bradford assay, and lysates were normalized in lysis buffer to contain the same amount of total protein. Normalized lysates were diluted in 4X Laemmli buffer. Standard SDS-PAGE and transfer techniques were used. Anti-RpoA-NTD antibody was used at a concentration of 1:5,000; secondary anti-mouse antibody was used at a concentration of 1:10,000.

Table A1.1: Bacterial strains used in this study

Strain	Description	Reference/ source
E. coli strains:		
NEB5-α F'I^q	DH5-α derivative containing an F' (Tet resistant) bearing *lacI*^{q}	New England Biolabs
FW102 O$_L$2-62	FW102 (4) containing an F' (Kan resistant) bearing the p*lac*OL2–62-*lacZ* fusion in which the λCI operator is centered at position –62 upstream of the *lac* promoter	(5)
BW27785	Δ(*araB-araD*)*567* Δ*lacZ4787*(::*rrnB-3*) LAM- Δ(*araH-araF*)*570*(::*FRT*) Δ*araEp-532*::*FRT* φ(*Pcp18-araE534*) Δ(*rhaB-rhaD*)*568 hsdR514*	(6)
DH73	BW27785 containing *ftsZ-L169P* allele at the endogenous *ftsZ* locus. This mutation is not linked to a selectable marker	This study
CH45/pDB346	*ftsZ*^{0}/*P*$_{\lambda R}$-*ftsZ, cI857; ftsZ* expression is repressed upon shift to 30 ºC ; plasmid confers resistance to Spec	(1,7); Generous gift of T. Bernhardt
B. subtilis strains:	All PY79 derivatives	(8)
DH84	*ycgO:: pHYPERSPANK-his*$_6$*-gfp erm*	This study
DH85	*ycgO:: pHYPERSPANK-his*$_6$*-cbtA-gfp erm*	This study
DH98	*ftsZ spec (spec* is immediately downstream of the wild-type *ftsZ* locus)	This study
DH99	*ftsZ*$_{Ecloop}$ *spec (spec* is immediately downstream of the *ftsZ* locus. The wt *ftsZ* allele is replaced with a chimeric *ftsZ* encoding Ec residues 168-182 in place of Bs residues 169-183 in the context of full-length Bs *ftsZ.*)	This study
DH100	*ftsZ spec, ycgO:: pHYPERSPANK-his*$_6$*-gfp erm*	This study
DH101	*ftsZ spec, ycgO:: pHYPERSPANK-his*$_6$*-cbtA-gfp erm*	This study
DH102	*ftsZ*$_{Ecloop}$ *spec, ycgO:: pHYPERSPANK-his*$_6$*-gfp erm*	This study
DH103	*ftsZ*$_{Ecloop}$ *spec, ycgO:: pHYPERSPANK-his*$_6$*-cbtA-gfp erm*	This study
DH104	*ycgO:: pHYPERSPANK-his*$_6$*-cbtA-F65S-gfp erm*	This study
DH105	*ftsZ*$_{Ecloop}$ *spec, ycgO:: pHYPERSPANK-his*$_6$*-cbtA-F65S-gfp erm*	This study

Table A1.2: Plasmids used in this study

Plasmid	Description	Reference/ source
pBRα	Encodes the full-length α subunit of RNAP under the control of tandem p*lacUV5* and p*lpp* promoters; confers resistance to Carb	(9)
pACλCI	Encodes λCI (residues 1-236) under the control of *lacUV5* promoter; confers resistance to Cm	(9)
pBRα-FtsZ (pMT153)	Encodes residues 1-248 of α fused by a three-alanine linker to full-length *E. coli* FtsZ under the control of tandem p*lacUV5* and p*lpp* promoters; confers resistance to Carb	This study; M. Tavag
pACλCI-FtsZ (pMT152)	Encodes λCI fused by a three-alanine linker to full-length *E. coli* FtsZ under the control of *lacUV5* promoter; confers resistance to Cm	This study; M. Tavag
pBRα-CbtA (pMT154)	Encodes residues 1-248 of α fused by a three-alanine linker to full-length CbtA under the control of tandem p*lacUV5* and p*lpp* promoters; confers resistance to Carb	This study; M. Tavag
pACλCI-CbtA (pMT155)	Encodes λCI fused by a three-alanine linker to full-length CbtA under the control of *lacUV5* promoter; confers resistance to Cm	This study; M. Tavag
pACλCI-ZipA-CTD (pDH159)	Encodes λCI fused by a three-alanine linker to residues 186-328 of ZipA under the control of *lacUV5* promoter; confers resistance to Cm	This study
pBRα-FtsZ-L169P	Encodes residues 1-248 of α fused by a three-alanine linker to FtsZ-L169P under the control of tandem p*lacUV5* and p*lpp* promoters; isolated in an α-FtsZ mutant screen; confers resistance to Carb	This study
pBRα-FtsZ-S177P	Encodes residues 1-248 of α fused by a three-alanine linker to FtsZ-S177P under the control of tandem p*lacUV5* and p*lpp* promoters; isolated in an α-FtsZ mutant screen; confers resistance to Carb	This study
pBRα-FtsZ-D180N	Encodes residues 1-248 of α fused by a three-alanine linker to FtsZ-D180N under the control of tandem p*lacUV5* and p*lpp* promoters; isolated in an α-FtsZ mutant screen; confers resistance to Carb	This study
pBRα-FtsZ-F182S	Encodes residues 1-248 of α fused by a three-alanine linker to FtsZ-F182S under the control of tandem p*lacUV5* and p*lpp* promoters; isolated in an α-FtsZ mutant screen; confers resistance to Carb	This study

Table A1.2 (Continued)

Plasmid	Description	Reference/ source
pBRα-FtsZ-L179R	Encodes residues 1-248 of α fused by a three-alanine linker to FtsZ-L179R under the control of tandem p*lacUV5* and p*lpp* promoters; isolated in an α-FtsZ mutant screen; confers resistance to Carb	This study
pBRα-FtsZ-D373G (pDH196)	Encodes residues 1-248 of α fused by a three-alanine linker to *E. coli* FtsZ-D373G under the control of tandem p*lacUV5* and p*lpp* promoters; confers resistance to Carb	This study
pBRα-FtsZΔ66 (pDH198)	Encodes residues 1-248 of α fused by a three-alanine linker to *E. coli* FtsZ (residues 2-317; the last 66 residues are deleted) under the control of tandem p*lacUV5* and p*lpp* promoters; confers resistance to Carb	This study
pACλCI-CbtA-V48E (pDH200)	Encodes λCI fused by a three-alanine linker to CbtA-V48E under the control of *lacUV5* promoter; isolated in λCI-CbtA mutant screen; confers resistance to Cm	This study
pBRα-FtsZ-G19V	Encodes residues 1-248 of α fused by a three-alanine linker to FtsZ-G19V under the control of tandem p*lacUV5* and p*lpp* promoters; isolated in an α-FtsZ mutant screen; confers resistance to Carb	This study
pBRα-FtsZ-ΔG19	Encodes residues 1-248 of α fused by a three-alanine linker to FtsZ (residue G19 is deleted) under the control of tandem p*lacUV5* and p*lpp* promoters; isolated in an α-FtsZ mutant screen; confers resistance to Carb	This study
pBRα-FtsZ-G22D	Encodes residues 1-248 of α fused by a three-alanine linker to FtsZ-G22D under the control of tandem p*lacUV5* and p*lpp* promoters; isolated in an α-FtsZ mutant screen; confers resistance to Carb	This study
pBRα-YkfI (pMT173)	Encodes residues 1-248 of α fused by a three-alanine linker to YkfI under the control of tandem p*lacUV5* and p*lpp* promoters; confers resistance to Carb	This study; M. Tavag
pACλCI-YkfI (pMT169)	Encodes λCI fused by a three-alanine linker to YkfI under the control of *lacUV5* promoter; confers resistance to Cm	This study; M. Tavag
pBRα-YpjF (pMT174)	Encodes residues 1-248 of α fused by a three-alanine linker to YpjF under the control of tandem p*lacUV5* and p*lpp* promoters; confers resistance to Carb	This study; M. Tavag
pACλCI-YpjF (pMT170)	Encodes λCI fused by a three-alanine linker to YpjF under the control of *lacUV5* promoter; confers resistance to Cm	This study; M. Tavag

Table A1.2 (Continued)

Plasmid	Description	Reference/ source
pACλCI-EcFtsZ$_{\text{Bsloop}}$ (pDH59)	Encodes λCI fused by a three-alanine linker to EcFtsZ with residues 168-182 replaced with BsFtsZ residues 169-183 under the control of *lacUV5* promoter; confers resistance to Cm	This study
pACλCI-BsFtsZ (pDH62)	Encodes λCI fused by a three-alanine linker to BsFtsZ under the control of *lacUV5* promoter; confers resistance to Cm	This study
pACλCI-BsFtsZ$_{\text{ECloop}}$ (pDH66)	Encodes λCI fused by a three-alanine linker to BsFtsZ with residues 169-183 replaced with EcFtsZ residues 168-182 under the control of *lacUV5* promoter; confers resistance to Cm	This study
pCX41	Bears a temperature-sensitive origin of replication and a HindIII/ClaI fragment containing *ftsZ* and flanking homology to *ftsA* and *lpxC*; confers resistance to Cm (10 µg/mL)	(10); Generous gift of T. Bernhardt
pCX41-F268C	Bears a temperature-sensitive origin of replication and a HindIII/ClaI fragment containing *ftsZ-F286C* and flanking homology to *ftsA* and *lpxC*; confers resistance to Cm (10 µg/mL)	Generous gift of T. Bernhardt
pCX41-D180N (pDH33)	Bears a temperature-sensitive origin of replication and a HindIII/ClaI fragment containing *ftsZ-D180N* and flanking homology to *ftsA* and *lpxC*; confers resistance to Cm (10 µg/mL)	This study
pCX41-S177P (pDH34)	Bears a temperature-sensitive origin of replication and a HindIII/ClaI fragment containing *ftsZ-S177P* and flanking homology to *ftsA* and *lpxC*; confers resistance to Cm (10 µg/mL)	This study
pCX41-L169P (pDH35)	Bears a temperature-sensitive origin of replication and a HindIII/ClaI fragment containing *ftsZ-L169P* and flanking homology to *ftsA* and *lpxC*; confers resistance to Cm (10 µg/mL)	This study
pDR3	Encodes full-length *E. coli* FtsZ under the control of *lac* promoter; ColE1 origin with *lacI*^{q}; confers resistance to Carb	(11,12); Generous gift of T. Bernhardt
pDR3-D180N (pDH27)	Encodes full-length *E. coli* FtsZ-D180N under the control of *plac* promoter; ColE1 origin with *lacI*^{q}; confers resistance to Carb	This study
pDR3-S177P (pDH28)	Encodes full-length *E. coli* FtsZ-S177P under the control of *plac* promoter; ColE1 origin with *lacI*^{q}; confers resistance to Carb	This study

Table A1.2 (Continued)

Plasmid	Description	Reference/ source
pDR3-F182S (pDH29)	Encodes full-length *E. coli* FtsZ-F182S under the control of *plac* promoter; ColE1 origin with *lacI^q*; confers resistance to Carb	This study
pDR3-L169P (pDH30)	Encodes full-length *E. coli* FtsZ-L169P under the control of *plac* promoter; ColE1 origin with *lacI^q*; confers resistance to Carb	This study
pMT139	Derivative of pCA24N; Encodes full-length His$_6$-CbtA-GFP under the control of pT_5/lac promoter; pBR origin and confers resistance to Cm	(13);This study
pDH84	Encodes His$_6$-GFP under the control of $p_{HYPERSPANK}$; confers resistance to Carb in *E. coli* and to MLS in *B. subtilis*	This study
pDH85	Encodes His$_6$-CbtA-GFP under the control of $p_{HYPERSPANK}$; confers resistance to Carb in *E. coli* and to MLS in *B. subtilis*	This study
pDH102	Encodes His$_6$-CbtA-F65S-GFP under the control of $p_{HYPERSPANK}$; confers resistance to Carb in *E. coli* and to MLS in *B. subtilis*	This study
pDR111	Used for integration of sequences into *B. subtilis amyE* locus; confers resistance to Carb in *E. coli* and Spec in *B. subtilis*	Generous gift of D. Rudner

Table A1.3: Important DNA oligonucleotides used in this study

Name	Sequence (5' to 3')	Description
pBRα_F	GAACAGCGTACCGACCTGGAC	Sequencing primer for all pBRα fusion constructs
pBRα_R	CCTATATCGCCGACATCACC	Sequencing primer for all pBRα fusion constructs
pACλCI_F	GATCAGGGATAGCGGTCAGG	Sequencing primer for all λCI fusion constructs
pACλCI_R	CCTACATCTGTATTAACGAAGC	Sequencing primer for all λCI fusion constructs
oDH70	TATATAGCGGCCGCATTTGAACCAATGGAAC	Forward primer for amplification of *ftsZ;* contains a NotI site
oDH71	TATATAGGATCCTTAATCAGCTTGCTTACGC	Reverse primer for amplification of *ftsZ*; contains BamHI site
oSG727	GGGGACAAGTTTGTACAAAAAAGCAGGCTTCGCGGCCGCAAAAACATTACCTGTATTACCCGGG	Forward primer for amplification of *cbtA;* contains a NotI site
oSG728	GGGGACCACTTTGTACAAGAAAGCTGGGTCGGATCCTTATTTCGCCTCCGGATACTTACC	Reverse primer for amplification of *cbtA*; contains BamHI site
oDH86	TATATAGCGGCCGCATTGGAGTTCGAAACAAACATAG	Forward primer for amplification of *B. subtilis ftsZ;* contains a NotI site
oDH87	TATATAGGATCCTTAGCCGCGTTTATTACGG	Reverse primer for amplification of *B. subtilis ftsZ;* contains a BamHI site
oSG729	GGGGACAAGTTTGTACAAAAAAGCAGGCTTCGCGGCCGCAAAAACTTTACCTGCAATAACTCAGCGG	Forward primer for amplification of *ykfI;* contains a NotI site
oSG730	GGGGACCACTTTGTACAAGAAAGCTGGGTCGGATCCTTATCGTACTACGTTGTTACGGC	Reverse primer for amplification of *ykfI*; contains BamHI site
oSG731	GGGGACAAGTTTGTACAAAAAAGCAGGCTTCGCGGCCGCAAACACTCTACCTGCTACAATTTCGC	Forward primer for amplification of *ypjF;* contains a NotI site
oSG732	GGGGACCACTTTGTACAAGAAAGCTGGGTCGGATCCTTATTTCACATTAGTTTTTAGCAAGCCGG	Reverse primer for amplification of *ypjF*; contains BamHI site
oDH237	TATATAGGATCCTCAGGCGTTGGCGTCTTTG	Reverse primer for amplification of *zipA-CTD;* contains a BamHI site
oDH238	TATATAGCGGCCGCAGATAAACCGAAGCGCAAAG	Forward primer for amplification of *zipA-CTD;* contains a NotI site
oDH239	CCGCGGTATCTCCCTGCTGAAAGCGTTTGGCGCAGCGAACG	For overlap PCR to generate *ftsZ-D180K*

Table A1.3 (Continued)

Name	Sequence (5' to 3')	Description
oDH240	CGTTCGCTGCGCCAAACGCTTTCAGCAGGGAGATACCGCGG	For overlap PCR to generate *ftsZ-D180K*
oDH278	TATATAGGATCCTTAATCAGCTTGCTTACGCAGGAATGCTGGGATACCCAGATAATCCGGCTCTTTC	Reverse primer to clone *ftsZ-D373G*; contains a BamHI site
oDH279	TATATAGGATCCTTACATGCCGATACCTGTCGC	Reverse primer to clone *ftsZΔ66*; BamHI site
oDH84	CATCGGTGTGTTTTTATCAACAATTTCAAGGATTTTGTCGTTCGGGATAGTGATCAGAG	For overlap PCR to generate *E. coli ftsZ*$_{Bsloop}$
oDH85	GATAAAAACACACCGATGCTTGAAGCATTCGGCGCAGCGAACGATGTACTGAAAGGCG	For overlap PCR to generate *E. coli ftsZ*$_{Bsloop}$
oDH101	CAGGGAGATACCGCGGCCCAGAACTTTCAGCAGACGGTCGTTCGGGATCACGATC	For overlap PCR to generate *B. subtilis ftsZ*$_{Ecloop}$
oDH102	TGGGCCGCGGTATCTCCCTGCTGGATGCGTTTCGCGAAGCGGATAACGTAC	For overlap PCR to generate *B. subtilis ftsZ*$_{Ecloop}$
oDH36	GCATTAAAGCTTCGCCAACAAGGGGTTAAACATCACCTGG	Forward primer to clone *ftsZ* alleles into pCX41; contains HindIII site
oDH37	GCTTATCATCGATGCCCAAGCCCGCGAGAGCAG	Reverse primer to clone *ftsZ* alleles into pCX41; contains ClaI site
oDH34	GACAAACTGCCGAAAGTTCTGGGCCGCGG	For overlap PCR to generate *ftsZ-L169P*
oDH35	CCGCGGCCCAGAACTTTCGGCAGTTTG	For overlap PCR to generate *ftsZ-L169P*
oDH32	GCGGTATCCCCCTGCTGGATGCGTTTGG	For overlap PCR to generate *ftsZ-S177P*
oDH33	CCAAACGCATCCAGCAGGGGGATACCG	For overlap PCR to generate *ftsZ-S177P*
oDH30	TCCCTGCTGAATGCGTTTGGCGCAGCG	For overlap PCR to generate *ftsZ-D180N*
oDH31	CGCTGCGCCAAACGCATTCAGCAGGG	For overlap PCR to generate *ftsZ-D180N*
oDH108	ATATATATGCTAGCTTATTTGTATAGTTCATCCATGCCATGTGTAATC	Reverse primer to clone *cbtA* alleles into *B. subtilis* integration constructs; Contains NheI site
oDH116	ATATATAAGCTTACATAAGGAGGAACTACTATGAGAGGATCTCACCATCACCATC	Forward primer to clone *cbtA* alleles into *B. subtilis* integration constructs; Contains HindIII site
oDH130	CTCCGCTGCGTTGAAAGAG	For construction of strain DH98

Table A1.3 (Continued)

Name	Sequence (5' to 3')	Description
oDH131	GGGCTGCAGGAATTCTTAGCCGCGTTTATTACGGTTTC	For construction of strain DH98
oDH132	TAATAAACGCGGCTAAGAATTCCTGCAGCCCTGGCG	For construction of strain DH98
oDH133	ATTTTGTCCTTTACAGATCCCCCTATGCAAGGGTT	For construction of strain DH98
oDH134	TTGCATAGGGGGATCTGTAAAGGACAAAATCGTTTTG	For construction of strain DH98
oDH135	AGATGTCACACTCACATTG	For construction of strain DH98
oDH141	GATTTGCTGAAAAAGCTG	For construction of strain DH99
oDH142	GTTTGTTTCGAACTCCAACATGCTAAATCCTCCTAATCTGCC	For construction of strain DH99
oDH143	TTAGGAGGATTTAGCATGTTGGAGTTCGAAACAAACATAG	For construction of strain DH99
oDH167	AAGCACATAAAAATATTCTG	Amplifies *B. subtilis ftsA ftsZ*
oDH168	GCCAGTCACGTTACGTTATTAG	Amplifies *B. subtilis ftsA ftsZ*
oDH127	TGACATGGTATTCGTGACAGC	Internal *B. subtilis ftsZ* sequencing primer
oDH124	ATATATGTCGACGTCTTAGGAGGATTTAGCATGTTGGAGTTCGAAACAAACATAG	*B. subtilis ftsZ* sequencing primer
oDH125	ATATATGGATCCTTAGCCGCGTTTATTACGGTTTC	*B. subtilis ftsZ* sequencing primer
oDH172	ATAATAAACAGAGCAAAATG	*B. subtilis ftsZ* sequencing primer
oDH173	TTATAACATGTATTCACGAAC	*B. subtilis ftsZ* sequencing primer
oPDR31	CCCTCTAGAAATAATTTTGTTTAACTTTAAGAAGGAGATATACATATGTTTGAACCAATGGAACTTAC	For cloning *ftsZ* alleles into pDR3; contains HindIII site
oPDR32	GCCAAGCTTGTCGACTCTTAATCAGCTTGCTTACGCAGG	For cloning *ftsZ* alleles into pDR3; contains XbaI site

Appendix 1.3: References

1. Raskin DM, de Boer PA. The MinE ring: an FtsZ-independent cell structure required for selection of the correct division site in E. coli. Cell. 1997 Nov 28;91(5):685–94.

2. Oliva MA, Cordell SC, Lowe J. Structural insights into FtsZ protofilament formation. Nat Struct Mol Biol. 2004 Nov 21;11(12):1243–50.

3. Schneider CA, Rasband WS, Eliceiri KW. NIH Image to ImageJ: 25 years of image analysis. Nat Meth. Nature Publishing Group; 2012 Jul 1;9(7):671–5.

4. Whipple FW. Genetic analysis of prokaryotic and eukaryotic DNA-binding proteins in Escherichia coli. Nucleic Acids Research. 1998 Aug 15;26(16):3700–6.

5. Deaconescu AM, Chambers AL, Smith AJ, Nickels BE, Hochschild A, Savery NJ, et al. Structural Basis for Bacterial Transcription-Coupled DNA Repair. Cell. 2006 Feb;124(3):507–20.

6. Khlebnikov A, Datsenko KA, Skaug T. Homogeneous expression of the PBAD promoter in Escherichia coli by constitutive expression of the low-affinity high-capacity AraE transporter. …. 2001.

7. Skoog K, Daley DO. The Escherichia coliCell Division Protein ZipA Forms Homodimers Prior to Association with FtsZ. Biochemistry. 2012 Feb 21;51(7):1407–15.

8. Youngman PJ, Perkins JB, Losick R. Genetic transposition and insertional mutagenesis in Bacillus subtilis with Streptococcus faecalis transposon Tn917. Proc Natl Acad Sci USA. 1983 Apr;80(8):2305–9.

9. Dove SL, Joung JK, Hochschild A. Activation of prokaryotic transcription through arbitrary protein-protein contacts. Nature. 1997 Apr 10;386(6625):627–30.

10. Wang XD, de Boer P, Rothfield LI. A factor that positively regulates cell division by activating transcription of the major cluster of essential cell division genes of Escherichia coli. EMBO J. 1991.

11. Bendezu FO, de Boer PAJ. Conditional Lethality, Division Defects, Membrane Involution, and Endocytosis in mre and mrd Shape Mutants of Escherichia coli. J Bacteriol. 2008 Feb 20;190(5):1792–811.

12. Bernhardt TG, de Boer PAJ. SlmA, a Nucleoid-Associated, FtsZ Binding Protein Required for Blocking Septal Ring Assembly over Chromosomes in E. coli. Molecular Cell. 2005 May;18(5):555–64.

13. Kitagawa M, Ara T, Arifuzzaman M, Ioka-Nakamichi T, Inamoto E, Toyonaga H, et al. Complete set of ORF clones of Escherichia coli ASKA library (a complete set of E. coli K-12 ORF archive): unique resources for biological research. DNA Res. 2005;12(5):291–9.